ABSTRACT

Title of Document: MICROSTRUCTURAL CHARACTERIZATION OF ULTRASONIC IMPACT TREATED AL-MG ALLOY

Kim Ngoc Thi Tran, Doctor of Philosophy, 2012

Directed By: Professor Lourdes Salamanca-Riba

Department of Materials Science & Engineering

Aluminum 5456-H116 has high as-welded strength, is formable, and highly corrosion resistant, however, it can become sensitized when exposed to elevated temperatures for a prolonged time. Sensitization results in the formation of a continuous β phase at the grain boundaries that is anodic to the matrix. Thus the grain boundaries become susceptible to stress corrosion cracking (SCC) and intergranular corrosion cracking (IGC). Cracking issues on aluminum superstructures have prompted the use of a severe plastic deformation processes, such as ultrasonic impact treatment (UIT), to improve SCC resistance. This study correlated the effects of UIT on the properties of 5456-H116 alloy to the microstructural evolution of the alloy and helped develop a fundamental understanding of the mechanisms that cause the microstructural evolution.

Ultrasonic impact treatment produces a deformed layer at the surface ~ 10 to 18 μm thick that is characterized by micro-cracks, tears, and voids. Ultrasonic impact

treatment results in grain refinement within the deformation layer and extending below the deformed layer. The microstructure exhibits weak crystallographic texture with larger fraction of high angle grain boundaries.

Nanocrystalline grains within the deformation layer vary in size from 2 to 200 nm in diameter and exhibit curved or wavy grain boundaries. The nanocrystalline grains are thermally stable up to 300°C. Above 300°C, grain growth occurs with an activation energy of ~ 32 kJ/mol. Below the deformation layer, the microstructure is characterized by submicron grains, complex structure of dislocations, sub-boundaries, and Moiré fringes depicting overlapping grains. The deformation layer does not exhibit the presence of a continuous β phase, however below the deformation layer; a continuous β phase along the grain boundaries is present.

In general the highest hardness and yield strength is at the UIT surface which is attributed to the formation of nanocrystalline grains. Although the highest hardness and yield strength was observed at the UIT surface, the results were mixed with some lower values. The lower hardness and yield strength values at the UIT surface are attributed to the voids and micro cracking/micro voids observed in the deformation layer. The fracture mode was transgranular ductile fracture with micro void coalescence and dimples. Both UIT and untreated material exhibit similar levels of intergranular corrosion susceptibility. Corrosive attack was intergranular with slightly deeper attack in the untreated material.

Numerical simulation modeling showed that the calculated residual stress under the tool, ~80 MPa, is of the same order of magnitude as the compressive residual stresses measured by XRD measurements near the surface. Modeling also

showed that high effective strains were induced almost immediately. The UIT process also resulted in rapid localized heating to a maximum temperature of ~32°C during the first eleven pin tool cycles. The model also showed that during UIT processing, the material undulates as the pin tool impacts and retracts from the surface of the material. The undulations represent the elastic response of the surface to the compressive stresses built up during a pin tool cycle.

MICROSTRUCTURAL CHARACTERIZATION OF ULTRASONIC IMPACT TREATED AL-MG ALLOY

By

Kim Ngoc Thi Tran

Dissertation submitted to the Faculty of the Graduate School of the
University of Maryland, College Park, in partial fulfillment
of the requirements for the degree of
Doctor of Philosophy
2012

Advisory Committee:
Professor Lourdes Salamanca-Riba, Dept. of Materials Science & Engineering, Chair
Professor Manfred Wuttig, Dept. of Materials Science & Engineering
Professor Luz Martinez-Miranda, Dept. of Materials Science & Engineering
Professor F. Patrick McCluskey, Dept. of Mechanical Engineering
Dr. Catherine Wong, Naval Sea Systems Command

Acknowledgements

The work herein was funded by the Office of Naval Research under Dr. William Mullins and PEO Ships. Many thanks to William (David) Sudduth at the Naval Surface Warfare Center Carderock Division for providing seed funding to kick start this research.

To my advisor, Dr. Lourdes Salamanca-Riba, my deepest thanks for all the support and guidance throughout this research. Your scientific insight and knowledge has been a valuable asset to my research. Thank you for allowing me the freedom to pursue and shape the research into its final form presented herein.

A big thank you to my committee for their guidance and the efforts put forth in reviewing this thesis. To Dr. Luz Martinez- Miranda, thank you for your technical guidance and support with the X-ray diffraction measurements. Many thanks to Dr. Catherine Wong who I know is incredibly busy for taking the time to sit on my committee and for her continual support.

To the individuals in the NISP lab at the UMD Nanocenter, I owe a big debt of gratitude. To Dr. Wen-An Chiou, thank you very much for the assistance with the *in-situ* TEM heating experiments and technical guidance. To Dr. Li-Chung Lai, many thanks for all the assistance with the microscopy work and assisting me with all the hiccups along the way.

To Dr. Robert Kelly, thank you for all the assistance with the confocal microscopy work. To Dr. Marc Zupan, thanks for the assistance with the micro specimen tensile testing.

I owe many thanks to a number of individuals within the metals department at Carderock. To my supervisor, John DeLoach, thank you for the support and encouragement. To Albert Brandmarte and Richard Stockhausen, many thanks for all the metallographic preparation work. To Caroline Scheck, thank you for all your efforts from micro specimen tensile testing to metallographic work. To Jennifer Wolk and Elissa Bumiller, thank you for all encouragement and advice. To Dr. David Forrest, a big thank you for all your fantastic DEFORM modeling work, encouragement, and support.

To my parents, Ky and Trang, thank you for all the encouragement, love, support, and many sacrifices. I would not be in this position without both of you. To my sister and best friend, Kimberly, thank you for all your encouragement.

To my hubby, David, thank you for all your love, support, and encouragement. Lastly, to my daughter Olivia, I hope I inspire you to pursue your dreams and be the very best someday.

Table of Contents

List of Tables

List of Figures

List of Acronyms

Al-Mg:	Aluminum-Magnesium
ASTM:	American Society for Testing and Materials
CLSM:	Confocal Laser Scanning Microscopy
EBSD:	Electron Backscatter Diffraction
ECAP:	Equal Channel Angular Processing
EDS:	Energy Dispersive X-ray Spectroscopy
FCC:	Face Center Cubic
HPT:	High Pressure Torsion
HRTEM:	High Resolution Transmission Electron Microscopy
IGC:	Intergranular Corrosion
OM:	Optical Microscopy
SCC:	Stress Corrosion Cracking
SEM:	Scanning Electron Microscopy
SPD:	Severe Plastic Deformation
TEM:	Transmission Electron Microscopy
XRD:	X-ray Diffraction
UIT:	Ultrasonic Impact Treatment
USSP:	Ultrasonic Shot Peening

Chapter 1: Introduction

1.1 Background

The most commonly used aluminum alloys in Navy ship construction are the 5xxx series marine-grade aluminum-magnesium (Al-Mg) alloys. This is because they have high as-welded strength and are weldable, formable, and highly corrosion resistant. Aluminum magnesium alloys are non-heat treatable alloys that derive their strength from solid solution strengthening and strain hardening. Of these alloys, the Navy has extensive experience with 5456-H116 for deckhouse structures on older classes of surface ships and in the construction of small high-speed, high performance ships. In service experience, these structures have been characterized by cracking due to low fatigue, corrosion fatigue and stress corrosion cracking (SCC).

On-going cracking issues on aluminum superstructures of Navy surface combatants prompted the investigation of ultrasonic impact treatment (UIT) as a technique to improve SCC resistance. Ultrasonic impact treatment is a mechanical surface treatment similar to methods such as shot peening, laser shock peening, and deep rolling that is used to generate severe plastic deformation (SPD) in the sub-surface layers of metals. Severe plastic deformation techniques, such as UIT, have been shown to produce fine grain microstructures and alter the material properties without changing the chemical composition [1,2,3,4]. Ultrasonic impact treatment in particular, has been shown to lead to the formation of highly developed dislocation/grain microstructures. This causes compressive residual stresses and

provides significant hardening in the material's surface layer, thereby increasing the material's resistance to fatigue, wear, and corrosion [5,6].

Currently, the Navy is using UIT experimentally to reduce residual stress on the surface of the material in order to mitigate cracking susceptibility in 5456-H116 aluminum alloy superstructures. Ultrasonic impact treatment is being used as part of crack repair welding and to treat affected areas prior to and during structural rip-out and re-installations. Ultrasonic impact treatment is used to treat the surrounding base metal prior to excavation of cracks for weld repair and to treat the root pass of each weld.

Although the results of the UIT experimental work on Navy ships have been successful to date, the effect of UIT on the material properties and microstructure of 5456-H116 material is not thoroughly understood. The literature shows that UIT leads to the formation of highly developed dislocation/grain microstructures and causes compressive residual stresses in 7075-T6511 aluminum, and 2024-T351 aluminum [3,6]. However, research on the effects of UIT on 5456-H116 has not been accomplished. This study aims to correlate the effects of UIT on the material properties to the microstructural changes imparted by UIT and to develop a fundamental understanding of the mechanisms that cause material property changes.

1.2 Pure Aluminum

Aluminum crystallizes with a face centered cubic (FCC) lattice structure that is stable from -269.2°C (4°K) to the melting point of 660.3°C (933.4°K) and does not undergo an allotropic transformation [7,8]. The lattice constant of aluminum (a_o) is

4.0414 Å at 25°C [9]. The effect of most alloying additions is small with the exception of magnesium at the limit of equilibrium solubility which expands the lattice to 4.117 Å [9]. The elements with the greatest solid solubility in aluminum are zinc, silver, magnesium and lithium, all greater than 10 atomic percent (at.%) [7].

1.2.1 Binary Al-Mg System

Aluminum-magnesium alloys are non-heat treatable binary alloys that derive their strength from solid solution strengthening and strain hardening. Magnesium has considerable solubility in solid aluminum, however binary alloys do not show significant precipitation hardening characteristics with magnesium concentrations below 7.0 weight percent (wt. %) [8]. The magnesium concentration available commercially for wrought Al-Mg alloys range from 0.5 to 6.0 wt. % [10]. Increasing magnesium concentration increases the strength of aluminum without disproportionately decreasing the ductility. Strength increases up to approximately 12 to 14 wt. % magnesium, higher magnesium content results in aged alloys that are too brittle for use [9]. Figure 1 shows the effects of magnesium content on the tensile strength, yield strength, and elongation of wrought Al-Mg alloys [11].

Of the commercially available wrought Al-Mg alloys, 5456 has the second highest concentration of magnesium, 4.7 to 5.5 wt.%. Aluminum 5456-H116 is a strain hardened, corrosion resistant temper where the H116 temper designation indicates that the product was strain hardened [12]. The digit following the H1 indicates the degree of strain hardening and the third digit indicates that the

mechanical properties are different but close to those with a two digit H temper designation [12].

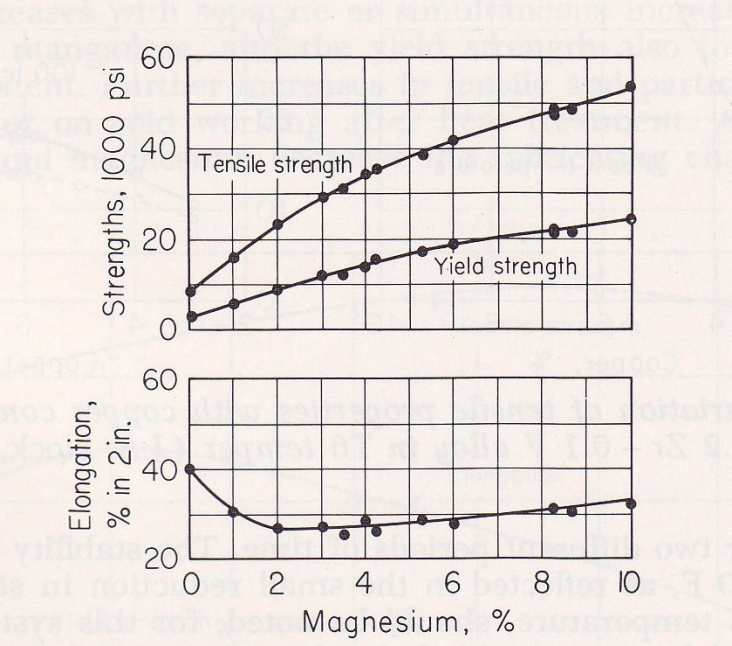

Figure 1. Effect of magnesium content on tensile strength, yield strength, and elongation [11]

The maximum solid solubility of Mg in aluminum, Figure 2, is 18.9 at.% or 17.4 wt.% at 450°C [7]. The Al-Mg supersaturated solid solution decomposes into an equilibrium phase Al_3Mg_2 or β phase. The precipitation of β phase in Al-Mg occurs by the following sequence [13]:

$$sss\alpha \rightarrow \text{GP zones} \rightarrow \beta'' \rightarrow \beta' \rightarrow \beta$$

where sssα is supersaturated solid solution, GP is the Guinier Preston zone, β" is an $L1_2$ ordered phase with an Al_3Mg composition, β' is a semi-coherent hexagonal intermediate phase with an approximate Al_3Mg_2 composition and then finally β [13]. The β phase has a complex FCC structure with 1173 atoms per unit cell and a lattice parameter, a_o = 28.13 Å [7]. β phase forms a eutectic with aluminum at 37.4 at.% (35 wt. %) and has a homogeneity range extending from 37.5 at.% (35.1 wt.%) to 40 at.% between 0 to 400°C, Figure 1 [7]. The β phase can only be redissolved by reheating Al-Mg to about 425°C [7].

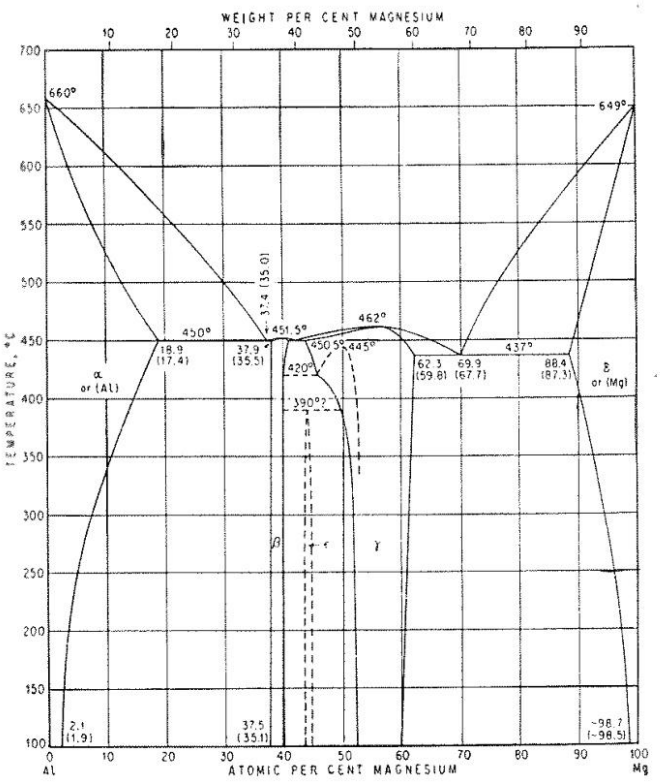

Figure 2. Al-Mg phase diagram. Figures in brackets are wt.%; others are at. % [8]

Aluminum-magnesium alloys also contain small additions of other transition elements. Iron and zirconium are added to increase the recrystallization temperature,

and manganese or chromium to correct for the corroding effect of iron [9]. Copper is added to reduce pitting corrosion and zinc to enhance castability and strength [9]. Elements such as boron are added as grain refiners, beryllium and lithium to reduce the oxidation of magnesium at high temperature. Silicon which is a master alloying element is added to Al-Mg to improve fluidity [9]. The chemical composition limits for aluminum 5456 in accordance with ASTM B928 *Standard Specification for High Magnesium Aluminum Alloy Sheet and Plate for Marine Service and Similar Environments* are shown in Table 1 [10].

The elemental additions of zinc and manganese are important as they have an influence on the corrosion resistance of Al-Mg alloys [14]. Zinc has been shown to promote magnesium precipitation inside the grains thus reducing the formation of β phase along the grain boundaries. Manganese can also reduce the precipitation of β phase along the grain boundaries because the formation of manganese dispersoids provides alternative precipitation sites. This disrupts magnesium diffusion to the grain boundaries thus reducing the formation of β phase at the grain boundaries.

Table 1. Chemical Composition Limits for 5456 [10]

Element	Chemical Composition Limits (wt. %)
Silicon	0.25
Iron	0.40
Copper	0.10
Manganese	0.50 to 1.0
Magnesium	4.7 to 5.5
Chromium	0.05 to 0.20
Zinc	0.25
Titanium	0.20
Other Elements	0.05 each, 0.15 total
Aluminum	Remainder

1.3 Sensitization

Al-Mg alloys containing more than 3 wt.% magnesium can develop a susceptible microstructure or become sensitized when exposed to elevated temperatures (> 50°C) for a prolonged period of time [15,16,17]. I. Oguocha et al. showed that aluminum 5083 could be sensitized after 168 hours at 175°C [15]. Sensitization results from the formation of a continuous network of β-phase at the grain boundaries [15]. The β-phase has been observed to occur initially at the grain boundary triple points and then along the grain boundaries [18]. Precipitation has also been observed at the interface between the matrix and Al_6Mn dispersoids and eutectic constituent particles [18]. The β-phase is anodic to the adjacent metal matrix thus the grain boundaries become highly susceptible to SCC and intergranular corrosion cracking (IGC) which is a localized type of attack at the grain boundaries, resulting in the loss of strength and ductility. The β-phase has also been observed to nucleate and grow intragranularly in Al-Mg alloys, however, intragranular β-phase does not contribute to IGC because it is not part of a continuous grain boundary network [19]. Because of concerns with SCC and IGC, commercially available wrought Al-Mg alloys usually do not exceed 5.5 wt.% Mg. [12]. Figures 3 and 4 show the microstructures of sensitized Al-Mg with a continuous network of β-phase along the grain boundaries and non-sensitized Al-Mg, respectively [21].

A continuous network of β phase can also form at room temperature in heavily cold worked materials over a number of years [7]. While exposure to slightly elevated temperatures over a prolong period of time results in a continuous network of β phase precipitates, exposure to temperatures greater than 180°C results in a

coarsening of the precipitates [7]. Coarse precipitates result in a discontinuous grain boundary structure which reduces or eliminates SCC susceptibility.

The degree of susceptibly to corrosive attack at a grain boundary has been found to depend on the grain's crystallographic orientation with low angle boundaries being more resistant to attack than high angle grain boundaries [15,17]. Low angle grain boundaries have been defined as having < 15° and high angle grain boundaries as having >15° [20]. Stress corrosion cracking and IGC susceptibility has also been found to depend on sensitization time and temperature with a critical temperature range between 150°C and 200°C where Al-Mg alloys are most susceptible to IGC [15].

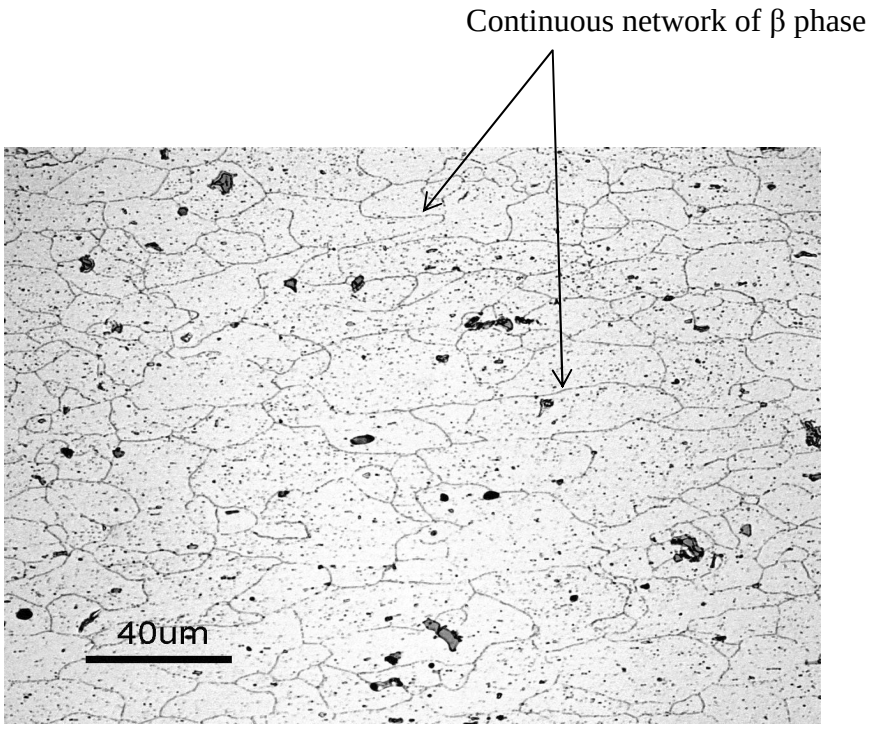

Figure 3. Sensitized Al-Mg; the dark lines are a continuous network of β phase along the grain boundaries [21]

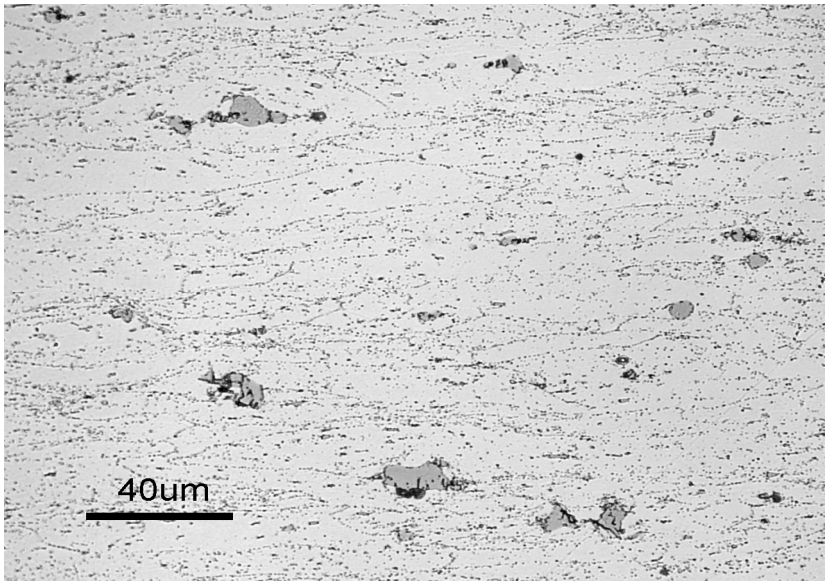

Figure 4. Non-sensitized Al-Mg [21]

With increasing sensitization time and temperature, a loss in the tensile and hardness properties can occur which is attributed to softening caused partly by a decrease in magnesium solute in solid solution concentration [15].

1.4 Stress Corrosion Cracking

Stress corrosion cracking occurs when a material is under the combined action of a continuous tensile stress and in a corrosive environment such as seawater. Stress corrosion cracking attack is usually intergranular therefore SCC susceptibility depends on the microstructure, particularly along the grain boundaries. For all wrought alloys, SCC susceptibility is the greatest in the plane where the most continuous grain boundary path is available. Thus in Al-Mg alloys, sensitized alloys are the most susceptible to SCC due to the presence of the continuous network of β

phase. Stress corrosion cracking does not occur in alloys containing less than 3 wt. % magnesium because these alloys do not sensitize.

Stress corrosion cracking can occur either when tensile stresses approach the yield strength of the material or at low stresses depending on the orientation. Namely, in the longitudinal or transverse directions, SCC may occur when the stresses are on the order of the yield strength. In the short transverse direction, SCC can occur at low stresses.

The fabrication processing of Al-Mg can also alter the type of corrosion observed after sensitization. If the material is fabricated with elongated, unrecrystallized grain structure, it will be more susceptible to SCC in the short transverse direction; however, it would be resistant to SCC in the longitudinal direction. If the fabrication results in equiaxed, recrystallized grains, Al-Mg will be susceptible to IGC and SCC in all orientations. [22].

1.5 Plastic Deformation

Aluminum has a high stacking fault energy (SFE – 250 mJ/m^2) therefore plastic deformation occurs primarily by dislocation slip [23]. Slip occurs most readily in a specific direction on certain crystallographic planes. In general, the slip plane is the plane of greatest atomic density and the slip direction is the closest packed direction within the slip plane. Aluminum which has a FCC lattice structure has twelve potential slip systems. For aluminum alloys at or below room temperature, slip is in the {111} planes and in the <110> directions [9]. Slip may also occur in the {100} planes along the <110> directions or {113} planes in the

<131> directions. Simultaneous slip or multiple slip in two directions may also occur which results in odd plane slip. For example, simultaneous slip in the [101] and [110] directions would result in odd plane slip in the [211] direction. The magnitude and direction of slip is defined by the Burgers vector **b**. For aluminum and other FCC metals, the Burgers vector is given by Equation 1 [24].

$$b = \frac{a}{2}\,[110] \qquad \textbf{(1)}$$

Slip is the displacement of planes oriented in the direction of highest resolved shear stress or critical resolved shear stress (CRSS). The value of the CRSS depends on composition and temperature. The critical resolved shear stresses for aluminum are roughly 7.9 x 10^5 N/m^2 and increases with decreasing temperature [23]. Slip is not a continuous process but rather takes place when the stresses build up until they reach the CRSS. Displacement along each slip plane may range from a few atoms to thousands of atoms and slip usually occurs as a band composed of a group of slip planes. The amount of deformation has an effect on the number of slip planes; the higher the deformation, the larger number of slip planes. Figure 5 shows the microstructure of aluminum that has been severely deformed.

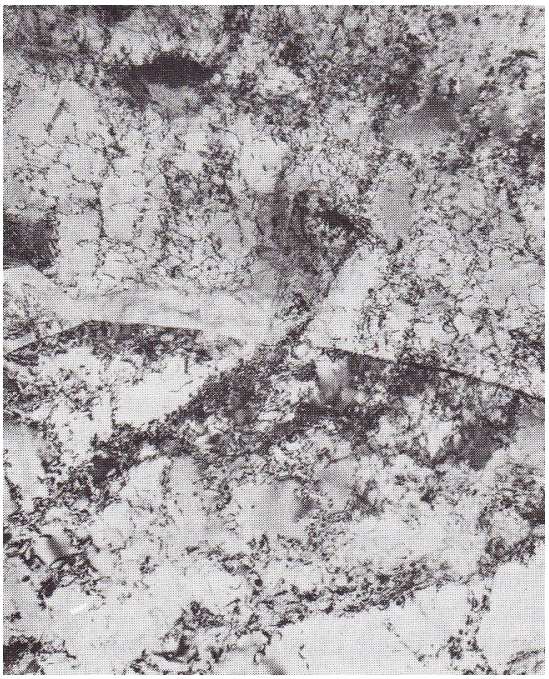

Figure 5. Heavily deformed aluminum microstructure [9]

1.6 Severe Plastic Deformation Techniques

Severe plastic deformation techniques have been shown to be effective methods for producing fine grain structure in metals [3,25,26,27]. The most common SPD techniques available are equal channel angular pressing (ECAP) and high pressure torsion (HPT). Severe plastic deformation techniques use very high plastic strains to produce fine grain structure that exhibit high yield strength, low strain hardening, and improved corrosion properties [3,28]. Severe plastic deformation is also used to impart deep compressive residual stresses into the surface of materials.

1.6.1 Ultrasonic Impact Treatment

The UIT process was originally developed in Russia in the early 1970's for the shipbuilding industry [29]. Currently, the technology is also employed for other industries such as transportation and pipe oil and has been used to treat 2XXX, and 7XXX aluminum alloys and steels.

The UIT process involves the use of a pin tool that behaves like an ultrasonic transducer that outputs continuous ultrasonic impulse or vibrations at the ultrasonic transducer output end to the treated surface. The technology is based on converting the ultrasonic oscillations of the transducer into impulses of ultrasonic impacts at the output end [3,5,29]. The output end employs needle indenters, strengthened with hard materials such as carbide containing alloys or artificial diamonds that are directed at the surface and are in continuous contact with the surface of the material [3,5,29]. Figure 6 shows a schematic diagram of the ultrasonic impact tool where; 1) is the magnetostrictive transducer 2) the waveguide 3) the indenter, 4) the treated surface, I) ultrasonic oscillations, II) impact pulses [29]. The continuous ultrasonic impact creates high rate straining and heating near the material surface which results in severe plastic deformation. The high rate straining generates energetically stable dislocation cells in aluminum alloys resulting in stable compressive residual stresses [3,5].

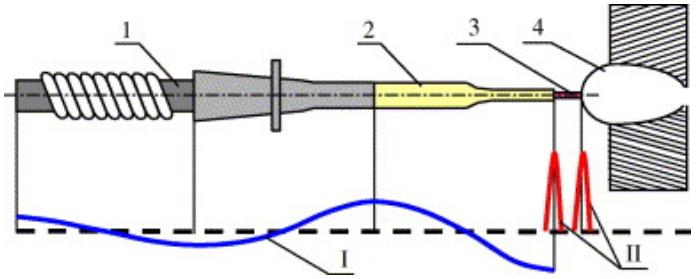

Figure 6. Schematic diagram of UIT tool [29]

1.7 Objectives

Ultrasonic impact treatment is a technique that results in SPD near the surface of materials resulting in the formation of highly developed dislocation and grain microstructures that alter the material's properties. The microstructural changes imparted by UIT and the mechanisms that result in material property changes are not thoroughly understood.

The main objectives of this thesis are twofold:

1. To correlate the effects of UIT on the properties of 5456-H116 alloys to the microstructural evolution of the alloy
2. To develop a fundamental understanding of the mechanisms that cause the microstructural evolution.

The effects of UIT on the microstructure of aluminum 5456-H116 were investigated through material properties testing and microstructural characterization techniques. The work included investigation of the plastic deformation imparted by UIT on sensitized 5456-H116 plate. Work also included investigation of untreated sensitized 5456-H116 plate to provide a basis for comparison.

Chapter 2: General Procedures

2.1 Base Metal Properties

The 5456 material was procured from a US naval combatant. The materials evaluated for this work included treated UIT samples and non- treated samples. The UIT treatment was provided by Applied Ultrasonics, Inc. The *Esonix* UIT equipment consisted of an indenter with four pins. Each pin had a pin tip radius of 3 mm. The UIT equipment was operated at a frequency of 27 kHz and power consumption of 80 volts and 11.2 amps. The treatment amplitude was 22 μm and travel speed was 10 cm/minute. Figure 7 shows a large sensitized 5456 plate with UIT processing and untreated areas and the plate orientations; samples for microscopy and materials testing were obtained from both areas. Figure 8 shows a sample obtained from a larger piece of material treated by UIT. The figure shows some gaps in the treatment of the surface due to the fact that it is a manual process and subject to operator error. There is also some overlap in indentations. Figure 8 shows schematics of the planar and transverse orientations that were used for specimen sectioning.

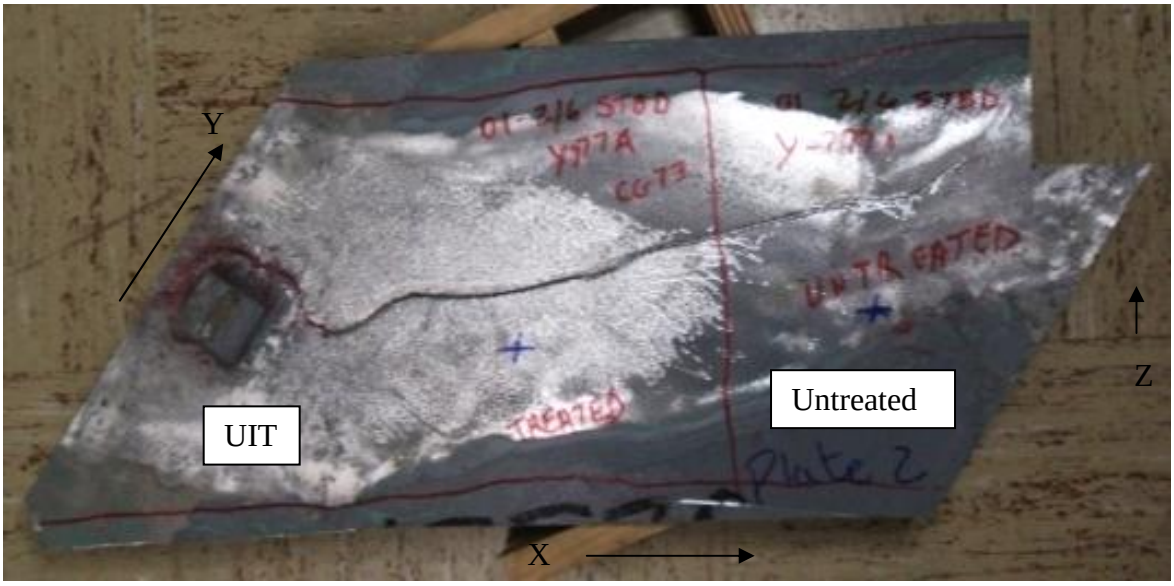

Figure 7. Large sensitized 5456 plate showing UIT and untreated areas; samples for microscopy were obtained from both UIT and untreated areas; x-direction is along the length of the plate, y-direction is transverse to the plate, z-direction is through thickness

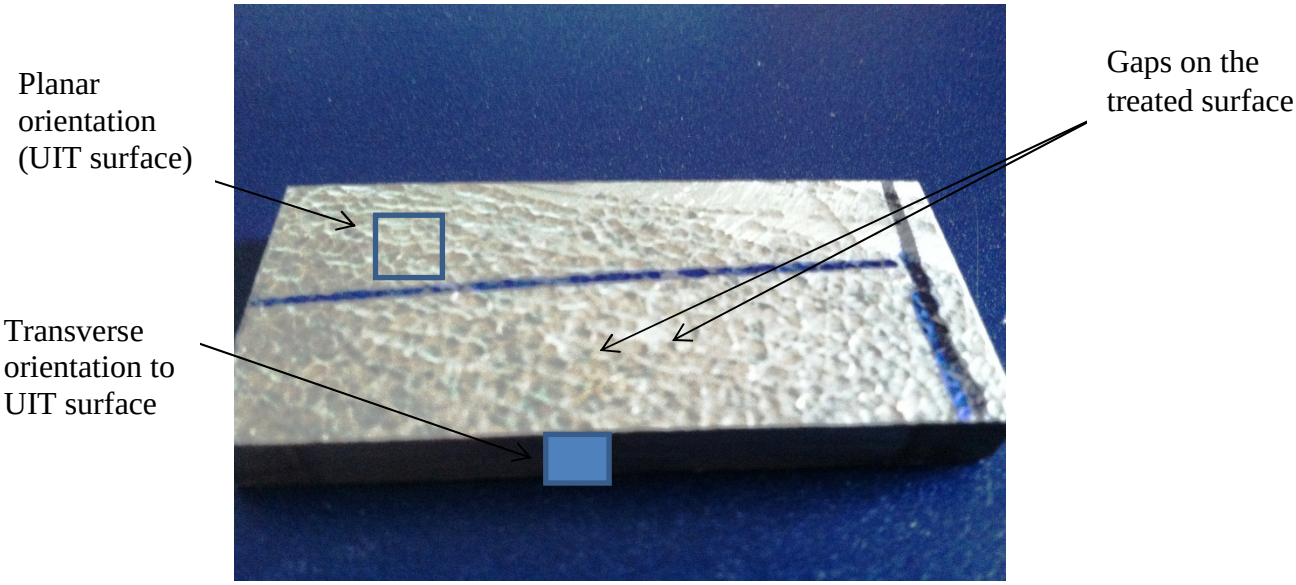

Figure 8. Sample from a large piece of sensitized 5456 treated with the UIT process

The chemical composition of the base metal was analyzed by direct current plasma emission spectroscopy at Luvak, Inc. The results of the chemical analysis are provided in Table 2 along with the requirements for 5456 in accordance with ASTM B928 *Standard Specification for High Magnesium Aluminum-Alloy Sheet and Plate for Marine Service and Similar Environments* [10]. The results of the chemical analysis show conformance to the specification requirements with the exception of magnesium which is slightly less than the range specified by ASTM B928 [10].

Table 2. Chemical analysis for 5456 base metal (weight percent)

Sample/Element	5456 Sensitized Material	ASTM B928 Requirements (maximum unless shown as a range)
Silicon	.16	.25
Iron	.19	.40
Copper	.061	.10
Manganese	.67	.50 to 1.0
Magnesium	4.6	4.7 to 5.5
Chromium	.073	.05 to .20
Zinc	.063	.25
Titanium	.014	.20
Total Others	<.15	.15
Aluminum	Remainder	Remainder

2.2 Intergranular Corrosion Testing Procedure

Testing of the base metal for intergranular corrosion susceptibility was performed in accordance with ASTM G67 *Standard Test Method for Determining the Susceptibility to Intergranular Corrosion for 5XXX Aluminum Alloys by Mass Loss After Exposure to Nitric Acid (NAMLT Test)* [30]. Tests were performed in

accordance with the standard procedure and a modified procedure as explained below.

Specimens measuring 50 mm x 6 mm were sectioned from a large plate and tested for volumetric mass loss for the standard test. Specimens were immersed in concentrated nitric (HNO_3) acid solution at a test temperature of 30 ±0.1 °C for 24 hours.

Specimens measuring 25 mm x 25 mm were sectioned from the larger plate with a SiC abrasive cut-off saw blade for the modified test. The test procedure was modified from a volumetric test to a test in which only one surface was exposed to nitric acid using a special Teflon test cell. Both UIT treated and untreated surface areas measuring approximately 175 mm^2 were exposed to HNO_3 acid solution with a test temperature of 30 ±0.1 °C for 24 hours in order to determine the mass loss on the UIT and untreated surfaces. The mass loss was determined by obtaining the difference between the mass pre and post exposure to HNO_3 acid.

2.3 Confocal Microscopy

Surface roughness measurements were obtained using a Zeiss LSM 510 confocal microscope. Samples measuring approximately 15 mm x 15 mm were sectioned from a larger plate using a SiC abrasive cut-off saw blade. Confocal microscopy was accomplished in a collaborative effort with Dr. Robert Kelly at the University of Virginia.

2.4 Scanning Electron Microscopy (SEM)

2.4.1 Specimen Preparation

Specimens measuring approximately 15 mm x 15 mm were sectioned from a larger plate with a SiC abrasive cut-off saw blade. Cross-sectional specimens were mounted in either a castable epoxy resin or thermosetting epoxy compound. The specimens were polished on a Stuers Abropol 2 automated polisher using an initial grinding plane with 120 grit SiC grinding paper at 100 N force for 30 seconds. The specimens were subsequently polished with 180 grit, 240 grit, 320 grit, 400 grit, 600 grit, and then a fine grit plane with 1200 grit SiC grinding paper. The specimens were polished with 100 N force for 30 seconds at each grit size. Following grinding with SiC grinding paper, the specimens were polished with 9 μmol diamond suspension at 100 N force with an alcohol based lubricant for 5 minutes. The specimens were then given a polish with 3 μmol diamond suspension with an alcohol based lubricant. Final polishing was with 0.04 μm neutral colloidal silica for 5 minutes.

2.4.2 SEM Operating Parameters

Scanning electron microscopy analysis was performed using a Hitachi 660 scanning electron microscope with an operating voltage of 15 kV at various magnifications up to 2000X.

2.5 Optical Microscopy (OM)

2.5.1 Specimen Preparation

Specimens measuring approximately 15 mm x 15 mm were sectioned from a large plate with a SiC abrasive cut-off saw blade. Planar and cross-sectional specimens were mounted in either a castable epoxy resin or thermosetting epoxy compound. The specimens were polished on a Stuers Abropol 2 automated polisher using an initial grinding plane with 120 grit SiC grinding paper at 100 N force for 30 seconds. The specimens were then subsequently polished with 240 grit, 320 grit, 400 grit, 600 grit, and then a fine grit plane with 2400 grit SiC grinding paper. The specimens were polished with 100 N force for 30 seconds at each grit size. Following grinding with SiC grinding paper, the specimens were polished with 3 μmol diamond suspension at 100 N force with a lube of 5 and suspension of 7 for 5 minutes. The specimens were then given a final polish with oxide polishing suspension (OP-U) on Chem polishing cloth at 100 N force for 2 minutes. The specimens that were examined optically under polarized light were etched in a Barker's reagent (1.8% HBF_4 in water) for 3 minutes. The specimens that were examined optically for β phase were etched with a 40% phosphoric acid for 3 minutes at 35ºC (95ºF).

2.5.2 OM Operating Parameters

Optical metallography and images were taken with a LECO Olympus optical microscope and Nikon digital camera at various magnifications. Cross polarized light was used to enhance the grain structure and grain boundaries.

2.6 Electron Backscatter Diffraction (EBSD)

2.6.1 Specimen Preparation

Specimens measuring approximately 15 mm x 15 mm were sectioned from a large plate with a SiC abrasive cut-off saw blade. Planar and transverse (cross-sectional) slices of ~0.5 mm in thickness were obtained from the specimens. Figure 8 shows schematics of the planar and transverse orientations. Planar samples were polished on the UIT surface while transverse samples were polished transverse to the UIT surface. The specimens were prepared by mechanical polishing. The specimens were mounted in either a castable epoxy resin or thermosetting epoxy compound. The specimens were polished on a Struers Abropol 2 automated polisher with the sequence shown in Table 3. The final polish was a vibratory polish in colloidal silica for 12 hours on a Buehler Vibromet.

Table 3. Mechanical polishing sequence for EBSD experiments

Surface	Abrasive Size	Load (N)	Time (minutes)
SiC grinding paper	320 grit	~20	12
SiC grinding paper	600 grit	~20	12
SiC grinding paper	1200 grit	~20	12
NAP Polishing cloth	3 μmol diamond suspension	120	5
NAP polishing cloth	1 μmol diamond suspension	120	3
Chem Polishing Cloth	Oxide polishing suspension (OP-U), 50 mL	100	3
NAP Polishing Cloth	Oxide polishing suspension, 50 mL	100	3

2.6.2 Operating Parameters

Electron backscatter diffraction (EBSD) analysis was performed using a Hitachi 660 scanning electron microscope with an EDAX detector with a typical working distance of 19 mm and accelerating voltage of 15 kV and current of 38 μA. Samples were inclined at 65° relative to the normal incidence of the electron beam. Data was obtained with the beam scanning over the sample area at various magnifications. Automated acquisition and pattern indexing was performed with TSL OIM Acquisition v.5 software. EBSD analysis was performed using TSL OIM Analysis v.5.3.1 software.

2.7 Transmission Electron Microscopy (TEM)

2.7.1 Sample Preparation

Electron backscatter diffraction samples were used for TEM analysis. Following EBSD analysis, the unpolished sides of the samples were mechanically polished with 600 grit SiC paper, 2400 grit SiC paper, and 4000 grit SiC paper for 5 minutes at each grit size. 3 mm TEM discs were removed from the polished samples using a South Bay slurry disc cutter with a diamond tool. The 3 mm discs were polished from the back side to ~ 100 μm thickness with a tripod polisher initially with 30 μm diamond paper and then 15 μm diamond paper.

Additional TEM samples obtained from the UIT surface were also used for TEM analysis. The UIT surface was left unpolished to preserve the UIT treated surface. The backside of the samples were mechanically polished using the

parameters described in the previous paragraph. 3 mm TEM discs were removed from the polished samples and polished to ~ 100 µm thicknesses with a tripod polisher with 30 µm diamond paper and then 15 µm diamond paper.

2.7.2 Specimen Thinning

The 3 mm TEM discs were electropolished using an Electron Microscopy Science Model 550D vertical jet polisher. The specimens were polished in an electrolyte of 25% nitric acid (HNO_3) and 75% methanol (CH_3OH) at 10 V and -40°C achieved using a bath of dry ice in methanol. Specimens were electropolished on both sides for approximately 3 to 4 minutes per side or until a hole was detected by the polisher. The samples obtained near the UIT surface were only electropolished on the mechanically polished side to preserve the UIT treated surface. After electropolishing, the specimens were ion milled in a Fischione Model 1010 ion mill using the parameters shown in Table 4. Lastly, the specimens were plasma cleaned in South Bay plasma cleaner for 10 minutes on each side.

Additional specimens were polished in an electrolyte of 10% perchloric acid ($HClO_4$) and 90% methanol at 5 V and -40°C using a bath of dry ice in methanol. Specimens were polished on both side for approximately 5 minutes per side or until a hole was detected by the polisher. After electropolishing, the specimens were ion milled using the parameters shown in Table 4. The specimens were also cleaned for 10 minutes per side in the plasma cleaner.

Table 4. Ion milling parameters for TEM sample preparation of 5456 aluminum

kV	mA	Rotation (°)	Degree	Time (min)
Specimens electropolished in 25% HNO_3 in 75% methanol				
5	5	360	15	5
5	5	360	10	5
3	4	360	8	5
1	3	360	5	5
Specimens electropolished in 10% $HClO_4$ in 90% methanol				
6	5	360	45	30
5	5	360	15	30
3	4	360	8	15
1	0.3	360	6	15

2.7.3 TEM Operating Parameters

All TEM analysis was performed on a JEOL 2100 LaB_6 and JEOL 2100 field emission gun (FEG) TEM. Analysis was carried out with an accelerating voltage of 200 kV and beam current of 106 μA for the LaB_6. Energy dispersive x-ray spectroscopy (EDS) was performed using an Oxford INCA 100 EDS system in the JEOL LaB_6 and Oxford INCA 250 EDS system in the JEOL FEG-TEM. In-situ temperature TEM analysis using a heating stage was performed with a Gatan heating holder and Smart Heater controller in the LaB_6 TEM.

2.8 X-ray Diffraction

Specimens measuring approximately 10 mm x 10 mm were sectioned from a large UIT plate with a SiC abrasive cut-off saw blade. Samples for X-ray diffraction (XRD) were prepared using the EBSD polishing procedure described in section 2.6.1. The samples were polished along the transverse orientation and measurements were

obtained as a function of depth and at the UIT surface. The UIT surface was not polished in order to preserve the treatment. X-ray diffraction measurements were obtained using a 18 kW Riguka diffractometer with a bent graphite monochromator and a resolution of $\Delta q = 0.012q_o$ ($Å^{-1}$) operating at 50 kV and 100 mA. In a diffractometer, the intensity of the diffracted beam is measured directly by an electronic counter that converts incoming x-rays into current pulses. The current pulses are counted as current pulses per unit and this number is directly proportional to the intensity of the x-ray beam.

Residual stress measurements were also obtained using XRD. The XRD measurements were outsourced to TEC Materials Testing Division and performed in accordance with ASTM E915 [31]. Measurements were obtained as a function of depth from the UIT surface.

2.9 DEFORM 3D Modeling

The surface roughness measurements for untreated material were used to develop the DEFORM 3D™ model and the results of the model compared to analytical data obtained through X-ray diffraction measurements. The DEFORM 3D™ model was developed by Dr. David R. Forrest at the Naval Surface Warfare Center, Carderock Division.

2.10 Micro specimen tensile testing and Microhardness Measurements

Micro specimen tensile testing was performed using specimens that were sectioned from UIT and untreated material as shown in Figure 7. The specimens were prepared by electrode discharge machining and measured ~ 3 mm L x 1 mm W x 207 µm T with a gage section of 250 μm^2. Micro indentations measuring 70 µm between indents were also made on the specimens for non-contact strain measurements. Testing was accomplished in a Micro Material Testing System (µMTS) utilizing a 44.43 kN load cell, a piezo stack with a stroke of 180 µm, a non-contact interferometer system, and control software. Samples for hardness measurements were also obtained from the larger plate shown in Figure 7. Micro hardness measurements were obtained as a function of depth from the surface. Tensile testing and microhardness measurements were accomplished in a collaborative effort with Dr. Marc Zupan at the University of Maryland Baltimore County.

Chapter 3: Metallurgy and Crystallographic Texture of Aluminum 5456 Plastically Deformed by UIT

3.1 Introduction

This chapter presents the study of the microstructure of UIT treated and untreated sensitized 5456 aluminum at the macroscopic and microscopic level using SEM, OM, and EBSD. This study contributes to the understanding of the effects of SPD on the grain structure including grain size measurements, grain orientation, and crystallographic texture of Al-Mg alloys.

Severe plastic deformation techniques have been shown to produce fine grain structuring in materials without changing the chemical composition. Research indicates that grain refinement to an ultrafine crystalline state with grain size ranging from 100 nm to 1 μm and nanocrystalline state with grain size less than 100 nm can have an effect on the material's properties [3]. The UIT process has been shown to produce average grain sizes of approximately 4.13 μm at a depth of 2.6 μm in 2024-T351 aluminum as compared to the base metal which has an average grain size of 16.52 μm at the same depth [3]. The grain structure was determined to consist of equiaxed nanograins of 8 to 10 nm at the top surface; equiaxed ultrafine grains mixed with micro bands at a depth of ~ 3 to 5 μm below the surface; and refined grains at a depth of 10 μm below the surface [3]. At a depth of 34.5 μm, the grain sizes for UIT material and base metal are similar and range from 36 to 39 μm [3] The work reported by X. An et al. used UIT processing parameters with a frequency of 36 kHz, 5.0 mm diameter pin, and amplitudes of 18 μm and 15 μm, and feed rates of 40

cm/min and 100 cm/min which differ from the UIT parameters used for this study that are presented in section 2.1 [3]. Further study by TEM showed the presence of a nanocrystalline layer with average grains on the order of 8 to 10 nm. X. An also reported that a larger amplitude and slower feed rate resulted in small average grain size at the subsurface.

Work by X. Wu et al. demonstrated that a similar technique, ultrasonic shot peening (USSP), can induce ultrafine grain structures in aluminum 7075 [25]. Ultrasonic shot peening involves the use of a shot transferred to the component by means of a high frequency ultrasonic wave inside of a chamber. For this particular work, 7.5 mm stainless steel shots were transferred with a high-energy ultrasonic generator with a frequency of 20 kHz [25]. The average grain size ~ 8 μm from the top surface was reported to be reduced to ~ 47 nm. The research also showed the presence of parallel, extended micro bands with interior elongated subgrains at a depth of ~ 60 μm from the treated surface and equiaxed, submicron-grain structure at ~ 50 μm from the treated surface [25]. The micro bands were ~ 0.6 to 1.0 μm wide and 3 to 12 μm long. The submicron grain structured varied from less than 200 nm to 500 nm [25].

Preferred orientation or crystallographic texture in aluminum alloys is more pronounced the larger the amount of deformation. Texture is hardly noticeable when deformation is below 10 to 15 percent [9]. Between 40 to 50 percent deformation, texture is still diffuse and does not become more pronounced until the deformation is above 70 to 80 percent [9]. The texture near the surface will vary with the deformation method, however at the center of the material; texture tends to be the

same regardless of the deformation method. Crystallographic texture in Al-Mg alloys that have been heavily deformed by SPD processes such as ECAP and cold rolling has been extensively studied, however not by processes such as UIT [32,33,34].

Crystallographic texture can be described through the use of a pole figure which is a stereographic projection of a three dimensional orientation on a unit sphere in a two dimensional plane [20,35]. The basis of the stereographic projection is the intersection of crystallographic poles with the plane normal on the surface of the sphere. The two dimensional projections directly map the angular relationships between projected normals and give a graphic representation of the orientation relationships. Figure 9 shows the stereographic projection of the (111) plane and the associated pole figure [35]. If crystallographic texture exist, the poles will tend to cluster together into certain areas of the stereographic projection as shown in the (100) pole figure in Figure 10 [36].

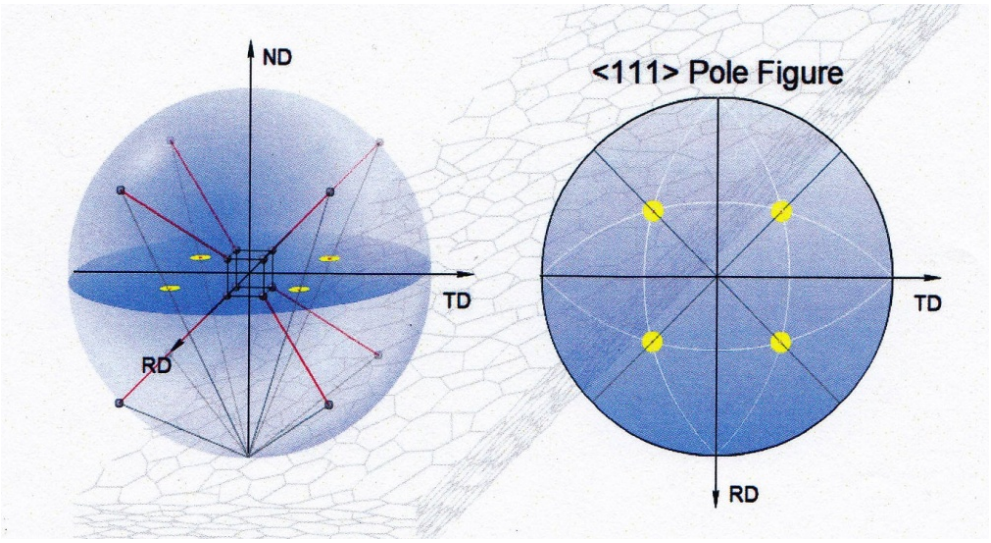

Figure 9. Stereographic projection of the (111) plane and associated pole figure [36]

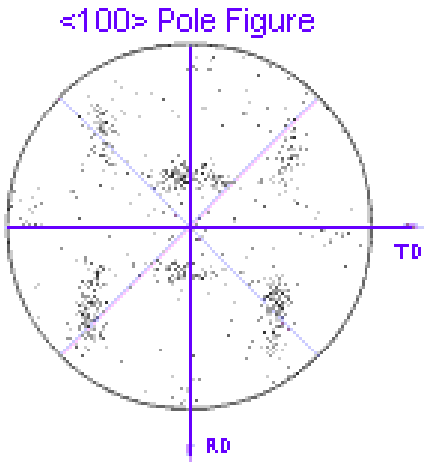

Figure 10. (100) pole figure of showing crystallographic texture [36]

3.2 Results

3.2.1 Scanning Electron Microscopy of UIT Sensitized 5456

The topography of the UIT material was examined in the SEM to observe for any damage on the material surface. The samples were observed at 25X, 50X and 250X magnifications. In general, the results indicated that the UIT treatment does not cause gross damage to the surface of the material; however, there were some flaws that appeared to be micro cracking or micro tearing. Figures 11 and 12 show the presence of flaws that appear to be micro cracks or micro tears on the surface of a UIT indentation. The SEM images reveal the randomness of the UIT indentations which is due to the manual nature of the UIT process. The indentations vary slightly in size with some measuring 3 mm x 3 mm and others measuring 3.5 mm x 5 mm. As noted in section 2.1, the pin tip of the UIT tool is 3 mm; therefore the variation in

some of the indentations may be due to overlapping indentations. Micrographs were also obtained in the transverse orientation at 2000X and 4000X to examine the physically deformed UIT layer. Figures 13 and 14 show that the UIT process results in tearing and void formation below the deformation layer. There is a distinct separation or delamination between the deformation layer and the adjacent metal matrix.

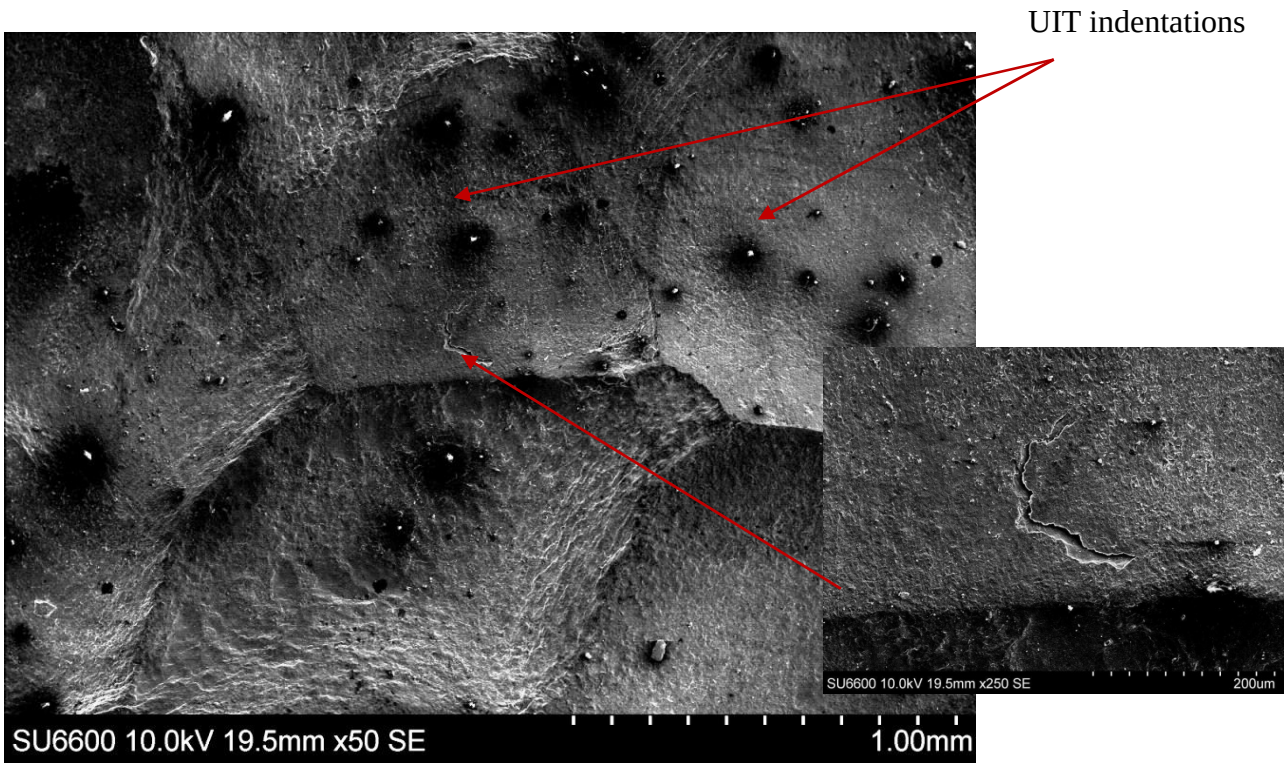

Figure 11. Scanning electron microscopy image showing the surface topography of UIT treated sensitized 5456 with a micro crack or micro flaw at 50X

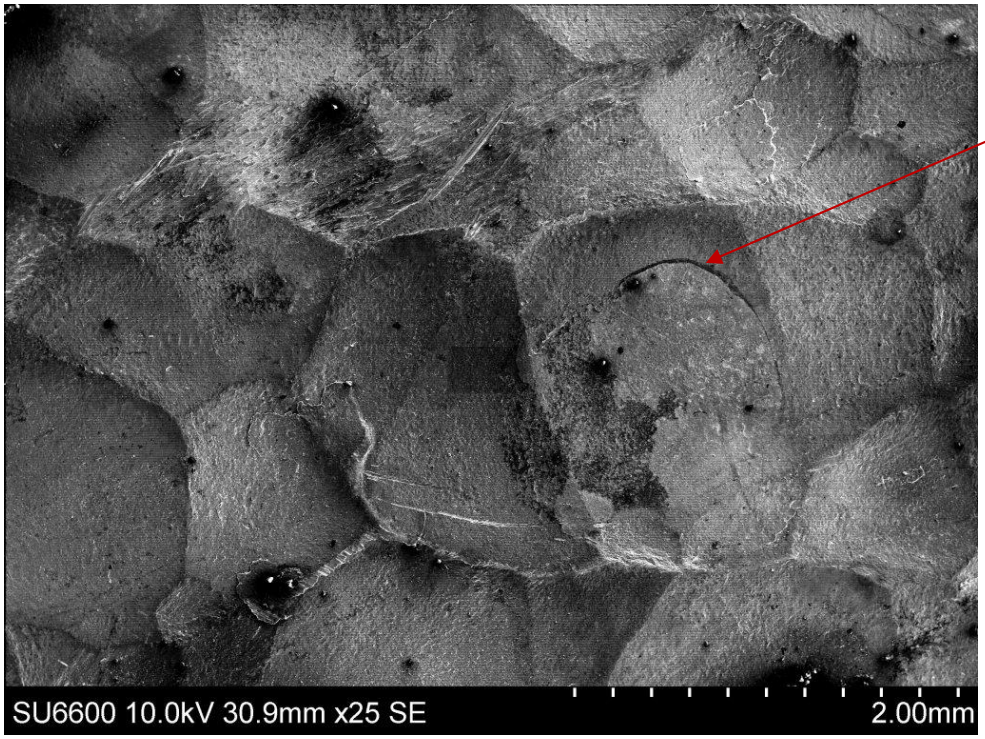

Figure 12. Scanning electron microscopy image showing the topography of UIT treated sensitized 5456 with a micro crack or micro flaw at 25X

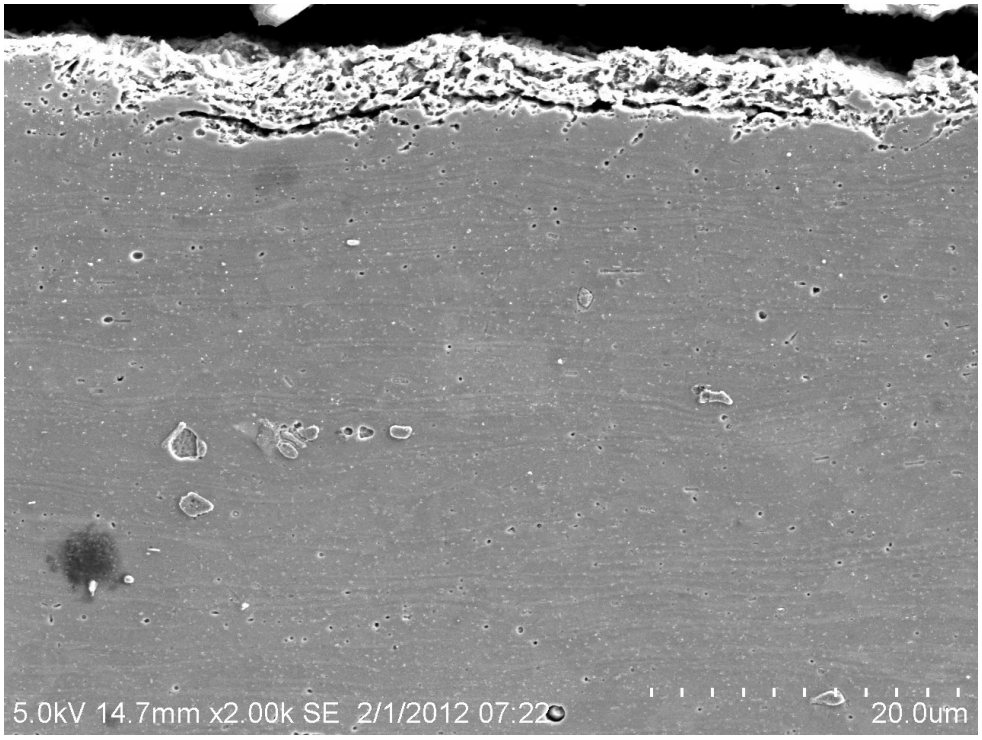

Figure 13. Scanning electron microscopy image showing the cross section of UIT deformation layer with tearing and void formation at 2000X

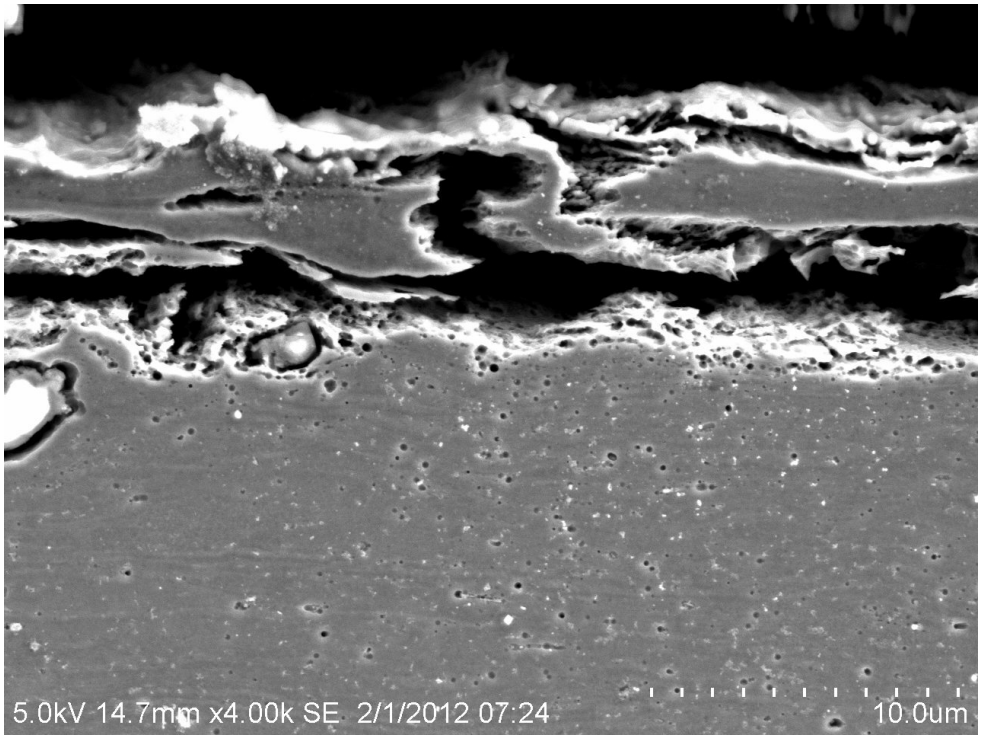

Figure 14. Scanning electron microscopy image showing the cross section of UIT deformation layer with tearing, void formation, and separation between the deformation layer and the metal matrix at 4000X

3.2.2 Optical Microscopy of UIT and Untreated Sensitized 5456 to Examine for β phase

Figure 15 shows an optical micrograph obtained at 100X of a sample etched with 40% phosphoric acid in the transverse orientation. The micrograph reveals the presence of a continuous network of β phase below the physically deformed UIT layer. ASTM G67 testing of the material revealed a mass loss of 52 mg/cm^2 which is considered to be severely sensitized. In accordance with ASTM G67, a mass loss of greater than 25 mg/cm^2 is considered sensitized [30]. The micrographs reveal that the

UIT treatment can vary the depth of the deformation layer from approximately 10 to 18 µm.

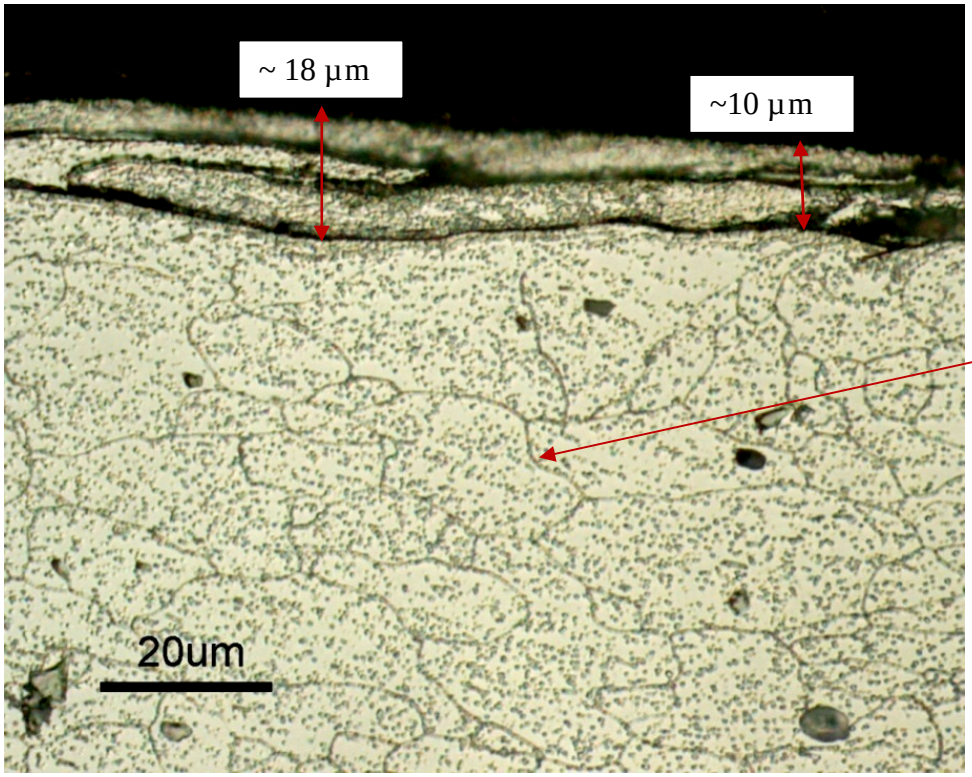

Figure 15. Transverse cross section of UIT treated sensitized 5456 showing continuous network of β phase

3.2.3 Optical Microscopy of UIT and Untreated Sensitized 5456 Under Polarized Light

Optical microscopy of UIT and untreated 5456 shows a difference in the grain size of the material. Under polarized light at a 50X optical magnification in the planar orientation, the UIT material shows some grain refinement. However grain size measurements were not obtained from the optical micrographs. Grain size measurements were obtained from EBSD images and TEM images as presented in

section 3.2.4 and 4.2.1.1, respectively. Optical micrographs of UIT and untreated material in the planar orientation are shown in Figures 16 and 17, respectively. In the transverse orientation, as shown in Figures 18 and 19, the grains have various sizes with an elongated grain structure which is representative of a rolled aluminum plate product.

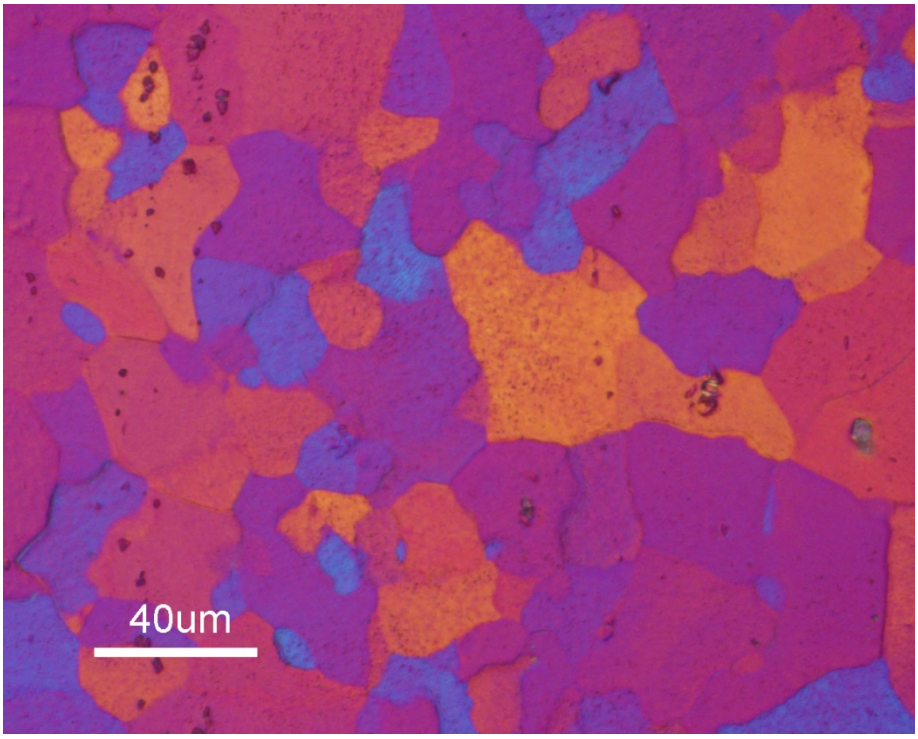

Figure 16. Planar orientation of UIT treated sensitized 5456 aluminum at 50X magnification

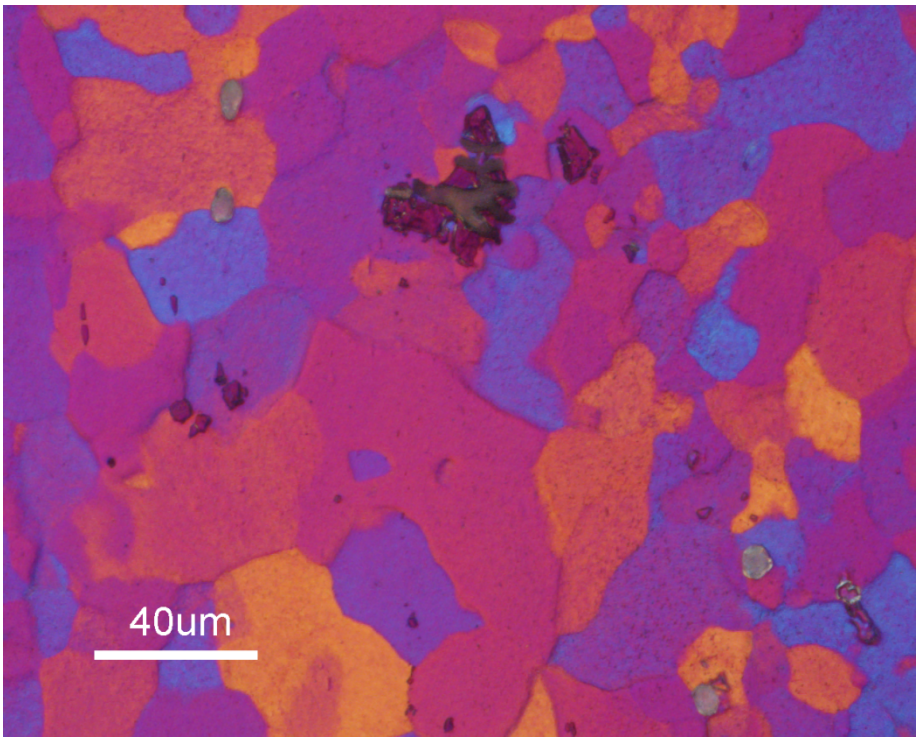

Figure 17. Planar orientation of non-treated sensitized 5456 aluminum at 50X magnification

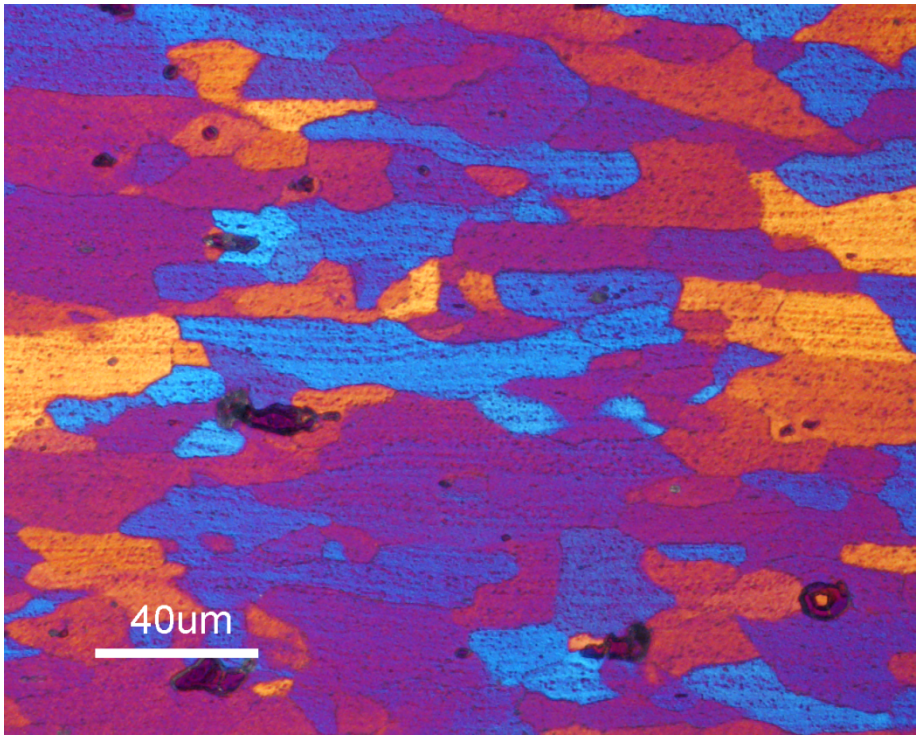

Figure 18. Transverse orientation of UIT treated sensitized 5456 aluminum at 50X magnification

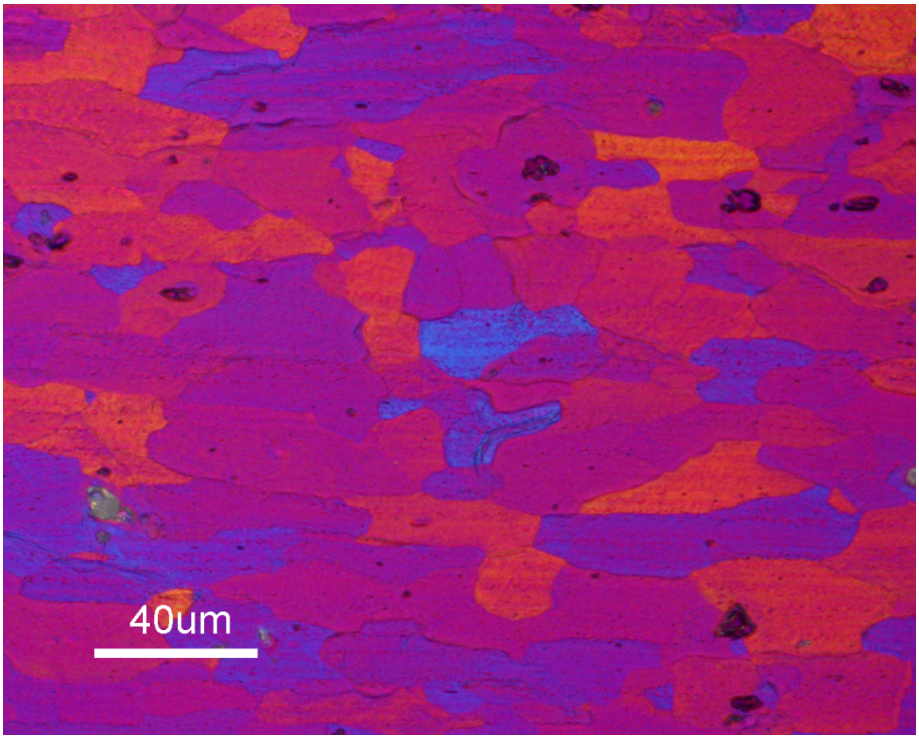

Figure 19. Transverse orientation of non-treated sensitized 5456 aluminum at 50X magnification

3.2.4 Electron Backscatter Diffraction of UIT and Untreated Sensitized 5456

Electron backscatter diffraction analysis was performed for both UIT and untreated material in the planar and transverse orientations below the UIT treated surface. The samples were examined approximately 100 µm (planar orientation) and 250 to 300 µm (transverse orientation) below the UIT surface. Electron backscatter diffraction surface preparation requires a mirror polish finish. Therefore the deformation layer was removed from the UIT sample in the planar orientation. Figures 20 and 21 are the inverse pole figures (IPF) which show the grain orientation of the UIT and untreated material, respectively, in the planar orientation at a magnification of 500X. The grain orientations for both UIT and untreated material

appear to be random which indicate that the material has a rather weak crystallographic texture. The grain boundary angle map shown in Figure 22 for the UIT treated material indicates that a 0.33 fraction of the grain boundaries are consider low angle grain boundaries (green and red boundaries) with boundary angles less than 15° and 0.63 fraction of the grains have high angle grain boundaries (blue boundaries) with boundary angles greater than 15°. For the untreated material, the grain boundary angle map, Figure 23, shows that only 0.2 fraction of the grains can be considered low angle grain boundaries while 0.75 fraction of the grains are high angle grain boundaries. The distributions of grain boundary angles are also represented in the histograms of the grain boundary misorientations or McKenzie plots in Figures 24 and 25 for UIT and untreated material, respectively. Both distributions of grain boundary orientations show that the mean boundary misorientation angle is ~ 40° which is characteristic for randomly oriented grains [37]. Strongly textured materials also have a large fraction of low angle grain boundaries. Based on the grain boundary angle maps, grain boundary misorientation and grain orientations observed in the IPF, both the UIT and untreated material have weak crystallographic texture. The grain boundary angle maps show the presence of marks that appear to be scratches on the surface; however they did not affect the EBSD analysis.

The grain sizes measured by EBSD show slight grain size reduction in the UIT material. The grain size maps do not reveal the presence of ultrafine or nanocrystalline grains, however, the maps show that there is slight grain size reduction between UIT treated and untreated material. The distribution of grain sizes

shown in Figure 26 for the UIT material shows that a 0.3 fraction of the grains have an average grain size diameter of ~44 μm. The remaining grains are less than 33 μm with ~ 0.06 fraction that are less than 10 μm. For the untreated material, the distribution of grain sizes shown in Figure 27 indicates that 0.4 fraction of the grains have average grain size diameters that range from 45 to 53 μm. The remaining grains have an average grain size diameter of 34 μm or less with a ~0.05 fraction with grain size diameters of less than 10 μm.

Although EBSD only showed slight grain reduction, TEM analysis showed significant grain reduction for the UIT material. The TEM images, section 4.2.1.1, showed the presence of nanocrystalline grains ranging in size from 2 to 200 nm in the UIT material. This discrepancy was due to the fact that EBSD was obtained from a subsurface region of the sample while TEM images were obtained from the surface of the treated sample.

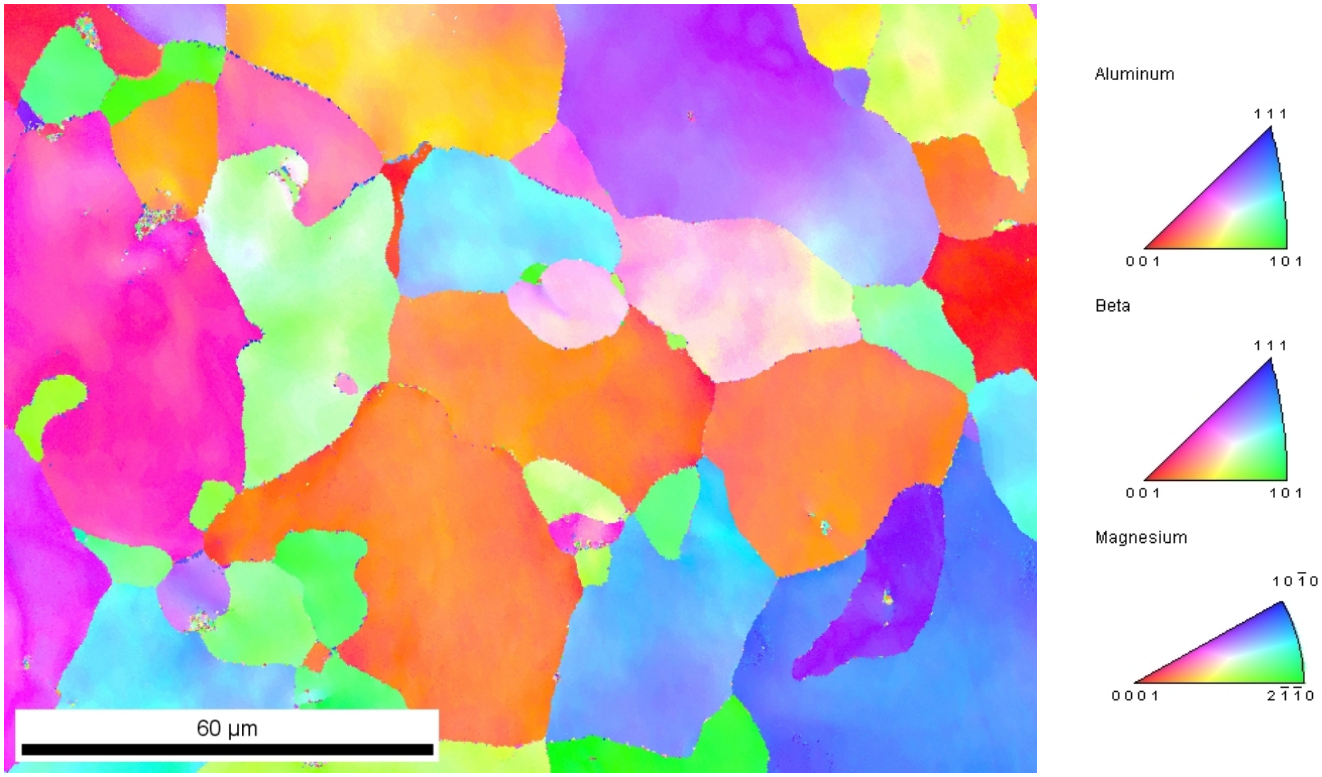

Figure 20. Inverse pole figure of UIT treated sensitized 5456 aluminum 500X in the planar orientation

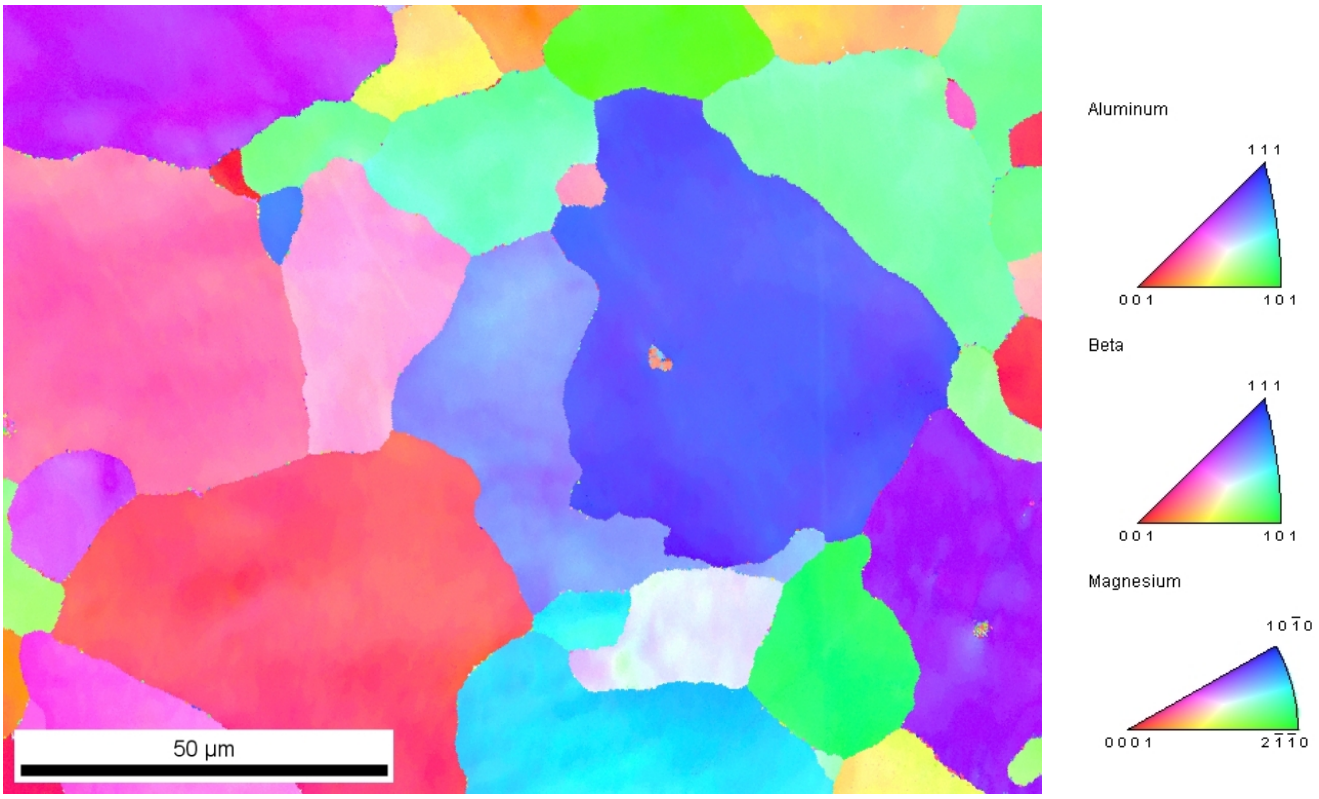

Figure 21. Inverse pole figure of untreated sensitized 5456 aluminum at 500X in the planar orientation

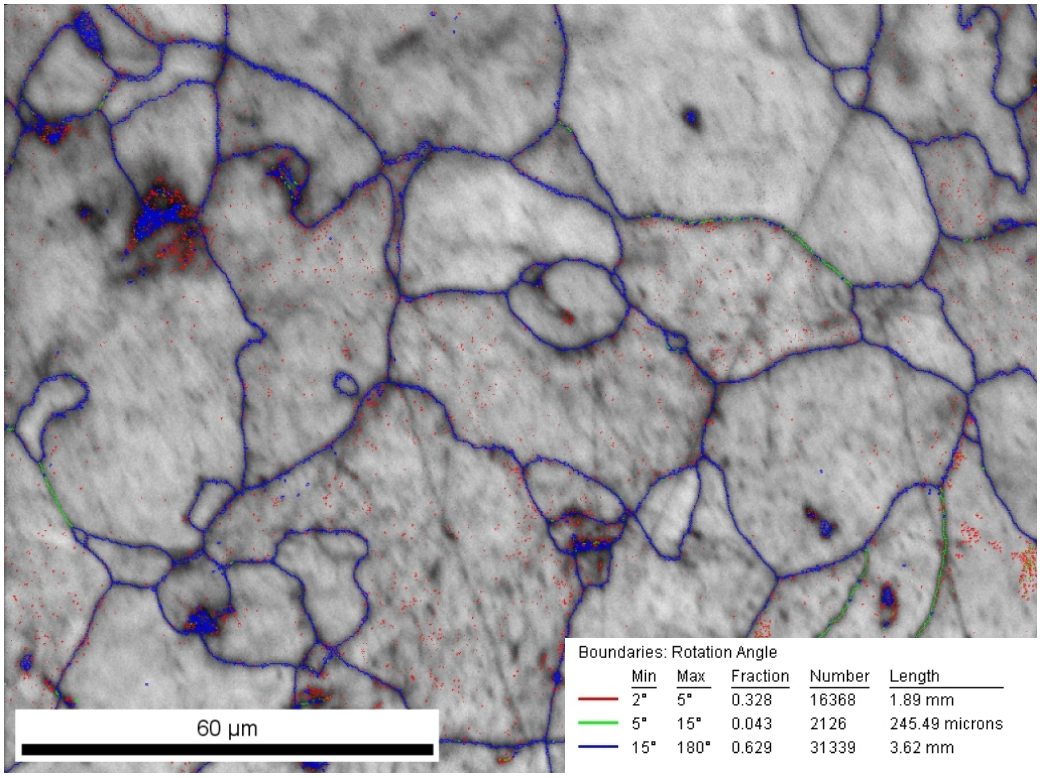

Figure 22. Grain boundary angle map of UIT treated sensitized 5456 aluminum at 500X in the planar orientation

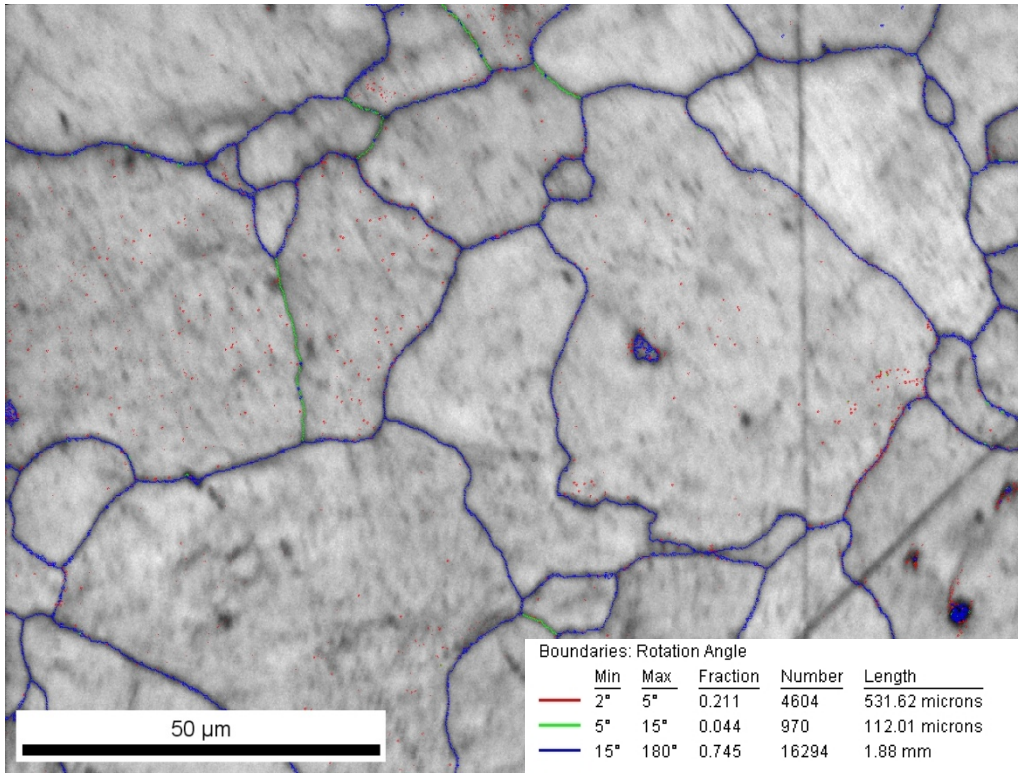

Figure 23. Grain boundary angle map of untreated sensitized 5456 aluminum at 500X in the planar orientation

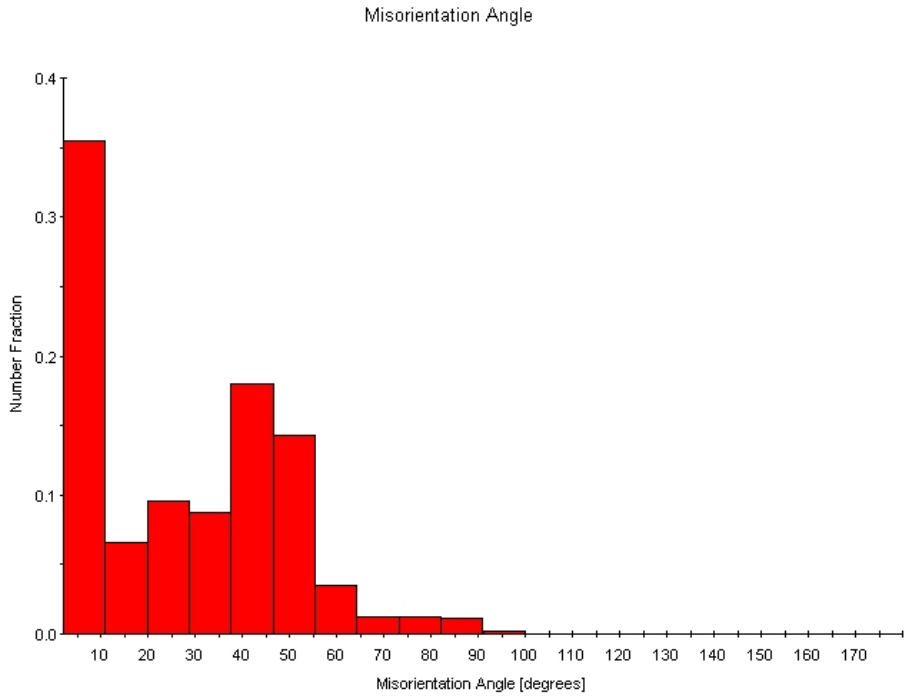

Figure 24. Distribution of grain boundary misorientation for UIT treated sensitized 5456 aluminum

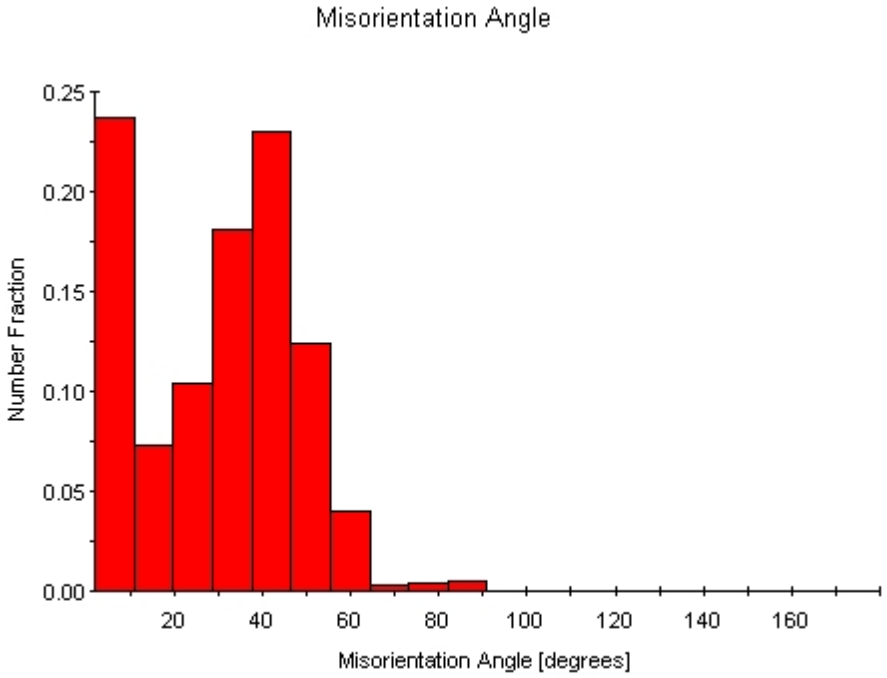

Figure 25. Distribution of grain boundary misorientation for untreated sensitized 5456

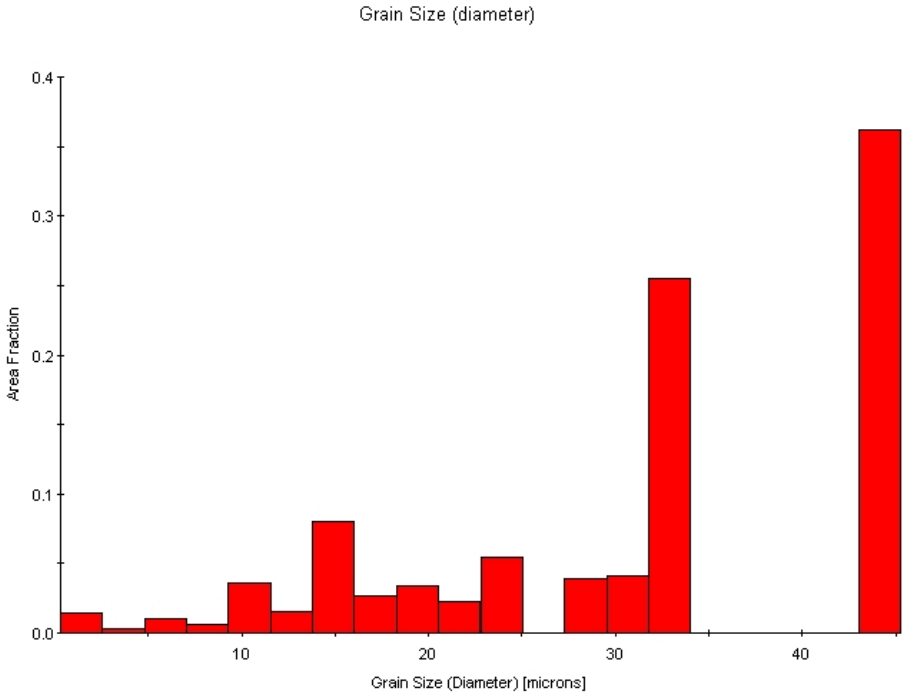

Chart: Grain Size (diameter)

Edge grains included in analysis

Diameter [microns]	Area Fraction
1.42109	0.0141848
3.66927	0.00307653
5.91745	0.00996589
8.16563	0.00657761
10.4138	0.0360179
12.662	0.0158297
14.9102	0.0799609
17.1583	0.0271473
19.4065	0.0335875
21.6547	0.0227889
23.9029	0.0543868
26.151	0
28.3992	0.0388688
30.6474	0.0408029
32.8956	0.255245
35.1438	0
37.3919	0
39.6401	0
41.8883	0
44.1365	0.361559

Average Number	0.843883
Standard Deviation	3.35772
Area	31.5618

Figure 26. Distribution of grain size for UIT treated sensitized 5456 aluminum

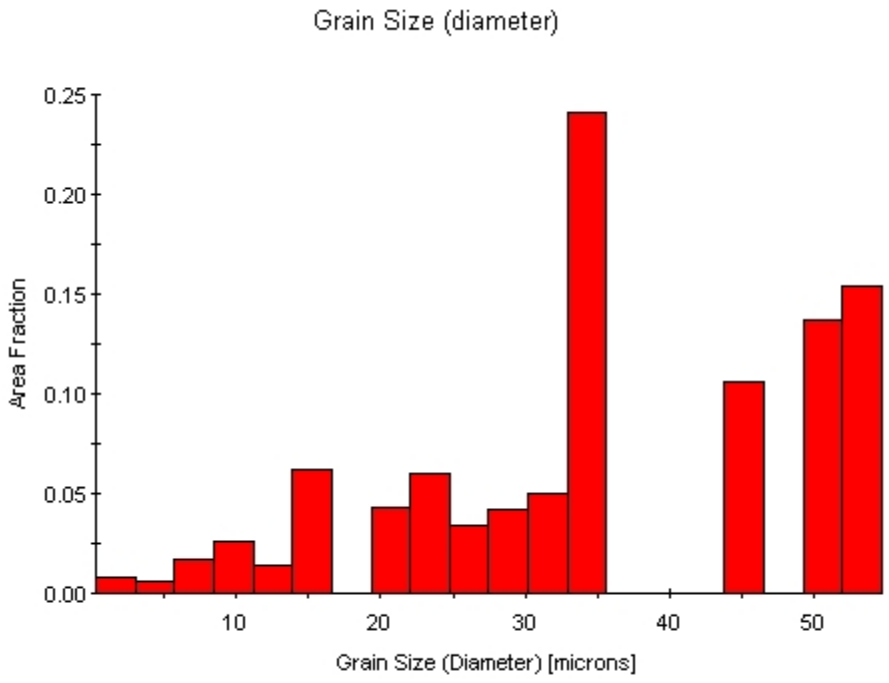

Chart: Grain Size (diameter)

Edge grains included in analysis

Diameter [microns]	Area Fraction
1.65653	0.00801789
4.37556	0.00566103
7.0946	0.0167576
9.81364	0.0263263
12.5327	0.0140091
15.2517	0.0617817
17.9708	0
20.6898	0.0428448
23.4088	0.06019
26.1279	0.0340982
28.8469	0.0417814
31.5659	0.0495169
34.285	0.241457
37.004	0
39.7231	0
42.4421	0
45.1611	0.106293
47.8802	0
50.5992	0.136912
53.3182	0.154353

Average Number	1.0631
Standard Deviation	4.33065
Area	36.0334

Figure 27. Distribution of grain size diameter for untreated sensitized 5456 aluminum

Figures 28 and 29 show the IPFs for UIT and untreated material, respectively, in the transverse orientation at a magnification of 500X. For the UIT and untreated material, both IPFs show elongated grains that are characteristic of rolled aluminum plate product with random grain orientations. The IPFs also show that the grain orientations for both the treated and untreated materials are random which indicates a weak crystallographic texture. The grain boundary angle maps shown in Figures 30 and 31 show that both the UIT and untreated material exhibit a large number of high angle grain boundaries, >15°. As previously noted, high angle grain boundaries are more susceptible to SCC. Although the grains are not equiaxed, the grains are elongated recrystallized grains which makes the material more susceptible to intergranular corrosion. The fraction of high angle grain boundaries for both the UIT and untreated material are approximately a 0.90 fraction with the UIT treated material exhibiting a slightly higher fraction of high angle grain boundaries. The McKenzie plots shown in Figures 32 and 33 show a mean boundary misorientation angle of ~ 40° for both UIT and untreated material which is characteristic of materials with weak crystallographic texture. The IPFs, grain boundary maps, grain boundary misorientations for the UIT and untreated material in the transverse orientation are consistent with the results for the UIT treated and untreated material in the planar orientation.

The grain size maps for the UIT treated and untreated material in Figures 34 and 35 reveal similar average grain sizes. For the UIT material, more than 0.5 fraction of the grains have an average grain size diameter between 25 to 38 μm. The smallest average grain size is 1.25 μm with only a 0.03 fraction. Similarly, the

untreated material also shows a 0.45 fraction of grains with average grain size diameters between 25 to 34 μm. A small fraction of the grains, 0.03, have an average grain size diameter of 1.14 μm. The grain size maps do not reveal the presence of ultrafine or nanocrystalline grains. In the transverse orientation, the grain size reduction between the UIT and untreated material is not as obvious as it was in the planar orientation due to the three dimensional sizes of the grains and grain shape.

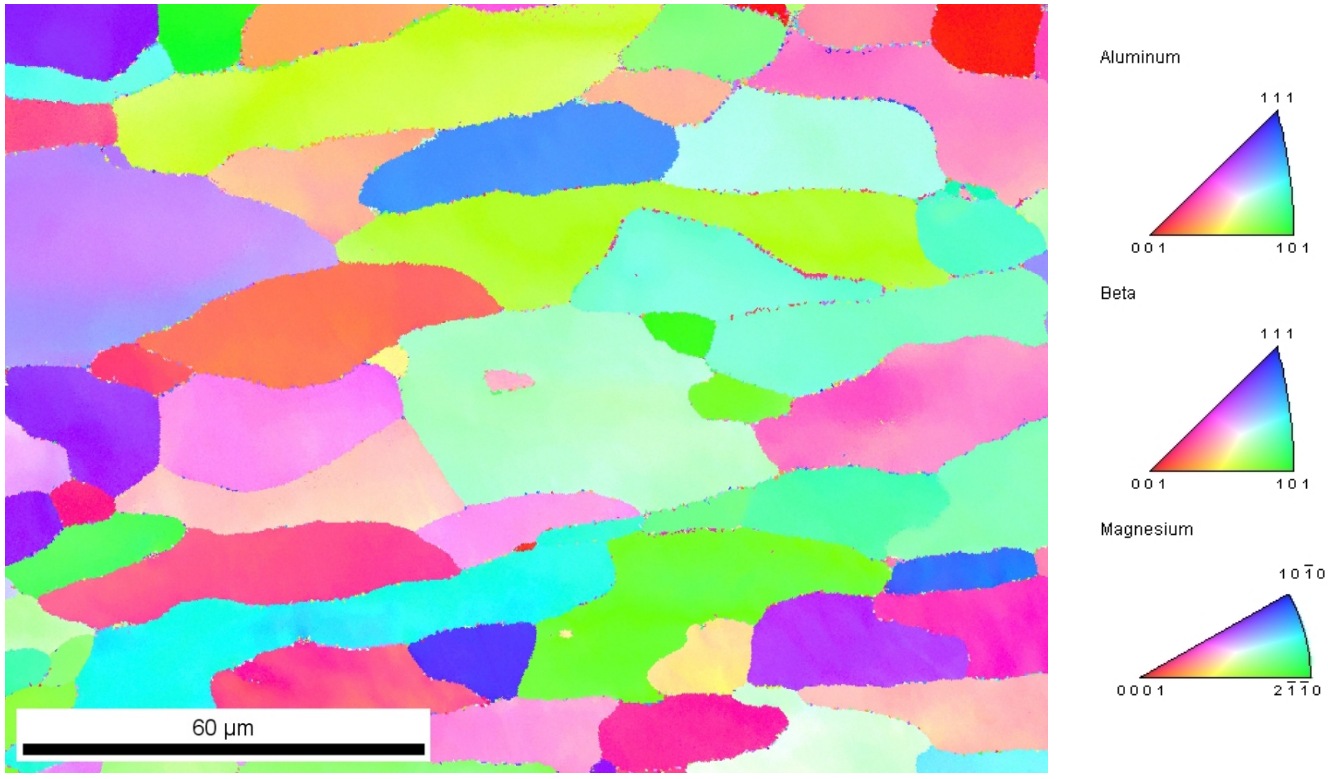

Figure 28. Inverse pole figure of UIT treated sensitized 5456 in the transverse orientation at 500X

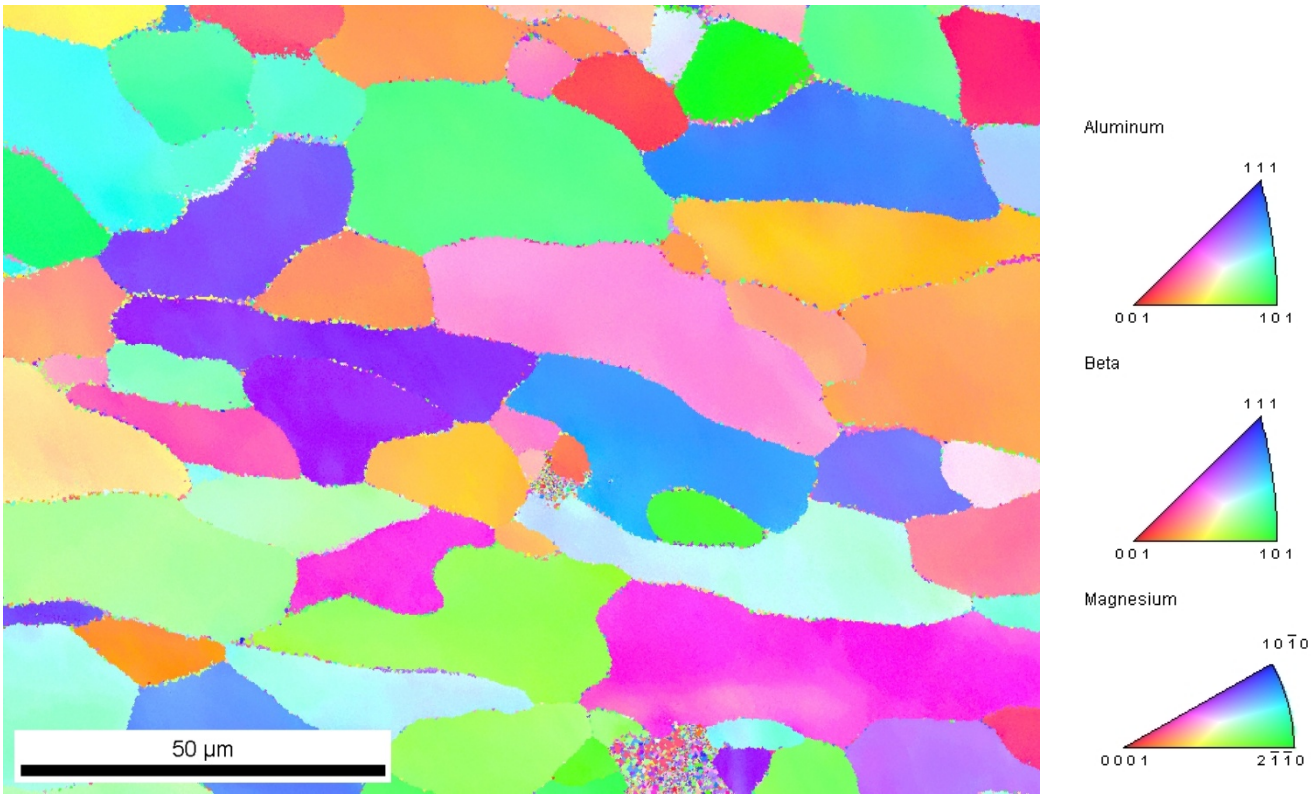

Figure 29. Inverse pole figure of untreated sensitized 5456 in the transverse orientation at 500X

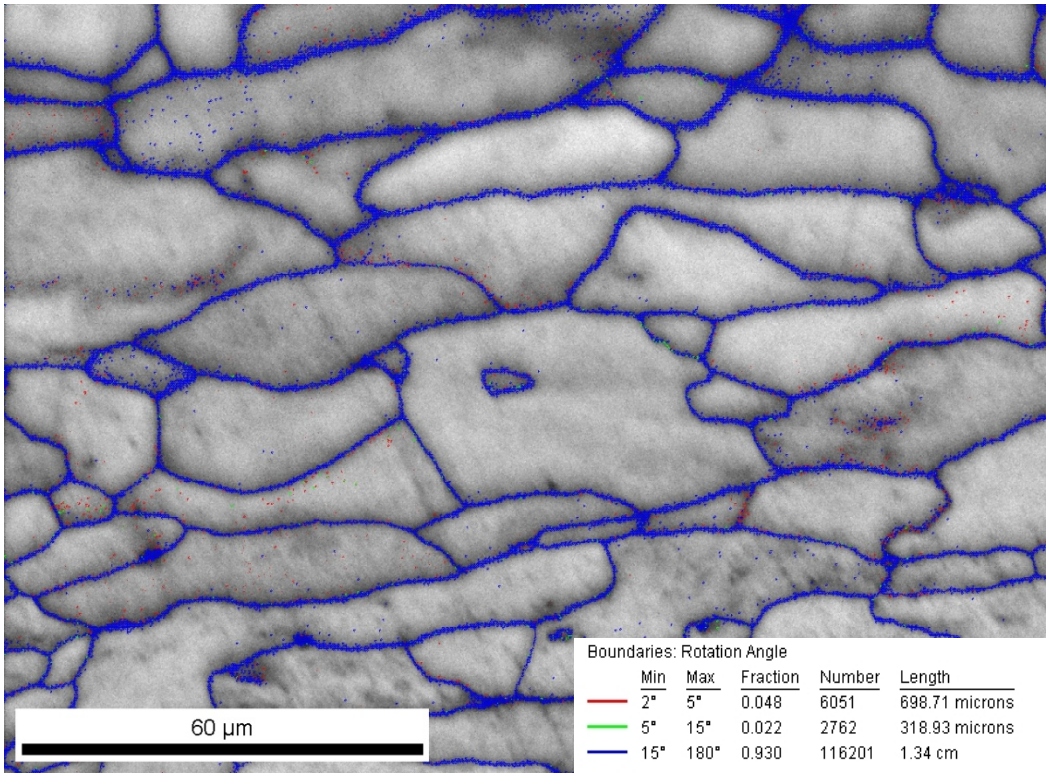

Figure 30. Grain boundary angle map for UIT treated sensitized material in the transverse orientation at 500X

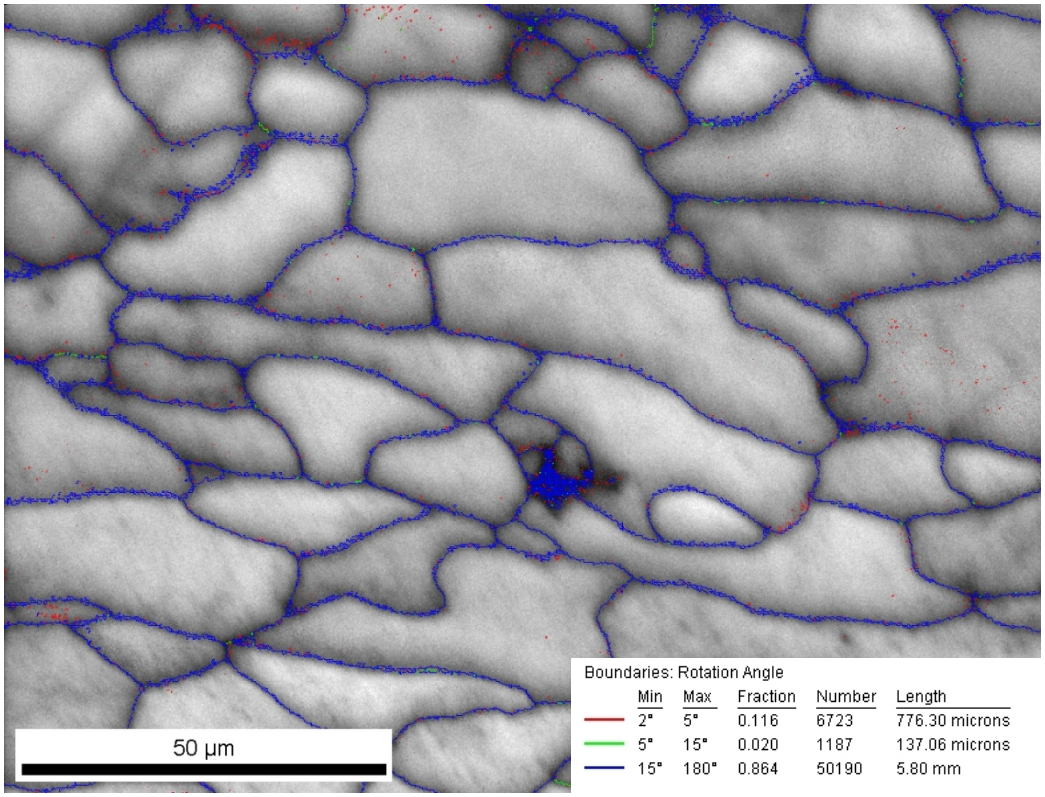

Figure 31. Grain boundary angle map for untreated 5456 in the transverse orientation at 500X

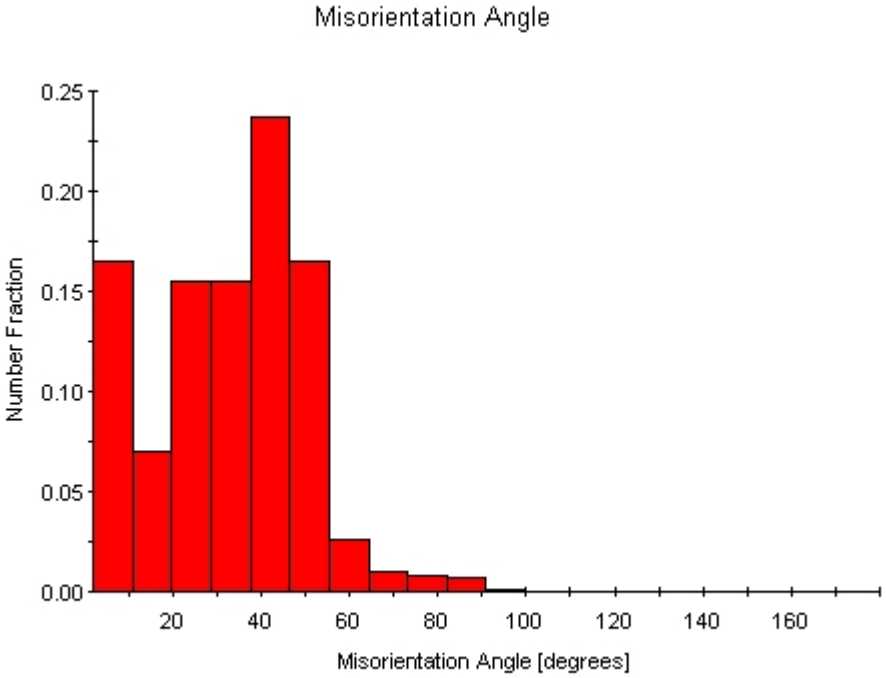

Figure 32. Distribution of grain boundary misorientation for UIT treated sensitized 5456 in the transverse direction

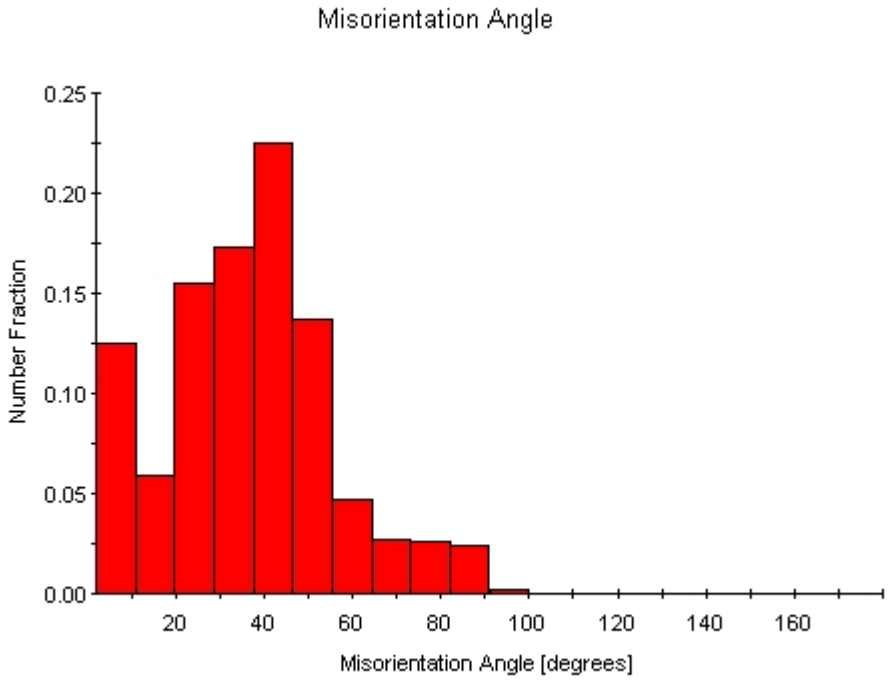

Figure 33. Distribution of grain boundary misorientation for untreated sensitized 5456 in the transverse direction

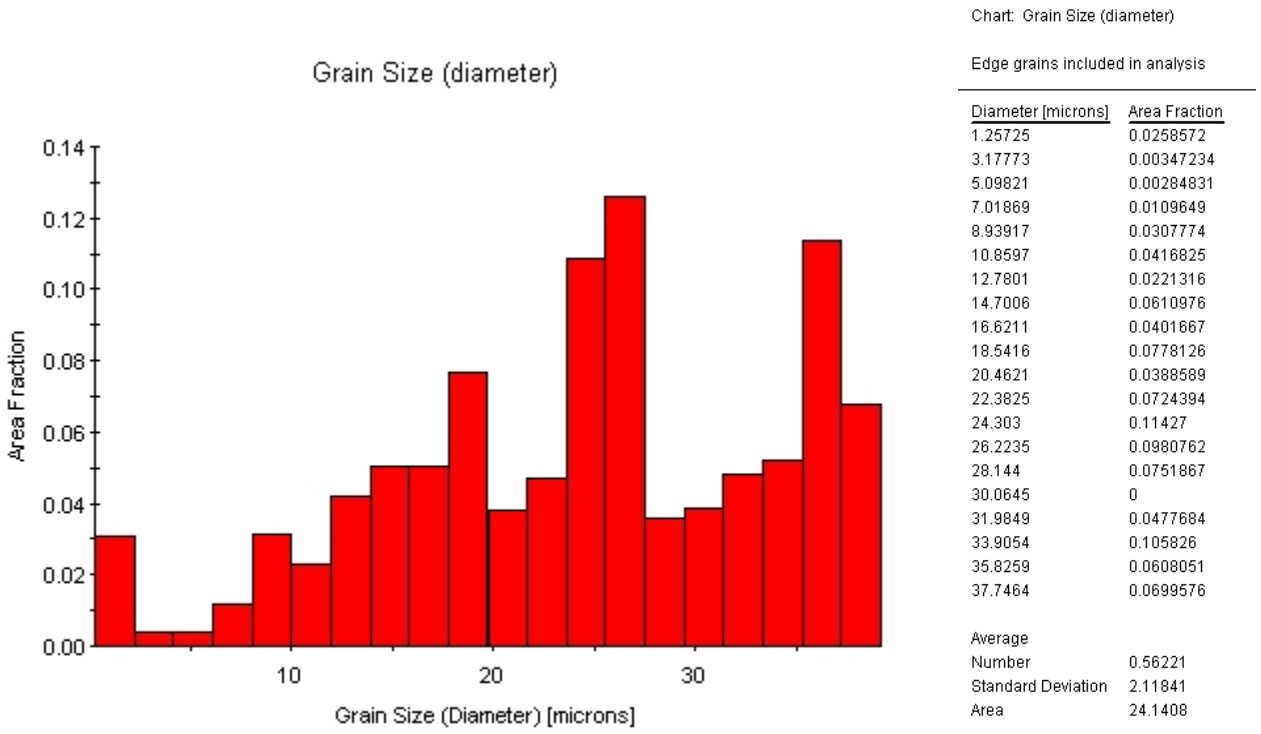

Figure 34. Distribution of grain size diameter for UIT treated sensitized 5456 aluminum in the transverse orientation

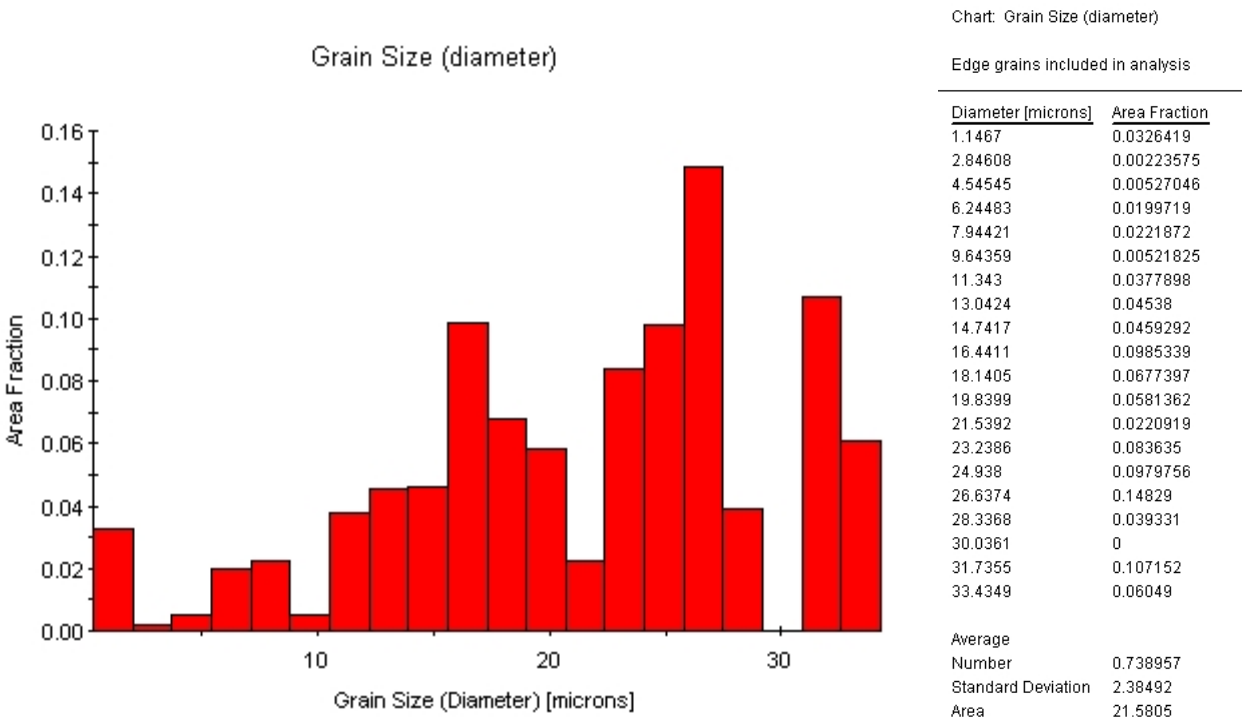

Figure 35. Distribution of grain size diameter for untreated sensitized 5456 aluminum in the transverse orientation

3.2.5 Crystallographic Texture of UIT and Untreated Sensitized 5456

Crystallographic texture was examined on the (111) plane because it is the dominant slip plane for aluminum alloys and on the (200) plane which is the second dominant orientation. Figures 36 and 37 show the (111) and (200) pole figures for the UIT and untreated material, respectively obtained from planar specimens along the rolling direction of the material. The pole figures show weak crystallographic texture for both the UIT and untreated material. The untreated material, Figure 37, shows a very random texture, however the pole figures for the UIT material, Figure 36, suggest a weak cube orientation on the (111) plane. The texture density

distributions are similar for both UIT treated and untreated materials. The texture maxima are comparable for both the UIT treated material (6.101 and 7.737) and the untreated material (7.192 and 8.176). It is noted that the texture strength is higher on the (200) plane for both UIT and untreated material.

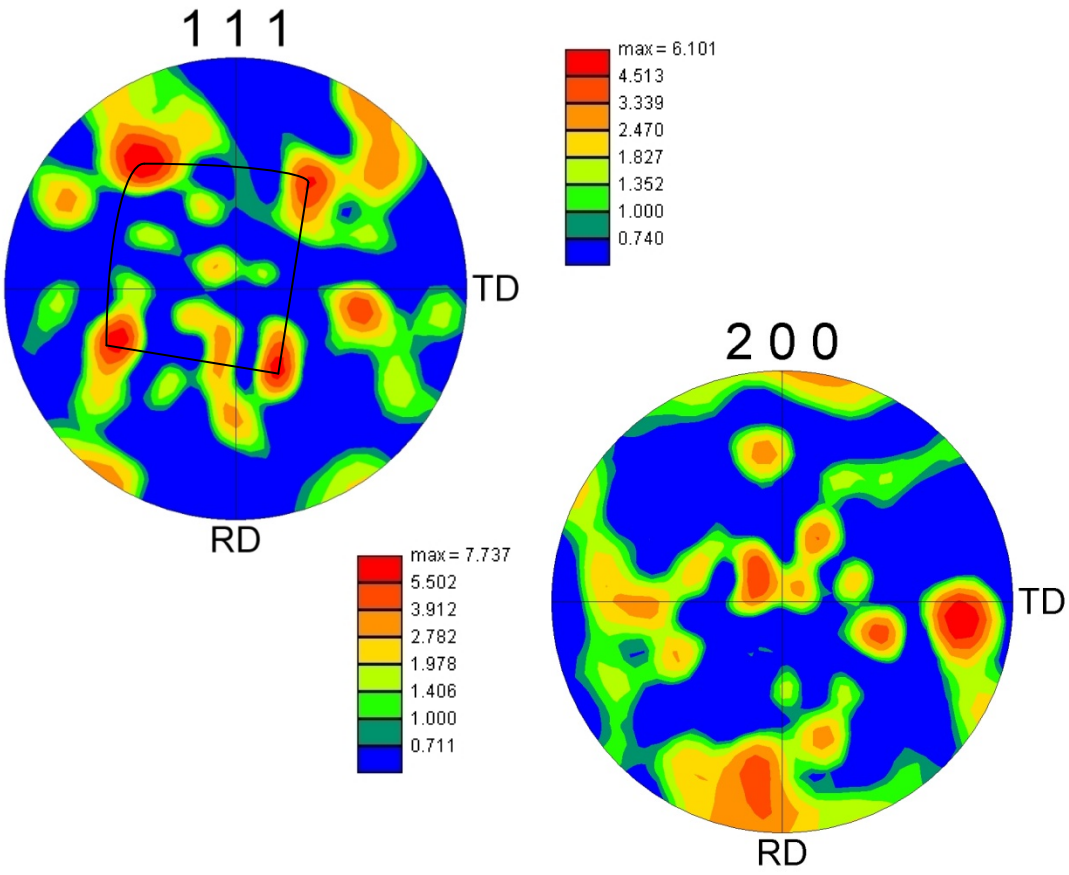

Figure 36. Pole figures showing texture analysis of UIT treated sensitized 5456 along (111) and (200) planes in planar orientations

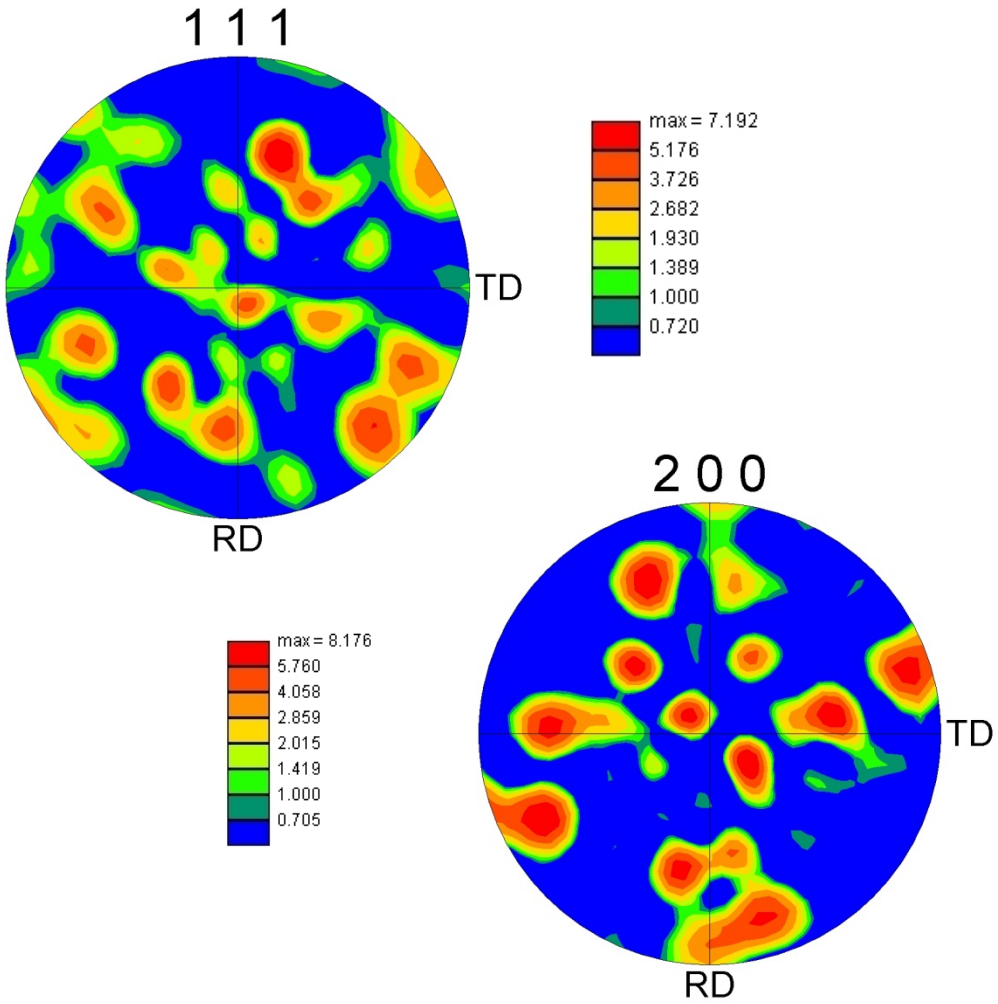

Figure 37. Pole figures showing texture analysis of untreated sensitized 5456 along (111) and (200) planes in planar orientations

Texture analysis for the transverse orientations was also examined on the (111) and (200) plane. The results are consistent with the analysis for the planar orientations. Both the UIT treated and untreated material exhibited weak crystallographic texture as shown in Figures 38 and 39. The texture density distributions are similar for both

UIT treated and untreated materials with texture maxima slightly higher for the UIT treated material (4.604 and 4.567) than untreated material (3.606 and 3.838).

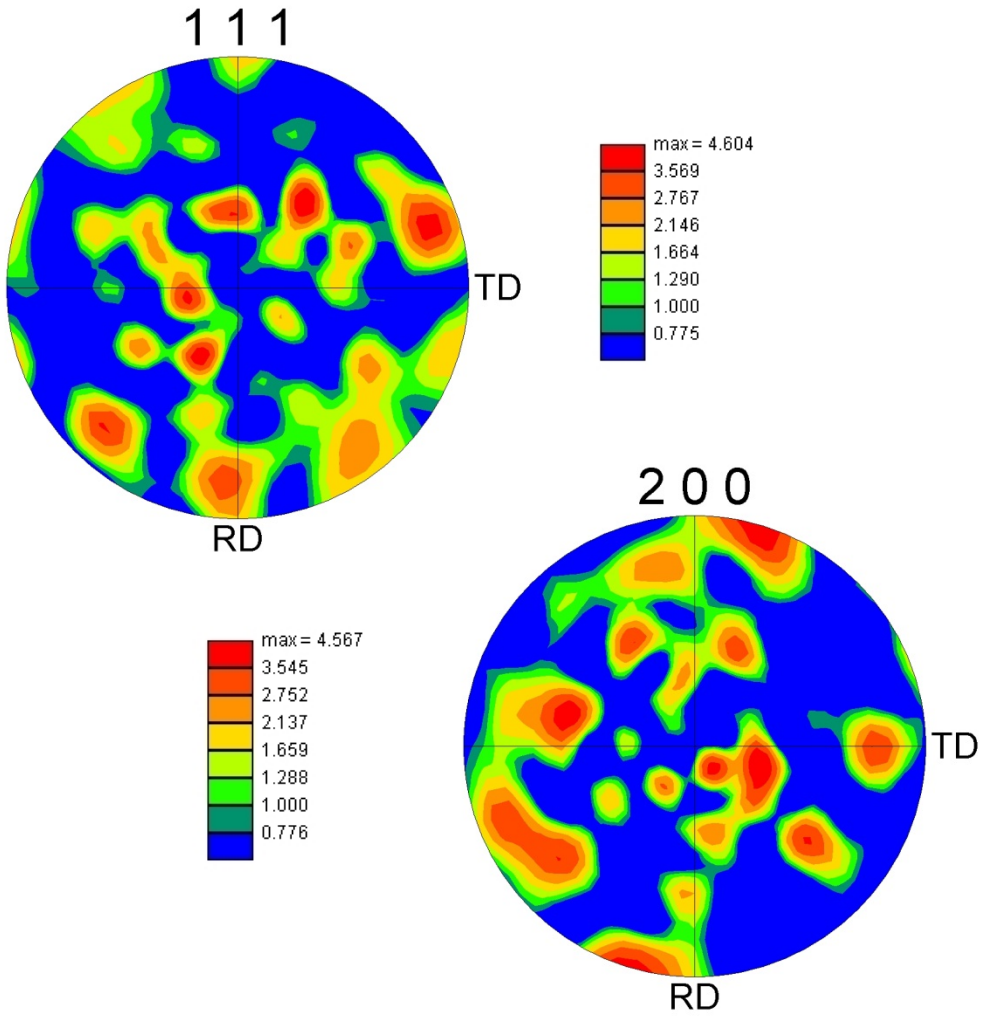

Figure 38. Pole figures showing texture analysis of UIT treated sensitized 5456 along (111) and (200) planes in the transverse orientation

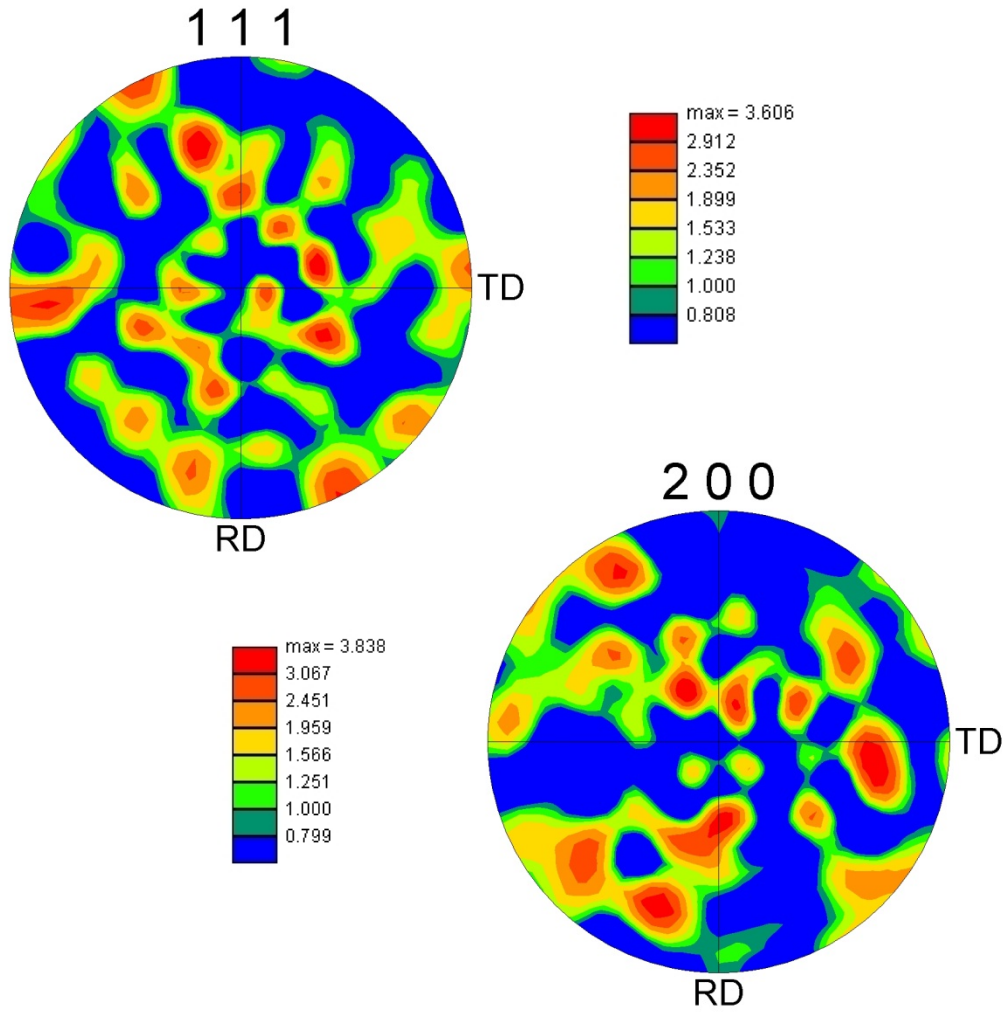

Figure 39. Pole figures showing texture analysis of untreated sensitized 5456 along (111) and (200) planes in the transverse orientation

X-ray diffraction measurements were also obtained to examine preferred orientations. X-ray diffraction allows one to ascertain the molecular structure of a crystalline material by diffracting x-rays through the sample. An XRD analyzer obtains interference patterns reflecting lattice structures by varying the angle of incidence of the x-ray beam with respect to the surface of the sample.

Measurements were obtained in the transverse orientation at the cross hairs (closest to UIT surface along the transverse orientation), just below the UIT surface (~0.1 mm) and at depths of 1.5-, 3.0-, 5- mm below the UIT surface. Measurements were also obtained in the planar orientation on the UIT surface. Measurements were obtained from untreated material at the cross hairs, just below the surface, and at the same depths (as for UIT sample) below the surface to provide a basis for comparison. X-ray intensities were measured at the (111) and (200) reflections.

For FCC structures, the peak intensity ratio for the (111) reflection/(200) reflection is $I_{(111)}/I_{(200)} \approx 2:1$ for random orientation of the grains [38]. Figures 40 and 41 show the (111) and (200) peak profiles of the UIT material (obtained from two samples) at various depths below the treated surface. As shown in Figure 40, at a depth of 5 mm below the UIT surface, the treated sample shows comparable peak intensities at the (111) reflection and (200) reflection. With decreasing depth towards the surface, the peak intensities at the (200) reflection become stronger and starts to dominate at depths of 3 mm and 1.5 mm below the UIT surface as shown in Figure 40. The peak intensity ratio $I_{(200)}/I_{(111)}$ is >2:1. The larger peak intensity at the (200) reflections indicates a preferred orientation along the [200] direction. Just below the cross hairs (0.1 mm from the surface), the peak intensity ratio, $I_{(200)}/I_{(111)}$ is ~ 2:1. At the cross hairs, the peak intensity at the (111) reflection are comparable to (200) reflection, however the (200) reflection is dominant. Figure 41 shows that at a depth of 5 mm, the peak intensity at the (111) reflection is greater than the (200) reflection. However, with decreasing depth towards the surface, the peak intensities for the (111) and (200) reflections are comparable at 3 mm, 1.5 mm, just below the surface,

and at the surface. Although the intensities at the (200) reflection appear to be equivalent to the (111) reflection, since the ratio of 2:1 is not satisfied, the intensity at the (200) reflection is considered dominant. The peak profile for the untreated material at a depth of 5 mm is shown in Figure 42. At all depths, the intensities for the untreated material is dominant for the (111) reflection with a ratio of $I_{(111)}/I_{(200)}$ of 4:3. Therefore, only one spectrum is shown. The results show that the UIT process induces a preferred orientation along the [200] direction when measured by XRD at a transverse orientation to the UIT surface.

At the cross hairs closest to the UIT surface, Figure 43, the peak profiles for the UIT material show a weak peak at 42.4° corresponding to an interplanar *d* spacing of ~2.05 which differs from the *d* spacing of 2.02 for the (200) reflection. The presence of the weak peak indicates the presence of a stress resulting in a shift in the *d* spacing of the reflected plane. The stress cannot be measured from the peak profiles; however, the strain can be calculated by measuring the difference in the interplanar *d* spacing between the weak peak (under stress) and the peak at the (200) reflection (absence of stress) using the following equation [38]:

$$\varepsilon = \frac{d_n - d_{200}}{d_{200}} \quad \textbf{(2)}$$

where d_n is the interplanar spacing for the weak peak and d_{200} is the spacing for the (200) reflection. Equation 2 results in a strain of -0.015 which indicates that part of the material has been slightly compressed.

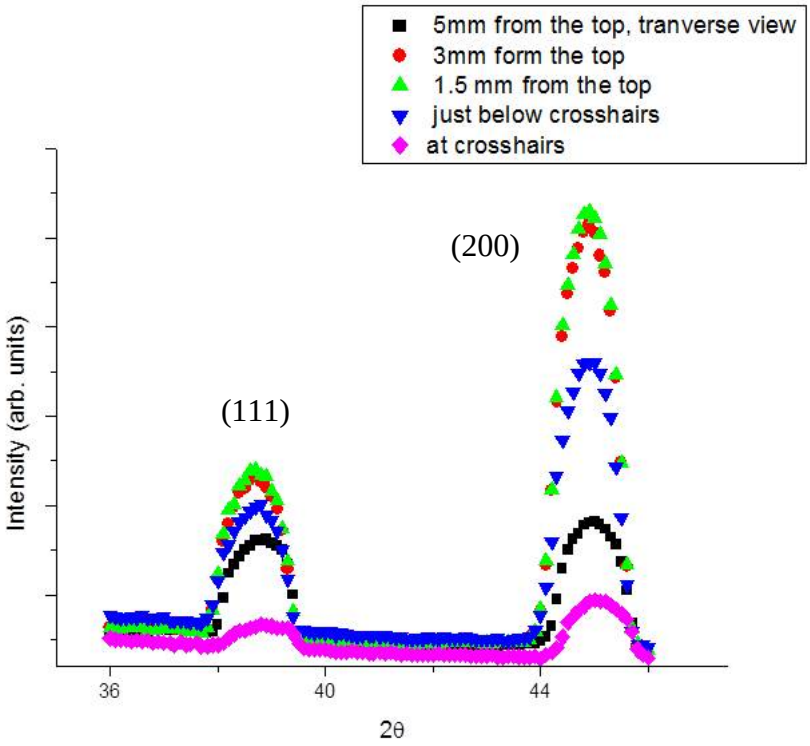

Figure 40. X-ray diffraction spectra of UIT material (sample 1) obtained at the surface and various depths below the treated surface in the transverse orientation for the (111) and (200) reflections

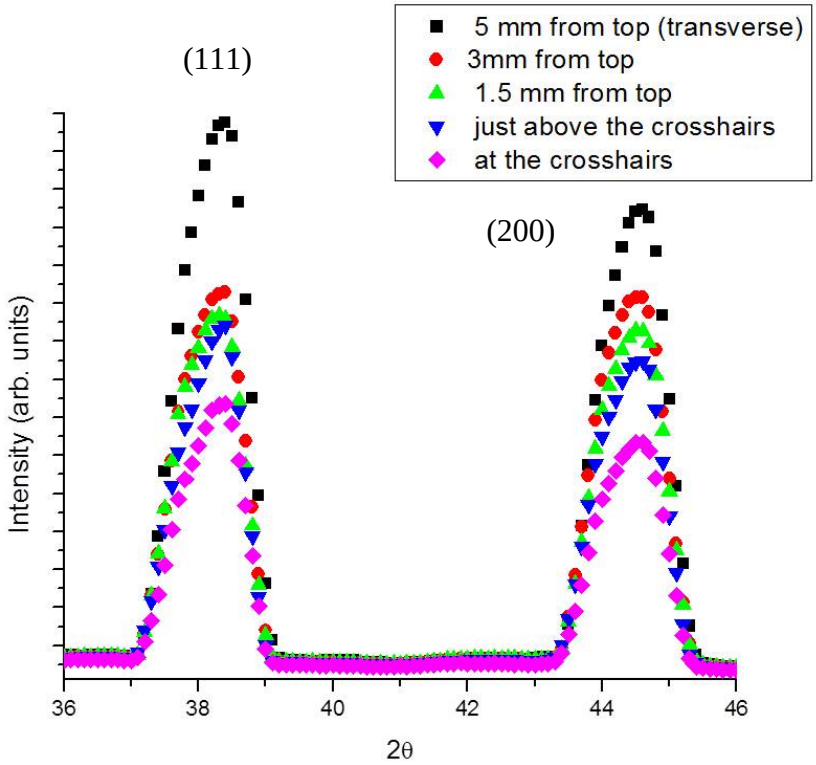

Figure 41. X-ray diffraction spectra UIT material (sample 2) obtained at various depths below the treated surface for the (111) and (200) reflections

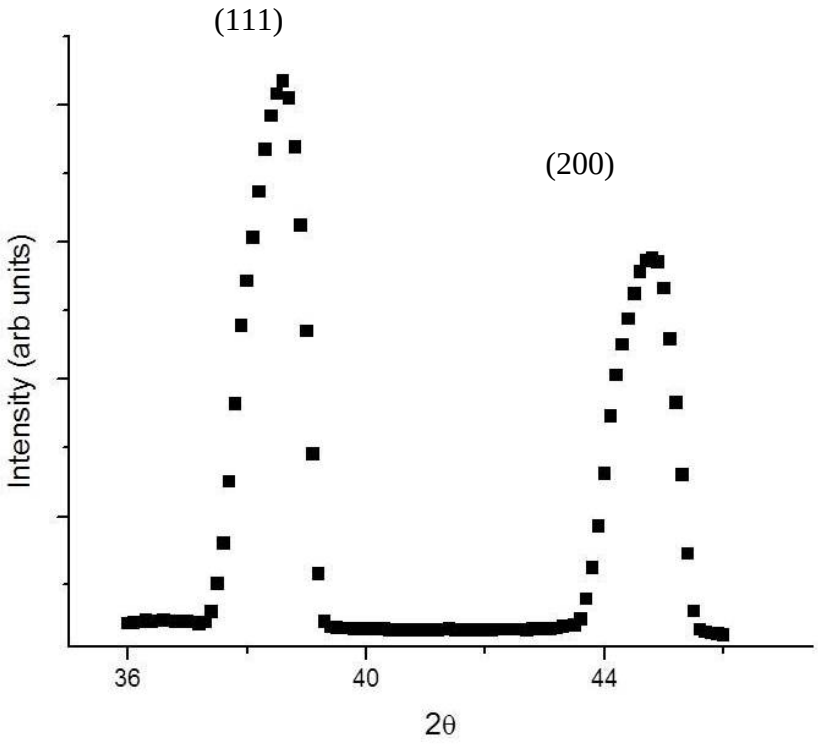

Figure 42. X-ray diffraction spectrum of untreated material at the (111) and (200) reflections at 5 mm below the surface

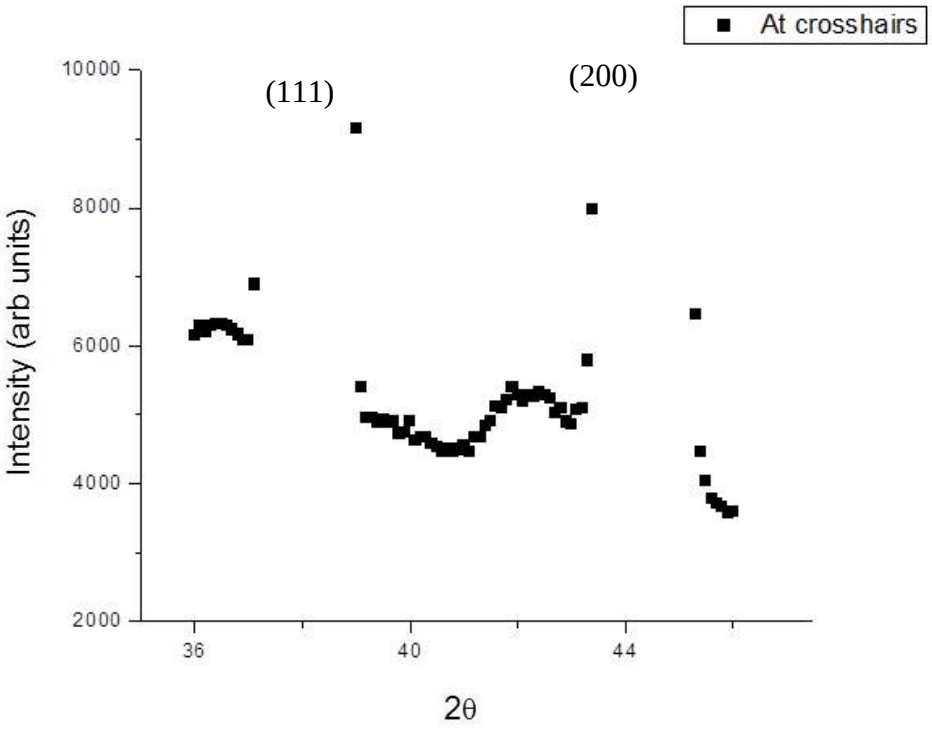

Figure 43. X-ray diffraction spectrum of UIT material showing the presence of a weak peak at 42.4° indicating that strain is present in the sample

3.3 Discussion

The SEM micrographs of the UIT samples show some damage at the surface induced by the UIT process. The damage is more notable in the transverse cross section as shown in Figures 13 and 14. The micrographs show tearing, void formation, and a distinct separation between the deformation layer and the metal matrix. These observations should be of concern and may have an impact on the mechanical and corrosion properties at the UIT surface.

The UIT process is accompanied by the ultrasonic impacts which induce plastic deformation near the surface. The distribution of ultrasonic waves which penetrate the subsurface material results in quick heating and cooling at the areas of deformation. Researchers have shown that the UIT process results in grain refinement [3,25,29] and the production of ultrafine and nanocrystalline grains. Although the results of optical microscopy and EBSD did not show the formation of ultrafine or nanocrystalline grains, the UIT process can reduce the average grain size diameter by more than 10 μm as compared to untreated material. Furthermore, TEM analysis of the UIT surface region did show smaller grain in the nano-meter range as discussed in section 4.2.1.1. The UIT material exhibited a number of grains that were less than 10 μm. The grain shape varied which indicates that the grain size reduction is not uniform. The non-uniformity of the grain size reduction may also be attributed to the manual nature of the UIT process.

X. An et al. found that the grain size can change within the impact effect zone from the top surface down to the matrix due to strain variations [3]. The variations in strain are attributed to UIT processing parameters; impact frequency, amplitude under

load, and feed rate control; all of which can control the average grain size and microstructure of 2024-T351 aluminum alloy. As previously noted in section 1.1, the processing parameters used for this study were a carrier frequency of 27 kHz, pin dimension of 3 mm, amplitude of 22 μm, and feed rate of 10 cm/min. In comparison, as noted in section 3.1, X. An et al. used a carrier frequency of 36 kHz, pin dimension of 5 mm, amplitude of 36 μm, and feed rates of 400 mm/min (40 cm/min) and 1000 mm/min (100 cm/min) [3]. These parameters result in a microstructure that exhibits equiaxed ultrafine, nanocrystalline grains at the top surface and equiaxed ultrafine, grain structure with extended micro bands at a depth of approximately 3 to 5 μm and refined grains of less than 10 μm (Section 3.1). Transmission electron microscopy micrographs show the formation of nanocrystalline grains in the UIT material which is discussed in section 4.2.1. The nanocrystalline grains ranged in size from 2 to 200 nm in diameter as measured from the TEM micrographs. Differences in the resulting microstructure observed by X. An et al. and this research may be due to the processing parameters. X. An et al. used two different sets of parameters for their study and found that a slower feed rate and larger amplitude under load resulted in larger average grain size at the top surface [3]. X. An et al. used a higher carrier frequency, pin dimension, amplitude, and feed rate than the parameters used for this study. The higher processing parameters likely resulted in more induced plastic deformation and larger ultrasonic stresses induced into the surface of the material.

Severe plastic deformation processes that result in random and multidirectional deformation could result in high angle boundary misorientations from low angle boundary misorientations [25,39,40]. The formation of high angle

boundary misorientations is thought to consist of two steps; the formation of subgrains through grain subdivision and evolution of the boundary misorientations due to subgrain rotation [25]. Grain subdivision does not continue indefinitely but rather levels off when a critical size is achieved given a certain amount of deformation [25,41]. With continued straining, the dislocation movement becomes restricted because the subgrains cannot continue to subdivide. As a result, the slip systems of adjacent grains rotate to more energetically favorable orientations due to the continuous straining [25]. The subgrains cannot accommodate deformation by dislocation glide along the same slip system, therefore they begin to rotate. With increasing rotation angle, the formation of highly misoriented grains is produced. Severe plastic deformation techniques such as shot peening and ultrasonic shot peening are effective in promoting subgrain rotation because of the multi-directional strain paths and high strain rates induced by the techniques [25,42].

The UIT process is a manual technique therefore the deformation induced by the technique is random and multidirectional which would result in highly misoriented grains. Although the grain boundary misorientation angle maps show a large fraction of high angle grain boundaries (> 15°), the fractions are similar for both UIT treated and untreated material. The results are not consistent with the literature which suggest that SPD techniques such as UIT and ECAP result in the formation of high angle grain boundaries and an increasing fraction of high angle grain boundaries with increased deformation [43].

Texture evolution in Al-Mg is strongly influenced by the alloy composition, initial microstructure, and processing prior to severe deformation [44,45]. The

magnesium content in aluminum alloys affects the development of rolling and recrystallization textures. Magnesium can affect the texture as a solute atom or as β phase particles and has been shown to induce shear banding during cold rolling [45]. The cube texture was first observed in FCC metals more than 70 years ago and was found in different FCC metal sheets after recrystallization [46]. In aluminum alloys, a very strong cube texture was obtained after crystallization of 95% rolled aluminum sheet.

Aluminum-magnesium alloys have been shown to exhibit strong crystallographic texture when subjected to severe plastic deformation such as heavy rolling reductions. However, when subjected to severe plastic deformation such as ECAP, the crystallographic texture is weak. For Al-Mg alloys containing more than 3 wt. % Mg, shear bands are formed when rolling reductions are greater than 50% [34,45]. However, with increasing Mg content above 5 wt. %, and increased rolling reduction up to 95%, the overall rolling texture becomes weaker [45]. Shear banding acts indirectly on texture formation resulting in the rotation of major texture components into more scattered orientations [34]. Equal channel angular pressing of aluminum 5109 has been shown to lead to a non-uniform texture, however the inhomogeneity decreases with increasing number of ECAP passes [34]. Equal channel angular pressing was shown to rotate part of the initial cube orientations to a non-ideal simple shear texture [34].

The 5456 material used for this study was cold rolled to an H116 temper and exhibits elongated grains which are similar to the initial texture observed by X. An for 2024-T351 [3] and O. Engler for 5005 aluminum [35]. The initial texture of Al-

Mg alloy 5005 cold rolled to an H14 temper with 1 mm gage has been shown to reveal a rolling texture with some cube texture [35] and deformed microstructure with elongated grains. However, based on the (111) and (200) pole figures shown in Figures 37 and 39, the untreated material does not exhibit any cube texture. In the planar orientation, the (111) pole figures shown in Figure 36 suggest that the UIT process may induce a weak cube texture. Although the (200) pole figure in the planar orientation, Figure 36 appears to be random, the texture strength is greater than the texture strength for the (111) pole figure. This concurs with the XRD results which showed stronger peak intensities at the (200) reflection for the UIT material. This suggests that the UIT process induces a slight (200) preferred orientation. The UIT process is similar to ECAP in that the process results in a weak crystallographic texture. In addition, since the UIT process is a manual process and the deformation is near surface and does not involve multiple passes such as ECAP or heavy roll reduction, a strong crystallographic texture should not be expected.

3.4 Summary

The result of the metallographic studies can be summarized as follows:

- Ultrasonic impact treatment produces a deformed layer near the surface that measures ~ 10 to 18 μm in thickness. The indentations vary, ranging in size from 3 mm x 3 mm to 3 mm x 5 mm.
- The deformation layer is characterized by tears and voids. There is a distinct separation between the deformation layer and the metal matrix. The surface topography also contains the presence of micro cracks and micro tears.

- The deformation layer does not exhibit the presence of β phase, however below the deformation layer, a continuous β phase is present along the grain boundaries.
- Grain refinement extends below the UIT surface and reduces the average grain size diameter by more than 10 µm as compared to untreated material.
- The fraction of high angle grain boundaries is comparable for both UIT treated and untreated material which suggests that the straining induced by the UIT processes was not effective in inducing a larger number of high angle grain boundaries.
- Both the UIT material and untreated material exhibited weak crystallographic texture which suggest that the UIT process does not induce enough deformation to result in crystallographic texture. However, XRD shows a slight preferred orientation along the <200> direction.

Chapter 4: Microstructural Evolution of Aluminum 5456 Plastically Deformed by UIT

4.1 Introduction

This chapter presents the study of the nanoscale microstructural evolution of UIT treated and untreated sensitized 5456 aluminum using TEM and high resolution TEM (HRTEM). This study contributes to the understanding of the mechanisms for the evolution of the microstructure of 5456 due to SPD. Transmission electron microscopy was used to examine secondary precipitates, dislocations, and grain, size and structure. X-ray measurements using a diffractomer as described in section 2.8 was used to examine the grain size at the UIT surface. As noted in section 3.1, SPD processes result in grain refinement and the formation of nanocrystalline grains in aluminum alloys. Transmission electron microscopy analysis included the examination of the grain structure for the formation of nanocrystalline grains. As noted in section 3.2.4, EBSD was not successful in identifying nanocrystalline grain formation probably because the top most surface layer of the treated material was removed during polishing for EBSD.

As previously noted in section 1.2.1, in Al-Mg alloys, the equilibrium phase with aluminum is the β phase. Precipitation occurs preferentially on the {100} planes and the {120} planes [7] and can be continuous or discontinuous. The continuous precipitation of β phase generates a Widmanstatten structure whereas the discontinuous precipitation is accompanied by the formation of a new solid solution [47].

Unlike Mg, Mn, a transition metal (see chemical composition in Table 1), is not expected to remain in solid solution but rather form complex precipitates. Two types of precipitates have been found to form in Al-Mg alloys, precipitates containing Cu and Mn rich precipitates. The Mn rich precipitate is likely Al_6Mn, an orthorhombic phase, which forms when Al rejects Mn from solid solution [7]. The Mn precipitates form coarse constituent particles and small dispersoids that act as nucleation sites for recrystallization and grain boundary migration [48].

4.1.1 Transmission Electron Microscopy Analysis

Transmission electron microscopy is a powerful tool for imaging at significantly higher resolution than other microscopy techniques due to the transmission of a beam of electrons through an ultra-thin specimen or foil. As the electrons travel through the specimen, they are either scattered or remain unaffected by the specimen. As a result, a non-uniform distribution of electrons emerges from the exit surface of the specimen. The non-uniform distribution of electrons is displayed by the electron microscope in two ways; angular distribution of scattering which can be viewed in the form of diffraction patterns or spatial distribution of scattering which can be observed as contrast in images of the specimen.

Indexing diffraction patterns for TEM analysis involves the comparison of the experimental *d*-spacing and theoretical *d*-spacing from Bragg's Law as shown in Equation 3 [49,50].

$$2dsin\theta = n\lambda \quad \textbf{(3)}$$

Where *n* is the order of the reflection and λ is the wavelength of the electrons [50]. If the reflecting planes have Miller indices *hkl*, then Equation 3 can be written as:

$$2d_{hkl}sin\theta = \lambda \quad \textbf{(4)}$$

$$d_{theoretical} = \frac{a}{\sqrt{h^2 + k^2 + l^2}} \quad \textbf{(5)}$$

where the theoretical d-spacing can be obtained from Equation 5 where *a* is the lattice constant and *h, k, l* are the reflection indices. For aluminum, the lattice constant, *a* is 4.0414 Å [9].

The experimental *d*-spacing can be measured directly from the diffraction patterns obtained from the TEM. The structure factor F is the unit cell equivalent of the atomic scattering amplitude, f_i, and can be thought of as the unit-cell scattering amplitude [49]. The structure factor F is given by:

$$F_{hkl} = \sum_i f_i \, e^{2\pi i(hx_i + ky_i + lz_i)} \quad \textbf{(6)}$$

in terms of the atom positions in the until cell (x_i, y_i, z_i). The structure factor rules are used to determine the allowed reflections in the diffraction pattern. For an FCC structure, there are four atoms in a unit cell. The coordinates of the atoms are (x, y, z)

= (0, 0, 0), (½, ½, 0) (½, 0, ½), (0, ½, ½). Substituting these values into Equation 6 gives the following [49]:

$$F = f\left(1 + e^{\pi i(h+k)} + e^{\pi i(h+l)} + e^{\pi i(k+l)}\right) \quad (7)$$

If all three integers *h, k, l* are either odd or even, all the exponential terms are $e^{2n\pi i}$ and all the phases of the diffracted waves are multiples of 2π and are in phase. If one of *h, k,* or *l* is odd but the other two are even or vice versa then two of the three phases factors will be odd multiples of π giving two terms of -1 in Equation 7. From Equations 7 the structure factor is given by the following rules below [49].

F = 0 if h,k,l are mixed even and odd
F = *4f* if *h, k, l* are all even or all odd

Two beam conditions, bright field and dark field imaging modes were used to obtain images for dislocation characterization. In order to characterize the dislocations, the visibility condition using $\vec{g} \bullet \vec{b}$ where $\vec{b}$, the Burgers vector must be evaluated. $\bar{g}$ is the vector in reciprocal space used to get the dark field image. In a dark field image, when $\vec{g} \bullet \vec{b} \neq 0$ dislocations are visible and when $\vec{g} \bullet \vec{b} = 0$ then dislocations are invisible. By solving the visibility condition, the possible Burgers vector for each dislocation can be determined. For a FCC crystal structure, dislocations will have a Burger's vector in the ½ <110> family. In order to identify the type of dislocation, the dislocation line direction, $\vec{t}$, must also be determined for

each dislocation. Valid dislocation lines for an aluminum structure are along the <110> and <211> directions. The type of dislocations can be determined by calculating the angle θ between the Burger's vector and the dislocation line direction as shown by Equation 8 [49].

$$\theta = \cos^{-1}\left(\frac{\vec{t} \bullet \vec{b}}{\left|\vec{t}\right|\left|\vec{b}\right|}\right) \quad \textbf{(8)}$$

Depending on the calculated value of θ, the dislocation type will either be an edge type for θ = 90°, screw type for θ = 0°, or mixed dislocation for θ = 60° or 30°.

The dislocation density, ρ, can be estimated by overlaying a transparent grid over the dark field image and counting the number, N, of intersections of dislocations by the grid lines. Equation 9 is used to evaluate ρ where L is the total length of the grid lines, M is the magnification, f is a correction factor which accounts for the fraction of invisible dislocations, and t is the thickness. The total length of the grid lines is $L = 2n_1n_2q$ where n_1 and n_2 are the number of lines in the grid and q is the unit length between n_1 and n_2 grid lines [51].

$$\rho = \frac{2NMf}{Lt} \quad \textbf{(9)}$$

4.2 *Results*

4.2.1 Transmission Electron Microscopy of UIT Sensitized 5456

4.2.1.1 Transmission Electron Microscopy Micrographs of UIT Sensitized 5456

Transmission electron microscopy samples of UIT sensitized 5456 were obtained from the treated surface to examine the surface microstructure. As noted in section 2.7.1, the samples were thinned only from the back side to preserve the UIT surface. Figure 44 and 45 show TEM micrographs and the associated selected area diffraction patterns obtained from planar samples prepared from the treated surface. The TEM micrographs show the presence of a nanocrystalline microstructure as verified by the diffraction pattern indicating random orientations in the selected field of view. The ring-like patterns indicate that the nanocrystals have random orientation with respect to each other. Moiré fringes corresponding to overlapping nanocrystalline grains are also visible in the images. The grain sizes were measured from the TEM micrographs and range in size from 50 to 200 nm with a larger grain that measures 200 nm (W) by 400 (L). Based on the OM and EBSD results of samples obtained just below the treated surface which did not show the presence of nanocrystals, the TEM results suggest that the nanocrystals are only present at the deformation layer. Optical microscopy of UIT treated material in the transverse orientation showed that the deformation layer varies in thickness between 10 to 18 µm. Figure 46 shows a closer examination of individual nanocrystalline grains from the micrographs in Figure 45. The nanocrystalline grains show grain boundaries that are curved or wavy along their lengths.

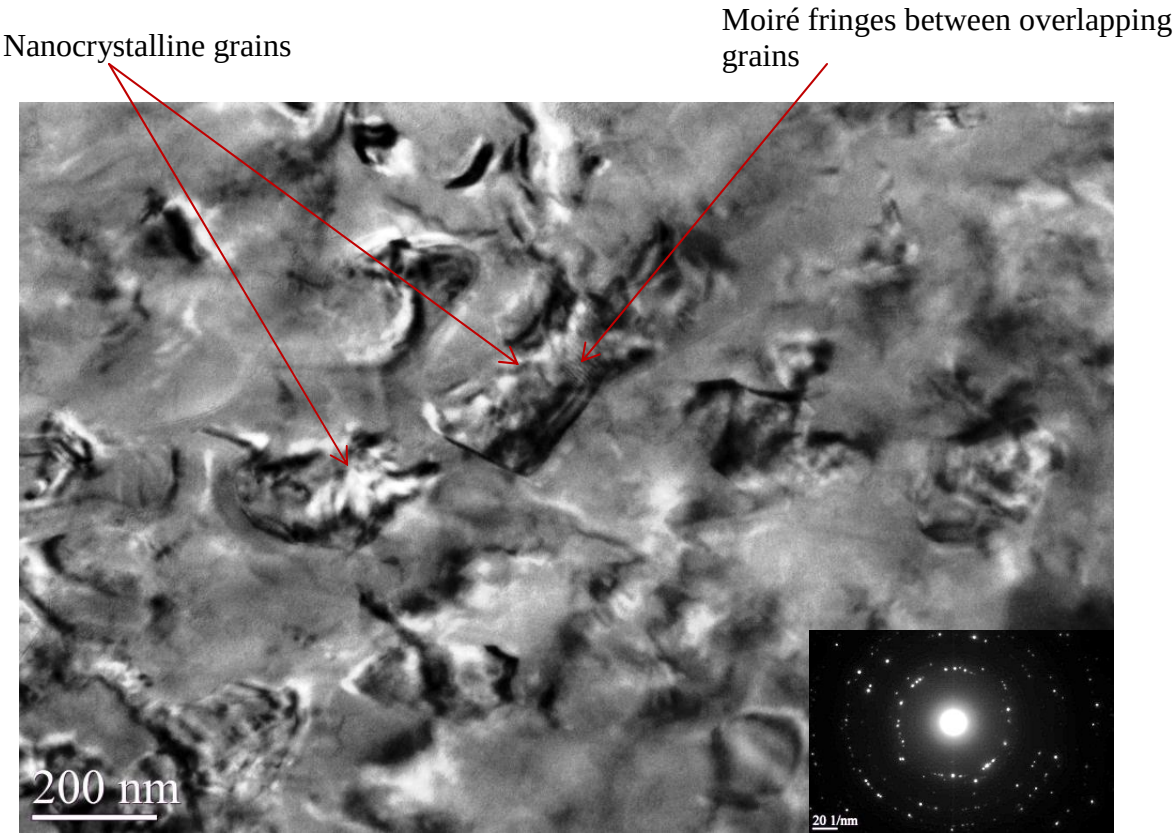

Figure 44. TEM micrograph and diffraction pattern of UIT sensitized 5456 showing a nanocrystalline microstructure at the treated surface

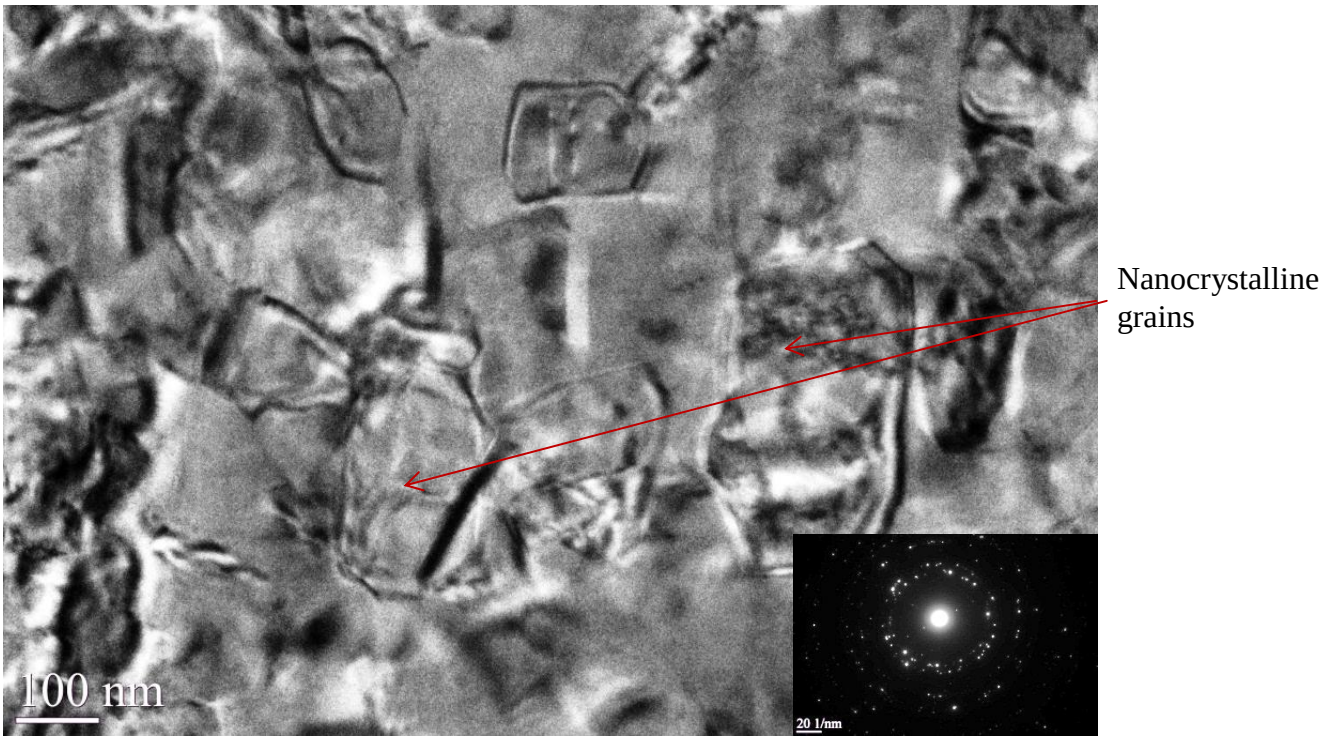

Figure 45. TEM micrograph and diffraction pattern of UIT sensitized 5456 showing a nanocrystalline microstructure at the treated surface

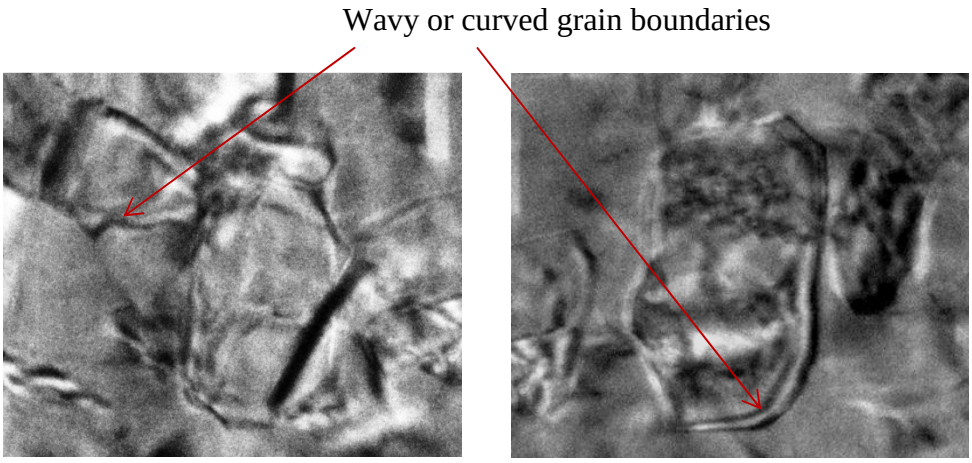

Figure 46. Closer examination of individual nanocrystalline grains showing the presence of wavy or curved grain boundaries

High resolution TEM was used to investigate the nanocrystalline layer of the UIT samples obtained from the treated surface. Figure 47 shows the interface between multiple nanocrystalline grains and larger submicron grains. The TEM micrograph illustrates notable grain size differences between the multiple nanograins (area A) and larger grains (areas B & C) which illustrate the inhomogeneity in grain reduction due to the UIT process. As previously mentioned in section 3.3, the UIT process is a manual process that results in random deformation on the surface. A higher magnification micrograph of the interface between area A and area B is shown in Figure 48 along with the associated diffraction pattern. The diffraction pattern shows both the presence of a ring pattern which is characteristic of nanocrystalline grains and a diffraction pattern with a [112] zone axis. The interatomic planes of the single larger submicron grain correspond to $(11\bar{1})$ planes. Figure 49 shows a

HRTEM micrograph of the nanocrystalline grains and diffraction pattern from area A in Figure 47. The grains range in size from ~2 to 6 nm in diameter as measured from the micrograph. The micrograph also confirms the presence of wavy or curved grain boundaries between the nanocrystalline grains. The diffraction pattern is a characteristic ring pattern for nanocrystalline grains; however, it also includes some diffracted spots characteristic of polycrystalline material with larger grains. The additional spots may be due to the fact that the selected field of view encompasses an area that includes nanocrystalline and submicron grain structure. Figure 50 shows a micrograph of the nanocrystalline grains with a number of overlapping nanocrystalline grains at various orientations.

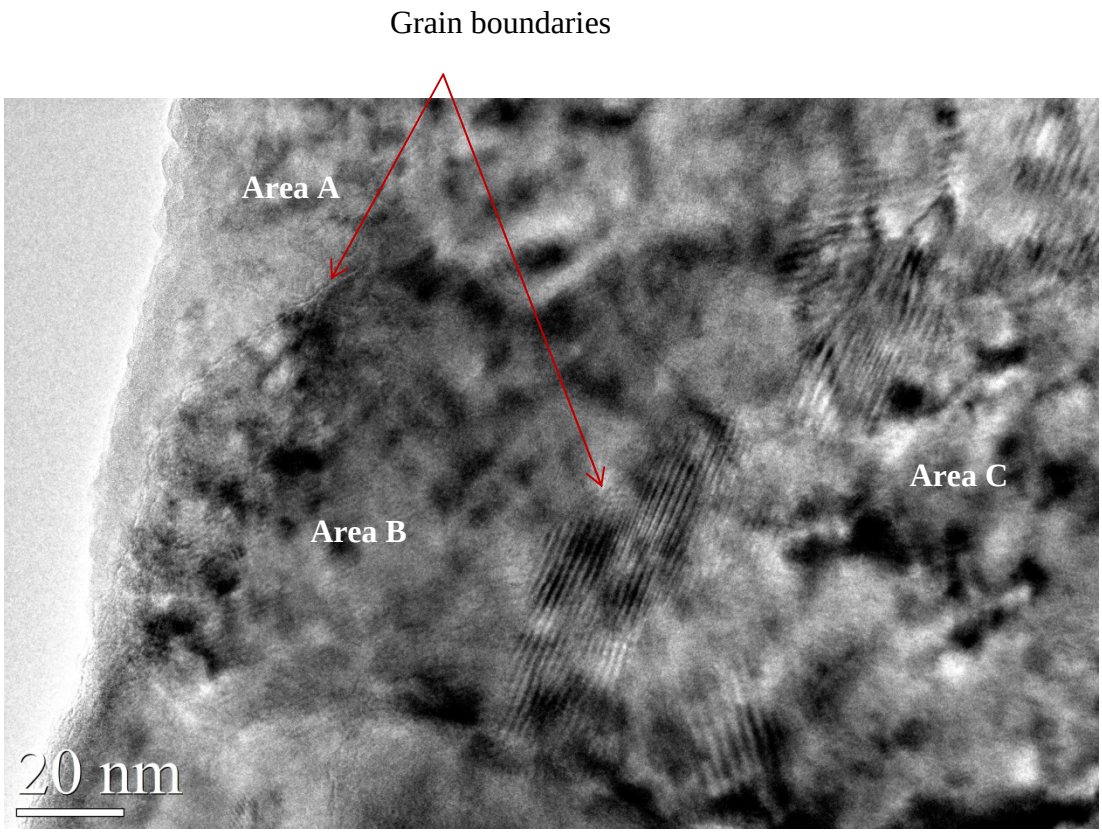

Figure 47. HRTEM micrograph showing the interface between nanograins and submicron grains at the UIT treated surface

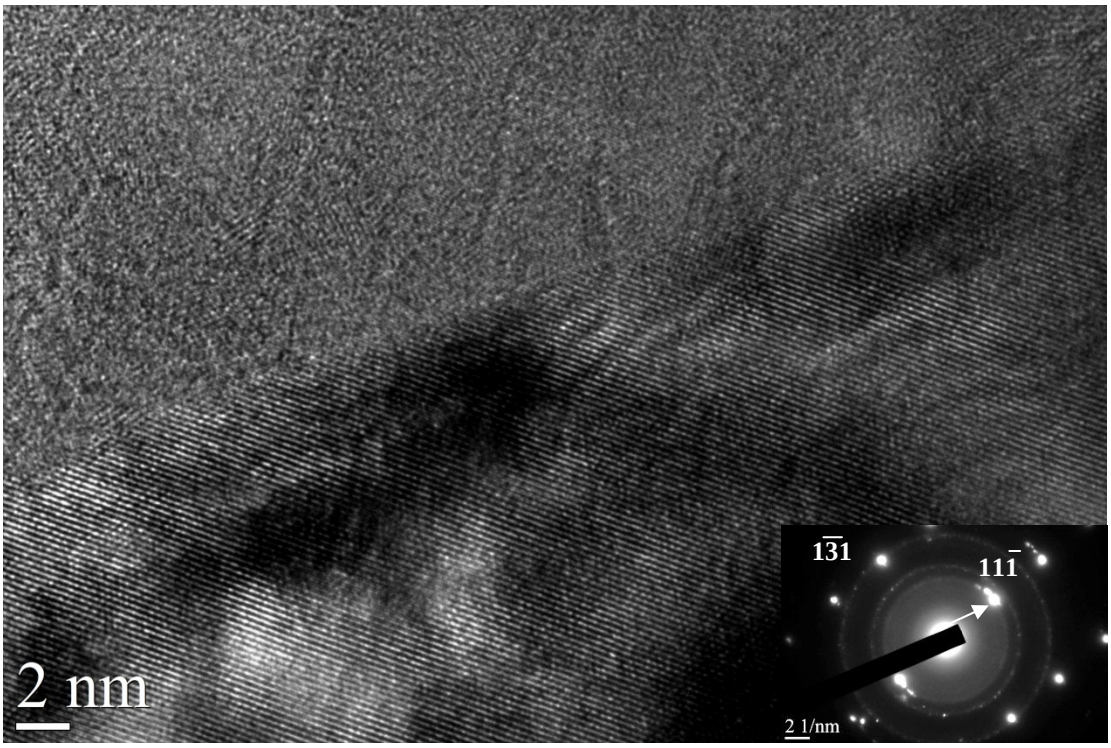

Figure 48. HRTEM micrograph showing the interface between nanograins and submicron grain oriented along the [112] direction

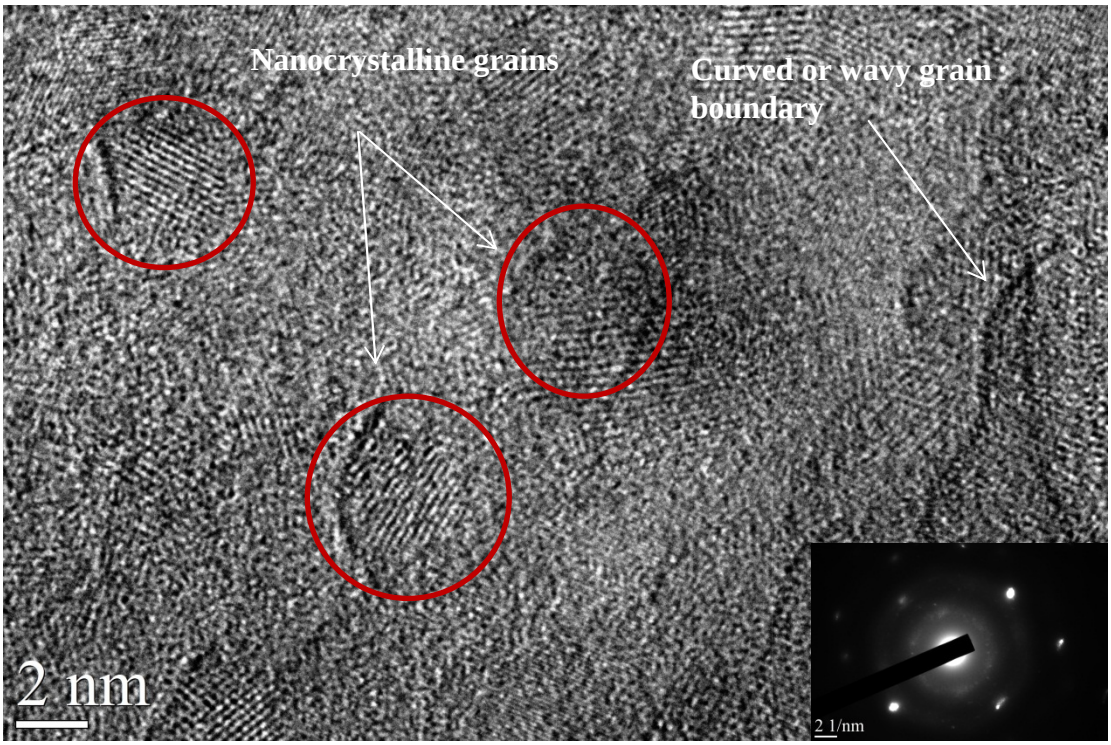

Figure 49. HRTEM micrograph showing nanocrystalline grains ranging in size from ~2 to 6 nm at the UIT treated surface

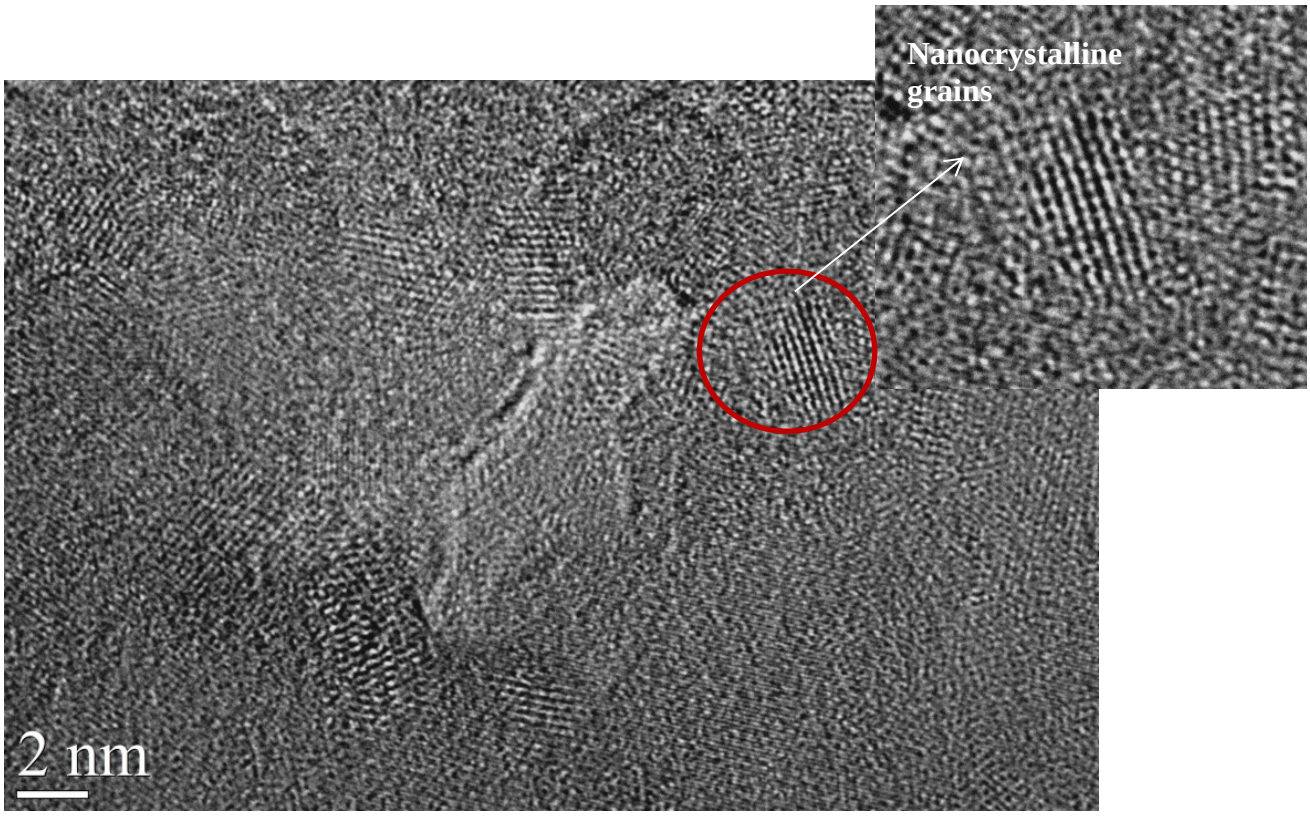

Figure 50. HRTEM micrograph showing nanocrystalline grains with overlapping grains at random orientations at the UIT treated surface

Figures 51 and 52 show representative TEM micrographs of UIT samples obtained in the planar orientation just below the UIT treated surface. The samples were prepared by mechanically polishing followed by electropolishing in an electrolyte of perchloric acid in methanol and ion milling as described in section 2.7.1. The samples were prepared such that only a thin layer on the order of ~ 20 µm was removed from the UIT treated surface. The micrographs reveal a heavily deformed microstructure with the presence of multiple grains and overlapping submicron grains on the order of 0.3 to 0.5 µm (300 to 500 nm) in diameter as measured from the micrographs. The microstructure also shows the presence of Moiré fringes along the grain boundaries. The presence of multiple grains of

nanoscale size is characteristic of SPD materials. The micrographs demonstrate that the UIT process results in grain modification below the deformation layer. Neither Figures 51 nor 52 reveals the presence of a continuous β phase along the grain boundaries. Dislocation analysis from this region is discussed in section 4.2.1.2 below.

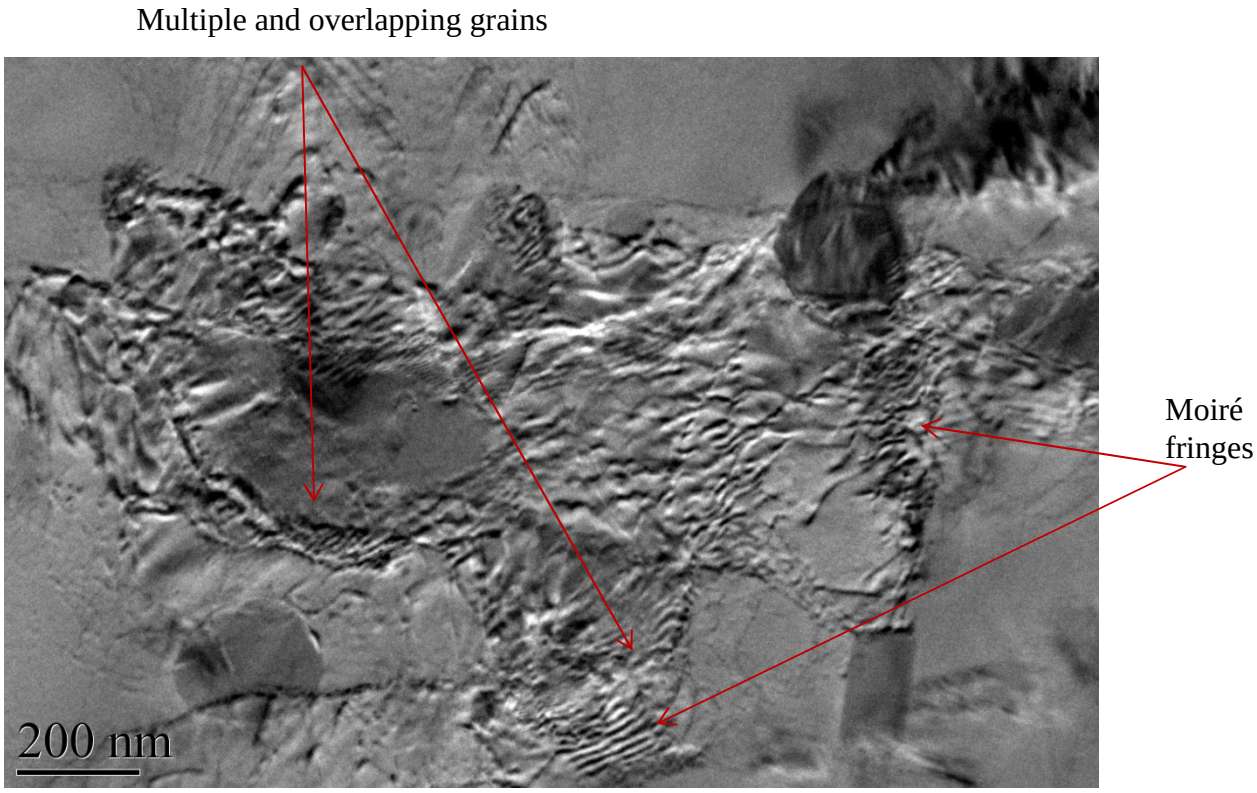

Figure 51. TEM micrograph of UIT sensitized 5456 showing a heavily deformed microstructure with multiple overlapping submicron grains

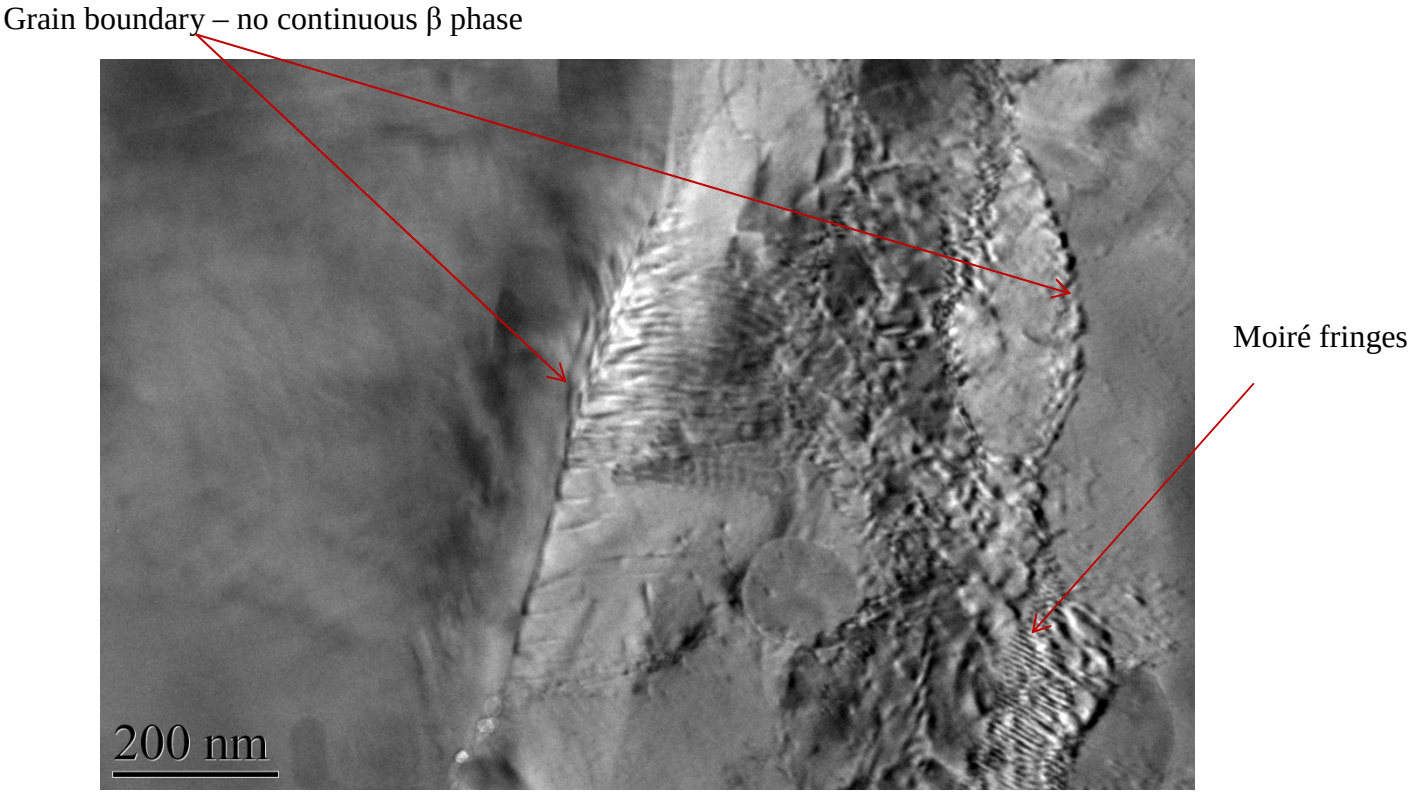

Figure 52. TEM micrograph of UIT sensitized 5456 at the grain boundary showing Moiré fringes at the grain boundary; but no presence of a continuous β phase

Transmission electron microscopy samples of UIT sensitized 5456 were obtained in the planar and transverse orientations to the UIT surface approximately 100 µm (planar orientation) and 250 to 300 µm (transverse orientation) below the UIT surface. Figures 53 and 54 show representative micrographs of the structure with secondary precipitate formation. The micrograph in the planar orientation in Figure 53 reveals a large number of rod-like shaped and irregular shaped precipitates within the matrix. Micrographs of samples obtained in the transverse orientation to the UIT surface also revealed the presence of a large number of rod-like precipitates and irregular shaped rich precipitates within the matrix as shown in Figure 54. The

rod-like shaped precipitates were identified to be Al-Mn-Cr-Cu rich precipitates through energy dispersive x-ray spectroscopy (EDS) analysis as shown in the EDS spectrum in Figure 55. The slight trace of Ag in the rod-like shaped precipitates is likely due to contamination during the specimen preparation since Ag is not an alloy element found in 5456 aluminum. The irregular shaped precipitates were found to be Mn rich. These precipitates are likely Al_6Mn particles. From the micrographs, the rod-like shaped precipitates were found to range in size from 100 to 500 nm in length. Both Figures 53 and 54 show extensive interaction between the dislocations and the secondary phase precipitates.

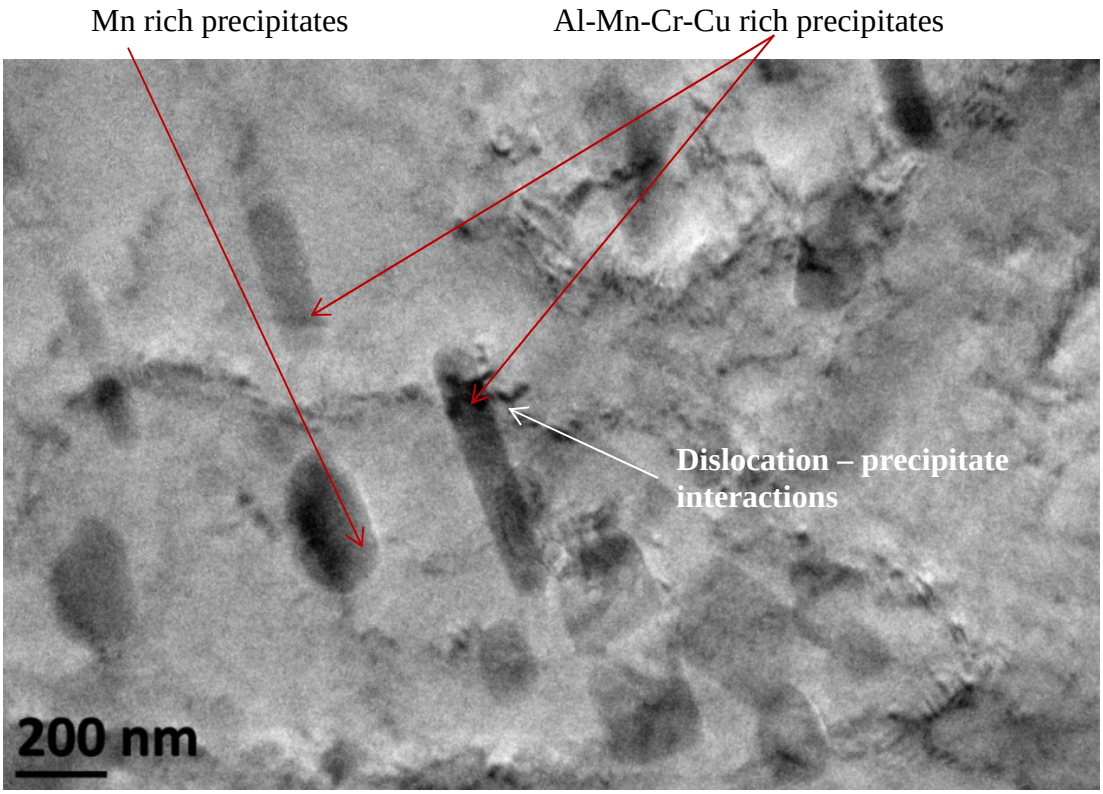

Figure 53. TEM micrograph of UIT sensitized 5456 in the planar orientation ~ 100 µm below the UIT surface showing a large number of Al-Mn-Cr-Cu and Mn-rich precipitates

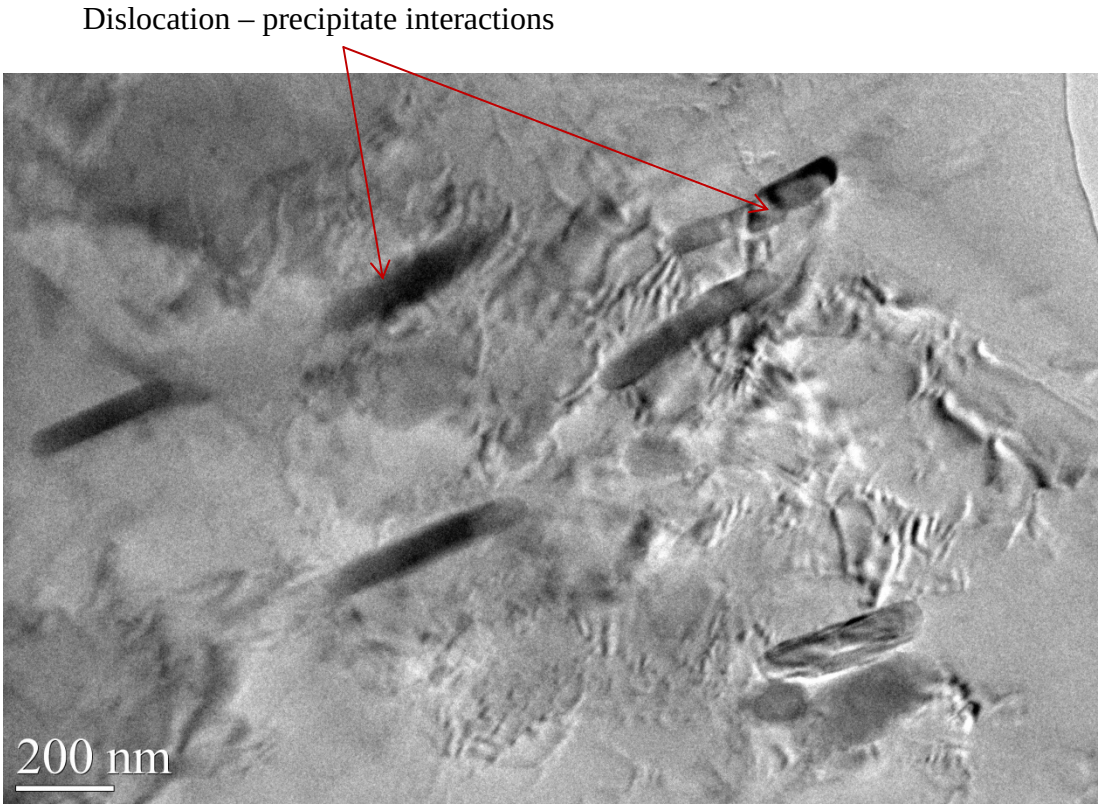

Figure 54. TEM micrograph of UIT sensitized 5456 in the transverse orientation showing a large number of Al-Mn-Cr-Cu and Mn-rich precipitates

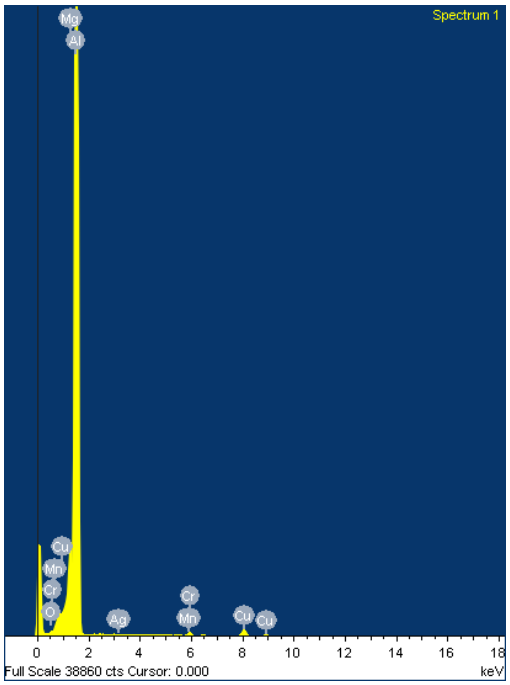

Figure 55. EDS spectrum for rod-like Al-Mn-Cr-Cu precipitates in UIT sensitized 5456

4.2.1.2 Dislocation Analysis of UIT Sensitized 5456

The TEM micrographs reveal a heavily deformed microstructure with a large number of dislocations in the UIT sensitized samples. For samples obtained below the UIT treated surface, the microstructure does not reveal the presence of Moiré fringes or multiple and overlapping grains. Using several two beam conditions, bright field images, dark field images, and the associated diffraction pattern were obtained from planar and transverse samples for dislocation analysis. Figure 56 shows the planar area that was selected for two beam analysis. Figure 57 shows the indexed diffraction pattern for the selected area. Using the analysis technique described in section 4.1.1, the zone axis was determined to be along the $[1\bar{1}\bar{2}]$ direction. The bright field and dark field images of the area are shown in Figure 58 and Figures 59 to 61, respectively. Dark field images were obtained for $\vec{g}$ = $(1\bar{1}1)$, $(13\bar{1})$, and (220). Each dark field image shows the diffraction pattern with the corresponding $\vec{g}$ in the lower right hand corner. The dislocations chosen for characterization are labeled as A, B, and C in the dark field images. Using the analysis described in section 4.1.1, the visibility condition using $\vec{g} \bullet \vec{b}$ were evaluated for the dislocations. Dislocations A and B were oriented along the $[\bar{2}\bar{2}0]$ direction, valid dislocation lines are $\overrightarrow{t_A}$ = $[\bar{1}\bar{1}0]$ and $\overrightarrow{t_B}$ = $[\bar{1}\bar{1}0]$. Dislocation C lies along the $[\bar{1}1\bar{1}]$, therefore a valid dislocation line direction of the family of <110> or <112> projects along the $[\bar{1}1\bar{1}]$ direction when viewed along the $[1\bar{1}\bar{2}]$ direction. Possible dislocation line directions for dislocation C are $\overrightarrow{t_C}$ = $[1\bar{1}0]$ or $[\bar{1}1\bar{2}]$. Table 5 shows the visibility conditions for the dislocations. For aluminum, perfect dislocations have Burgers vector in the ½ $\langle 110 \rangle$ family. Using the possible Burgers vectors for

dislocations A, B, and C and the dislocation line directions to calculate θ in Equation 8, the dislocation types are identified in Table 6. From Table 6, dislocations A and B are either a screw or mixed dislocation depending on the possible Burgers vector. Dislocation C is a mixed dislocation with different possible Burgers vectors.

Equation 9 was used to determine the dislocation density. Using a 5 x 5 cm grid with 5 grid spacings at q = 1.0 cm/spacing overlaid on the dark field image for $\vec{g}$ = $(1\bar{1}1)$, there were N = 78 dislocation intersections of the grid lines. The total length of the grid lines, L is 50 cm and the correction factor, f for $\vec{g}$ = $(1\bar{1}1)$ is 6/3. The correction factor is the reciprocal of the fraction that is visible under the two-beam condition used which was obtained by calculating $\vec{g} \bullet \vec{b} = 0$ for all possible Burger's vectors for an FCC structure with $\vec{g} = (1\bar{1}1)$. The sample thickness is assumed to be t = 0.5 μm. The sample thickness is an assumption since the thickness fringes in the bright field and dark field images are not clear thus cannot be accurately calculated. The magnification, M for the dark field image is 150 K. Solving Equation 9, the dislocation density for the UIT sensitized 5456 is 1.9×10^{10} dislocation/cm^2. It is noted that the dislocation density for a UIT sample obtained at the surface would be expected to be much higher.

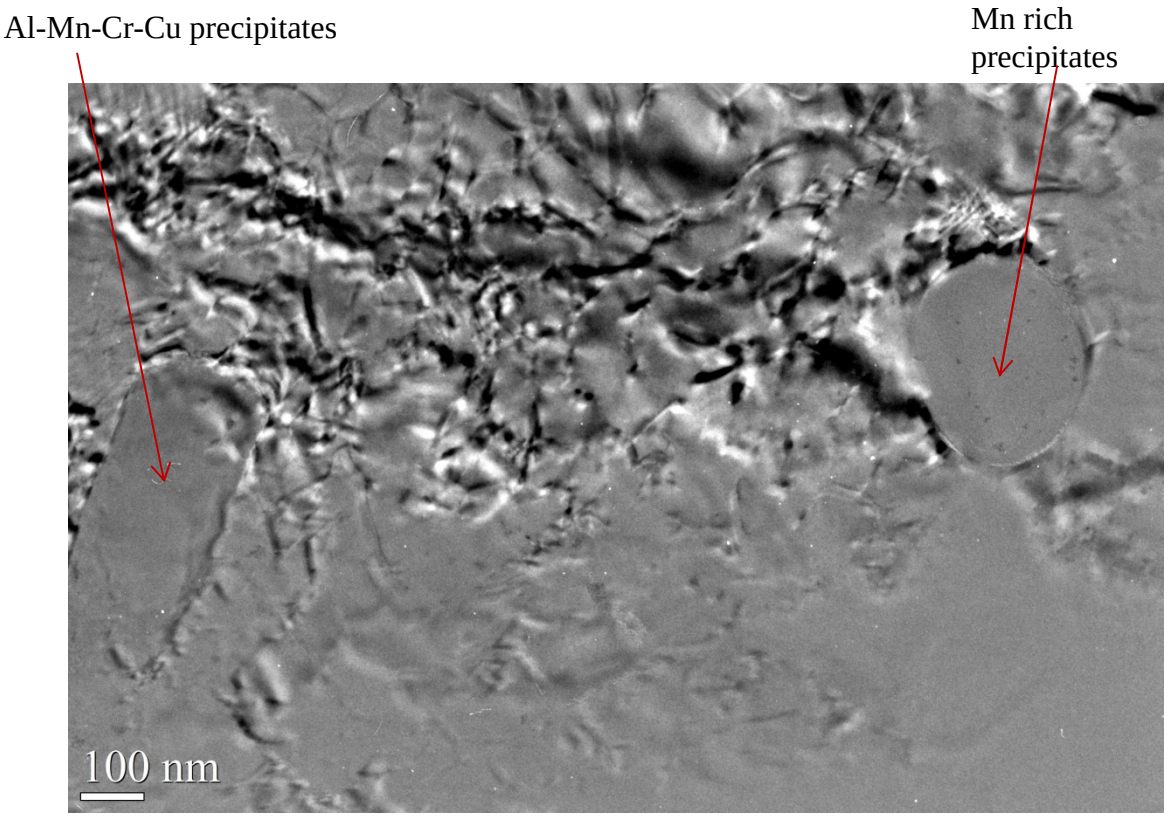

Figure 56. TEM micrograph of UIT sensitized 5456 area analyzed under two beam conditions in the planar orientation

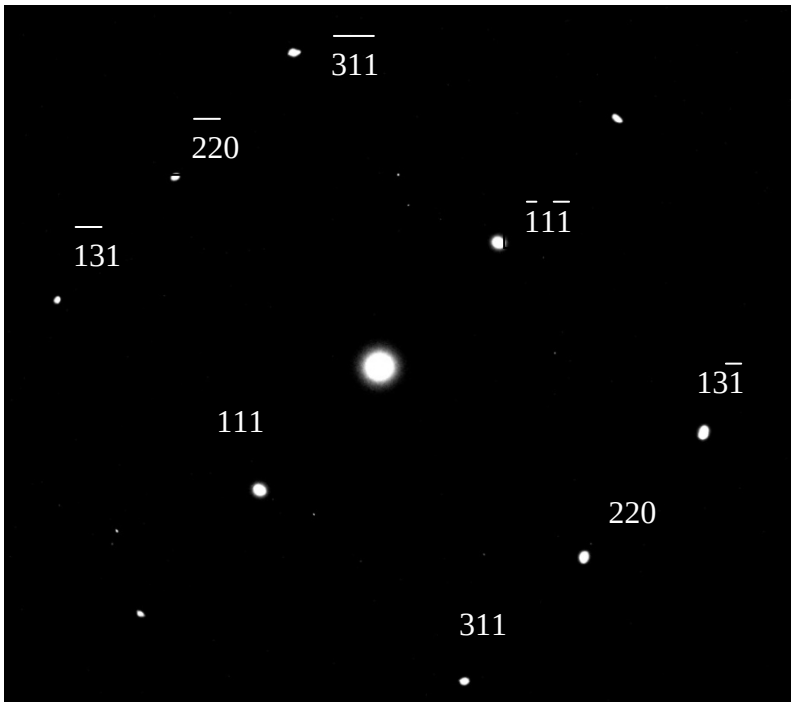

Figure 57. Indexed diffraction pattern for UIT sensitized 5456 area in the planar orientation analyzed under two beam condition with zone axis at $[1\bar{1}\bar{2}]$

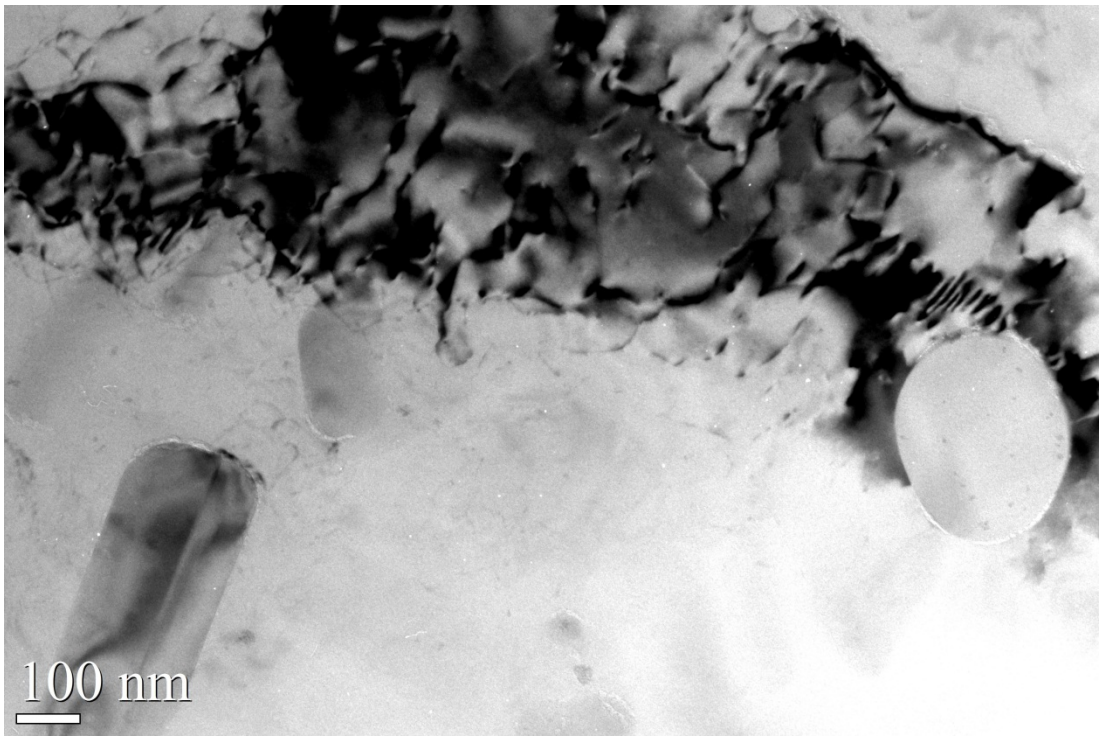

Figure 58. Bright field TEM micrograph of UIT sensitized 5456 area in the planar orientation analyzed under a two beam condition

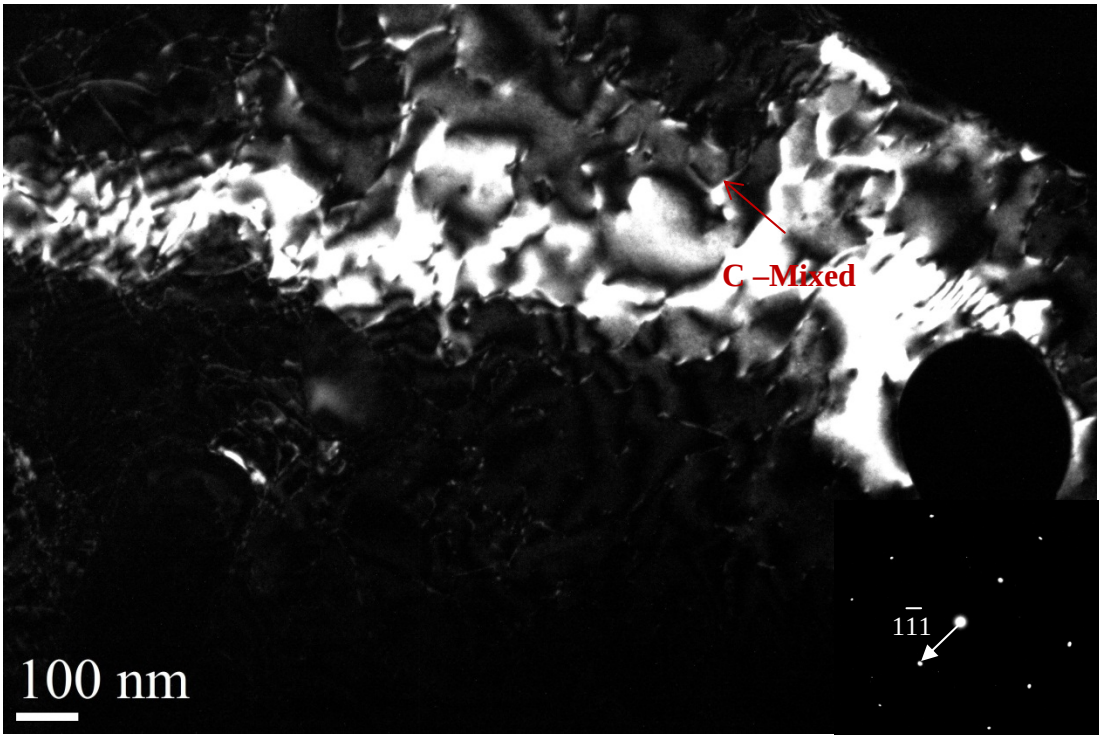

Figure 59. Dark field image of UIT sensitized area in the planar orientation analyzed under $\vec{g}$ = $(1\bar{1}1)$ two beam condition

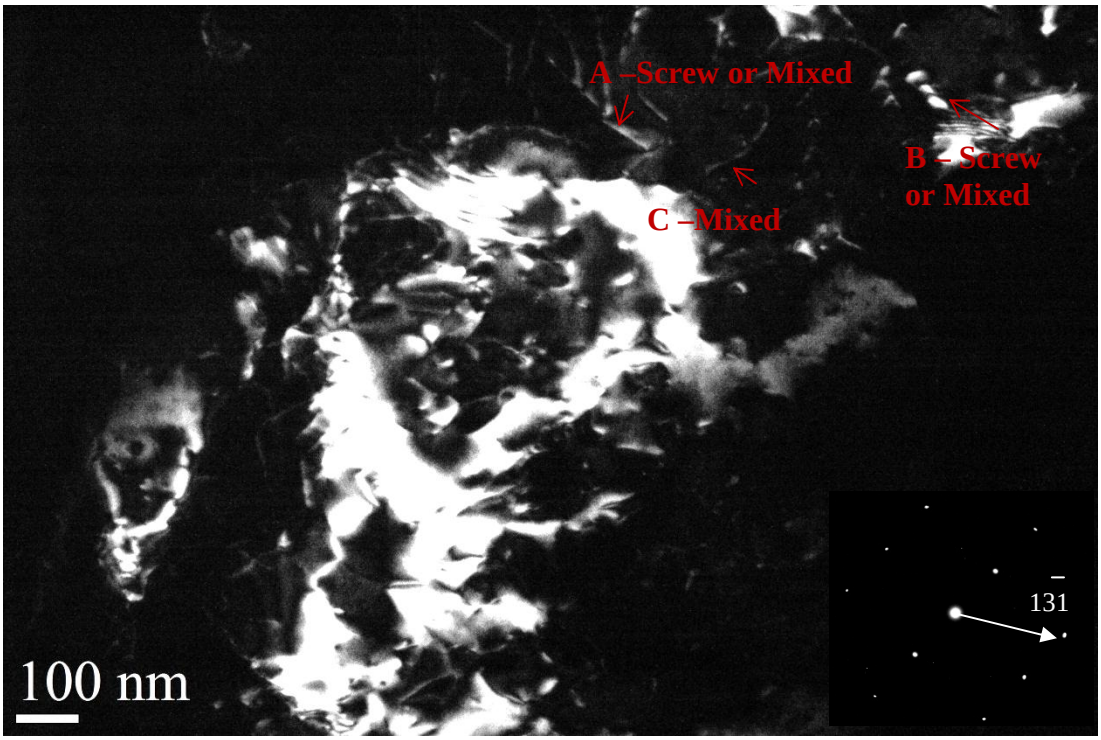

Figure 60. Dark field image of UIT sensitized area in the planar orientation analyzed under $\vec{g}$ = $(13\bar{1})$ two beam condition

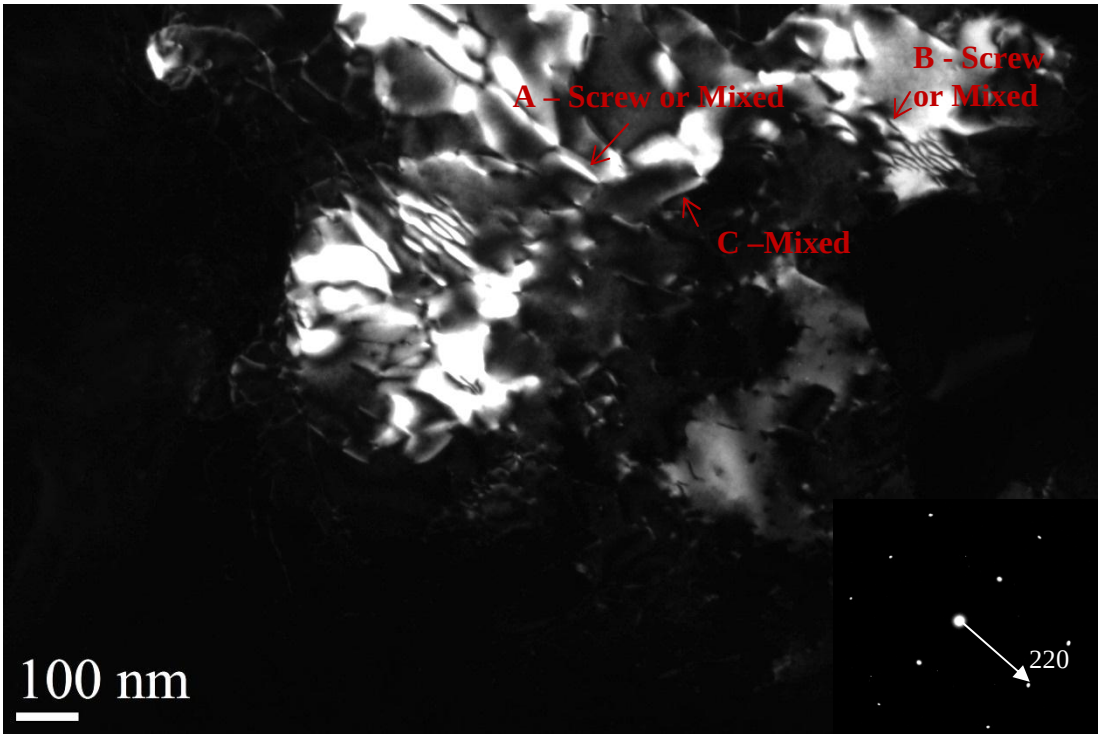

Figure 61. Dark field image of UIT sensitized area in the planar orientation analyzed under $\vec{g}$ = (220) two beam condition

Table 5. Visibility condition for UIT sensitized 5456 dislocations in the planar orientation analyzed under two beam condition

Dislocation	$\vec{g} = (220)$	$\vec{g} = (13\bar{1})$	$\vec{g} = (1\bar{1}1)$
A	Visible	Visible	Invisible
B	Visible	Visible	Invisible
C	Visible	Visible	Visible

Table 6. Dislocation types for dislocation A, B, and C for UIT sensitized 5456 in the planar orientation

Dislocation	Dislocation line direction ($\vec{t}$)	Burger's vector ($\vec{b}$)	Dislocation type
A	$[\bar{1}\bar{1}0]$	$\frac{a}{2}[110]$, $\frac{a}{2}[\bar{1}\bar{1}0]$	0° Screw
		$\frac{a}{2}[011]$, $\frac{a}{2}[\bar{1}01]$, $\frac{a}{2}[10\bar{1}]$	60° Mixed
B	$[\bar{1}\bar{1}0]$	$\frac{a}{2}[110]$, $\frac{a}{2}[\bar{1}\bar{1}0]$	0° Screw
		$\frac{a}{2}[011]$, $\frac{a}{2}[\bar{1}01]$, $\frac{a}{2}[10\bar{1}]$	60° Mixed
C	$[1\bar{1}0]$ or	$\frac{a}{2}[0\bar{1}1]$, $\frac{a}{2}[01\bar{1}]$	60° Mixed
	$[\bar{1}1\bar{2}]$		30° Mixed

Figure 62 shows the UIT sensitized 5456 area in the transverse orientation that was selected for analysis using two beam condition. The zone axis was determined to be along the $[1\bar{1}0]$ direction from the selected area diffraction pattern from the above area. Dark field images were obtained for $\vec{g}$ = $(\bar{2}\bar{2}0)$, (111) (Figure 63), and $(00\bar{2})$. Three dislocations were chosen for characterization and the visibility condition evaluated for each dislocation. Dislocation A lies along the $[\overline{22}0]$, a valid dislocation line direction would lie along $\overrightarrow{t_A}$ = $[\overline{11}0]$. Dislocation B lies along the $[\overline{11}3]$, a valid dislocation line would project along $[\overline{11}3]$ if $\overrightarrow{t_B}$ = $[1\bar{2}1]$. Dislocation C lies along the $[33\bar{1}]$ direction, a valid dislocation line would project along the $[\overline{33}1]$ if $\overrightarrow{t_C}$ = $[21\bar{1}]$ or $[\overline{12}1]$. Based on the possible Burgers vectors, dislocation A is a screw dislocation and dislocation C is a mixed dislocation as shown in Figure 63. No possible $\overrightarrow{b_s}$ were found to satisfy the visibility conditions for b = ½<110> family for the dislocations B that was selected for analysis. The dislocation density was determined to be 1.5×10^{10} dislocation/cm^2 based on Equation 9.

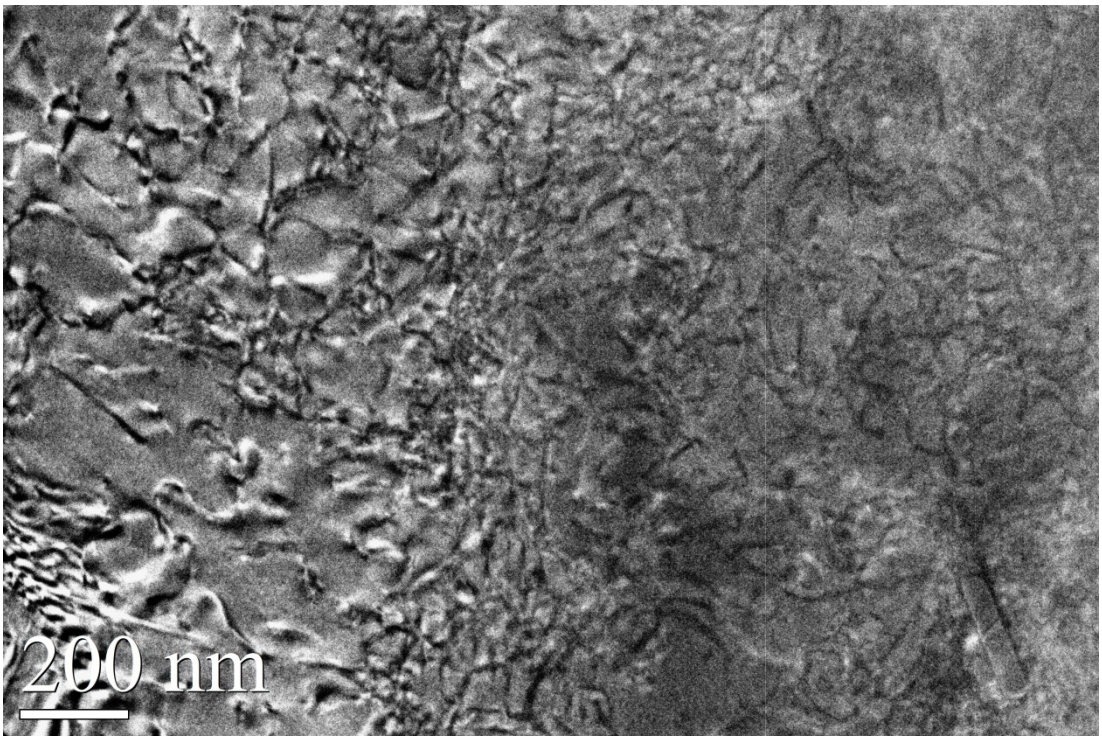

Figure 62. TEM micrograph of UIT sensitized 5456 in the transverse orientation analyzed under two beam conditions

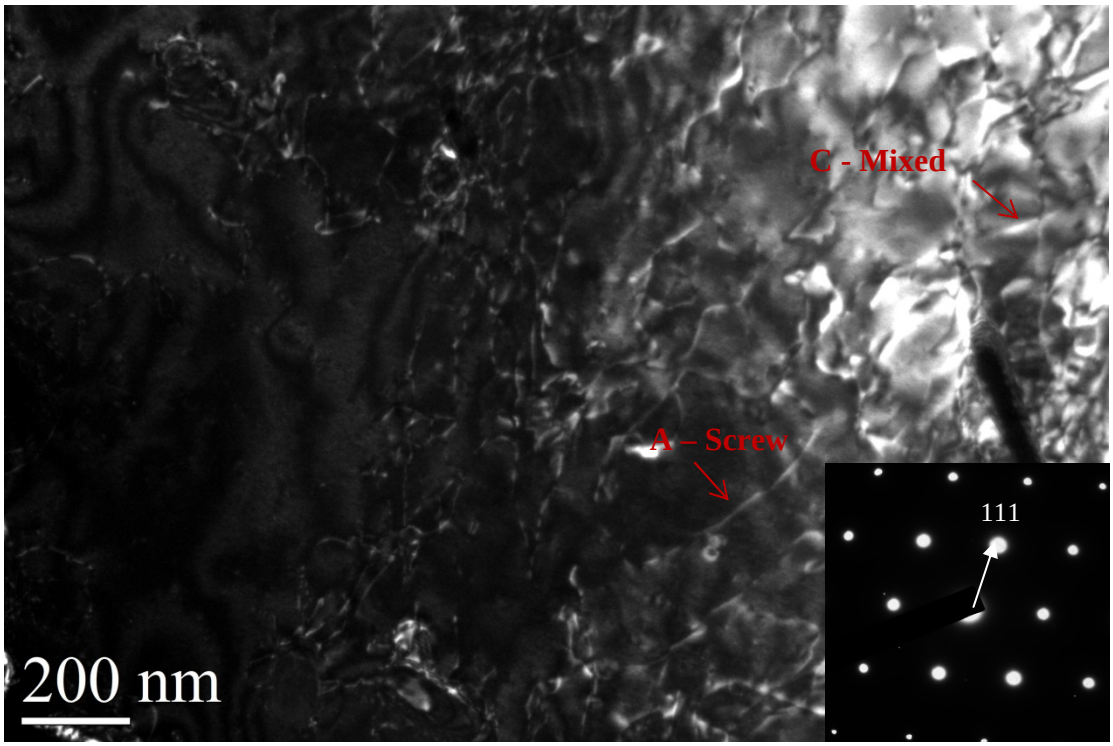

Figure 63. Dark field image of UIT sensitized area in the transverse orientation analyzed under two beam condition at $\vec{g} = (111)$ showing screw and mixed dislocations

4.2.2 Transmission Electron Microscopy of Untreated Sensitized 5456

4.2.2.1 Transmission Electron Microscopy Micrographs of Untreated Sensitized 5456

Transmission electron microscopy samples of untreated sensitized 5456 were obtained in the planar and transverse orientations below the UIT surface. Figures 64 and 65 show representative TEM micrographs of untreated samples obtained in the planar orientation just below the surface. These samples were prepared by mechanically polishing, electropolishing in perchloric acid in methanol, and ion milling as described in section 2.7.1. Unlike the UIT regions presented in section 4.2.1.1, these micrographs do not reveal a heavily deformed microstructure. Dislocations are present which will be discussed in section 4.2.2.2. Examination of the grain boundaries in the planar orientation reveals features that are characteristic of a continuous secondary β phase and Mg and Cu enrichment phase as confirmed by EDS.

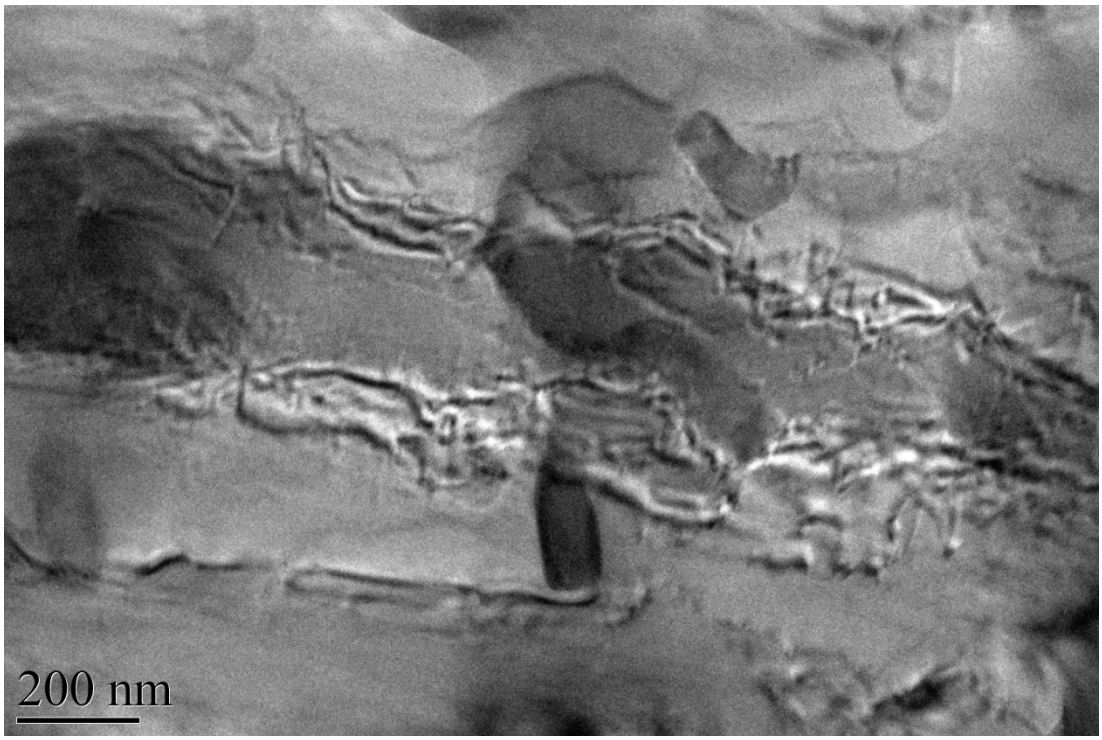

Figure 64. TEM micrograph of untreated sensitized 5456 showing multiple dislocations and the presence of precipitates

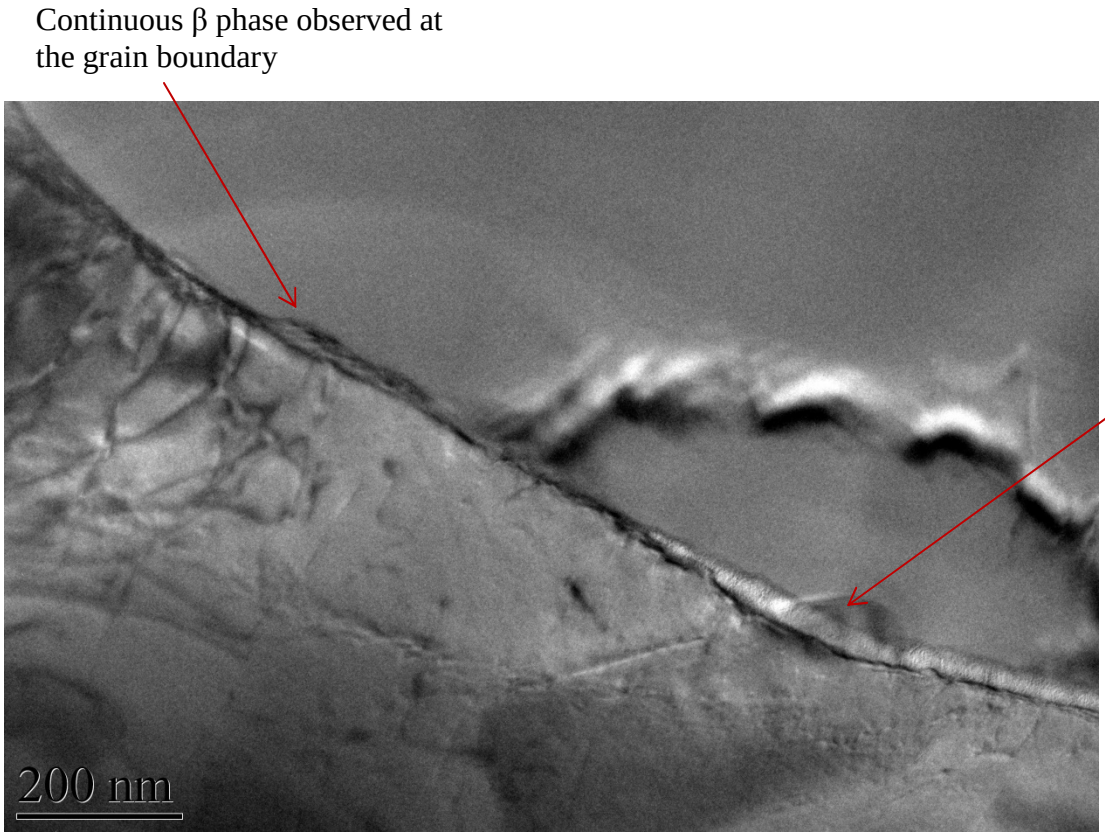

Figure 65. TEM micrograph of untreated sensitized 5456 at the grain boundary showing a continuous β phase and magnesium rich area

Figure 66Figures 66 and 67 show additional micrographs of untreated sensitized 5456 in the planar and transverse orientations, respectively. Similarly to the region below the UIT sensitized 5456, the micrograph in the planar orientation of an untreated sample in Figure 66 reveals a large number of rod-like shaped and irregular shaped precipitates within the matrix. The rod-like shaped precipitates were identified to be Al-Mn-Cr-Cu rich precipitates and the irregular shaped precipitates to be Mn rich through EDS. As previously noted, the rod-like shaped precipitates were found to range in size from 100 to 500 nm in length. Figure 67 obtained at a grain boundary in the transverse orientation reveals an enrichment of Mg and Cu as confirmed by the EDS spectrum in Figure 68.

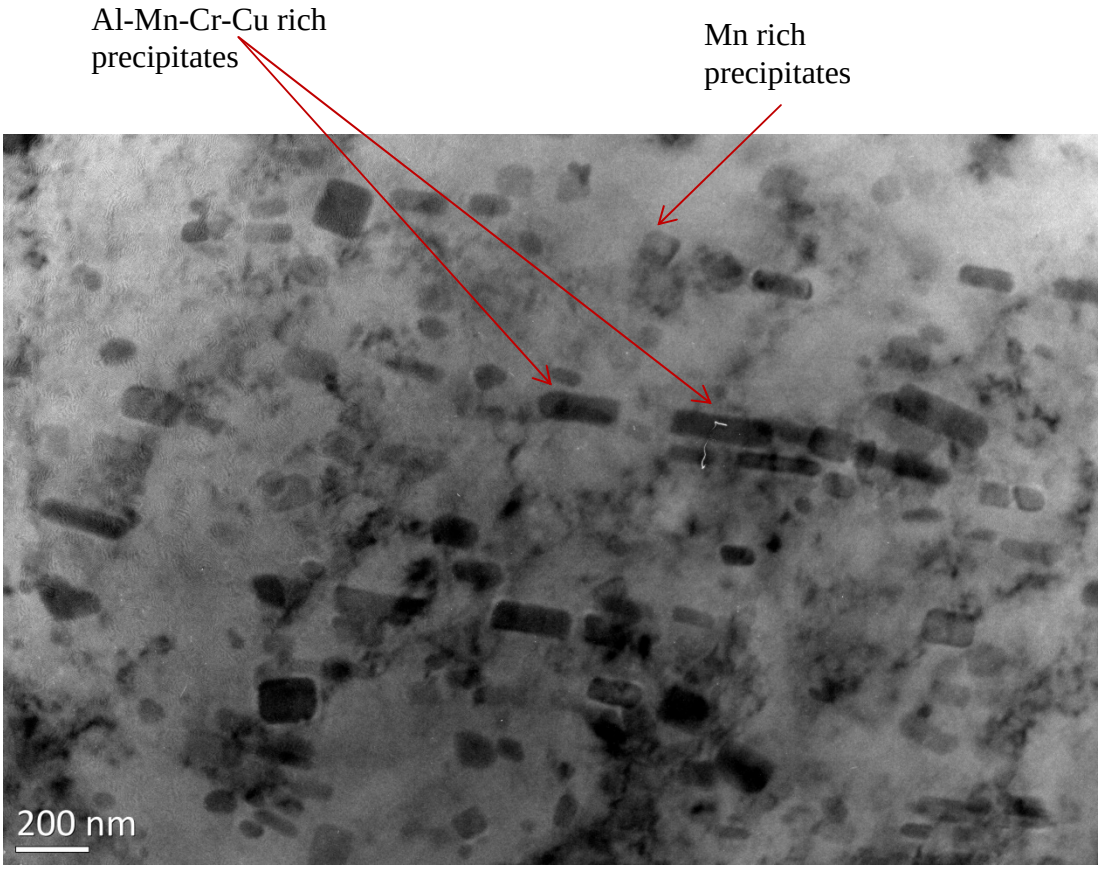

Figure 66. TEM micrograph of untreated sensitized 5456 in the planar orientation showing a large number of Al-Mn-Cr-Cu and Mn-rich precipitates

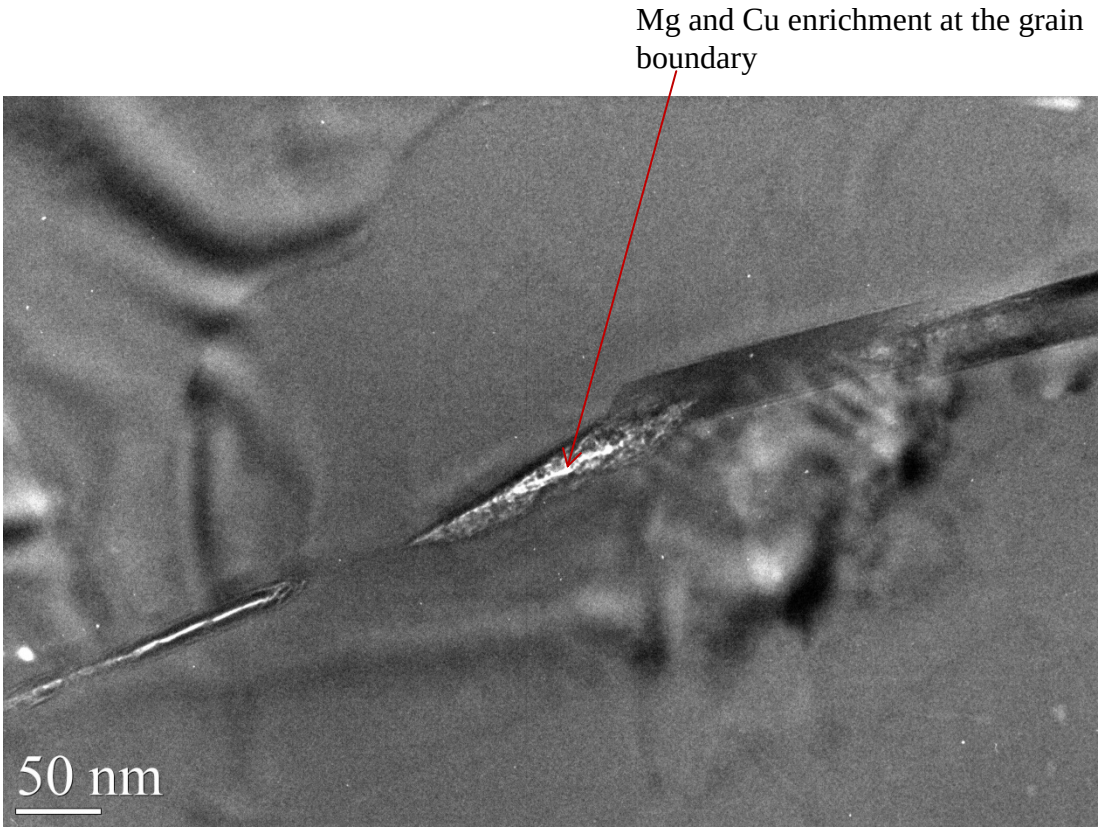

Figure 67. TEM micrograph of untreated sensitized 5456 in the transverse orientation at the grain boundary showing a magnesium rich phase at the boundary

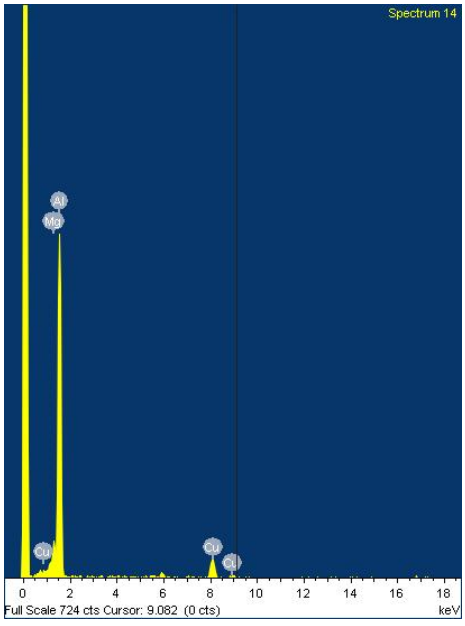

Figure 68. EDS spectrum for Mg - Cu rich phase at the grain boundary in Figure 67 in untreated sensitized 5456

4.2.2.2 Dislocation Analysis of Untreated Sensitized 5456

Using two beam condition, bright field images, dark field images, and the associated diffraction patterns were obtained from planar and transverse samples for dislocation analysis of the untreated sensitized 5456. Figure 69 is an image along the planar orientation and shows a heavily deformed microstructure that was selected for two beam analysis. The zone axis was determined to be along the $[0\overline{11}]$ direction. Dark field images were obtained for $\vec{g}$ = (200), $(\bar{1}1\bar{1})$, and $(02\bar{2})$ and three dislocations chosen for characterization. The visibility condition using $\vec{g} \bullet \vec{b}$ were evaluated for the dislocations and found to be oriented along the line directions of $\overrightarrow{t_A}$ = $[1\overline{21}]$, $\overrightarrow{t_B}$ = $[\overline{112}]$, and $\overrightarrow{t_C}$ = $[01\bar{1}]$. Based on the visibility conditions for the dislocations and the possible Burgers vector for each dislocation, dislocations A and B are mixed dislocations. Figures 70 and 71 show the dark field images showing dislocations A and B, respectively. Dislocation C was determined to be an edge dislocation. The dislocation density for the untreated sensitized 5456 is 7.2×10^9 dislocation/cm^2.

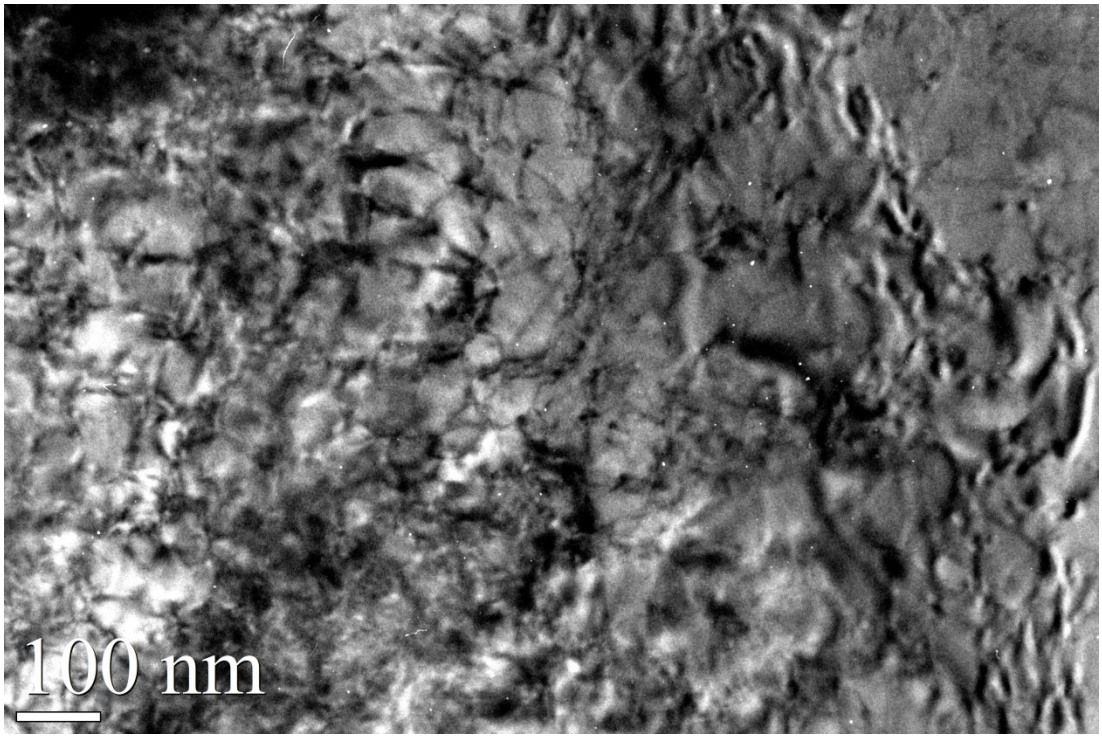

Figure 69. TEM micrograph of untreated sensitized 5456 area in the planar orientation analyzed under a two beam condition

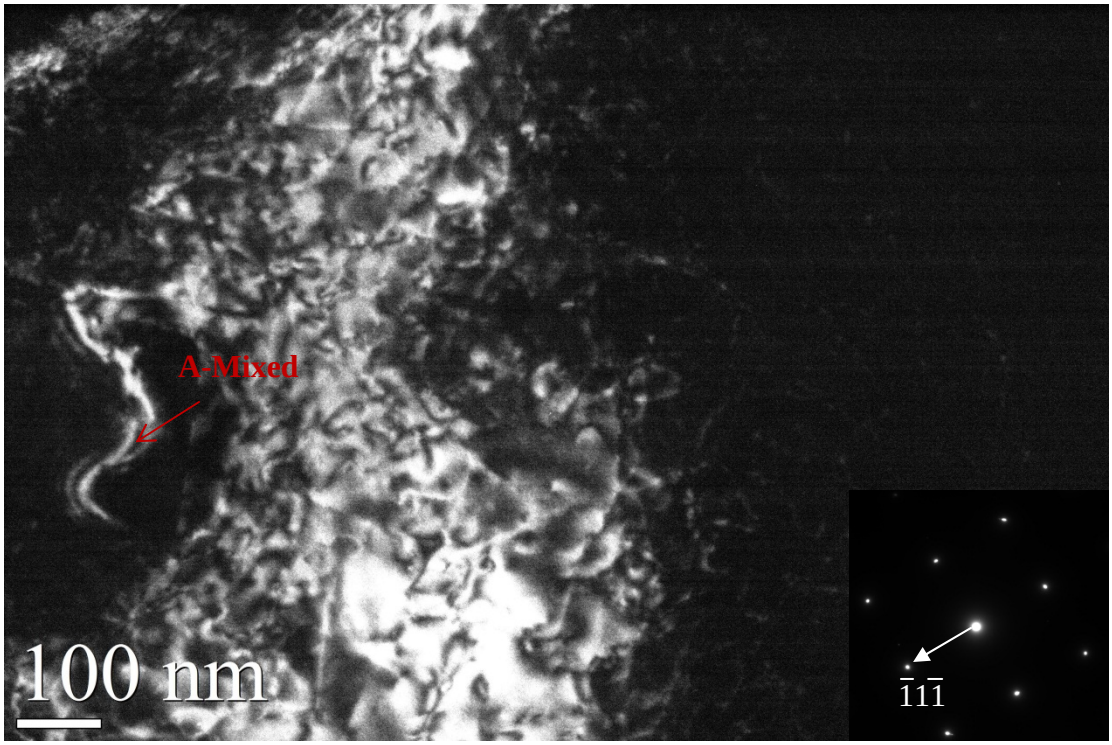

Figure 70. Dark field image of untreated sensitized area in the planar orientation analyzed under $\vec{g}$ = $(\bar{1}1\bar{1})$two beam condition

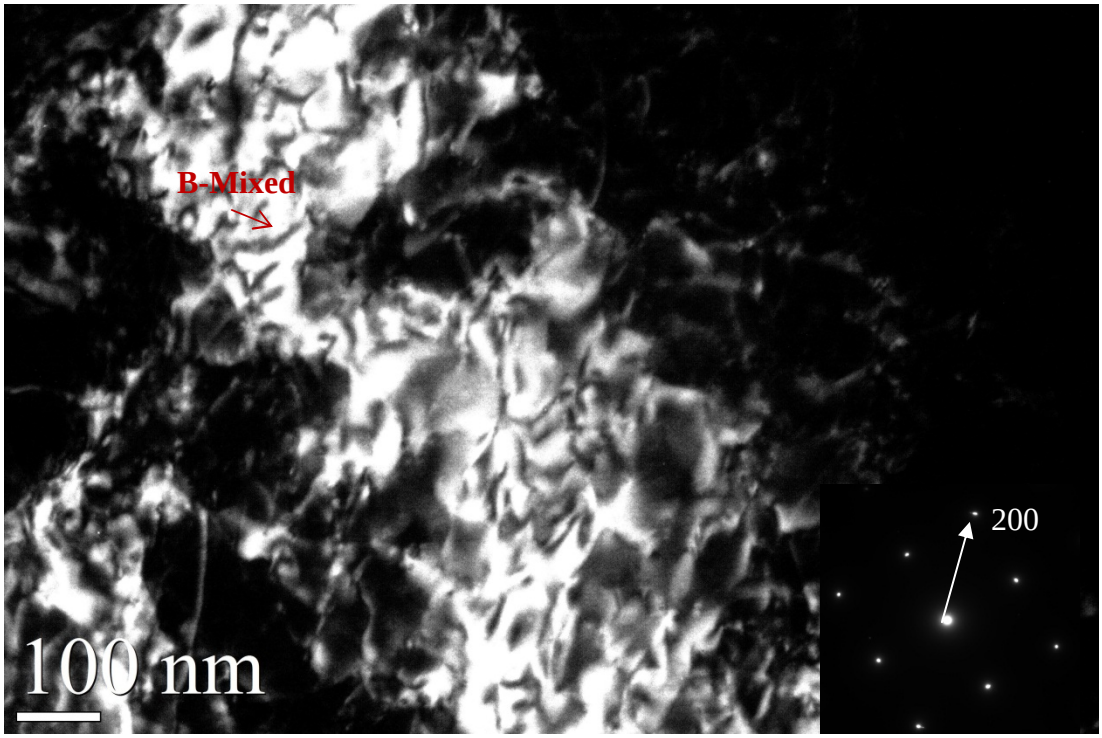

Figure 71. Dark field image of untreated sensitized area in the planar orientation analyzed under $\vec{g}$ = (200) two beam condition

Figure 72 shows the untreated sensitized 5456 area in the transverse orientation that was selected for analysis in the two beam condition. The zone axis was determined to be along the $[1\bar{1}0]$ direction. Dark field images were obtained for $\vec{g}$ = (200), $(\overline{111})$, and $(11\bar{1})$. Three dislocations were chosen for characterization and analyzed using the visibility condition using $\vec{g} \bullet \vec{b}$. Dislocation A lies along the $[\overline{11}1]$ direction, therefore a valid dislocation line would project along $[11\bar{1}]$ direction if $\overrightarrow{t_A}$ = $[2\overline{11}]$ or $[\overline{12}1]$. Dislocation B lies along the $[11\bar{3}]$, a valid dislocation line would project along $[\overline{11}3]$, if $\overrightarrow{t_B}$ = $[1\bar{2}1]$ or $[2\overline{11}]$. Dislocation C lies along the $[\overline{113}]$ direction, a valid dislocation line would also projection along the [113] if $\overrightarrow{t_C}$ =

$[1\bar{2}\bar{1}]$ or $[2\bar{1}1]$. Based on the visibility conditions and the possible Burgers vectors, dislocation A is a screw or edge dislocation. Dislocation B is a mixed dislocation. Dislocation C is either a screw or mixed dislocation. Figures 73 and 74 show the dislocations. The dislocation density was determined to be 5.3×10^9 dislocation/cm^2.

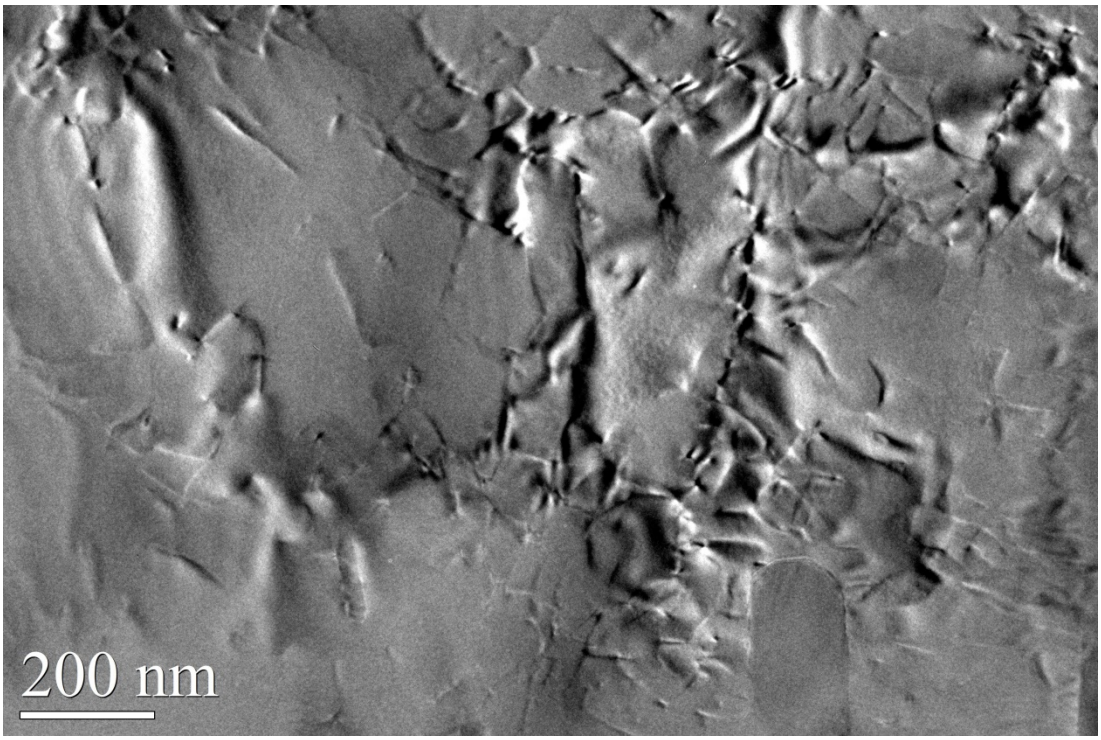

Figure 72. TEM micrograph of untreated sensitized 5456 area in the transverse orientation analyzed under two beam conditions

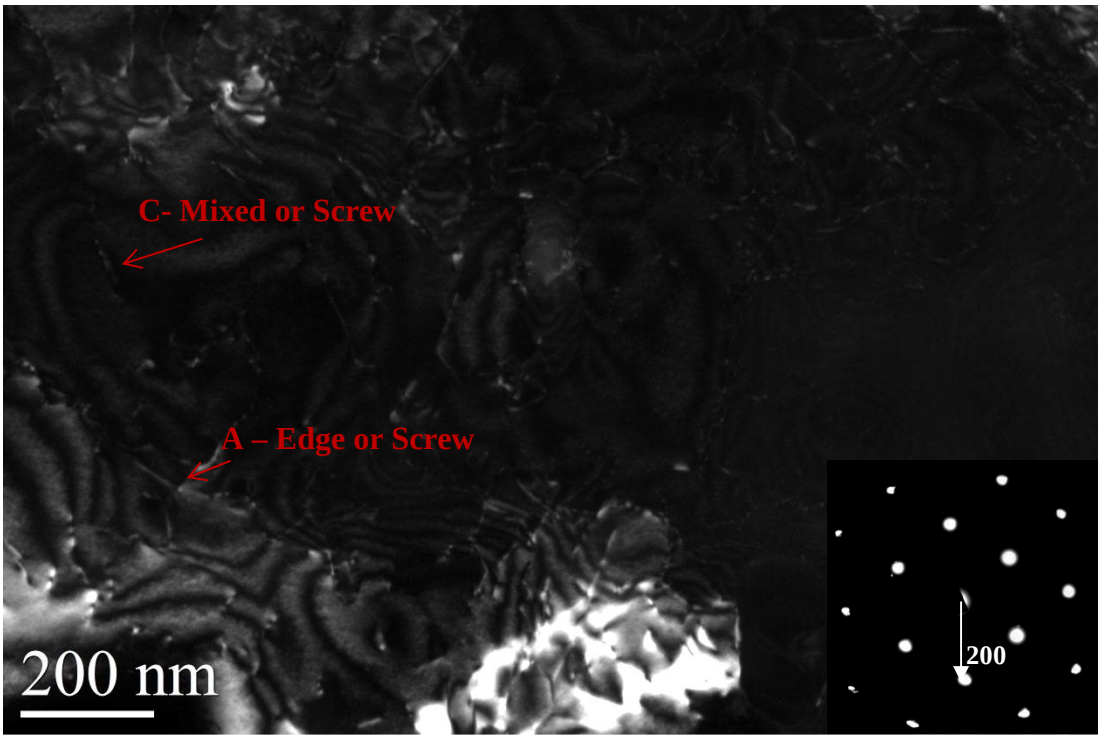

Figure 73. Dark field image of untreated sensitized area in the transverse orientation analyzed under $\vec{g}$ = (200) two beam condition

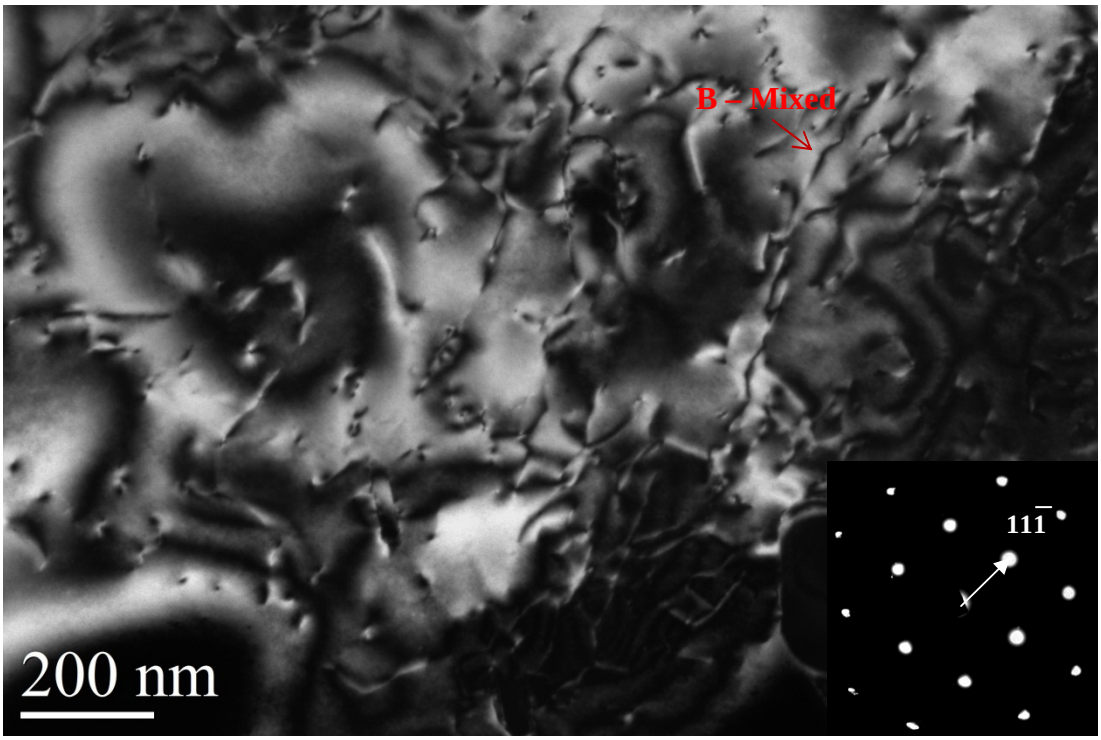

Figure 74. Dark field image of untreated sensitized area in the transverse orientation analyzed under $\vec{g}$ = $(11\bar{1})$ two beam condition

4.2.3 *In-situ* Elevated Temperature TEM of UIT Sensitized 5456

Elevated temperature TEM was used to investigate UIT sensitized 5456 samples obtained at the treated surface to examine the kinetics of grain growth in the nanocrystalline microstructure. The samples were polished only on one side to preserve the UIT surface as noted in section 2.7.1. The first experiment involved heating the sample from room temperature to 50°C and increasing to a maximum temperature of 450°C in 50°C increments. The sample was held for 10 minutes at each temperature. After heating to 450°C, the samples were cooled to room temperature. A second sample was heated from room temperature to 100°C, 200°C, 300°C, 350°C, 400°C, and 450°C. The samples were held at each temperature for 10 minutes between 100°C to 400°C. The sample was held for 40 minutes at 450°C to investigate the grain growth at that temperature. The experiment was conducted at an operating voltage of 200 kV and 103 μA in the LaB_6 TEM. Micrographs were obtained at a 10 K magnification on the microscope screen.

Figures 75 to 81 show bright field and dark field micrographs that represent the changes in the grain structure from room temperature to 450°C along with the associated diffraction patterns obtained at room temperature, 300°C, and 450°C. At room temperature, the microstructure is nanocrystalline as previously discussed in section 4.2.1.1. From the micrograph obtained at room temperature, Figure 75, the nanocrystalline grains range in size from 100 to 300 nm with an average grain size diameter of 200 nm. Heating between room temperature and 250°C, Figure 76, results in no grain growth but rather changes in grain orientation due to thermal expansion and sample bending. Diffraction patterns were not obtain at 100°C, 150°C,

and 250°C since no appreciable grain growth was observed at these temperatures. Upon heating the sample to 300°C, Figures 77 and 78, grain growth starts to occur and the nanocrystalline grains start to grow in size. Between 350°C to 450°C, Figures 79 to 81, significant grain growth occurs with some grains as large as 600 nm. Although significant grain growth occurs at 400°C, the microstructure exhibits some nanocrystalline grains which are still present even upon heating to 450°C. As the grain structure changes, the diffraction pattern changes from distinct broad ring patterns typical of a nanocrystalline structure to diffraction patterns with stronger and sharper spots indicating grain growth from 300°C to 450°C. Weak ring patterns are still visible at 300°C and even at 450°C confirming the presence of small random grains. At 300°C, two strong spots labeled as 1 and 2 in Figure 77 were used to get dark field images shown in Figure 78. Significant grain growth occurs at 400°C as shown in the dark field image, Figure 80, with an average grain size diameter of 500 nm. Grain growth continues at 450°C with grains that average 600 nm in diameter. The dark field image at 450°C, Figure 81, shows a number of small white spots that appear to be precipitates within each individual grain and at the grain boundaries. The precipitates started to form upon heating to 300°C and were more pronounced with increasing temperature to 450°C. Figure 82 shows that the grain growth remains stable after cooling to room temperature from 450°C.

The results from a second heating experiment concurred with the results of the first heating experiment. Grain growth began when the sample was heated above 300°C. Holding at each temperature for 10 minutes did not result in any significant changes in the growth rate or grain sizes. Holding the sample for 40 minutes did not

result in any observable changes in grain growth or significant increase in grain size once the sample was heated to 450°C. Figure 83 shows the dark field images after initial heating to 450° and held at 450°C for 15 minutes, 30 minutes, and 40 minutes. Upon heating to 300°C, a number of small precipitates were observed in the microstructure which is consistent with the first observations in Figures 75 to 81.

The activation energy for grain growth can be determined by the relationship between the average final grain size (d) and initial grain size (d_o) [52,53]:

$$d^2 - d_o^2 = k_g t^n \quad \textbf{(10)}$$

where *t* is time, n is a constant usually taken as unity. k_g is a temperature dependent constant given by:

$$k_g = A\, exp(-{}^{Q}/_{RT}) \quad \textbf{(11)}$$

where *Q* is the activation energy for grain growth, R is the gas constant, T is the absolute temperature and A is a constant. Grain growth can be then written as follows:

$$d^2 - d_o^2 = A\, t^n\, e^{-{}^{Q}/_{RT}} \quad \textbf{(12)}$$

Rearranging Equation 11 and taking the log of both sides gives the following expression [52,53]:

$$log\,\frac{d^2 - d_o^2}{t^n} = -\frac{Q}{2.3\ RT} + \log A \qquad \textbf{(13)}$$

The average grain size diameters as determined from the micrographs in Figures 75 to 81 were used to construct the semi-logarithmic plot (d^2-d_o^2) versus 1/T in Figure 84. The initial diameter, d_o, is the average grain size diameter at room temperature which is 200 nm. From the plot, the slope of the curve, m= -1244, is used to calculate the activation energy, *Q*, where R = 8.314 J/mol-K:

$$Q = 2.3\ (8.314\ \text{J /mol-K})\ (1244) = 31{,}953\ \text{J/mol or } \sim 32\ \text{kJ/mol}$$

Therefore, the activation energy required for grain growth in the UIT material is ~ 32 kJ/mol.

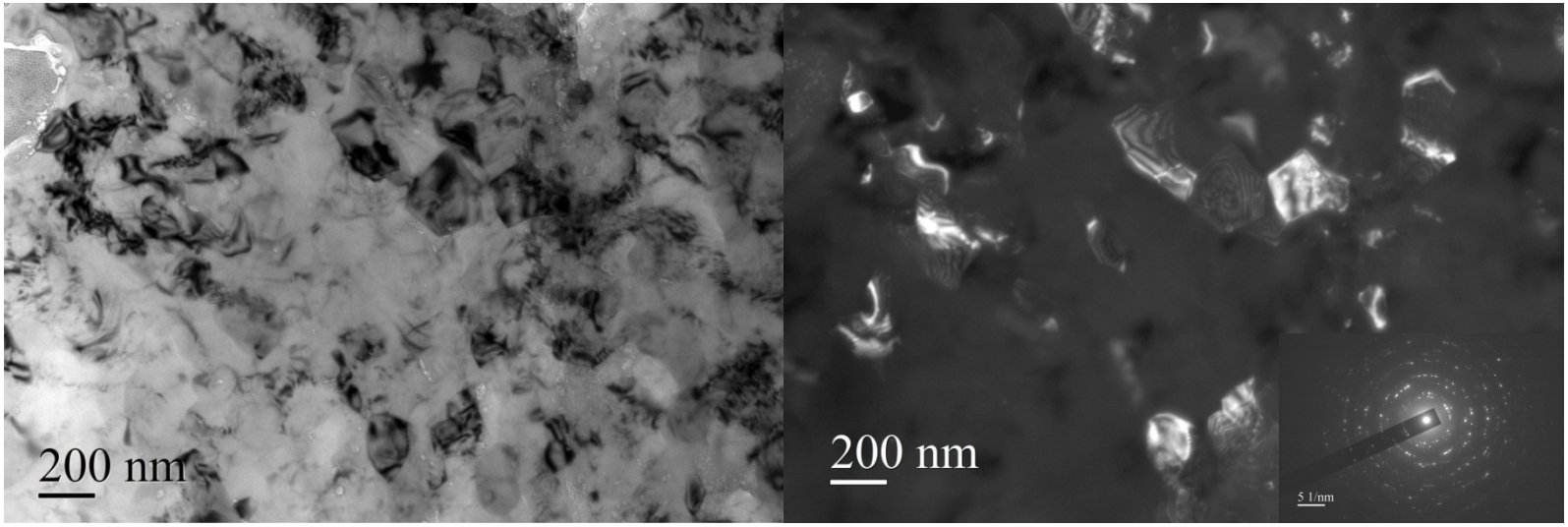

Figure 75. Bright field (left) and dark field (right) TEM micrographs of UIT sensitized 5456 at room temperature showing the presence of nanocrystalline grains. The inset in the bottom right is the diffraction patter from the area

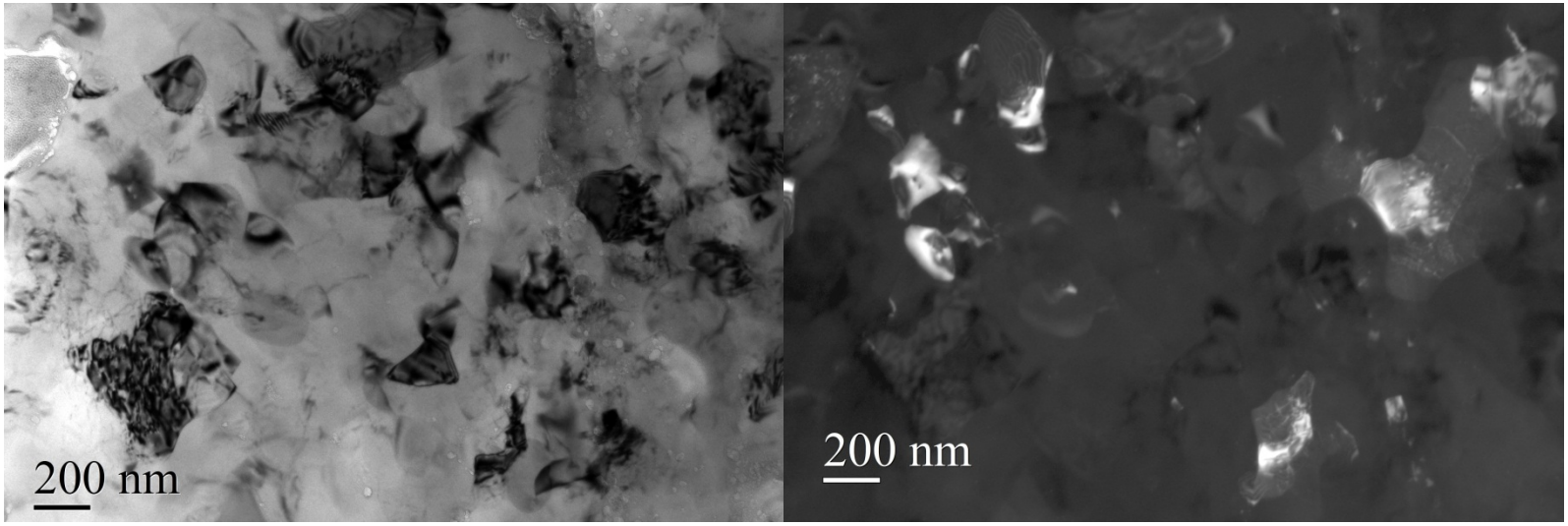

Figure 76. Bright field (left) and dark field (right) TEM micrographs of UIT sensitized 5456 at 250°C showing the presence of nanocrystalline grains with grain orientation changes from room temperature

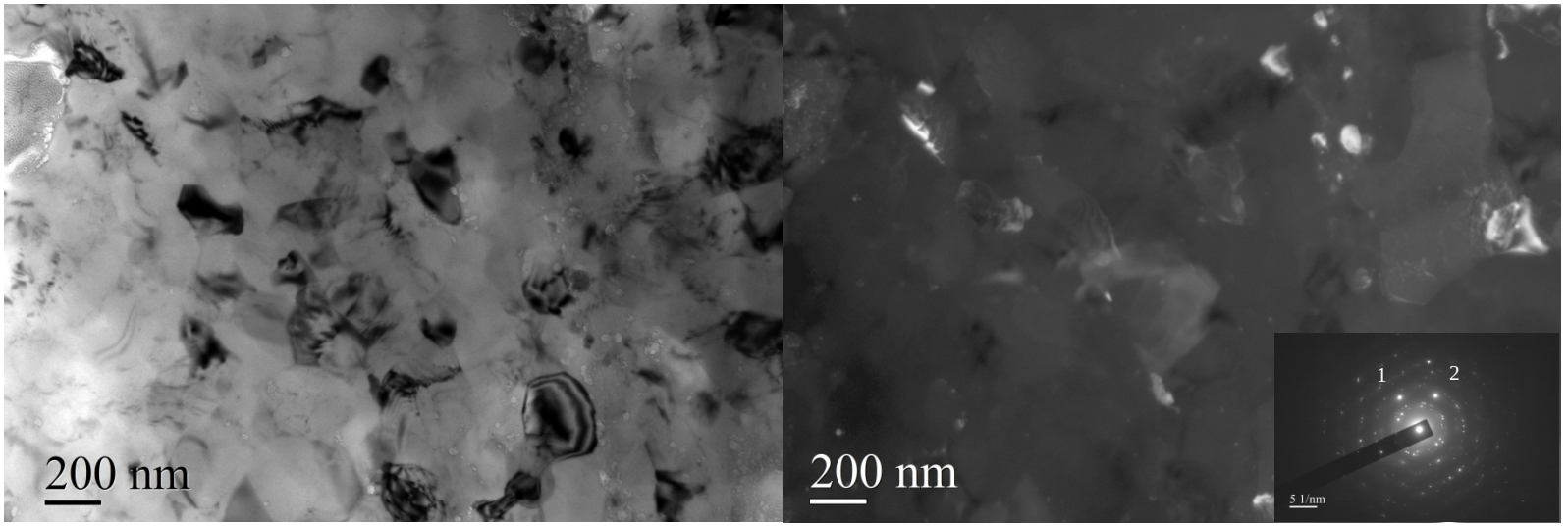

Figure 77. Bright field (left) and dark field (right) TEM micrographs of UIT sensitized 5456 at 300°C showing the presence of nanocrystalline grains and grain growth. The inset at the bottom right is the diffraction pattern of the area and shows typical ring pattern characteristic of nanocrystalline grains with some strong spots indicating grain growth.

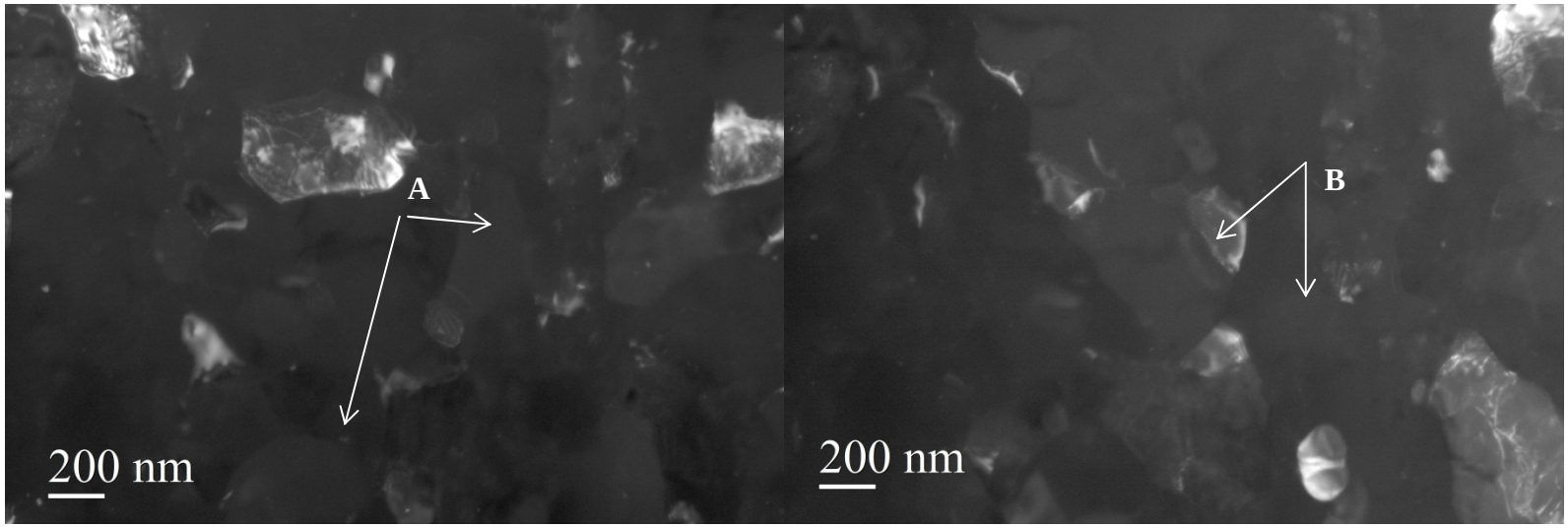

Figure 78. Dark field under two beam condition of diffraction spots 1 (A) and spot 2 (B) in Figure 77 of UIT sensitized 5456 heated to 300°C; presence of nanocrystalline grains and grain growth

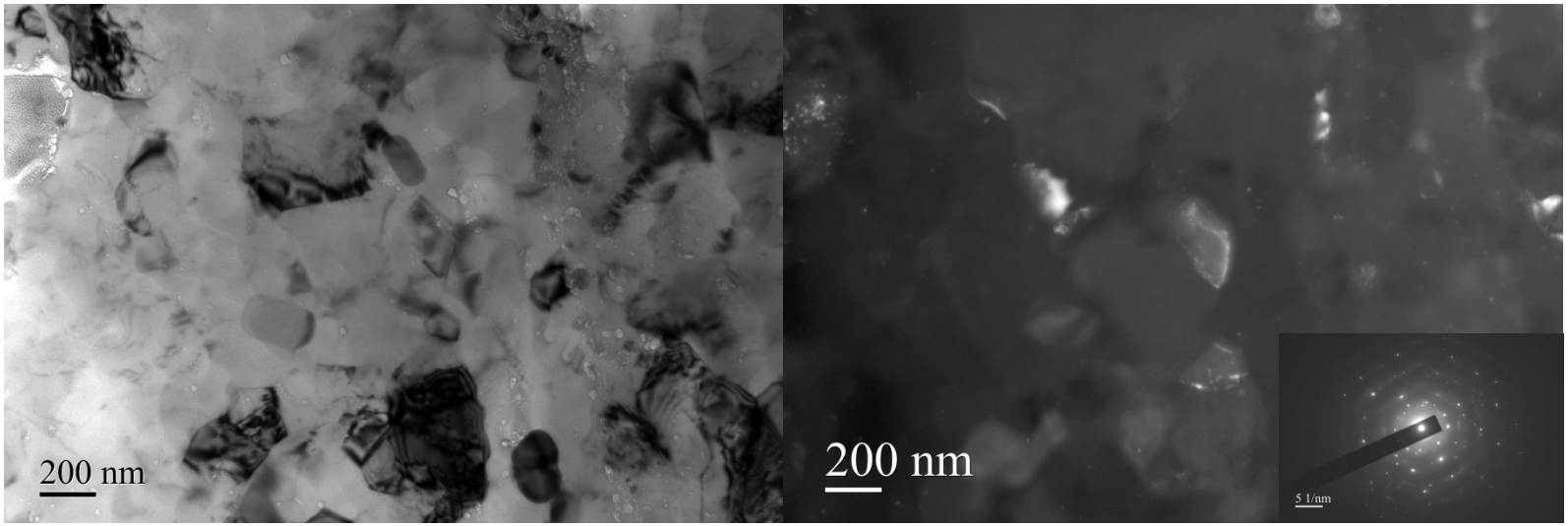

Figure 79. Bright field (left) and dark field (right) TEM micrographs of UIT sensitized 5456 at 350°C showing both nanocrystalline grains and grain growth. The inset at the bottom right is the diffraction pattern and shows stronger and sharper spots indicating grain growth

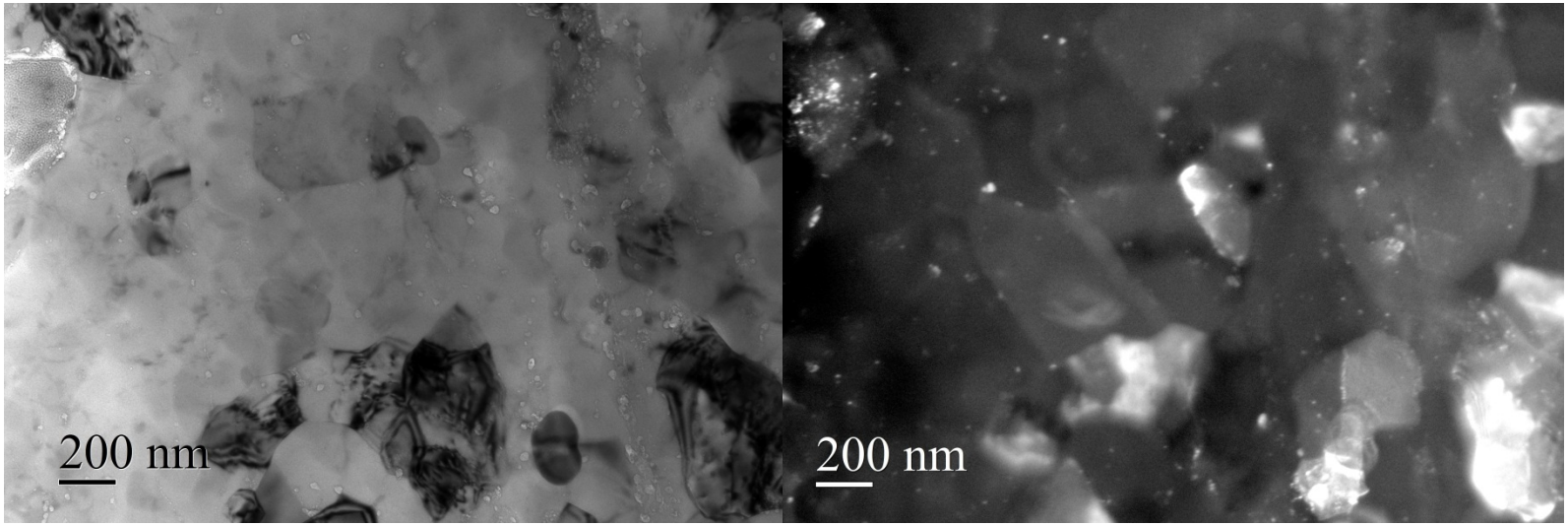

Figure 80. Bright field (left) and dark field (right) TEM micrographs of UIT sensitized 5456 at 400°C showing significant grain growth

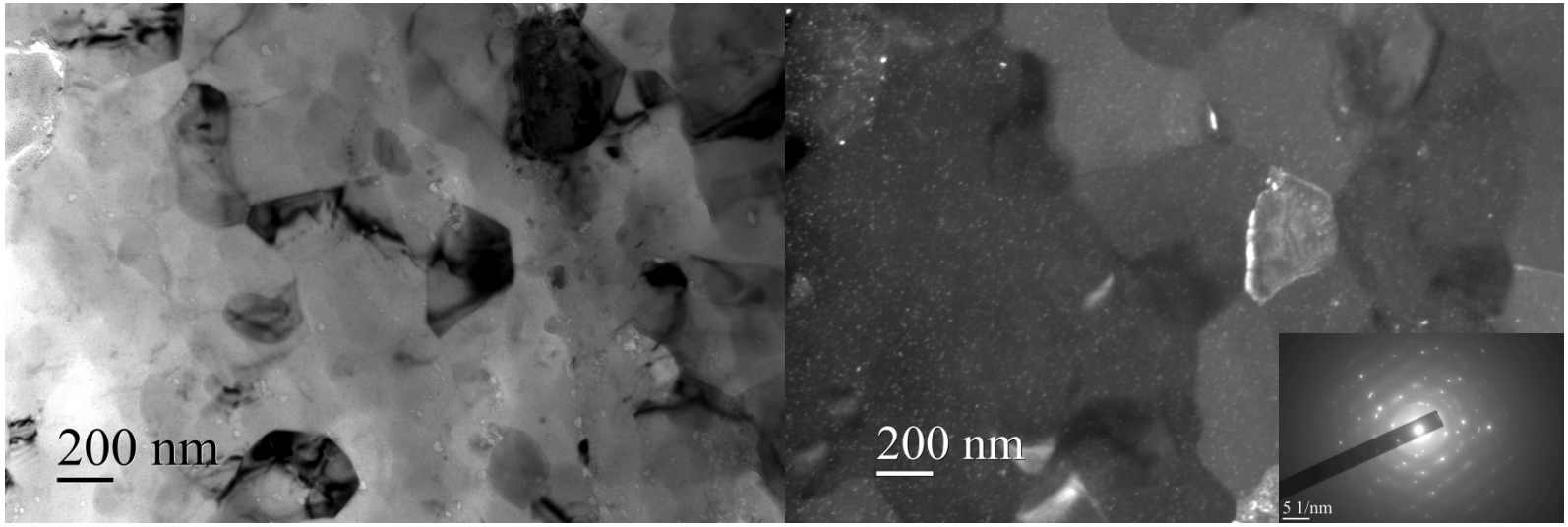

Figure 81. Bright field (left) and dark field (right) TEM micrographs of UIT sensitized 5456 at 450°C showing significant grain growth and the formation of small precipitates. The inset at the bottom right is the diffraction pattern from the area

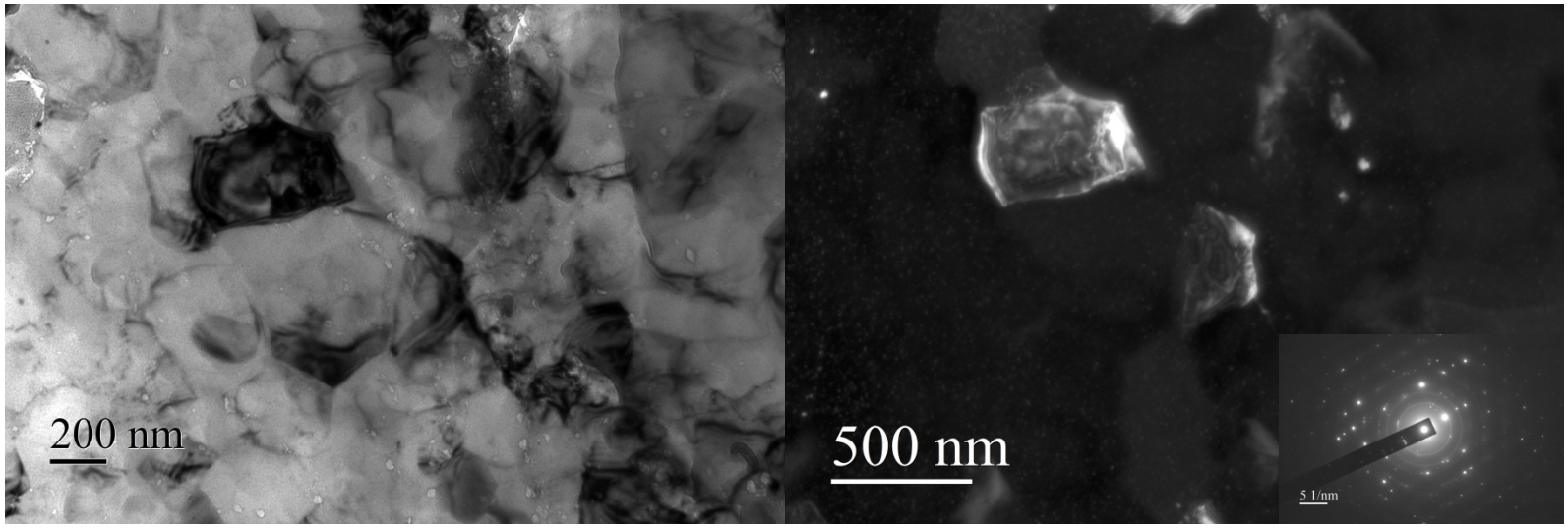

Figure 82. Bright field (left) and dark field (right) TEM micrographs of UIT sensitized 5456 cooled to room temperature after heating to 450°C showing stable grain growth. The inset at the bottom right is the diffraction pattern of the area

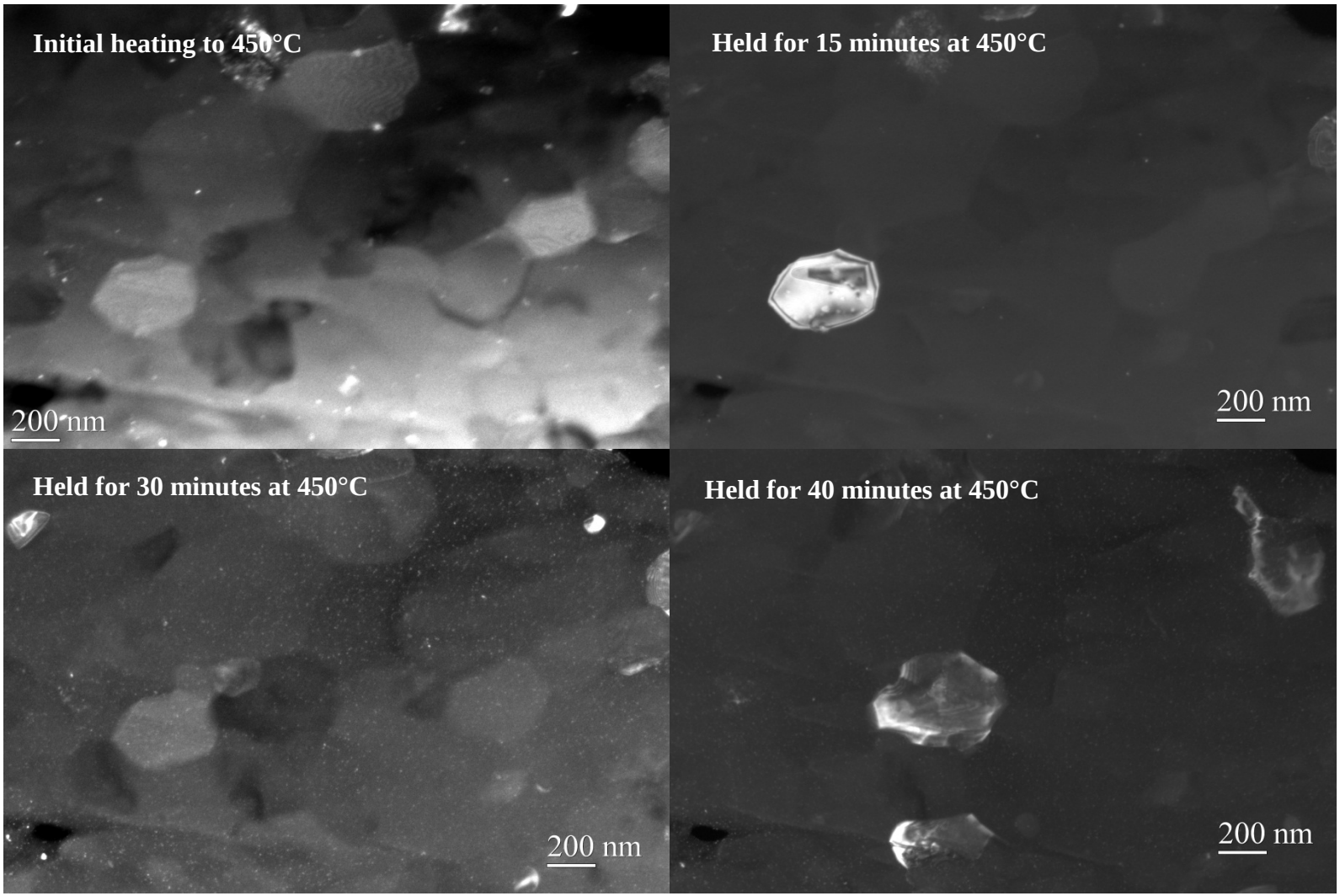

Figure 83. Dark field images of UIT sensitized 5456 heated to 450°C and held for various lengths of time following significant grain growth; holding for 40 minutes did not result in further grain growth

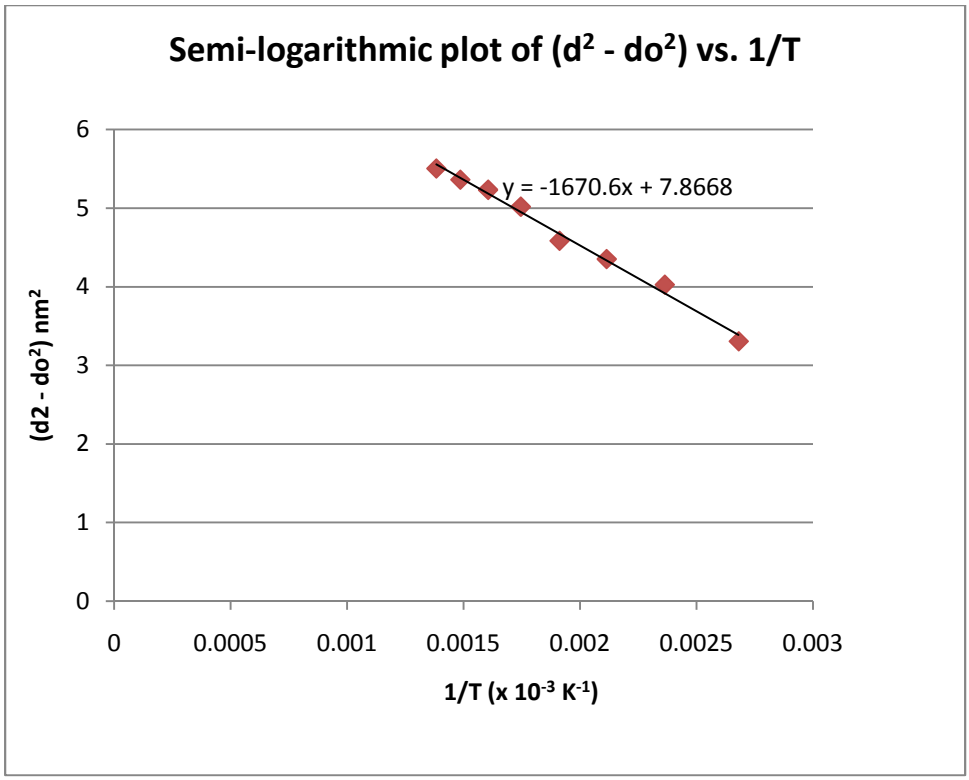

Figure 84. Semi-logarithmic plot of (d^2-do^2) versus 1/T for grain growth from *in-situ* heating TEM of UIT material; Slope of the line is Q/2.3R

4.2.4 X-ray Diffraction Measurements to Examine Grain Size at the UIT Surface

X-ray diffraction measurements using a diffractometer were obtained at the UIT surface in the planar orientation to examine the grain structure. The grain size can be determined by Scherrer's equation based on the width of the peak profiles [38, 54]:

$$d = \frac{\lambda}{\Delta(2\theta)cos\theta_B} \quad \textbf{(14)}$$

Where *d* is the average crystallite size, λ is the x-ray wave length, Δ(2θ) is the peak width, and θ_B is the Bragg angle from Equation 3 [38, 54]. The peak width is usually measured, in radians, at an intensity equal to half the maximum intensity [38].

Figures 85 and 86 show the peak profiles for the UIT material in the planar orientation at the surface for two samples. For sample 1, the peak width at the (200) reflection is 0.3 radians at a 2θ angle of 44.8 °. The peak width for sample 2 is 0.5 radians at a 2θ angle of 44.5°. The calculation of Equation 14 with these values results in grain sizes of 33 nm (sample 1) and 19 nm (sample 2). These grain size values are consistent with the grain sizes (ranging from 2 to 200 nm) determined from the TEM analysis as discussed in section 4.2.1.1.

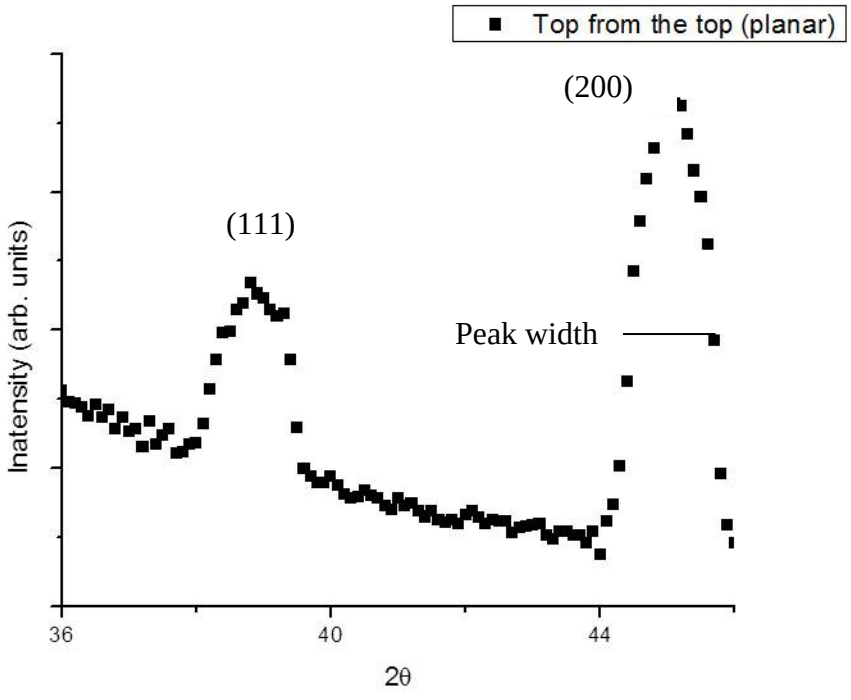

Figure 85. X-ray diffraction peak profile of UIT material (sample 1) in the planar orientation at the treated surface for the (111) and (200) reflections

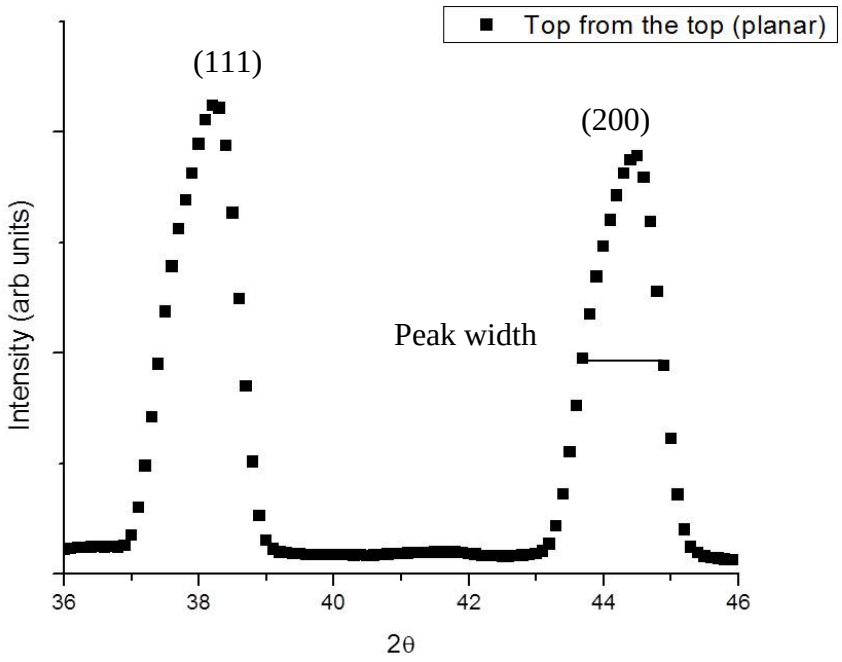

Figure 86. X-ray diffraction peak profile of UIT material (sample 2) in the planar orientation at the treated surface for the (111) and (200) reflections

4.3 Discussion

The observed nanocrystalline structure at the UIT surface in Figures 44 and 45 concurs with work by several authors regarding nanocrystalline grain growth due to SPD [3,28,55,56,57,58,59]. TEM investigations show that the nanocrystalline layer is near surface and is only present to a depth that is equivalent to the thickness of the deformation layer (10 to 18 μm). The formation of the nanocrystals within the deformation layer suggest that the nanocrystals form in the area of highest strain

which is at the surface. Samples obtained just below the surface, Figures 51 and 52, did not reveal any nanocrystalline grains, however submicron grains were present. The formation of the nanocrystalline layer is also inhomogeneous and the nanocrystals vary in size from 2 to 200 nm (from TEM and HRTEM). The inhomogeneity may be due to the random nature of the UIT process. As previously noted in section 3.3, the process is a manual process which results in random deformation at the surface.

Severe plastic deformation techniques such as UIT, ECAP, and HPT have been shown to form nanocrystals in aluminum alloys [3,28,55,56,57,58,59]. The nanocrystalline layer is near surface with subgrains observed at regions of various depths below the surface. In 2024-T351, nanocrystals ranging in size from 8 to 15 nm were observed from the top surface to a depth of 5 μm from the surface when treated by the UIT process as previously discussed in section 3.1 [3]. The nanocrystalline grains that range in size from ~ 4 to 6 nm as shown in Figure 45 and subgrain formation shown in Figure 51 concur with the work reported by X. An et al. [3]. The micrographs show that the nanocrystalline grains did not form uniformly within the material. A similar finding was reported by M. Sato et al. [28]. In 5083 aluminum subject to wire brushing, the nanocrystals that were formed near the surface were not shown to be uniform or distinct and this was also true for other alloys with relatively high concentrations of alloying elements. Equal channel angular pressing and HPT have also been shown to result in an inhomogeneous nanostructure in Al-Mg alloys [57,59].

Although the alloying content results in an inhomogeneous microstructure when subject to SPD, increasing the alloying elements results in a finer microstructure. Both J. May et al. and M. Liu et al. report that increasing the amount of magnesium in Al-Mg decreases the grain size and increases the dislocation density [57,59]. The increase in dislocation density is attributed to the smaller grain size and solute interaction effects [59]. The increase in magnesium results in more dislocations being trapped by the solute atoms which has an effect on the formation of subgrains or dislocation cell structure. In HPT of Al-Mg alloys, the process of grain refinement occurs through the formation of dislocations at the grain interiors and grain boundaries due to the solute effect and the large strains induced by HPT [59]. As more and more dislocations are generated, the dislocation density reaches some critical value with increasing strain which results in an increase in the misorientations across sub-boundaries due to dislocation annihilation and accumulation. As the misorientations become larger, low angle grain boundaries are transformed to high angle grain boundaries. The transformation of low angle grain boundaries to high angle grain boundaries due to HPT is consistent with the finding by X. Wu et al. as previously discussed in section 3.3 [25]. The grain refinement is also due to grain subdivision as a result of formation of dislocation cells and subgrains. When the local temperature is higher than the recrystallization temperature, dynamic recrystallization occurs and forms nanograins. The nanograins were found to form in regions were the highest strain is generated. Figure 87 illustrates the schematic of the grain refinement process of Al-Mg alloys during HPT [59].

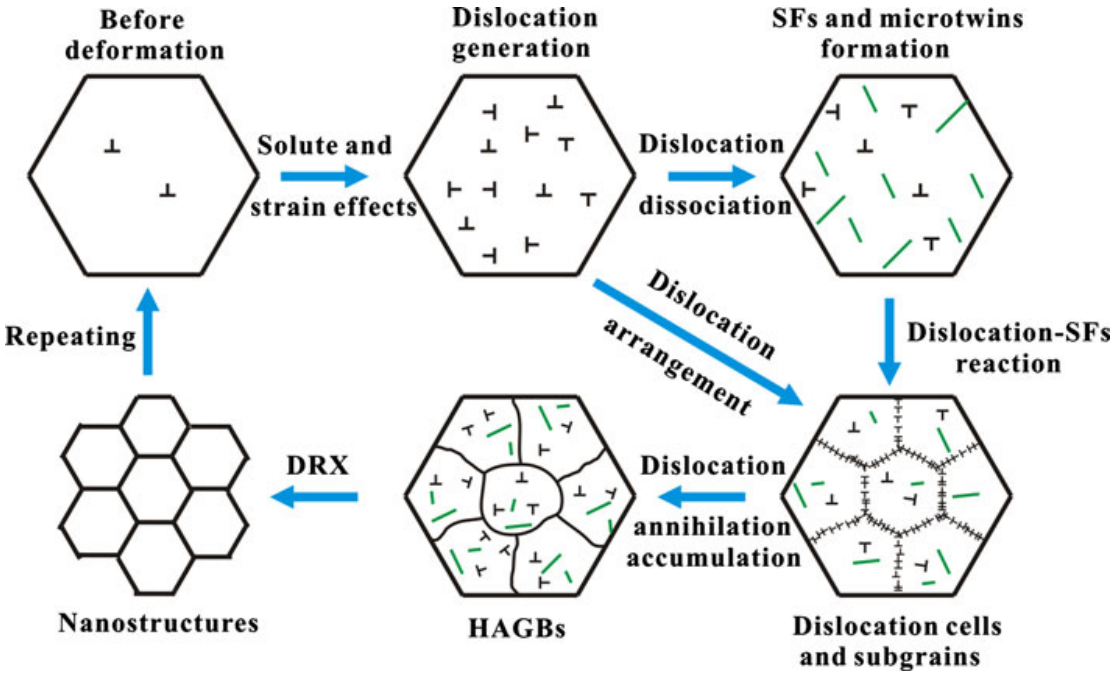

Figure 87. Schematic of the grain refinement process of Al-Mg alloys during high pressure torsion [59]

Dynamic recrystallization is the occurrence of recrystallization during deformation. In general because aluminum and its alloys exhibit very high rates of dynamic recovery, dynamic recrystallization is inhibited and rarely observed. However, researchers have reported that dynamic recrystallization can occur in severely plastically deformed aluminum [60,61]. In aluminum alloys, dynamic recrystallization can occur through three processes: 1) Discontinuous dynamic recrystallization which is considered exceptional because of aluminum's high stacking fault energy [60,62]. Discontinuous dynamic recrystallization occurs through the nucleation of grain embryos and subsequent grain growth. 2) Continuous dynamic recrystallization where dislocations accumulate in low angle grain

boundaries, resulting in an increase in misorientation and subsequent grain formation. 3) Geometric dynamic recrystallization where the initial grains are deformed and their boundaries become progressively serrated while high angle grain boundaries created by subgrain formation are pinched-off and annihilated [60,62,63]. In Al-Mg alloys, geometric dynamic recrystallization has been shown to occur in Al-Mg alloys subject to torsion or compression with large strains at a temperature $T \geq 400°C$ [64]. P.B. Prangnell el al. report that submicron grain structure can be produced by severe plastic deformation when processed at temperatures of $< 0.4T_m$ where T_m is the melting temperature, while nanocrystalline structures can be only be formed at $0.2T_m$ [65]. The recrystallization temperature depends on a variety of factors: deformation time, percentage of deformation, deformation temperature, purity and grain size [9]. Dynamic recrystallization is less sensitive to temperature than static recrystallization, however it is more sensitive to strain rate. The plastic strains necessary to severely plastically deform metals to bulk submicron grains is on the order of $\varepsilon_{vm} > 7$ where ε_{vm} is the effective Von Mises strain [65].

The formation of the nanocrystalline grains observed in Figures 44 and 45 concur with the results reported by M. Liu et al. in which Al-Mg undergoes a dynamic recrystallization when severely plastically deformed [59]. X. An et al. also suggest that aluminum 2024-T351 undergoes a geometric dynamic recrystallization during the UIT process [3]. Although the material temperature when subject to the UIT process was not measured for this research, based on findings by M. Liu et al. and P.B. Prangnell el al., the material surface temperature due to the UIT process must be at least $0.2T_m$ since nanocrystalline grains did form [59,65]. The melting

temperature range of 5456 for wrought product of ¼ inch thickness or greater is 568.3 to 638°C [12]. The UIT process is a non-thermal process, however based on the temperature suggested by P.B. Prangnell el al. for nanocrystalline grains to form, the temperature increase during the UIT process ranges from 114 to 128°C [65].

The deformation of nanocrystalline materials is believed to take place through a different mechanism than for coarse grain materials. Researchers have observed stacking faults and twinning at the grain boundaries in nanocrystalline materials [66,67,68,69]. Experimentally, deformation twinning has been observed in other FCC metals such as copper and nickel, however they have not been observed in aluminum alloys. Research by X. Liao et al., M. Chen et al., and L. Manping et al. demonstrate otherwise in nanocrystalline Al-Mg alloys [66,67,69]. High resolution TEM investigations of Al-Mg alloys subject to HPT reveal a high density of stacking faults and deformation twinning in the microstructure [69]. The stacking faults and twinning are believed to result from partial dislocation emission from the grain boundaries. In FCC metals, stacking faults and twins can be formed from the dissociation of either a 0° screw dislocation, a 60° dislocation, or by two 30° Shockley partials that dissociated from the end of a 0° screw dislocation [69]. Twins are also thought to be formed by dynamic overlapping of stacking faults of dissociated dislocations on adjacent slip planes [66,69]. This twinning mechanism differs from the pole mechanism in which one partial dislocation forms a whole twin by climbing a screw dislocation pole to an adjacent slip plane. M. Chen et al. proposes that the twinning and stacking fault formation in nanocrystalline grains can be understood by comparing the critical shear stress needed to nucleate a perfect

dislocation with a Burger's vector of ½ ⟨110⟩ with an approximate grain size and shear stress, τ_N, required to initiate the Shockley partial 1/6 ⟨112⟩ twinning dislocation to generate stacking faults and deformation twins [67]. Comparing the required shear stress, τ_N, and critical shear stress, τ_P, given by the following equations [67]:

$$\tau_N = \frac{2\alpha\mu b_N}{D} \quad \textbf{(15)}$$

$$\tau_P = \frac{2\alpha\mu b_p}{D} + \frac{\gamma}{b_p} \quad \textbf{(16)}$$

where μ is the shear modulus, γ is the stacking fault energy, b_N is the magnitude of the Burgers vector for the perfect dislocation and b_p is the magnitude of the Burgers vectors for the Shockley partial dislocation. The parameter α is specific to the dislocation type and contains the scaling factor between the length of the dislocation source and the grain size, for an edge dislocation, α = 0.5 and for a screw dislocation, α = 1.5 [67]. For aluminum, μ is ~ 35 GPa and γ is 142 mJ/m^2 [67]. Equating Equation 15 and Equation 16 gives the equation for the critical grain size, D_c, required for twinning and stacking fault formation to occur [67].

$$D_C = \frac{2\alpha(b_n - b_p)b_p}{\gamma} \quad \textbf{(17)}$$

Assuming that α is equal to 1, the approximate grain size required for twinning and stacking fault formation to occur in aluminum alloys is between 10 to 15 nm. The

HRTEM micrographs shown in Figures 47 and 50 show nanocrystalline grains that are ~ 2 to 200 nm. Although the presence of stacking faults and twinning was not observed in the nanocrystals in Figures 49 and 50, the size of the nanocrystalline grains suggest that twinning and stacking fault formation may occur. However additional analysis would be required to confirm the research reported by X. Ziao et al., M. Chen et al., and L. Manping et al. who suggest that twinning and stacking faults resulting from partial dislocations emissions from the grain boundaries is a deformation mode in nanocrystalline aluminum [66,67,69].

An examination of the grain boundaries of the nanocrystals in Figures 44 and 45 and the HRTEM micrograph in Figure 49 show that the grain boundaries are curved or wavy which suggest that the grain boundaries are in a high energy nonequilibrium state [69,70]. The submicron grains in Figure 51 also show a complex structure of dislocation, sub-boundaries, and Moiré fringes along with curved or wavy grain boundaries. The presence of curved or wavy grain boundaries have been found to be characteristic of SPD Al-Mg alloys [69,70]. Nonequilibrium grain boundaries that contain a very high density of extrinsic grain boundary dislocations can result in high internal stresses and high energies which will have a direct impact on the mechanical properties [70]. Extrinsic grain boundary dislocations are extraneous dislocations produced by external influences such as plastic deformation or quenching [71].

R. Goswami et al. studied 5083 aluminum both unsensitized and sensitized by TEM [19]. In unsensitized, as received material, the microstructure showed a number of rod-like and equiaxed precipitates in the aluminum matrix. The rod-like and

equiaxed precipitates were found to be rich in Mn, Fe, and Cr. No β phase was observed in the unsensitized, as received material. In the sensitized material which was sensitized by annealing at 175ºC for 10 days, Mg-rich precipitates were found to have precipitated on top of the Mn-rich rod like and equiaxed precipitates [19]. The Mg-rich precipitates were determined to be β phase. β phase was found to also form a continuous network at a number of grain boundaries. The morphology of the β phase was either equiaxed or more elongated and measured in length from 50 to 1000 nm. A. Eikum and G. Thomas report that Mg atoms cluster prior to the precipitation of β phase [72]. Because of the high binding energy between Mg atoms and vacancies, the cluster involves Mg atom-vacancy complexes and prior to β phase precipitation, a critical Mg vacancy ratio must be attained in the complexes [72]. The results indicate that at the physically deformed surface where the microstructure has been transformed to nanocrystalline grains, a continuous secondary β phase is not present as is the case in the present study and as shown in Figures 44 to 52. Below the physically deformed layer as observed in Figure 15, a continuous network of β phase exists along with Mg and Cu enrichment at the grain boundaries as shown in Figure 65. The Mg and Cu enrichment at the grain boundaries concurs with the work reported by R. Jones et al. for the sensitization heat treatments of aluminum 5083 [18]. Copper in aluminum is added to increase resistance to pitting, however there is evidence that intergranular corrosion resistance decreases with increasing levels of copper due to increased precipitation at the grain interior during sensitization heat treatments of 5083. As noted in section 1.2.1, the β phase can only be redissovled into solution by heating Al-Mg to about 425°C. The absence of a continuous β phase

at the physically deformed surface in the UIT material is likely due to the severe plastic deformation induced by the UIT process and dynamic recrystallization near the surface which resulted in grain subdivision and nanocrystalline grain growth.

E. Huskins et al. also studied unsensitized 5083 aluminum by TEM and found two types of precipitates within the matrix, one rod-like shape and another with an irregular shape [73]. The rod-like shape structures consisted of Al, Mn, Cr, and Cu while the irregular shaped precipitates were Mn rich. As previously mentioned in section 4.1, Mn does not remain in solid solution but rather forms complex precipitates. Any strengthening due to Mn is precipitate strengthening rather than through precipitate hardening [73]. Precipitates strengthen the material by acting as obstacles to dislocation motion. Figures 54 and 56 provide TEM micrographs in which Mn rich precipitates are surrounded by dislocations and act as obstacles to dislocation motion.

The dislocation types observed between the UIT and untreated material were not distinguishable in the planar orientation. The UIT material exhibited screw and mixed dislocations while the untreated material in the planar orientation exhibited edge and mixed type dislocations. The most notable difference between the dislocation types was observed in the transverse orientation. The UIT treated sample primary had screw and mixed type dislocations while the untreated material exhibited edge, mixed, and screw type dislocations. The dislocation density was slightly higher in the UIT material as expected since the UIT process imparts deep compressive stresses and plastically deforms the surface of the material. Although the deformation layer is on the order of 10 to 18 µm, the deformation imparted by the process extends

below the surface region. One dislocation was observed to slip along the $[11\bar{2}]$. Slip along the [112] plane is odd slip that occurs due to simultaneous slip in the [101] and [110] directions.

Figures 53 and 54 also show extensive interactions between the dislocations and the secondary phase precipitates. Based on the micrographs, the dislocations appear to climb over the precipitates, however, additional analysis would be required to confirm this interaction. In SPD Al-Mg alloys, interactions between dislocations and secondary phase precipitates suggest the occurrence of dislocation glide along the matrix particle interface which is already under an applied stress [74]. R. Kaibyshev et al. report similar findings for Zr modified 5083 aluminum (Al-4.7Mg) subject to HPT and subsequent annealing [74]. Transmission electron microscopy investigations showed lattice dislocations attached to small particles. The dislocations climbed over the particles and were captured at the detachment side of the particles after the climb when heated to a temperature of $T \geq 550°C$ [74]. The materials used for this study were not annealed, however the results shown in Figures 53 and 54 suggest that the UIT process leads to extensive dislocation and secondary precipitate interactions.

The results of the heating stage TEM demonstrate that the nanocrystalline grains in SPD Al-Mg are stable to approximately 300°C. Annealing above 300°C results in grain growth and a microstructure with both submicrometer grains and random nanocrystalline grains that are less than 100 nm. Significant grain growth occurs at 400°C as shown in Figure 80. Heating to 450° resulted in additional grain growth as shown in Figure 81, however holding at 450° for a prolonged period of

time did not significantly increase the grain growth or growth rate, Figure 83. These results concur with the findings by Z. Horita et al. who reported that subsequent annealing of 5083 processed by ECAP at various temperatures for one hour did not result in significant grain growth until 300°C [58]. The microstructure after annealing at 100°C was essentially identical to the microstructure following ECAP processing in which the grains had an average size of less than 1 µm [58]. Annealing at 200°C reduces the dislocation density within the grain, however there was little or no grain growth. At 300°C, significant grain growth was observed and the microstructure consisted of grains that exceeded 1.0 µm. In a similar study, D.G. Morris and M.A. Munoz-Morris found grain growth to occur in ECAP processed Al-3Mg following a one hour anneal at 250°C [75]. The ECAP microstructure before annealing consisted of elongated grains measuring 0.1 µm wide by 1.0 to 1.2 µm in length. Annealing for one hour at 250°C resulted in a duplex microstructure consisting of bands of slightly coarsened grains and regions of coarser grains of 5 to 10 µm. Annealing at 250°C for 5 to 15 minutes lead to a slightly coarsened microstructure with near equiaxed grains.

The observed grain growth in this thesis work is due to recrystallization. The in-situ heating stage TEM experiments reported in section 4.2.3 indicate that the recrystallization temperature for UIT 5456 is 300°C which concurs with the work reported by Z. Hortia et al. for 5083 processed by ECAP [70]. However, these results differ from those of D.G. Morris and M.A. Munoz-Morris [75]. The experiments also indicate that the grain growth rate is constant up to 450°C. As noted above, the recrystallization temperature depends on a variety of factors. In aluminum alloys, the

recrystallization temperature has also been found to be influenced by the addition of Mg [76,77]. M. Koizumi et al. found that in Al-Mg with various contents of Mg cold rolled to 95 percent reduction and annealed at temperatures between 200 and 450°C, the Mg content strongly influences the recrystallization temperature and rate [76]. At 1.0 weight percent Mg, recrystallization is retarded; however with increasing Mg content above 2 weight percent, recrystallization was accelerated and occurs at a lower temperature. For Al-5Mg, 100 percent recrystallization was found to occur at ~ 300°C following annealing treatments for 5 minutes at 225°C, 250°C, 275°C, and 300°C. At high Mg solute concentrations, the rate of recrystallization becomes constant and at very high Mg concentrations where the solubility limit is exceeded, secondary phase particles are precipitated. In 80 percent cold rolled Al-5Mg annealed for one hour between 260 to 350°C, N. Ryum and J.D. Embury reported that Mg serves to reduce both the growth rate and final grain size and gives greater non-uniformity in the scale of the recrystallized structure [77].

Research by J. Wang et al. reports different activation energies for grain growth to fully recrystallized and to unrecrystallized grains in an Al-3Mg with an initial submicrometer grain structure of ~ 0.2 μm produced by ECAP and subsequently annealed at various temperatures [52]. Annealing heat treatments were performed at constant temperature in the range from 443 to 548°K (170 to 275°C) in silicon oil or 563 to 803°K (290 to 530°C) in an Ar atmosphere furnace for 1 hour [52]. Significant grain growth occurred at 503°K (230°C) resulting in a duplex microstructure consisting of unrecrystallized grains with non-equilibrium grain boundaries and recrystallized grains [52]. The material was fully recrystallized at

563°K (290°C) with grains greater than 100 µm in diameter [52]. The activation energy for grain growth to a fully recrystallized structure was determined to be ~ 90 kJ/mol which is consistent with the activation energy required for grain boundary diffusion in aluminum, ~ 86 kJ/mol. For the unrecrystallized grains, the activation energy is ~ 30 kJ/mol [52].

The grain growth activation energy, ~ 32 kJ/mol, calculated from the *in-situ* elevated temperature experiments for the UIT material in the current work is very low compared to the activation energy for fully recrystallized grains reported by J. Wang et al [52]. However, the activation energy concurs with the findings by J. Wang et al. for unrecrystallized grains of ~ 30 kJ/mol [52]. In a related study, M. Furukawa et al. reported an activation energy of ~25 kJ/mol for unrecrystallized grain growth of Al-3Mg with initial grain size of 0.09 µm produced by torsional straining and subsequently annealed between 323 to 793°K (50 to 520°C) [78]. The activation energy is of the order of $0.2Q_i$ where Q_i is the activation energy for self-diffusion in pure aluminum [78]. M. Furukawa et al. state that the low activation is consistent with the high atomic mobility anticipated in non-equilibrium grain boundaries and is a consequence of the significant distortion and excess dislocations [78]. The *in-situ* TEM experiments reported in section 4.2.3 resulted in a duplex microstructure indicating that the microstructure was not fully recrystallized. The low activation energy concurs with the findings by J. Wang et al. and M. Furukawa et al. for unrecrystallized grain growth in Al-3Mg alloys [52,78]. The results also concur with the concept of a low activation energy for grain diffusion in ultrafine grain materials

because of the non-equilibrium grain boundaries which are characteristic of nanocrystalline grains as observed in Figures 44 and 45 [69,70].

M. Kubota reported the formation of plate and lath-shaped precipitate particles during the early stages of ageing of Al-10Mg alloy aged at 200°C [79]. The plate-like precipitates were identified as β' phase or the metastable intermediate phase with a similar composition to the equilibrium β phase [79]. The *in*-situ heating experiments in this thesis resulted in the formation of fine precipitates upon heating at 300°C, however it is unclear as to whether these precipitates are intermediate β' phase. Therefore additional TEM analysis is required.

4.4 Summary

The results of TEM and XRD analysis can be summarized as follows:

- The nanocrystalline grains formed within the deformation layer vary in size from 2 to 200 nm in diameter.
- The nanocrystalline grains are characterized by curved or wavy grain boundaries.
- A continuous β phase was not observed within the deformation layer.
- Below the deformation layer, the microstructure is characterized by submicron grains, complex structure of dislocations, sub-boundaries, and Moiré fringes (overlapping grains).
- Magnesium and Cu enrichment was observed at the grain boundaries below the deformation layer.

- Below the deformation layer, extensive interactions between the dislocation and secondary phase precipitates is observed.
- The dislocations observed in the UIT sample in the planar orientation included screw and mixed type dislocations. The untreated material in the planar orientation exhibited mixed and edge type dislocations. In the transverse orientation, the UIT material was characterized primarily by screw and mixed type dislocations while the untreated material was characterized by edge, mixed, and screw type dislocations.
- The dislocation density of the UIT treated material was slightly higher than untreated material, on the order of 1.9×10^{10} dislocations/cm^2 (planar) and 1.5×10^{10} dislocations/cm^2 (transverse) versus 5.3×10^{9} dislocations/cm^2 (planar) and 7.2×10^{9} dislocations/cm^2 (transverse).
- The nanocrystalline grains are thermally stable to ~ 300°C. Grain growth starts to occur above 300°C with extensive grain growth at 400°C. The microstructure consists of a duplex microstructure with submicron and nanocrystalline grains. Holding for 40 minutes at 450°C did not significantly increase the grain growth nor did it result in significant changes in grain size.
- The activation energy required for grain growth is ~ 32 kJ/mol.

Chapter 5: Mechanical and Corrosion Properties of Aluminum 5456 Plastically Deformed by UIT

5.1 Introduction

This chapter presents the study of the material properties of UIT treated and untreated sensitized 5456 aluminum. The material properties that were examined include hardness, yield strength, and susceptibility to intergranular corrosion using the ASTM G67 Test. This study contributes to the understanding of the effects of SPD on the material properties of Al-Mg alloys.

Magnesium is known to increase the strength of Al-Mg alloys through solute strengthening. Increased Mg concentration results in increased strength. Manganese may also provide solute strengthening provided Mn remains in solid solution [70]. However, most of the Mn has been found to form secondary precipitates, and therefore any strengthening effect is due to precipitation hardening [73]. Other trace elements such as Fe and Si have also been found to have a strengthening effect on Al-Mg provided they remain in solid solution [48].

Severe plastic deformation techniques have been shown to improve the mechanical properties of Al-Mg alloys through grain refinement. Techniques such as ECAP and HPT have been shown to produce ultrafine grain or nanocrystalline grains which can significantly enhance the hardness and strength of the material. In 6061 aluminum alloy with majoring alloy elements of Mg and Si, ECAP processing showed that the hardness of the material could be significantly increased from 38 H_V to 75 H_V after four passes of processing. The larger increase in hardness was attributed to the grain refinement from 71.6 μm to 3.9 μm using the ECAP process

[80]. The grain refinement was also found to contribute to the significant increase in the strength of the material. M. Fu et al. reported that the ultimate tensile strength increased 52 percent after four passes of processing; however the ductility was decreased by about half [80].

Strengthening due to grain refinement is important in Al-Mg alloys because of the relatively large Hall-Petch slope. The influence of grain size on the yield strength is given by the Hall-Petch equation [24]:

$$\sigma_y = \sigma_o + kD^{-\frac{1}{2}} \quad \textbf{(18)}$$

where σ_y is the yield stress, σ_o is the frictional stress with both thermal and athermal components, k is a constant, and D is the grain size. For aluminum alloys, k is typically in the range of 0.06 to 0.15 MN $m^{-3/2}$ [81].

For Al-Mg alloys, grain refinement has been shown to occur by the arrangement of dislocations into cell walls that minimize the strain energy and have low angle grain boundary characteristics [1]. With increasing deformation, the cell boundaries are transformed into high angle grain boundaries because the cell boundaries may increase, the boundary thickness decreases, and the grain boundary misorientations increase [1]. The microstructure may exhibit both low angle cell boundaries and high angle cell boundaries at certain strains. Under these conditions, strengthening is due to two contributions: 1) dislocation strengthening due to the presence of low-angle grain boundaries and 2) strengthening due to the presence of medium to high angle grain boundaries.

Low angle grain boundaries can exist as subgrains in which the difference in orientation across the boundary may only be a few degrees. Low angle grain boundaries are low energy boundaries that are characterized by simple dislocation arrays [24]. High angle grain boundaries are boundaries of random misfit between the adjoining crystal lattices and are characterized by high surface energy. As a result, high angle grain boundaries are more likely to contain a higher concentration of solute atoms at the boundary and serve as preferential sites for solid-state reactions such as diffusion, phase transformations, and precipitation reactions.

As previously noted in section 1.3, low angle grain boundaries are more resistant to intergranular corrosion than high angle grain boundaries. A. Davenport et al. reported that when the misorientation angle is over 25°, the grain boundaries can exhibit continuous, discontinuous, or no intergranular attack in sensitized aluminum 5182 [17]. However when the misorientation angle was less than 20°, no precipitates were observed at the grain boundaries.

5.2 Results

5.2.1 Micro-hardness Measurements

Micro-hardness measurements were obtained under a collaborative effort with Dr. Marc Zupan at the University of Maryland, Baltimore County using a Vickers micro-indenter [82]. Samples for hardness measurements were cut from larger samples, mounted in an epoxy resin and polished to a mirror finish. More than 200 indentations were obtained using a 25 gF load and time of 5 seconds. The hardness

measurements were obtained as a function of distance from the UIT treated surface in order to map the hardness variation. Figure 88 shows the hardness values as a function of depth from the UIT surface [82]. The highest hardness values were obtained near the UIT surface which show hardness values that average 1.04 GPa (at the UIT surface to a depth of 0.272 mm). The hardness values range from 0.9 GPa to 1.14 GPa at the UIT surface and at depths of 0.141 mm to 2.24 mm below the treated surface. With increasing depth to 2.24 mm, the hardness values are lower and become constant with an average value of ~ 0.9 GPa. The average hardness at the UIT surface (1.01 GPa) is slightly lower than the hardness at a depth of 0.141 mm below the surface (1.14 GPa).

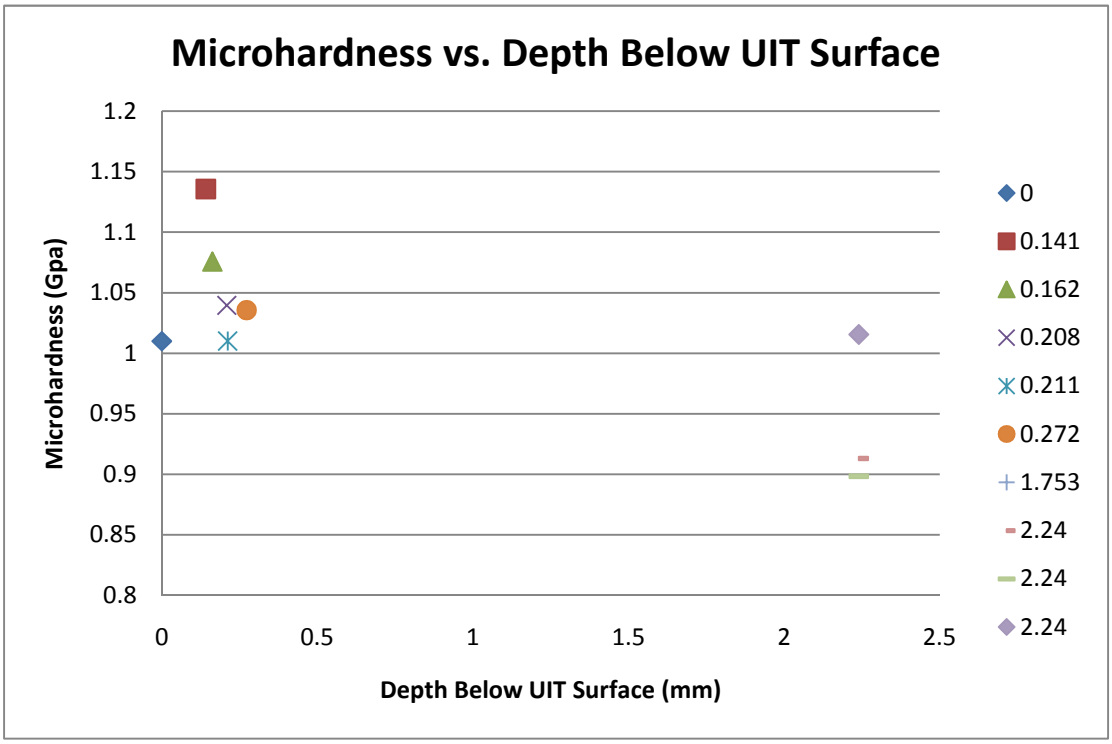

Figure 88. Vickers hardness measurements as a function of depth from the UIT treated surface in sensitized 5456 aluminum [82]

5.2.2 Micro Specimen Tensile Testing

Localized tensile properties were measured using specimens obtained near the UIT surface and at several depths from the UIT surface. Specimens were obtained at a depth of less than 0.3 mm from the surface, a depth of greater than 1.0 mm from the surface, and at a depth of 2.0 mm from the surface.

The results show the highest yield strength, 290 MPa and 250 MPa, at the UIT surface and near the surface at a depth of 0.141 mm, respectively. With increasing depth, the yield strength is lower with values less than 250 MPa. There is some variability in the data as shown in the yield strength as a function of depth from below the UIT treated surface in Figure 89. A specimen obtained at a depth of 2.24 mm exhibited a high yield strength of 253 MPa which is higher than the yield strength obtained closer to the UIT surface at a depth of 0.141 mm. The variability in the yield strength is likely due to the manual nature of the UIT process which results in random deformation on the surface of the material. There is also some variability in the yield strength at the treated surface where the average yield strength was 221 MPa. At the UIT surface, two specimens measuring 181 µm and 192 µm thick exhibited yield strengths and hardness values of 200 MPa and 0.92 GPa and 172 MPa and 1.03 GPa, respectively as shown in Table 7 which provides a summary of the yield strength and Vicker's microhardness from specimens at different depths below the surface. The specimen at the UIT surface that exhibited the highest yield strength was ~ 66 µm thick. The thickness of the specimens likely included some voids and tearing as observed in Figures 13 and 14 which is attributed to the variability in the yield strengths and hardness.

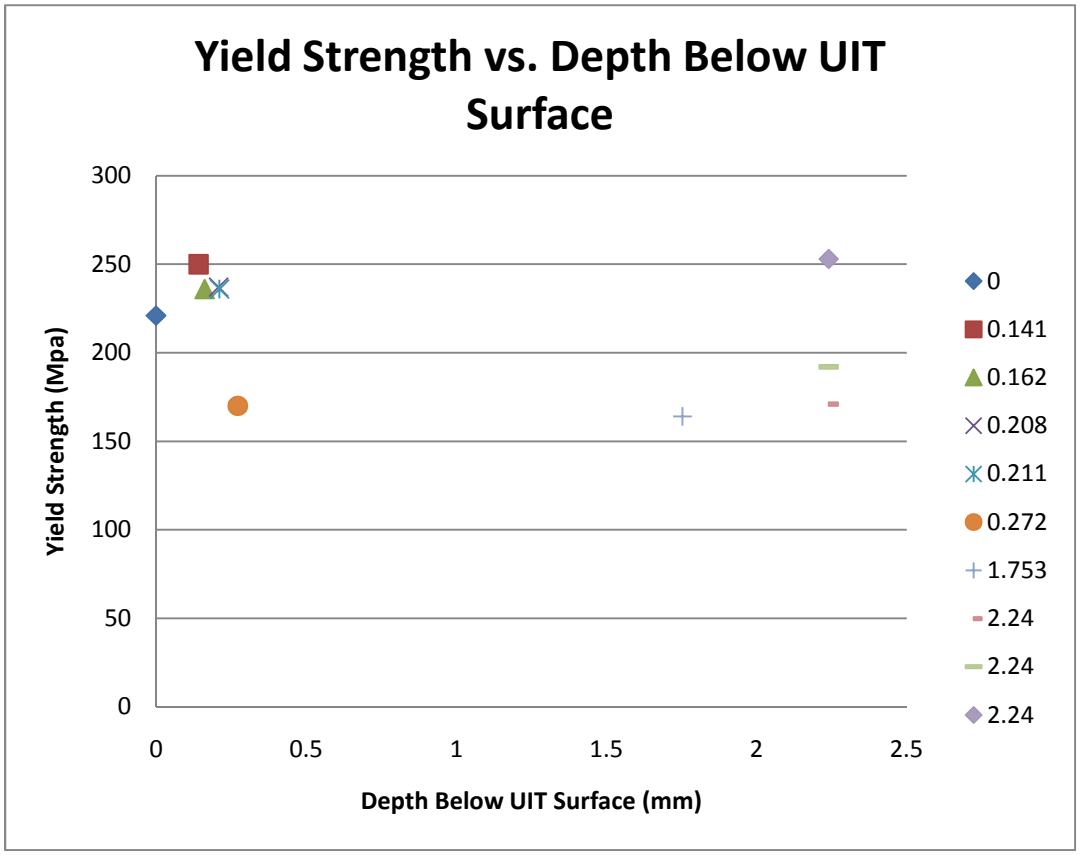

Figure 89. Yield strength as function of depth below the UIT treated surface; micro specimen tensile testing of UIT 5456 aluminum [82]

Table 7. Summary of specimen location, yield strength, and microhardness values for micro specimen tensile testing of UIT treated 5456 aluminum [82]

Depth below UIT Surface (mm)	Yield Strength (MPa)	Micro hardness (GPa)
At the UIT surface	290, 200, 172	1.08, 0.92, 1.03
0.141	250	1.14
0.162	236	1.08
0.208	237	1.04
0.211	236	1.01
0.272	170	1.04
1.753	164	N/A
2.24	171	0.91
2.24	192	0.90
2.24	253	N/A

5.2.3 Fractography of Micro Specimen Tensiles

Fractographs of broken micro tensile specimens were obtained for both UIT and untreated sensitized 5456 in order to examine the fracture mode. For the UIT material, specimens closest to the surface and from the surface were examined in order to see if the UIT would result in different fracture modes since the tensile properties differ at various depths below the UIT surface. For the untreated sensitized material, specimens were only examined at a depth of 1.686 mm below the surface as the fracture modes are expected to be similar regardless of the depth in which the specimen is obtained. The specimens were observed under the SEM at various magnifications ranging from 250X to 2000X. Figures 90 and 91 show fractographs of the UIT sensitized micro tensile specimens obtained at a depth of 0.150 mm below the UIT surface at magnifications of 300X and 1000X, respectively. The fractographs show a transgranular ductile fracture mode with micro void coalescence and dimples. The fractographs also reveal the presence of larger voids. Figures 92 and 93 show fractographs of the UIT sensitized micro specimen tensile obtained at a depth of 3.976 mm below the UIT surface at magnifications of 450X and 2000X, respectively. The fractographs reveal a similar ductile fracture mode as the micro specimen tensiles obtained closest to the UIT surface. The fracture mode is transgranular with ductile, micro void coalescence, and dimples.

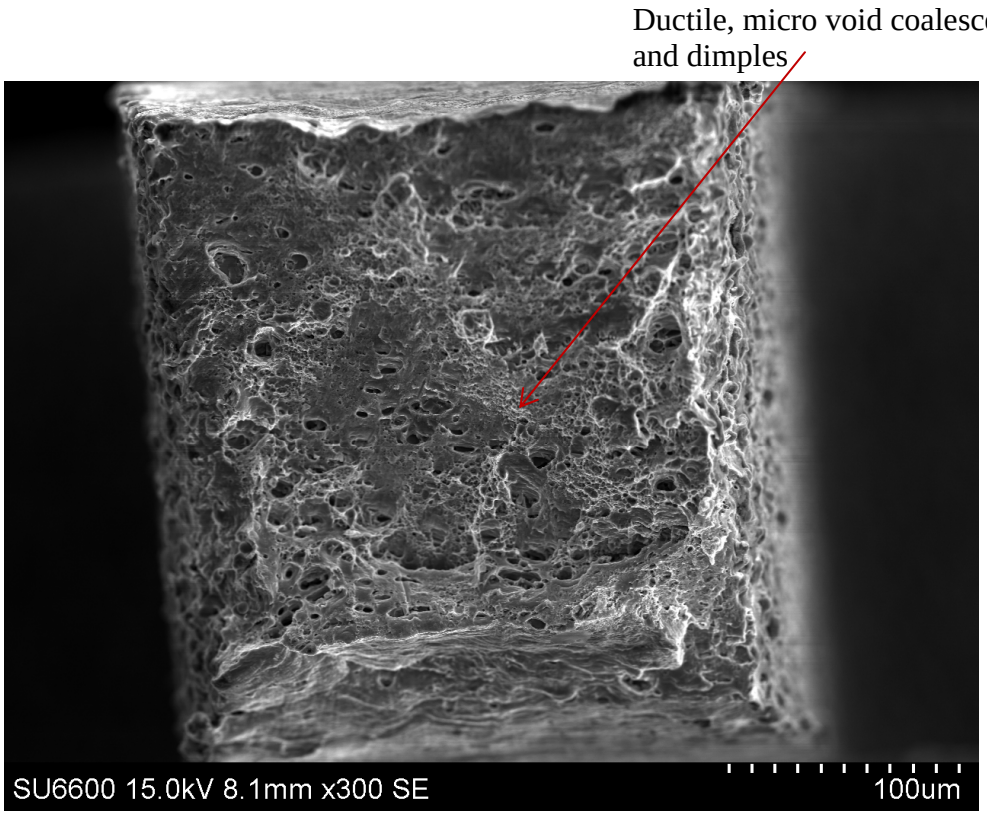

Figure 90. Fractograph of micro tensile specimen obtained from UIT sensitized 5456 at a depth of 0.150 mm below the UIT surface at 300X

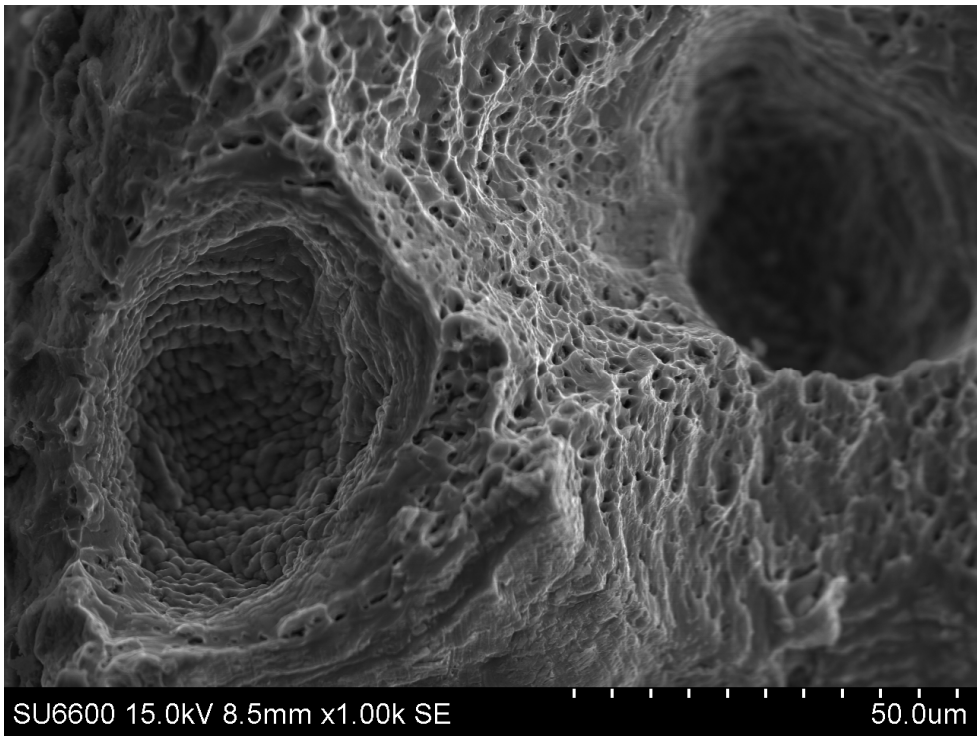

Figure 91. Fractograph of micro tensile specimen obtained from UIT sensitized 5456 at a depth of 0.150 mm below the UIT surface at 1000X showing voids

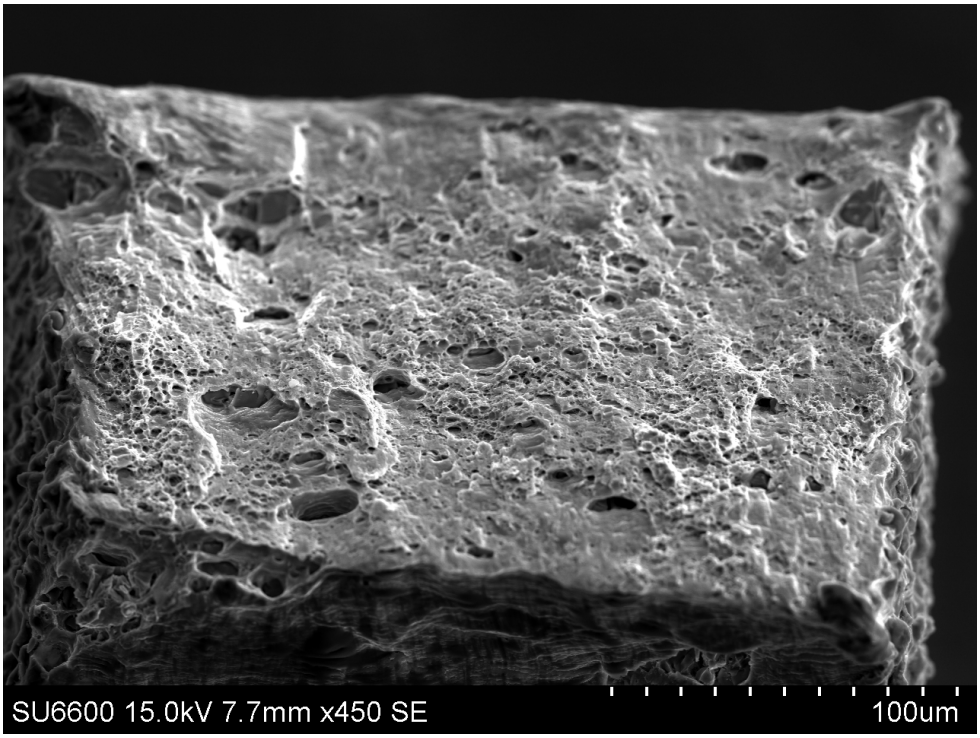

Figure 92. Fractograph of micro tensile specimen obtained from UIT sensitized 5456 at a depth of 3.976 mm below the UIT surface at 450X

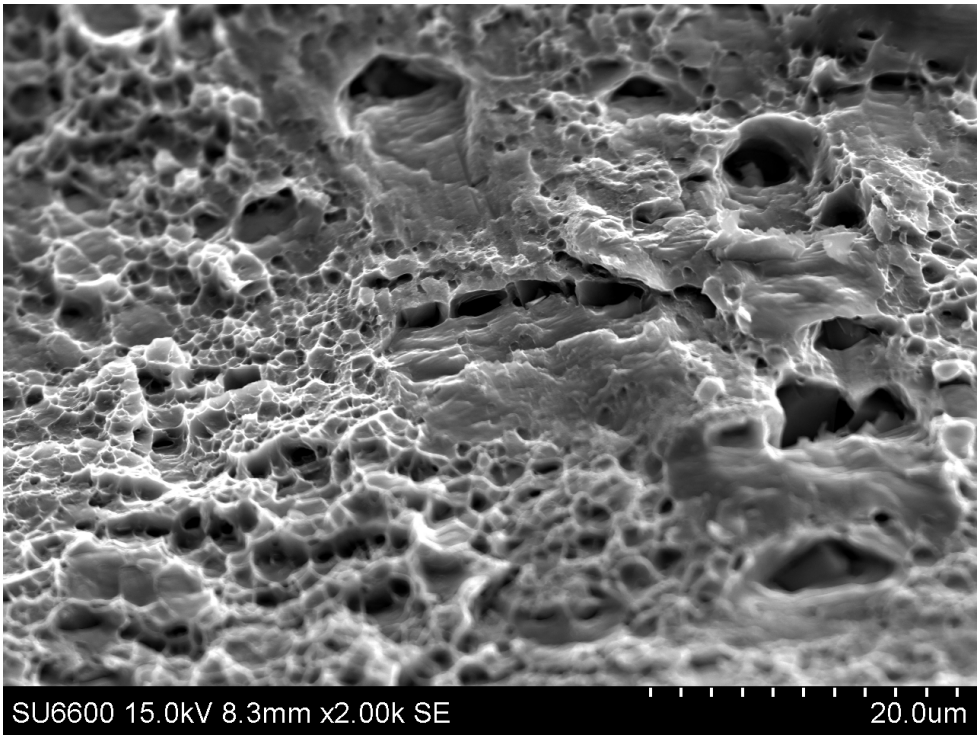

Figure 93. Fractograph of micro tensile specimen obtained from UIT sensitized 5456 at a depth of 3.976 mm below the UIT surface at 2000X

Figures 94 and 95 show the fracture surface of the untreated sensitized 5456 micro specimen tensiles obtained at a depth of 1.686 mm below the material surface at 300X and 1000X magnification. The fracture mode is similar to that observed for the UIT micro specimen tensiles. The fracture mode is primarily transgranular, ductile with micro void coalescence and dimples. There is also some evidence of cleavage fracture in Figure 94.

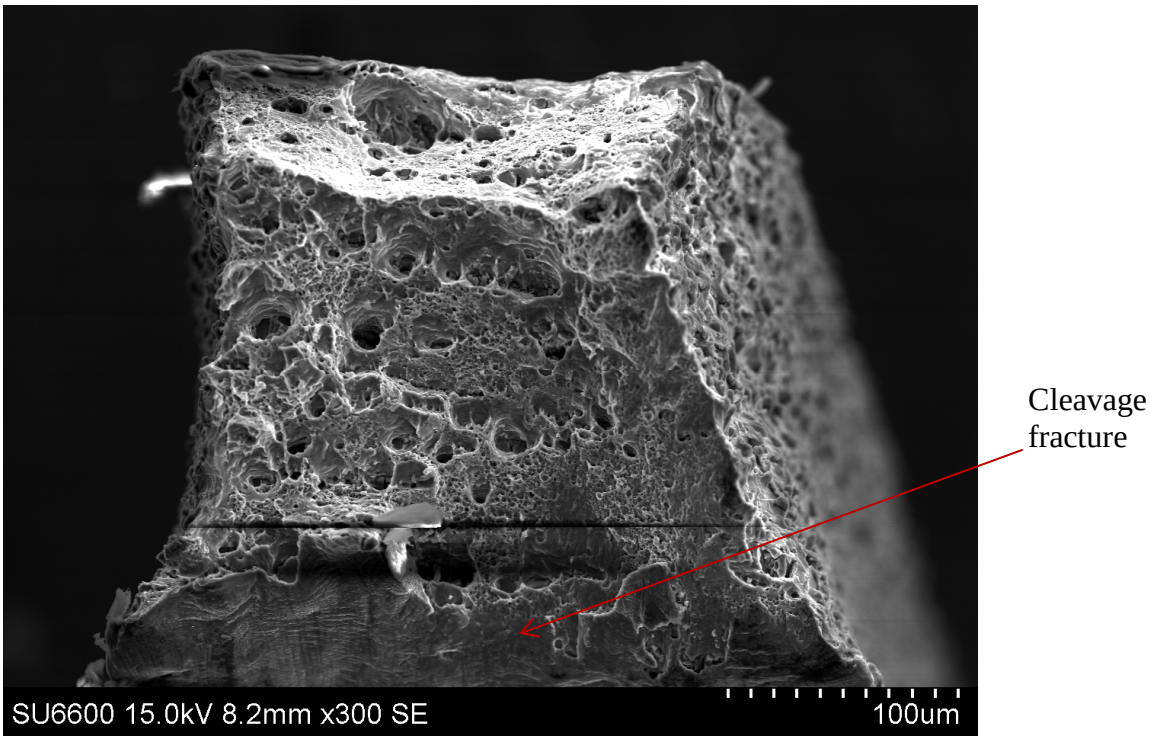

Figure 94. Fractograph of micro tensile specimen obtained from untreated sensitized 5456 at a depth of 1.686 mm below the surface at 300X

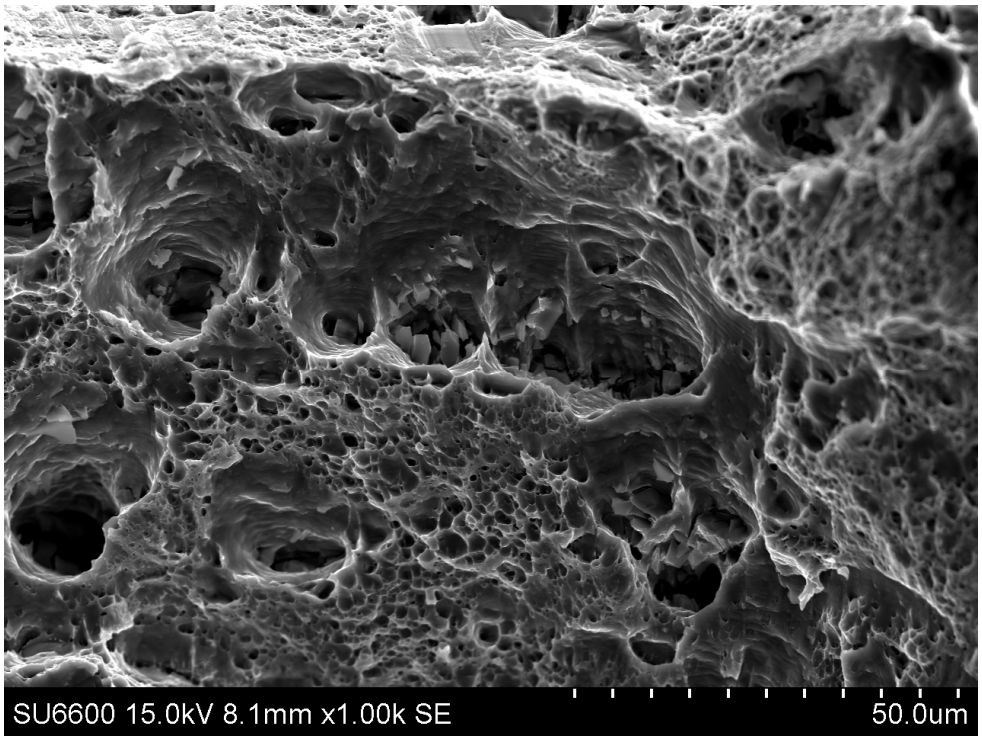

Figure 95. Fractograph of micro tensile specimen obtained from untreated sensitized 5456 at a depth of 1.686 mm below the UIT surface at 1000X

5.2.4 Intergranular Corrosion Testing

The susceptibility of UIT and untreated sensitized 5456 to intergranular corrosion was tested in accordance with ASTM G67 and a modified ASTM G67 test as described in section 1.2 to isolate the effects of the UIT process on corrosion resistance. Standard ASTM G67 testing results were mixed. The results given in Table 8 show comparable mass loss for the UIT and untreated material. The mass loss for one UIT sample is greater than the mass loss for the untreated samples. As previously noted in section 2.2, the standard ASTM G67 test involves immersing the specimen in HNO_3 for a period of 24 hours. Since the test involves immersing the

entire sample, the results likely include mass loss from the other surfaces and not just the UIT surface. Therefore it is difficult to isolate the mass loss at the UIT surface.

The results of the modified ASTM G67 testing also show varied results for the UIT material and untreated material. One UIT sample exhibited greater mass loss than an untreated sample. The mass loss measured in milligrams per cm^2 is shown in Table 8 for UIT and untreated samples. The area of exposure was a circular area with a radius of 0.5 cm thus the total area is ~ 0.80 cm^2. The mass loss values are 25.5 mg/cm^2 and 33.1 mg/cm^2 for the UIT material. The untreated material has mass loss values of 30.6 mg/cm^2 and 54.8 mg/cm^2.

Table 8. Results of intergranular corrosion testing for UIT treated sensitized 5456 and untreated sensitized 5456 using standard and modified ASTM G67 test

Sample	**Mass Loss mg/cm^2**	
Standard ASTM G67 Testing		
UIT sensitized 5456	59.62	56.73
Untreated sensitized 5456	56.21	56.91
Modified ASTM G67 Testing		
UIT sensitized 5456	25.5	33.1
Untreated sensitized 5456	30.6	54.8

5.2.5 Scanning Electron Microscopy of Intergranular Corrosion Tested Specimens

The planar sections of standard ASTM G67 tested specimens were examined in the SEM to observe the extent of corrosion and depth of attack on the surface. The specimens were observed at various magnifications. Figure 96 shows the planar micrographs for the UIT treated material at 1000X and 2000X magnifications. Figure 97 shows the planar micrograph for the untreated material at the same magnifications. The micrographs show intergranular attack along the grain boundaries in both the UIT and untreated specimens. The results are comparable with slightly wider fissures in the untreated material. From the micrographs, the fissures in the untreated material are ~ 11.6 µm wide while the fissures in the UIT material are ~ 5.8 µm wide. Both specimens also exhibited a number of pits within the grains. The pits do not appear to be more prevalent in one specimen as compared to the other specimen. As noted in Table 8, the mass loss results are comparable for both UIT and untreated materials.

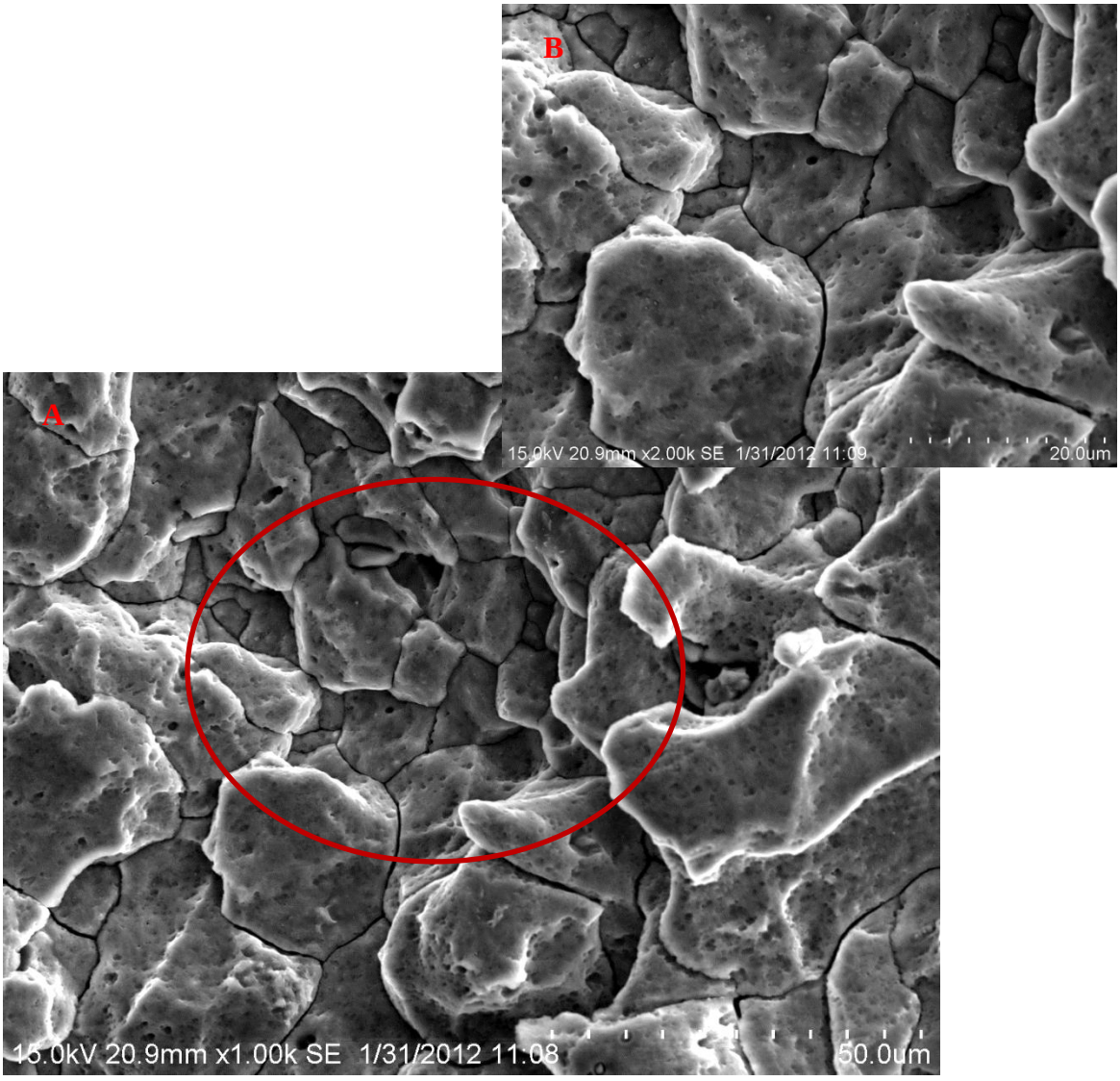

Figure 96. Scanning electron microscopy image showing the planar orientation of UIT treated sensitized 5456 tested for intergranular corrosion at 1000X (A) and 2000X (B), standard ASTM G67 test

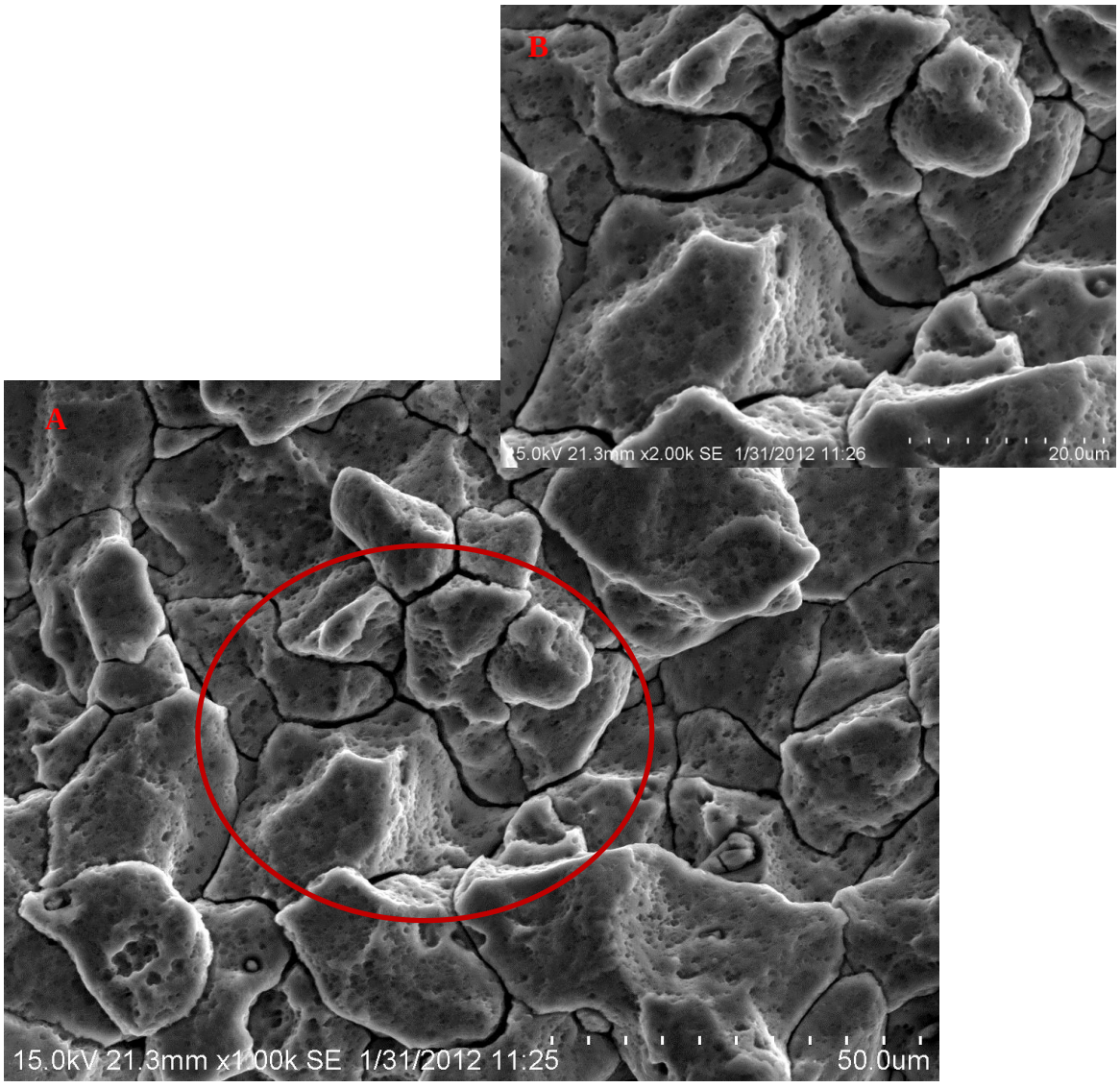

Figure 97. Scanning electron microscopy image showing the planar orientation of untreated sensitized 5456 tested for intergranular corrosion at 1000X and 2000X, standard ASTM G67 test

The planar and transverse cross sections of modified corrosion tested specimens were also examined in the SEM to observe the corrosive and depth of attack on the surface. The transverse micrographs were examined in backscatter mode to eliminate charging due to the mounts. The planar micrographs indicate that the UIT treated samples experienced worse attack on the surface grains as compared to the untreated sensitized material. The corrosive attack resulted in larger and wider fissures, ~ 17.4 µm, between grains as shown in Figure 98 at magnifications of 1000X and 2000X. Figure 99 shows the planar micrograph of the untreated sensitized material. Both micrographs show that the corrosive attack is along the grain boundaries. Both micrographs also show that the corroded surface contains a number of pits which appear to be more prevalent in the UIT material. The micrographs obtained in the transverse cross section show a deeper penetration of corrosive attack for the untreated sensitized material as compared to the UIT treated material. Examination of the transverse micrographs show that the corrosive attack on both the UIT and untreated material resulted in fine secondary cracks. Figures 100 and 101 show the transverse micrographs of the UIT treated and untreated sensitized material, respectively at 1000X. From the micrographs, the depth of corrosive attack in the UIT treated sample measures ~28.0 µm. In comparison, the depth of corrosive attack in the untreated sensitized material is ~37.4 µm.

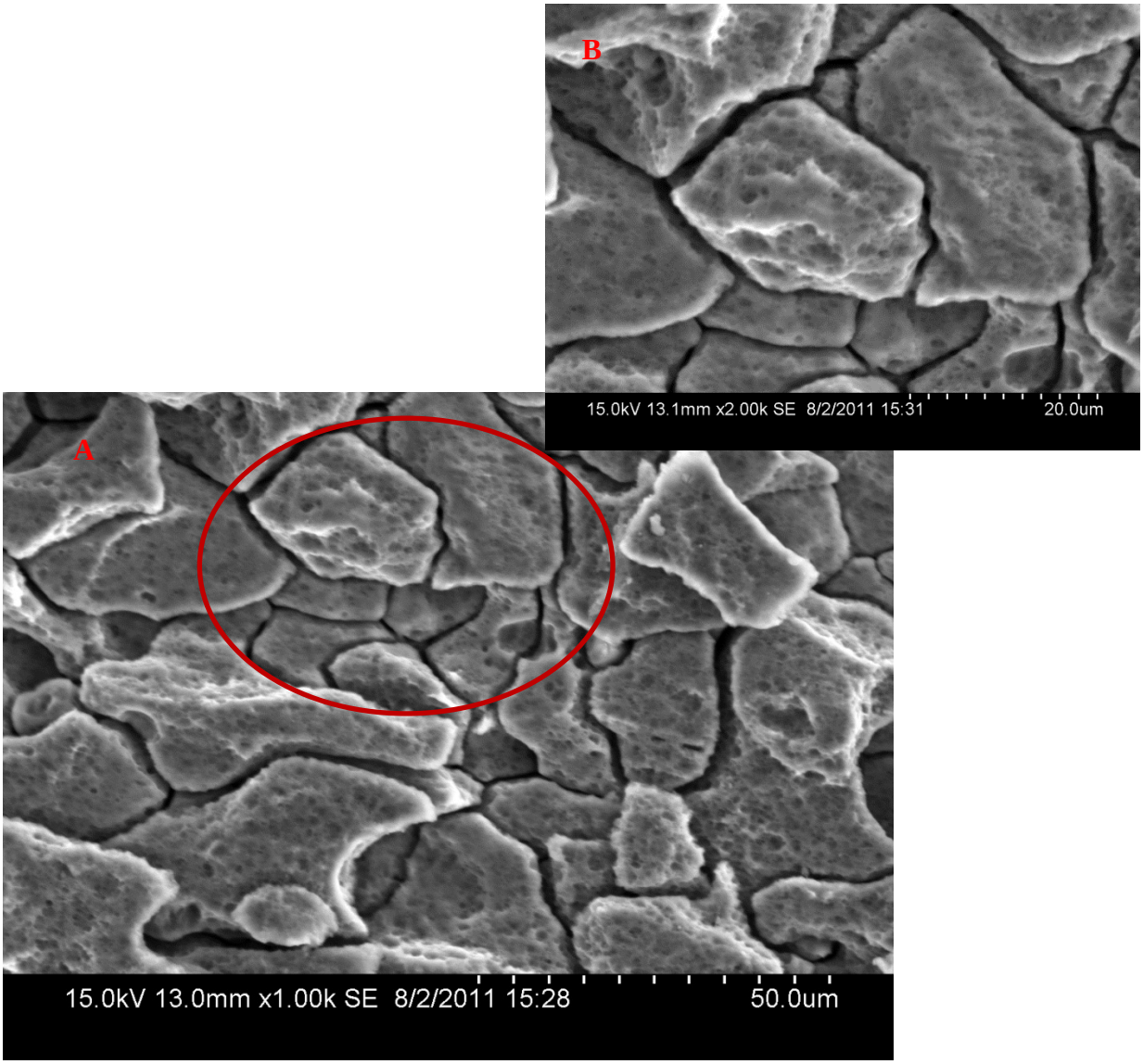

Figure 98. Scanning electron microscopy image showing the planar orientation of UIT treated sensitized 5456 tested for intergranular corrosion at 1000X (A) and 2000X (B), modified ASTM G67 test

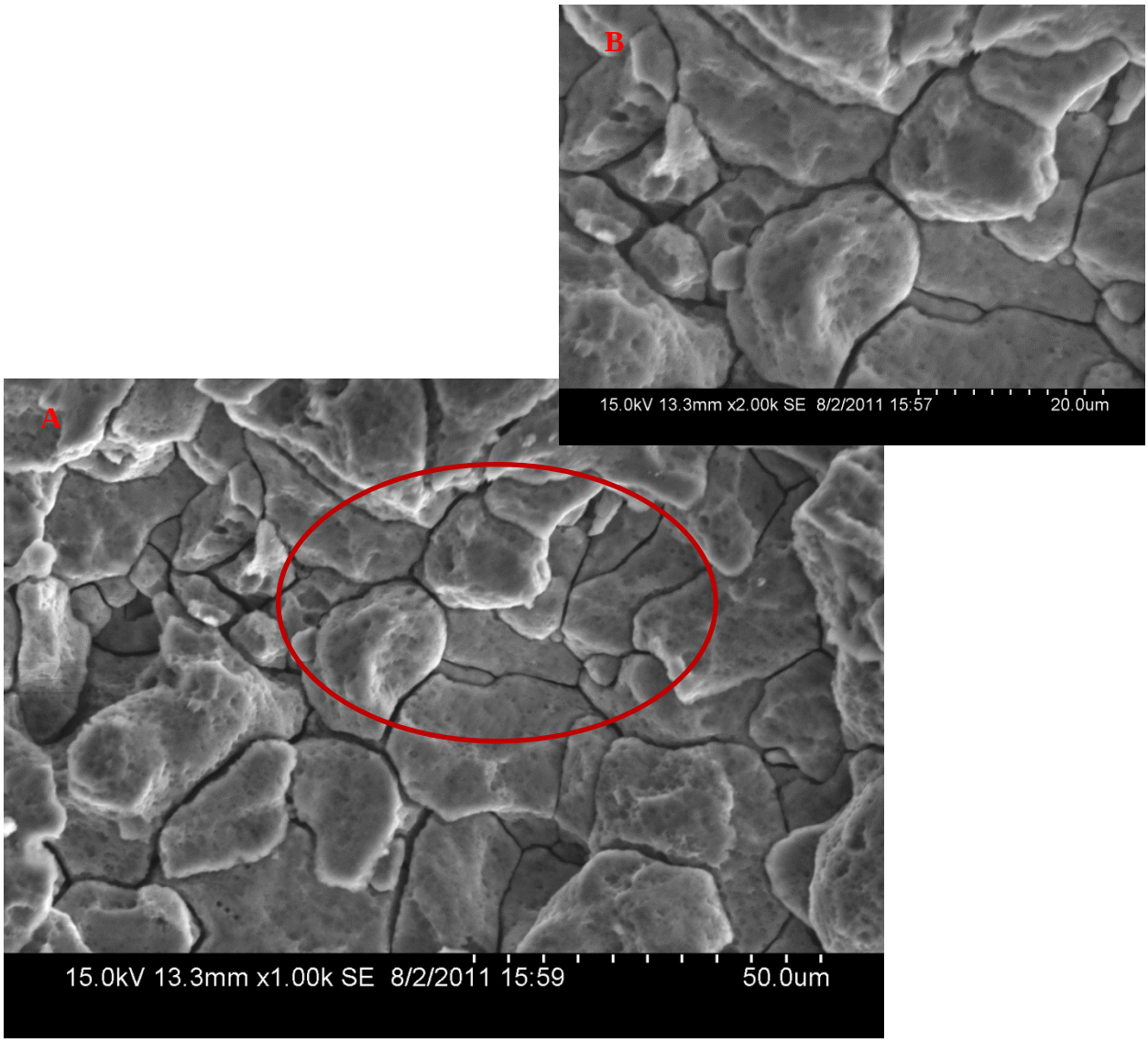

Figure 99. Scanning electron microscopy image showing the planar orientation of untreated sensitized 5456 tested for intergranular corrosion at 1000X (A) and 2000X (B), modified ASTM G67 test

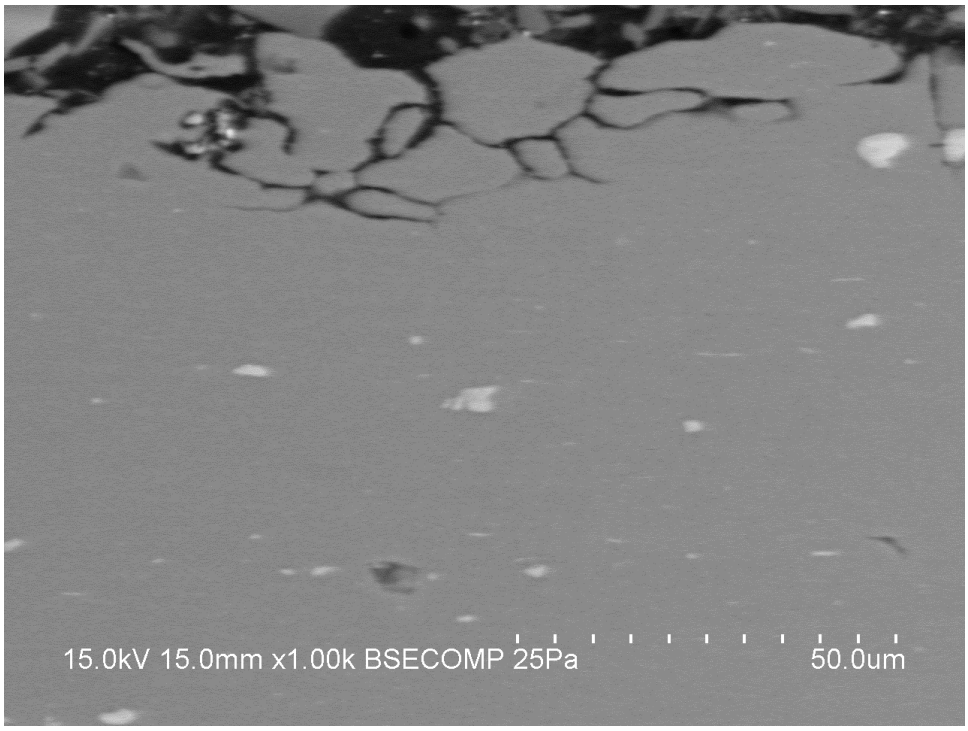

Figure 100. Scanning electron microscopy image showing the transverse cross section of UIT treated sensitized 5456 tested for intergranular corrosion at 1000X

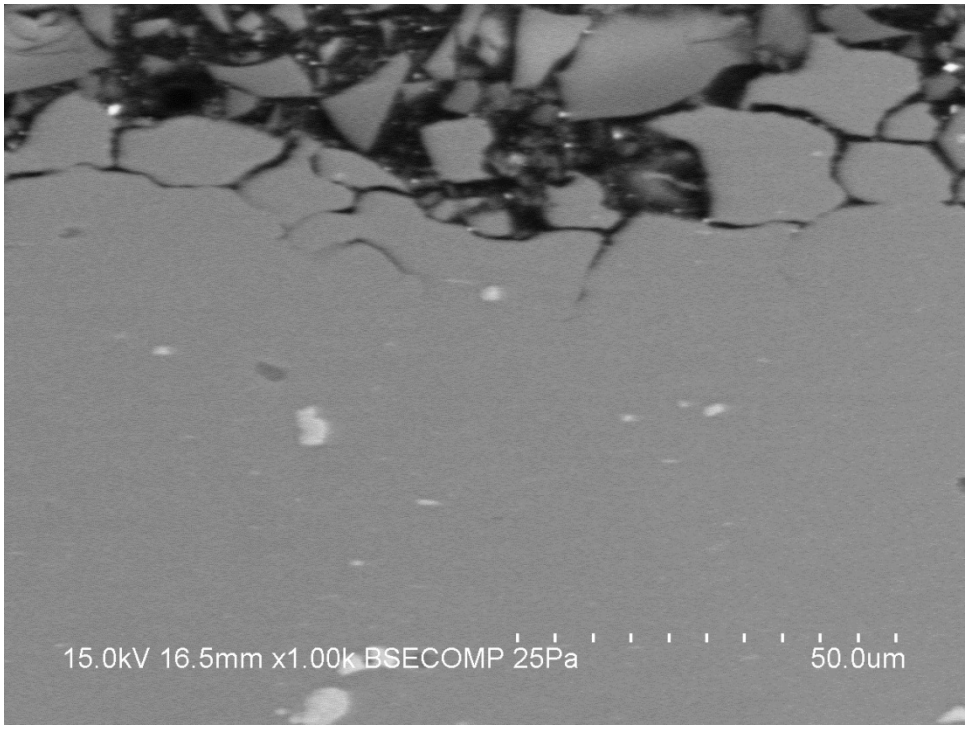

Figure 101. Scanning electron microscopy image showing the transverse cross section of untreated sensitized 5456 tested for intergranular corrosion at 1000X

5.2.6 Transmission Electron Microscopy of Intergranular Corrosion Tested Specimens

Transmission electron microscopy was used to investigate the microstructure of the deformed UIT surface after modified corrosion testing. Samples were obtained at the UIT surface and prepared by polishing only on one side to preserve the corroded UIT surface. These samples were mechanically polished followed by ion milling and plasma cleaning. The micrographs show the presence of nanocrystalline grains following corrosion testing. Figure 102 shows nanocrystalline grains with Moiré fringes and a number of overlapping grains with submicron grains. The associated diffraction pattern shown as an inset to Figure 102 shows a typical ring-like pattern characteristic of nanocrystalline grains. There is no β phase present at the grain boundaries of the submicron grains which should be expected since corrosion testing in HNO_3 results in the β phase to fall out. Figure 103 shows submicrometer grains with features at the grain boundaries that appear to be similar to the fissures observed in the SEM micrographs in Figures 96 to 99. The fissures are due to intergranular attack and β phase fall out. Figure 104 shows the presence of features that appear to be aluminum oxide (Al_2O_3) particles along the grain boundaries. It is noted that EDS was not available to confirm whether the particles are Al_2O_3, however these findings are consistent with the work by R. Jones et al. [83] which is discuss in section 5.3.

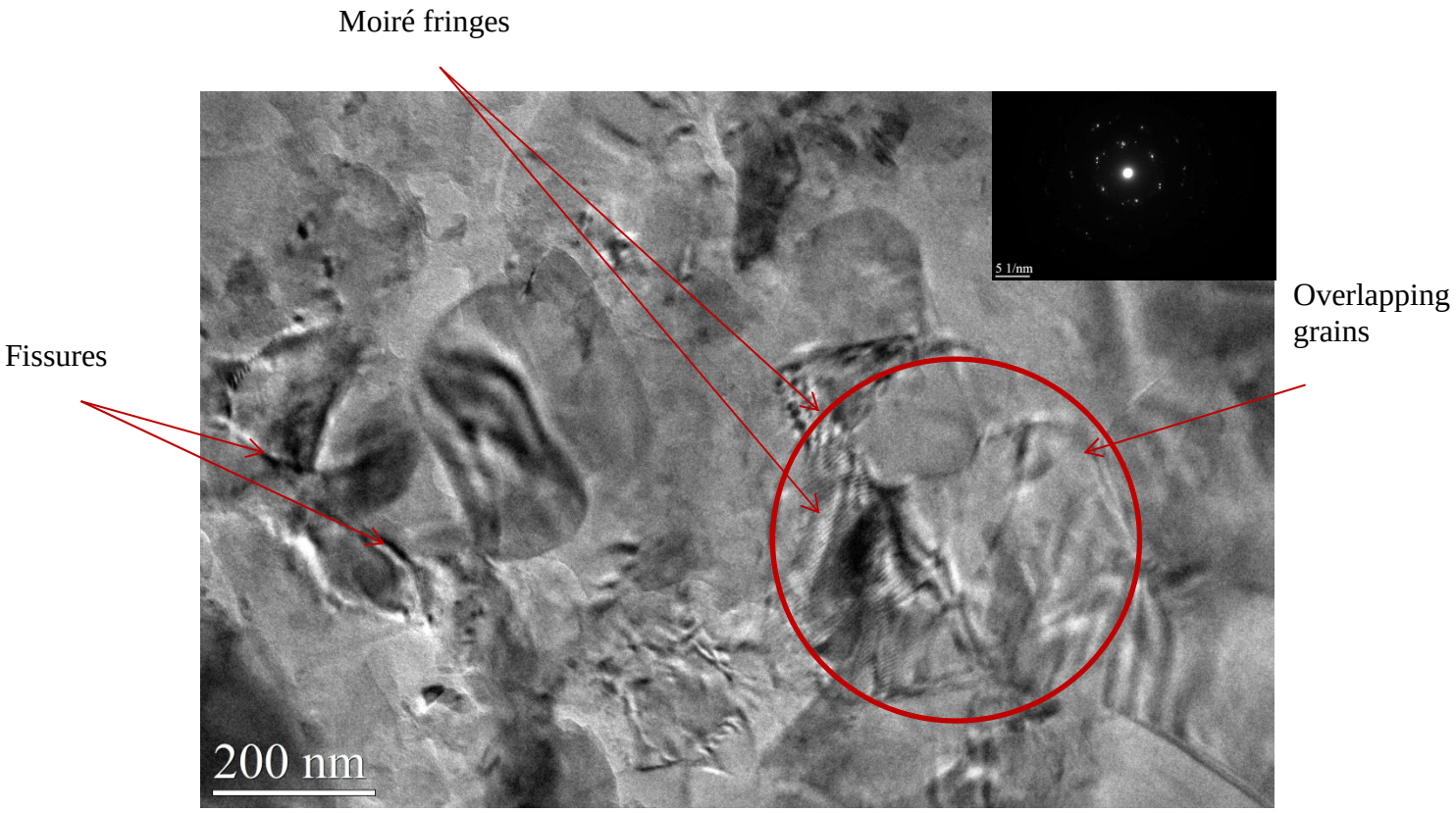

Figure 102. Transmission electron micrograph of UIT material at the surface after ASTM G67 corrosion testing showing nanocrystalline and submicrometer grains

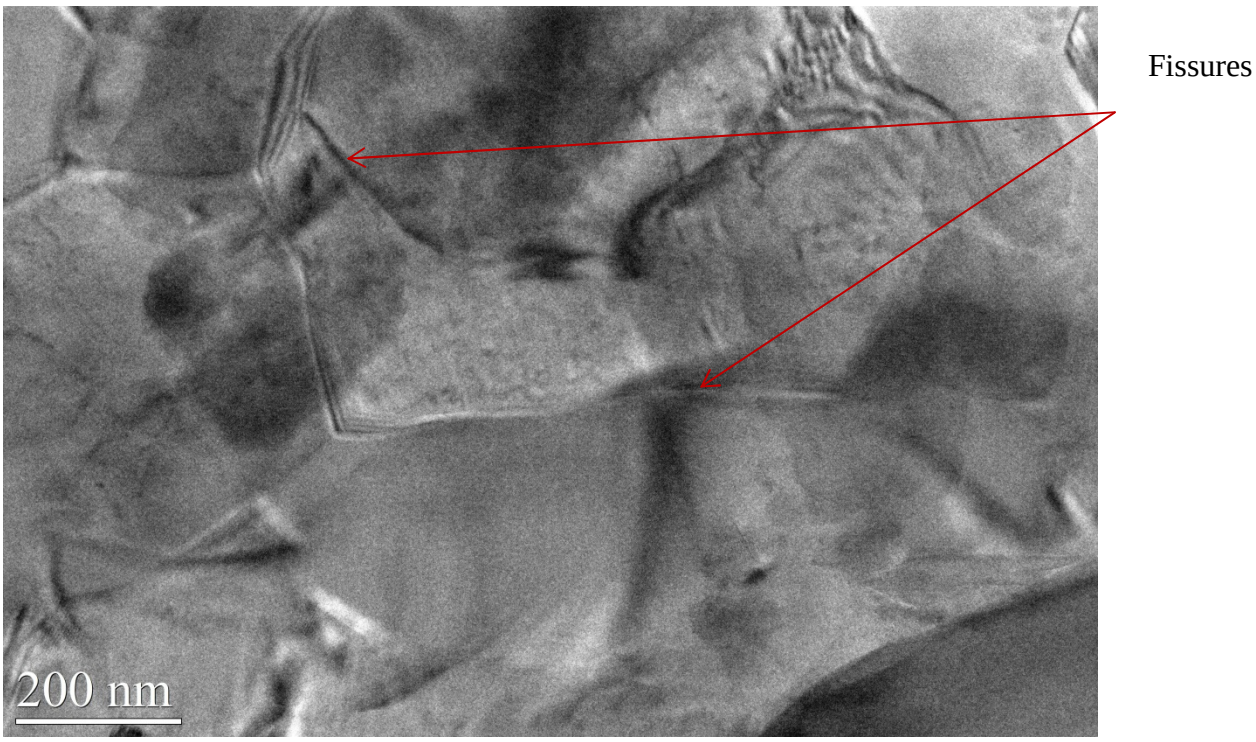

Figure 103. Transmission electron micrograph of UIT material at the surface after ASTM G67 corrosion testing showing nanocrystalline and submicrometer grains

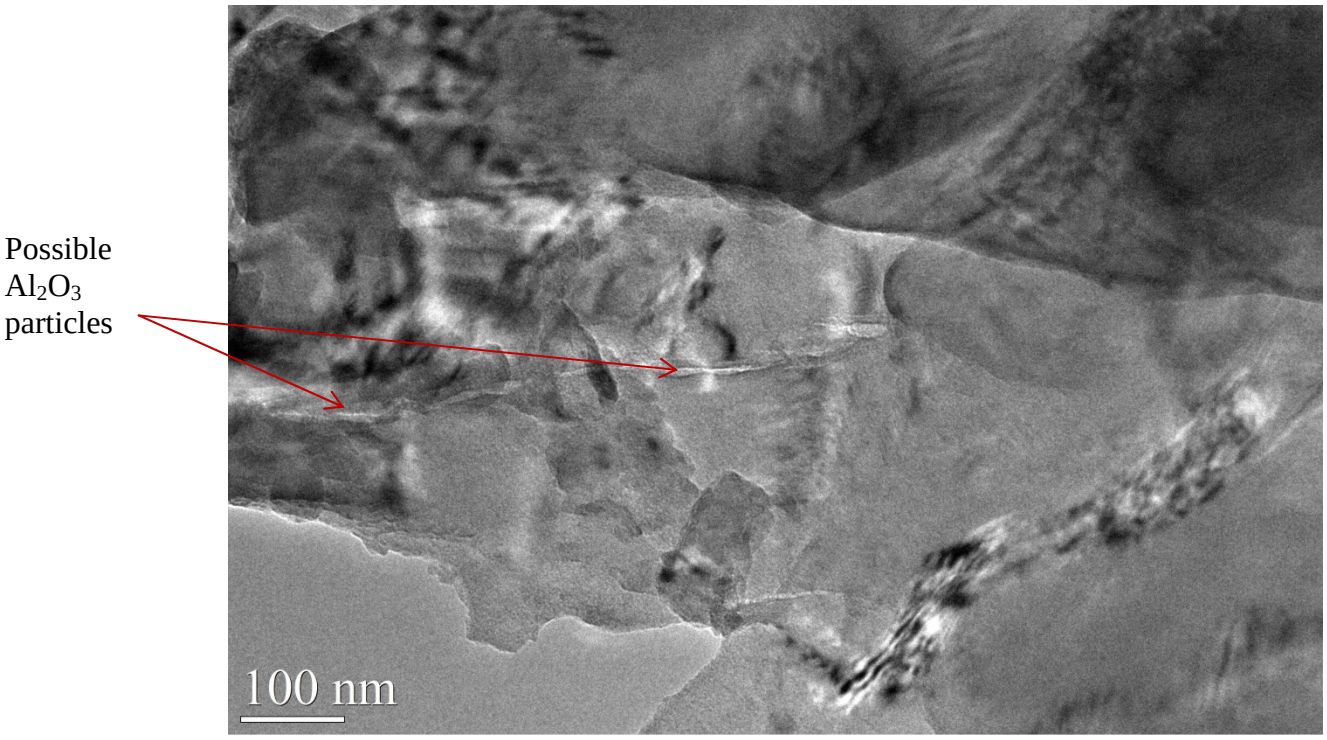

Figure 104. Transmission electron micrograph of UIT material at the surface after ASTM G67 corrosion testing showing intergranular oxide particles along the grain boundaries

5.3 Discussion

Research has shown that SPD processes can improve the mechanical properties of various metals due to the formation of ultrafine grains or nanocrystalline grains [3,25,29]. As previously noted in section 5.1, M. Fu et al. reported that ECAP processing results in a significant increase in hardness properties in 6061 aluminum due to grain refinement induced by the ECAP process [80]. The results of Vickers microhardness testing in this thesis show an increase in hardness with the highest values near the UIT surface followed by a decrease in hardness which starts to become constant at 2.4 mm below the surface. The results concur with our TEM examination which shows the formation of a nanocrystalline layer at the surface,

Figures 44 and 45, and the formation of subgrains below the nanocrystalline layer, Figure 51. The increase in hardness may be attributed to the grain refinement induced by the UIT process. As previously noted in section 4.2.1.1, UIT results in the formation of nanocrystalline grains near the surface. Both M. Fu et al. and J. May et al. agree that increased hardness in aluminum alloys is due to grain refinement, however J. May et al. suggest that the higher hardness may also be attributed to dislocation and subgrain hardening [57,80]. J. May et al. suggest that in Al-Mg alloys, hardening is due to a number of factors [57]. For conventionally processed materials that do not exhibit ultrafine grains or nanocrystalline grains, hardness is due to solid solution hardening in which the strength τ depends on the concentration of solute atoms *c*, as $\tau \sim c^q$, where q is an exponential factor on the order of 0.34 [57]. Upon severe plastic deformation after one ECAP pass, the additional hardening is due to dislocation and subgrain hardening. After additional ECAP passes, the additional hardening is due to grain refinement. J. May et al. state that the exponent *q* does not change with increasing ECAP passes therefore the contribution of dislocation hardening and grain refinement are weakly dependent on the concentration of solute atoms [57].

The results of micro specimen tensile testing in this work show that the highest strength is achieved near the UIT surface where the highest hardness is also observed. The yield strength value of 290 MPa at the UIT surface is less than the yield strength of 380 MPa for Al-3Mg casting subject to four passes of ECAP [84]; however it is higher than typical yield strength values for sensitized 5456 [85]. With increasing depth below the UIT surface, the strength values decrease and become

constant 2.24 mm below the treated surface. The yield strength values, 171- and 192 MPa for specimens obtained at depths of 2.24 mm are comparable to the yield strength values obtained for conventional specimen size tensile testing of sensitized 5456 without UIT in accordance with ASTM E8 [86]. The typical yield strength values for sensitized 5456 are 189- and 192 MPa [85]. For unsensitized material, the typical yield strength values are 271- and 286 MPa. The results indicate that with the UIT process, the yield strength can be substantially increased by 60 to 100 MPa for sensitized materials. The UIT process would also be expected to increase the yield strength in unsensitized material as the results of this work show that the yield strength near the surface for sensitized material is ~50 MPa greater than unsensitized material.

The high strength near the surface is attributed to the formation of nanocrystalline grains. As noted in section 5.1, strength due to grain refinement in Al-Mg alloys is important because of the Hall-Petch relationship. Among the commercially available aluminum alloys, the Al-Mg alloys exhibit the largest grain size dependence on yield strength because of the stress required to initiate plastic flow in Al-Mg alloys [84]. In severely plastically deformed alloys processed at ambient temperatures, the strength may be influenced by the formation of dislocations, long range internal stresses and low angle grain boundaries. Thus, there can be a deviation from the Hall-Petch relationship with submicron grain sizes which would result in a lower rate of increase in the yield stress. To study the relationship between the Hall-Petch equation and Al-Mg alloys with submicron grain size, M. Furukawa et al. examined the microhardness data of material subject to SPD [78,87].

In the absence of appreciable work hardening, the hardness of a material follows the relationship of $H_v \sim 3\sigma_y$ [87]. From this relationship, the Hall-Petch equation may be rewritten as follows [87]:

$$H_v = H_o + k_H d^{-1/2} \quad \textbf{(19)}$$

where H_v is the Vicker's hardness value, H_o and k_H are hardness constants and d is the grain diameter [87]. Using this relationship, M. Furukawa et al. found that for an Al-3Mg alloy subject to ECAP and HPT where the smallest grain size is 0.2 µm (200 nm) and 0.09 µm (90 nm), respectively, the data followed the Hall-Petch equation. J. Hayes et al. found that with Al-3Mg alloys subject to ECAP and subsequent annealing between 100 to 300°C, the yield stress follows the Hall-Petch relationship after grain refinement to submicron grain sizes ranging between 0.2 to 11 µm (200 to 1100 nm) [88]. The results by J. Hayes et al. also suggest that the yield strength increase in SPD materials is dominated by grain boundary spacing width. The results of micro specimen tensile testing and Vickers hardness testing presented in this thesis deviate from the relationship $H_v \sim 3\sigma_y$. The calculated values of H_v/σ_y near the treated surface are 4.5, 4.6, 4.4, and 4.3. These ratios suggest that a deviation from the Hall-Petch relation may occur for nanocrystalline grains that are less than 90 nanometers in size. The results of TEM as discussed in section 4.2.1.1 show that at the UIT surface, nanocrystalline grains range in size from 2 to 200 nm.

The primary strengthening mechanism in Al-Mg alloys is by solute strengthening. The primary alloying element in Al-Mg alloys is Mg which influences

the stacking-fault energy. Therefore the strength, the recovery and recrystallization characteristics of aluminum are strongly controlled by Mg incorporation [39]. Magnesium also acts as a point defect within the crystal lattice and as an obstacle to dislocation motion. In metals, the strength is determined by the applied stress required to overcome the obstacles that interfere with dislocation motion [39,73]. J. Gubicza et al. reports that SPD is more effective in grain refinement and increasing the dislocation density of aluminum alloys if the Mg content is high [39]. During deformation, Mg also acts to hinder the annihilation of dislocations because it tends to be located preferentially around the dislocations and exerts a pinning effect on the dislocations. This leads to an increase in dislocation density (dislocation-dislocation interaction) and an increase in the yield strength [39]. As discussed in section 4.2.1.2, the dislocation density of the UIT treated material is higher than that in the untreated material which is attributed to the severe deformation imparted by the UIT process. In metals, grain refinement through SPD occurs by the arrangement of dislocations into cell walls so that the higher dislocation density results in a decrease in the crystallite size for higher Mg concentration [39].

The fractographs shown in Figures 90 and 92 show that the micro specimen tensiles exhibit necking before failure. All the specimens failed in a ductile, transgranular manner consisting of numerous dimples which are the result of void nucleation and subsequent coalescence. A ductile failure mode consisting of dimples and transgranular failure is typical for Al-Mg alloys [89] and has been reported by D. Fang et al. for Al-3Mg subject to the ECAP process [84]. A comparison of the fractographs show that the dimple sizes are smaller for the specimen obtained closest

to the UIT surface at a depth of 0.150 mm. This indicates that the dimple decreases with increasing depth from the treated surface. Similar findings were observed in the tensile testing of Al-3Mg subjected to ECAP; the dimples size continued to decrease with increasing ECAP passes [84].

As previously noted in section 1.3, Al-Mg alloys containing more than 3 wt.% Mg can sensitize when exposed to elevated temperatures for a prolonged period of time and become susceptible to SCC and IGC. Because the continuous β phase formation at the grain boundaries due to sensitization is anodic to the metal matrix, galvanic attack occurs at the grain boundaries. Galvanic corrosion or dissimilar metal corrosion occurs when two dissimilar metals with different electrochemical potentials are coupled in a corrosive electrolyte. The metal that is more anodic will corrode first. As previously mentioned in section 1.3, researchers have shown that β phase precipitation at the grain boundaries is related to grain boundary crystallographic orientation [15, 17]. Low angle grain boundaries are more resistant to SCC and IGC than high angle grain boundaries. High angle grain boundaries are boundaries of high surface energy which serve as preferential sites for solid state reactions such as diffusion, phase transformations, and precipitation [24]. Grain boundary orientation maps of both the UIT and untreated material showed mainly high angle grain boundaries (see section 3.2.4) with similar fractions for the UIT and untreated material. Based on the EBSD results, it is not a surprise that the mass losses were somewhat comparable.

The micrographs of the specimens tested for IGC susceptibly shown in Figures 96 to 99 clearly show that the corrosive attack is intergranular for both the

UIT and untreated material. The results are varied when comparing the specimens tested with the standard ASTM G67 test and the modified test. The specimens tested in accordance with the standard ASTM G67 test resulted in comparable mass loss. The modified corrosion test also shows comparable mass loss for the UIT and untreated material, however the attack was more aggressive and deeper in the untreated specimens. The micrographs also show the presence of pitting within the grains which appears to be more prevalent in the UIT material than the untreated material. The intergranular attack confirms that β phase is present at the grain boundaries below the deformation layer. The ASTM G67 test involves the use of concentrated HNO_3 which dissolves the β phase along the grain boundaries. The preferential attack results in corrosion at the grain boundaries causing the grains to fall out. From the modified tests, both Figures 98 and 99 show intergranular attack at the grain boundaries, Figure 101 shows that the depth of attack in the untreated material is deeper than the UIT material shown in Figure 100. The comparable mass loss results for both UIT and untreated material and the results of SEM analysis suggest that the UIT treated samples are not immune to intergranular corrosion. Both the standard and modified ASTM G67 tests show that the corrosive attack extends below the deformation layer as shown in Figures 100 and 101. The depth of attack was measured to be ~ 28.0 µm while the deformation layer is approximately 10 to 18 µm. It is not surprising that intergranular corrosion extended beyond the deformation layer. As shown in Figures 13 and 14 in section 3.2.1, the SEM micrographs show that the deformation layer is characterized by tearing and voids. These features allow for the corrosive solution to penetrate below the deformation layer.

Transmission electron microscopy analysis confirms the presence of nanocrystalline grains following intergranular corrosion testing. However, the microstructure is characterized by both nanocrystalline grains and submicron grains with a number of overlapping grains. There are features along the grain boundaries of the submicron grains that appear to be similar to the fissures observed in the SEM micrographs of Figures 96 to 99. Additional TEM analysis is required to confirm if these are the same features. Figure 104 shows the presence of features at the grain boundary that appear to be Al_2O_3 which could be converted from the β phase during intergranular corrosion of Al-Mg [83].

The ASTM G67 test is an unloaded accelerated corrosion test, however there was some secondary cracking observed in both the UIT and untreated material. These results suggest that in a corrosive environment under a loading condition, SCC would occur in both the UIT and untreated materials. The SCC is strongly influenced by the presence of the β phase even for the UIT treated material. As previously noted, below the physically deformed UIT surface, β phase precipitates are still present in the material. Stress corrosion cracking and crack growth in sensitized Al-Mg alloys has been attributed to either an anodic dissolution or hydrogen induced crack growth mechanism [18]. The β phase may also act as a catalyst to generate and enhance the ingress of hydrogen [18]. R. Jones et al. also suggest that when tested in artificial seawater, 3.5% NaCl + 0.1 M K_2CrO_4, the β phase particles are converted to Al_2O_3, oxide particles [83]. When H absorption occurs during the corrosion of the β phase and cracking occurs, the crack traverses through or around the Al_2O_3 particle.

The crack growth between the Al_2O_3 particles is thought to result from the uptake of hydrogen and hydrogen induced crack growth [83].

Research to investigate the IGC of nanocrystalline Al-Mg alloys is limited and the results are varied. E. Sikora et al. reported that nanocrystalline 5083 aluminum was not resistant to IGC, however conventional 5083 was resistant to IGC [90]. The nanocrystalline 5083 was synthesized by cryomilling of powers and subsequent consolidation to form a material with grain sizes of 80 to 200 nm [90]. E. Sikora et al. tested both conventional and nanocrystalline 5083 aluminum in accordance with ASTM G67 and found that the nanocrystalline 5083 was not resistant to intergranular corrosion; however the conventional 5083 was resistant. The researchers also performed additional testing at 50°C for two minutes and found that the nanocrystalline 5083 was severely corroded at the grain boundaries while the grain boundaries of the conventional 5083 were intact [90]. Conversely, E. Kus et al., reported that nanocrystalline 5083, which was also consolidated from a cryomilled prealloy, was more resistant to IGC than conventional 5083 wrought product [91]. ASTM G67 testing of nanocrystalline 5083 resulted in a mass loss of 8.39 mg/cm^2 and 7.89 mg/cm^2 while the mass loss for conventional 5083 was 18.82 mg/cm^2 [91] . Scanning electron microscopy examination of the tested specimens showed that nanocrystalline 5083 had rough circular holes spread over the entire surface while the conventional 5083 exhibited attack along the grain boundaries. The results of the testing of 5083 aluminum concur with the work by E. Kus et al. [91]. Although, intergranular corrosion cracking was observed in both UIT and untreated material in this thesis work, the mass loss was somewhat less for the UIT material which

suggests that the nanocrystalline layer may result in some improvement in corrosion resistance. It is noted that the deformation imparted by the UIT process is random and results in gaps of treated and untreated surface area which may result in random localized corrosive attack on the surface.

The micrographs of the standard corrosion tested specimens showed comparable amounts of pits forming within the grains, however the modified corrosion tested specimens showed varied results. The pitting appeared to be more prevalent in the UIT specimens. Research to examine pitting corrosion in nanocrystalline and conventional Al-Mg is also varied. Research by E. Sikora et al. to examine the pitting corrosion of nanocrystalline Al-Mg materials show that nanocrystalline 5083 is more resistant to pitting than conventional 5083 [90]. The pits on the nanocrystalline 5083 were smaller which may be due to pitting occurring only around inclusions and that the pit size depended on the inclusion size [90]. The nanocrystalline material had smaller inclusions than the conventional material which resulted in smaller pits. The pitting observations were based on cyclic polarization experiments in which the specimens were immersed in 0.1 M sodium sulfate ($NaSO_4$) solution with chloride concentrations varying from 0.005 M to 1.0 M. In a related study, M. Sharma and C. Ziemian reported superior pitting resistance in nanocrystalline Al-8.6Mg and Al-Mg7.5 as compared to conventional 5083 in short term alternate immersion SCC testing in 3.5% sodium chloride (NaCl) [92]. However, for long term (1 to 6 months) SCC alternate immersion testing, deeper pits developed in the nanocrystalline Al-7.5Mg alloy. With increasing testing periods, the pitting depths for all the alloys were comparable. Conversely, E. Kus et al. reported

that when subjected to 0.5 NaCl, pits that formed on conventional 5083 were more numerous however smaller than the pits that formed on nanocrystalline 5083 [91].

5.4 Summary

The results of materials properties testing can be summarized as follows:

- The highest hardness is near the UIT surface, 1.13 GPa at a depth of 0.141 mm below the surface and becomes constant at the depth of 2.24 mm below the treated surface. The hardness values measured at the UIT surface show some variability with values ranging from 1.08 GPa to 0.92 GPa.
- The highest yield strength is at the UIT surface, 290 MPa, however the results show variability. A yield strength of 253 MPa was observed 2.24 mm below the treated surface.
- The tensile fracture mode was transgranular ductile fracture with micro void coalescence and dimples for specimens obtained at the surface and below the surface
- Standard ASTM G67 testing for intergranular corrosion susceptibility showed comparable results between UIT and untreated material with mass losses ranging from 56.21 mg/cm^2 to 59.62 mg/cm^2. Modified ASTM G67 testing showed mixed results for UIT and untreated material; 25.5 mg/cm^2 and 33.1 mg/cm^2 (UIT) and 30.6 mg/cm^2 and 54.8 mg/cm^2 (untreated).
- Corrosive attack was intergranular for both UIT and untreated material. Wider fissures were noted in the untreated corrosion specimens for the standard ASTM G67 testing; however, wider fissures were noted for the UIT corrosion specimens for the modified ASTM G67 testing. Pitting was

observed within the grains and appeared to be more prevalent in the UIT material (from modified ASTM G67 testing).

- Depth of corrosive attack is deeper in the untreated material, ~ 37.4 µm as compared to UIT material, ~ 28 µm.

Chapter 6: Characterization and Analysis of Deformation and Stress During the UIT Process

6.1 Introduction

This chapter presents the study of UIT processing parameters on sensitized 5456 aluminum and the effects on the residual stresses through numerical simulation of the deformation process using DEFORM 3D™ software. The surface roughness due to the deformation imparted by UIT is investigated by confocal microscopy. The surface roughness measurements for untreated material were used as inputs for the deformation process model and the results of the model are compared to analytical data obtained through X-ray diffraction measurements.

Confocal laser scanning microscopy (CLSM) is an advanced technique based on confocal microscopy that allows for determination of a specimens surface roughness in 3D. The confocal microscope is an optical microscope that has the capability to create a bright image of the in-focus region of the specimen while causing out-of-focus regions to appear dark [93]. The confocal microscope assembles a series of optical sections each at a different focal plane to create a "through-focus" image which has an indefinite depth of field [93]. The ability to create an image with an indefinite depth of field allows for the imaging of non-flat specimens and can be used to measure the surface roughness of a specimen.

The data and parameters that can be obtained using 3D CLSM include the average roughness, S_a, and root mean square roughness, S_q. These parameters are evaluated over the complete 3D surface. Mathematically, S_a, and S_q, are evaluated by the equations below [94]:

$$S_a = \iint_a |Z(x,y)| dxdy \quad \textbf{(20)}$$

$$S_q = \sqrt{\iint_a (Z(x,y))^2 \, dxdy} \quad \textbf{(21)}$$

where *x, y* are in the specimen plane and *z* is along the optical axis [94]. The maximum peak height or height of the highest peak is denoted as S_p, the maximum valley depth, the depth of the lowest point is S_v, usually indicated as a negative number. The maximum change in height of the surface, S_z, is found from $S_z = S_p - S_v$ [94].

DEFORM 3D is a finite element engineering software that can be used to simulate deformation, stress analysis, and complex heat transfer. DEFORM 3D is capable of modeling complex three dimensional material flow patterns and can be used to model complex interactions between deformation, temperature, and distortion. The software has been used to analyze three dimensional flow of complex metal forming processes such as forging, rolling, drawing, and extrusion [95]. To the best of this author's knowledge, this is the first time a numerical simulation of the UIT deformation process has been performed. Due to constraints on computational resources, the analysis was limited to only a few dozen cycles for a preliminary study.

Severe plastic deformation processes such as UIT and shot peening have been shown to impart deep compressive residual stresses into the surface of aluminum [96, 97,98]. The presence of compressive residual stresses have beneficial effects on

fatigue life and prevents tensile and corrosion cracks in structural parts [97,98]. The residual stresses of the UIT material as a function of depth are measured by standard XRD techniques.

The technique of residual stress measurements using XRD involves the determination of the strain in the surface layers of the material by measuring the shift in the position of the diffraction peak of the set of planes [99]. The strains are then converted into stresses analytically. The measurement of the diffraction peak shift in the selected set of planes is based on Bragg's law deduced from Equation 3. The changes in the interplanar spacing, *d*, can be determined using Bragg's law to obtain the elastic strain, ε [38]:

$$\varepsilon = \frac{d_n - d_o}{d_o} \quad \textbf{(22)}$$

where d_n is the spacing of the planes parallel to the bar axis under stress (n indicates that the reflecting plane normal is normal to the specimen surface) and d_o is the spacing of the same planes in the absence of stress [38]. The stress is evaluated from the measured strains using Young's modulus [E], Poisson's ratio [v], and taking into consideration the elastic anisotropy of the material. Using Equation 23, the stress in any chosen direction from the corresponding plane spacing can be determined from two measurements made in the plane normal to the surface and containing the direction of the stresses to be measured [38].

$$\sigma_{\phi} = \frac{E}{(1+\nu)sin^2\,\psi}\left(\frac{d_o - d_n}{d_n}\right) \quad \textbf{(23)}$$

Additional information regarding the determination of residual stresses using XRD can be found in *Elements of X-ray Diffraction* by B.D. Cullity [38].

6.2 Procedure and Results

6.2.1 Confocal Microscopy of UIT surface

Confocal microscopy measurements were obtained on both UIT and untreated material. Surface roughness measurements of three UIT samples were obtained using a Zeiss LSM 510 confocal microscope and Zeiss LSM 510 V.3.2 software over multiple areas of 1.8 mm x 1.8 mm on each sample. The smaller images were stitched together using the same software to form stitched images that measured 5 mm x 5 mm. The parameters that were obtained include S_a, S_q, S_p, S_v (absolute value), and S_z. Figure 105 shows the surface topography of two smaller surface areas prior to stitching the images together. The images clearly show the indentations produced by the UIT process. The average surface roughness values vary from 13.619 µm to 17.946 µm indicating variability on the UIT surface. The values for maximum peak height, S_p, also show variability with a large range between 117.977 µm to 68.179 µm (S_p). The maximum valley depth which measures the lowest point, S_v, maximum height, S_z, of the surfaces are comparable across the samples ranging between 52.765 µm to 65.265 µm (S_v) and 63.348 µm to 49.318 µm (S_z).

S_a = 17.946 µm
S_q = 22.415 µm
S_p = 117.977 µm
S_v = 52.765 µm
S_z = 63.348 µm

S_a = 13.619 µm
S_q = 17.203 µm
S_p = 68.179 µm
S_v = 65.265 µm
S_z = 49.318 µm

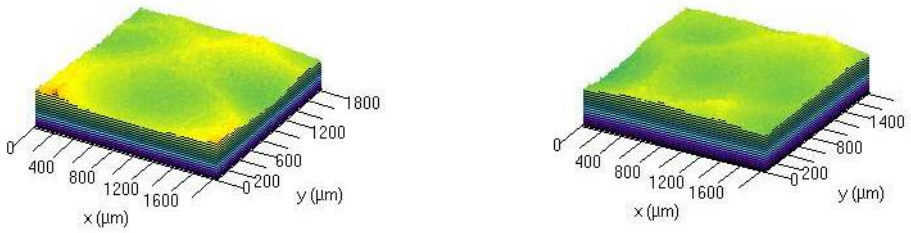

Figure 105. Confocal laser scanning microscopy of UIT surface over two 1.8 mm x 1.8 mm surface areas

The larger stitched images, Figure 106 show comparable surface roughness for two of the samples. From these two samples (A & B), the average surface roughness is 23.673 µm and 22.073 µm, respectively. There is variability in the maximum peak height and the maximum valley depth ranging from 101.369 µm to 68.198 µm (S_p) and 40.563 µm to 78.103 µm (S_v) , however the maximum height of the surfaces is comparable ranging between 87.892 µm to 95.969 µm (S_z). Sample A clearly shows the indentations produced by the UIT process. The results indicate that the average surface roughness from samples A and B are comparable to the UIT processing parameter amplitude of 22 µm.

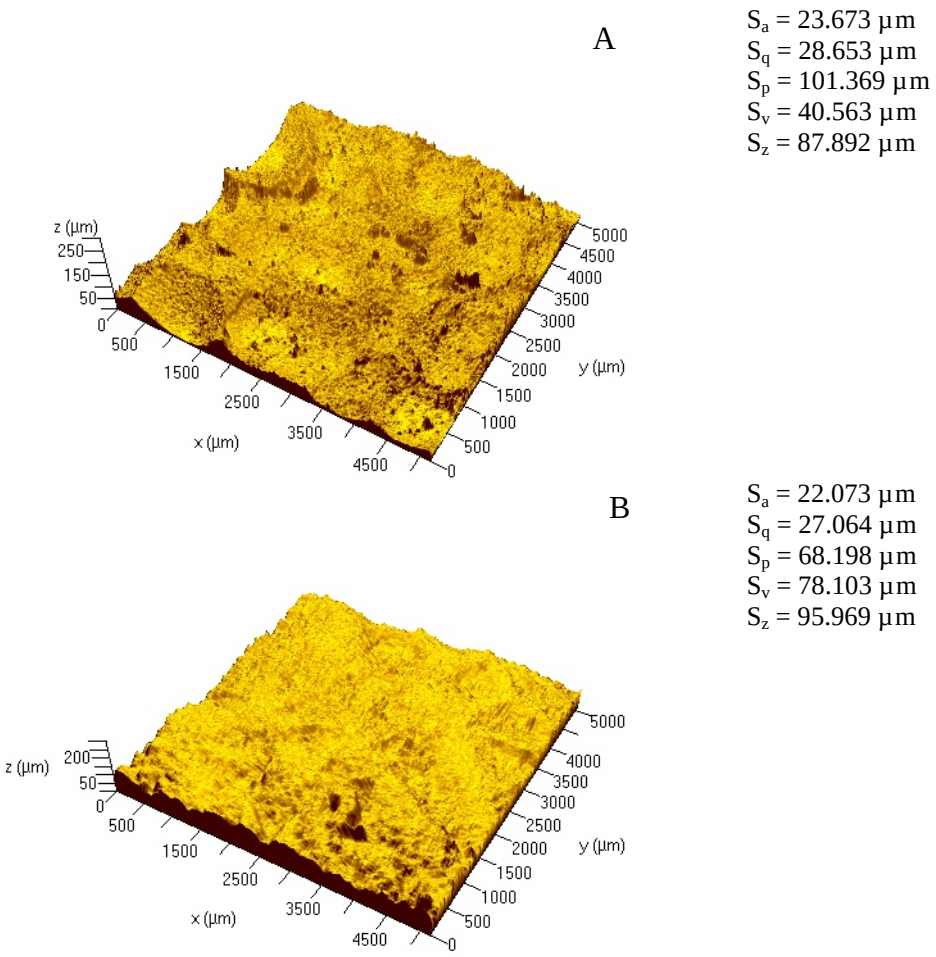

Figure 106. Larger confocal laser scanning images of two UIT surfaces, 5 mm x 5 mm surface area

Surface roughness measurements were also obtained for untreated material and two larger stitched images are shown in Figure 107. The images show that untreated material exhibits a surface roughness with average surface roughness values of 18.860 µm and 14.521 µm which are slightly less than the average surface roughness values for the UIT material. The average surface roughness of the untreated material will have an effect on the stresses induced by the UIT processing

which is observed by the deformation modeling and discussed below in section 6.2.2. The maximum peak heights are comparable, 95.895 µm to 87.826 µm (S_p), however the maximum valley depth varies from 75.555 µm to 203.206 µm (S_v). The maximum valley depth of 203.206 µm for sample B is larger than the maximum valley depths observed for the UIT sample. The maximum height of the surfaces also vary and range between 58.020 µm to 95.492 µm (S_z). The surface roughness measurements from sample B in Figure 107 were used for the numerical analysis.

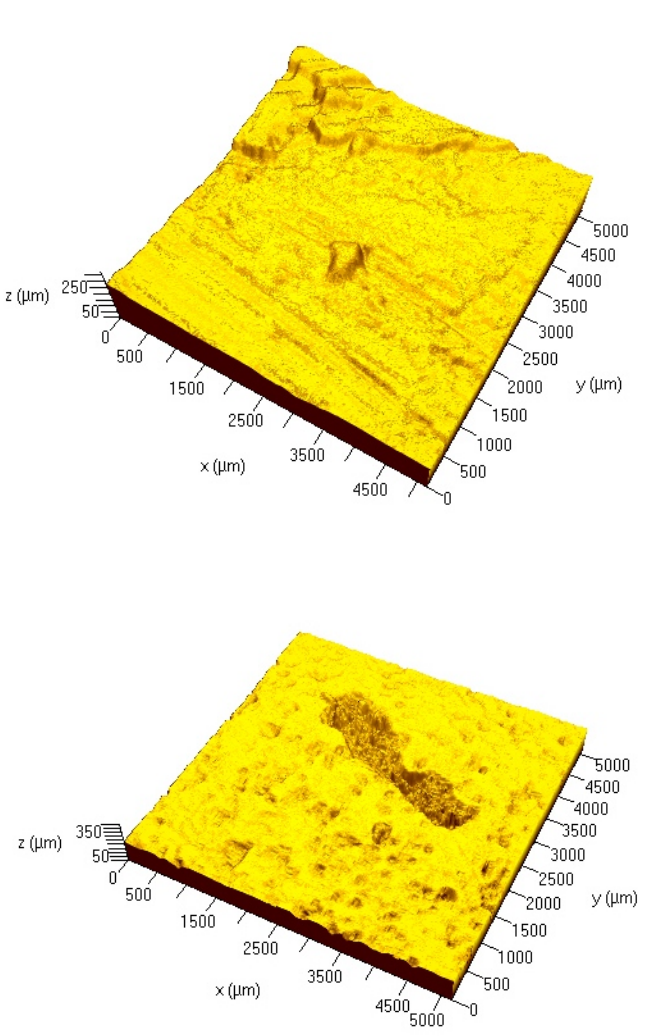

Figure 107. Larger confocal laser scanning images of two sensitized untreated surfaces, 5 mm x 5 mm surface area

6.2.2 X-Ray Diffraction Measurements to Determine Compressive Residual Stress

Using XRD, residual stress measurements as a function of depth were obtained along the x- (longitudinal along the plate rolling direction) and y- axis (transverse to the plate rolling direction) of UIT and untreated material (see Figure 7). Figure 108 shows the compressive residual stresses for the UIT treated and untreated material as a function of depth. X-ray diffraction measurements were obtained at a depth of 0.05, 0.1, 0.15, 0.2, and 0.25 mm. The results show that the compressive residual stresses for the UIT material are greater than the compressive residual stresses for the untreated material particularly in the longitudinal direction. A comparison of the results show that the compressive residual stress along the longitudinal axis for the UIT material is ~2X greater than the compressive residual stresses of the untreated sample. Along the transverse direction, the UIT material exhibits compressive residual stresses that are ~20 MPa greater than the untreated material. A large difference in compressive residual stresses along the longitudinal and transverse directions is observed for the untreated material than the UIT treated material. The large difference in residual compressive stresses may be attributed to the stresses imparted during the cold rolling of the plate during production which by definition is typically along the longitudinal direction. The results also show that the compressive residual stresses imparted by UIT are less than the yield strength of the material as measured by bulk tensile testing. The maximum residual stress for the UIT material is -177 MPa in the longitudinal direction and -165 MPa in the transverse direction.

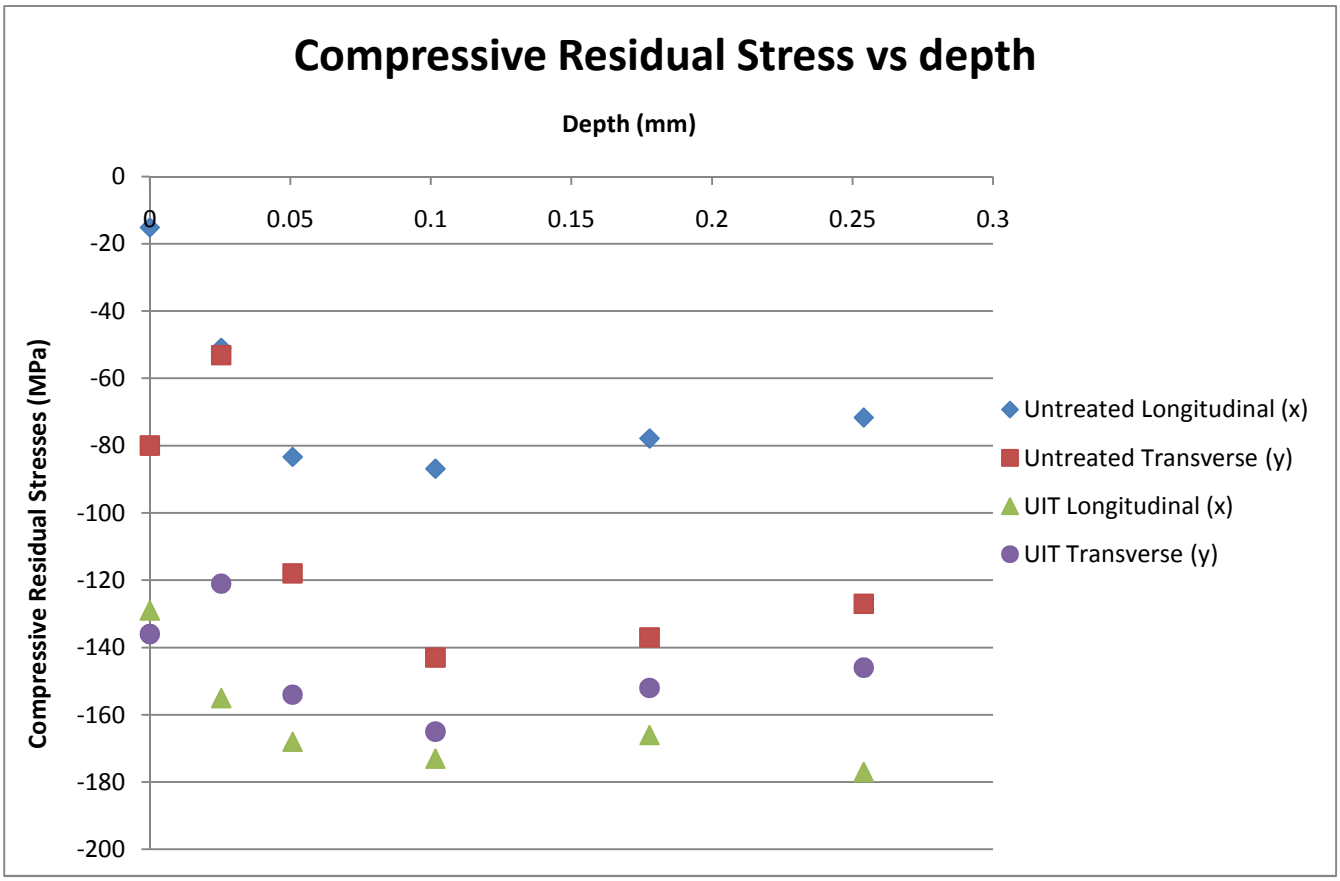

Figure 108. Compressive residual stresses as a function of depth in UIT and untreated material

6.2.3 Deformation Modeling of UIT Process

Numerical modeling was used to estimate the effective strains, stresses, and temperature during a few cycles of the UIT process. The deformation of the surface was modeled using elasto-plastic analysis available within DEFORM 3D.

The constitutive parameters used to develop the model were based on room temperature properties for aluminum 5454 which are standard parameters available in the software. Aluminum 5454 is an Al-Mg with 2.4 to 3.0 wt% Mg which is slightly

lower than aluminum 5456 [100]. The material properties were: Young's Modulus = 68.9 MPa, Poisson's ratio = 0.33, and a coefficient of thermal expansion = 2.2×10^{-5} $°C^{-1}$ which are comparable for 5454 and 5456. The constitutive properties for plastic flow were defined by internal data tables for flow stress as a function of temperature, strain, and strain rate. The DEFORM 3D software interpolates the data to calculate the flow stress based on the strain and strain rate at each nodal location.

The topographic data from the confocal microscopy analysis were used to develop a solid model for numerical analysis. Surface heights at the x, y positions from a 4.94 × 4.94 mm section of the untreated sensitized plate (Figure 107B) were used to define the topography of the solid model. The surface volume was completed by giving the surface topography a thickness of about 0.5 mm and then meshing the solid with tetragonal finite elements. This surface volume was coupled to a support block and meshed into a larger finite element model as shown in Figure 109. Sticking conditions were applied to the surface volume and support block such that the elements represented a single unit. A second surface volume was added in the same manner. The surface volume forms the contour surface plate.

A few assumptions were incorporated into the model based on the UIT processing parameters discussed in section 2.1. The pin tool was modeled to have 3 mm pin tip radius and specified to be rigid such that it would not undergo any deformation. The pin tool stroke is based on a frequency of 27 kHz and amplitude of 22 µm. Therefore one complete pin stroke is 37 µs long that results in a displacement of 22 µm in the -z direction into the surface contour plate. The boundary conditions were set such that the support block had fixed points in the z and x directions and

traversed in the –y direction at a speed of 1.66 mm/sec which is based on the UIT travel speed of 10 cm/min.

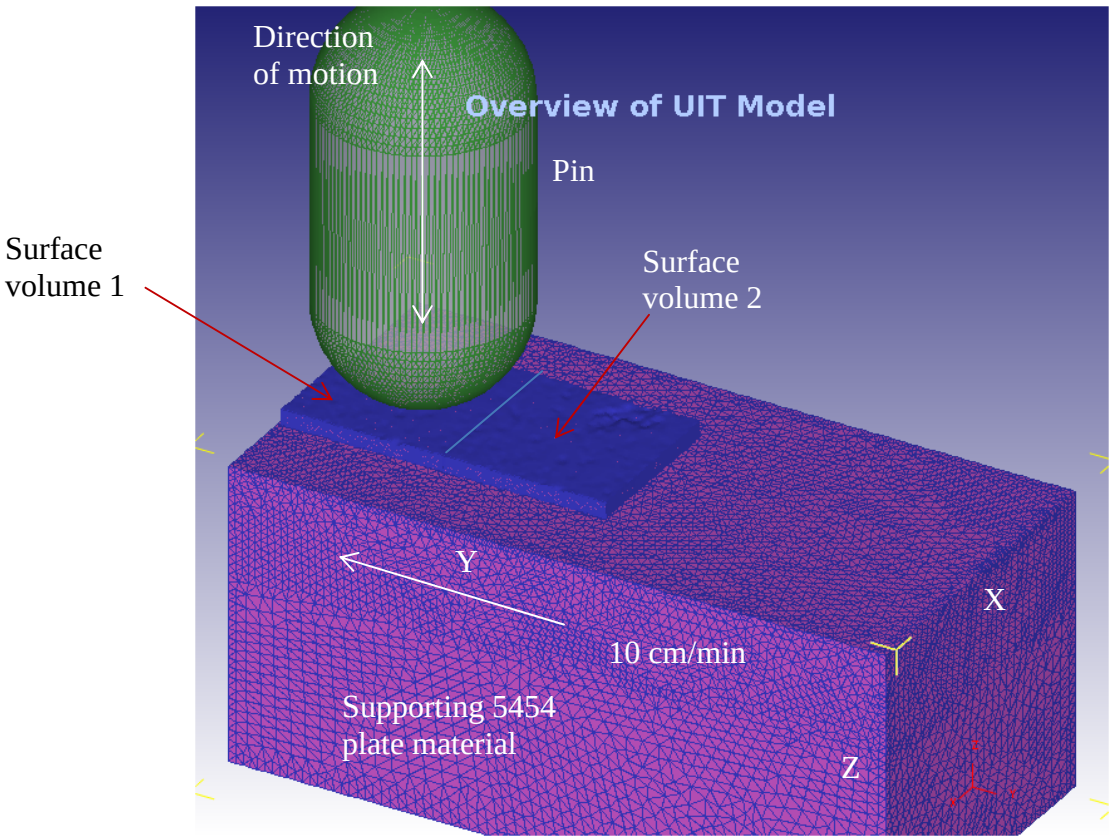

Figure 109. Overview of DEFORM 3D UIT model with surface contour plate on a support block and pin tool

The preliminary modeling results show that the plate material undulates as the pin tool impacts and retracts from the surface of the material. The undulations represent the elastic response of the surface to the compressive stresses built up during a pin tool cycle. The timescale of the response is of the same order as the frequency of the pin tool. The calculated residual stress under the tool, ~80 MPa, is

of the same order of magnitude as the XRD measurements near the surface as shown in section 6.2.2 and as shown in Figure 110.

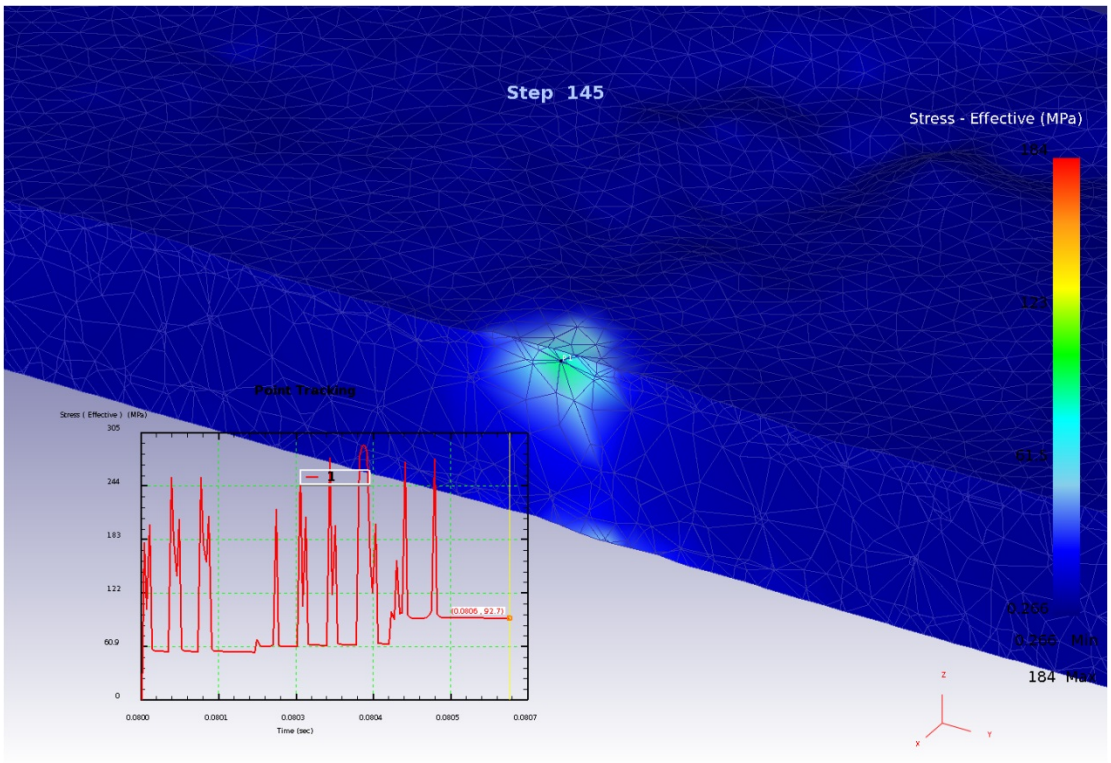

Figure 110. Residual stress equilibration showing that the calculated stress under the tool is the same order of magnitude as XRD measurements.

The effective stresses imparted by the UIT process are shown in Figure 111. DEFORM 3D modeling simulation snapshots of the UIT process showing the effective stress after various pin tool cycles; A (1.1), B (2.4), C (7), D (8.4), E (13), and F (14.6) are shown in Figure 111. The effective stresses imparted into the material are immediately noticeable after one complete pin tool stroke and shown to be greater than 200 MPa. With increasing pin tool cycles, the amount of stresses

imparted into the material surface fluctuates until some regions of the material are permanently strained beyond the elastic limit. The stressed depth and area also varies and is most notable between Figure 111 (B) and (C). The maximum depth of the stressed region extends below the thickness of the contour surface plate (0.5 mm) as shown in Figure 112. The maximum effective stress observed by the material is shown to be 325 MPa which exceeds the yield strength values obtained from micro specimen tensile testing, section 5.2.2. It is noted that the effective stresses observed in the model simulation are after 18 pin tool cycles and not equivalent to the permanent residual stresses induced by the UIT process as measured by XRD. However, the model demonstrates that the UIT process can induce high levels of effective stresses almost immediately.

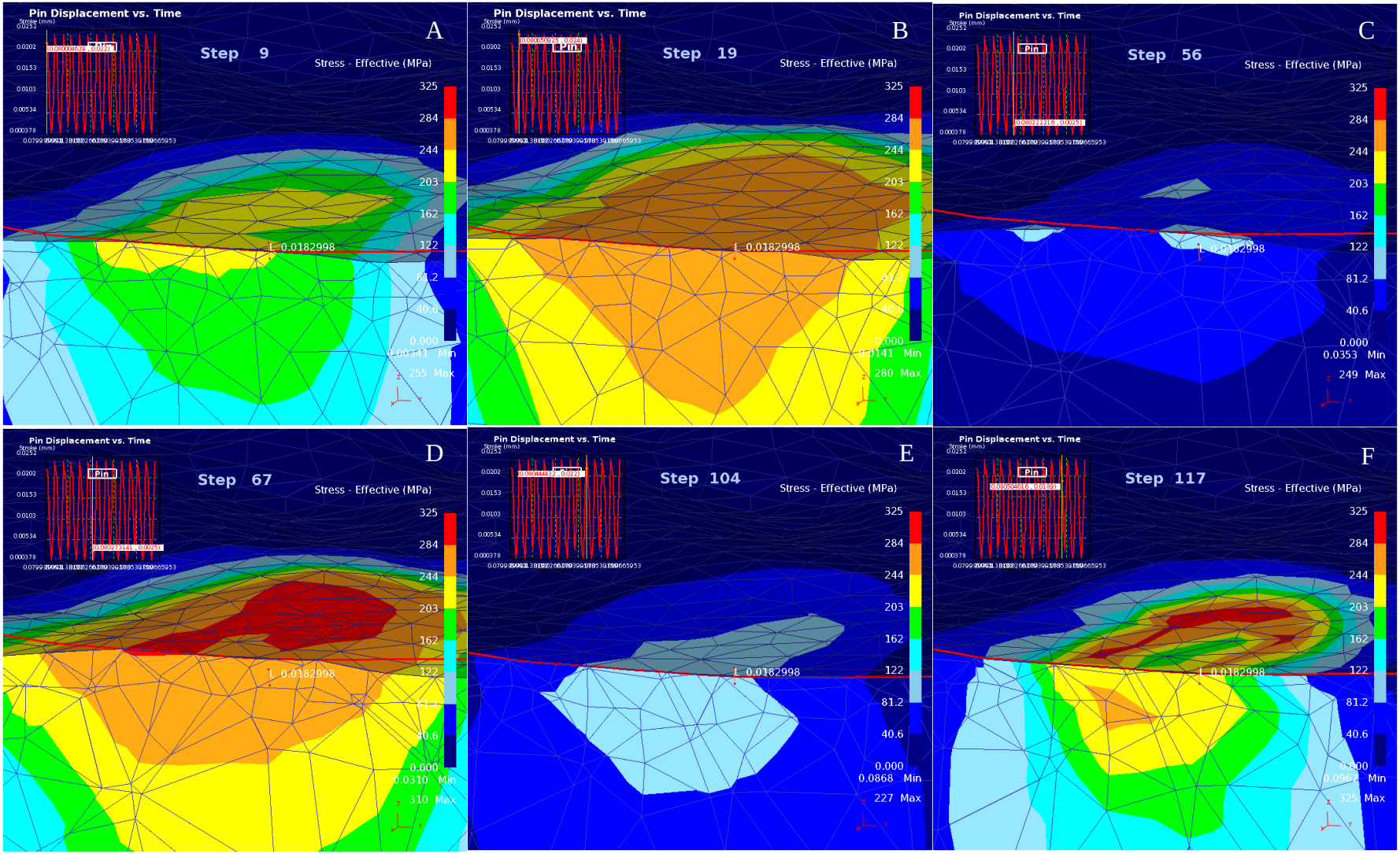

Figure 111. DEFORM 3D modeling simulation snapshots of the UIT process showing the effective stresses after various pin tool cycles: A (1.1), B (2.4), C (7), D (8.4) E (13), F (14.6)

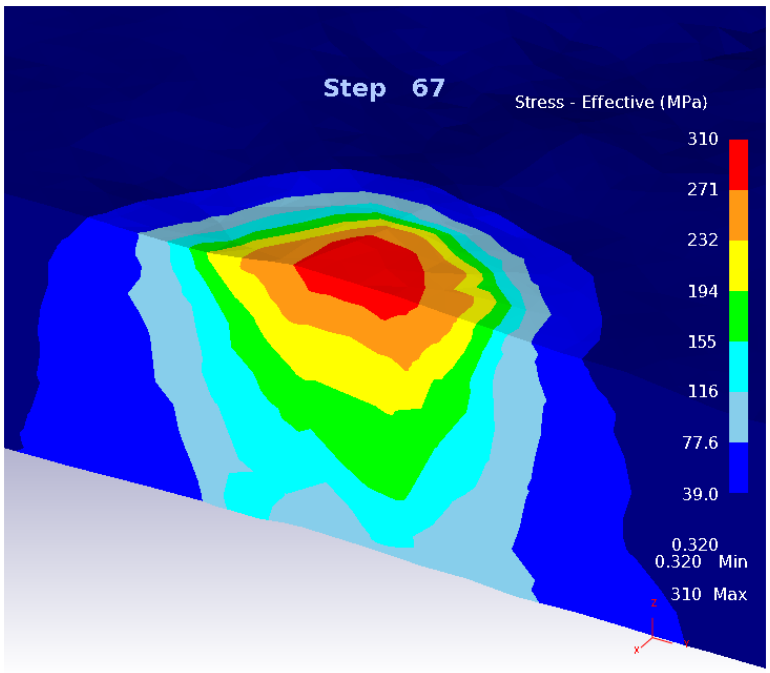

Figure 112. Maximum depth of the stressed region; extends below the thickness of the contour surface volume

Figure 113 shows snap shots of the UIT model for strain obtained at various pin tool cycles: A (2.4), B (7), C (10), D (12), E (15), and F (18). The snaps shots show a transverse cross section of the model in Figure 109 with the red line representing the pin tool. The model was simulated for 145 steps which is equivalent to 18 complete pin tool cycles where eight steps is a complete pin tool stroke (pin impact and retract). The notable effects of the strain on the material surface occur approximately after seven complete pin tool cycles (Figure 113 B). The effective strain increases as the number of pin tool cycles increases resulting in a maximum strain of 0.616 mm/mm after 12 complete pin tool cycles. As the number of pin tool cycles increases, the strain effects dissipate resulting in broadening deformation on the material surface. Figure 114 shows that the maximum effective strain extends to a depth of 0.174 mm below the surface.

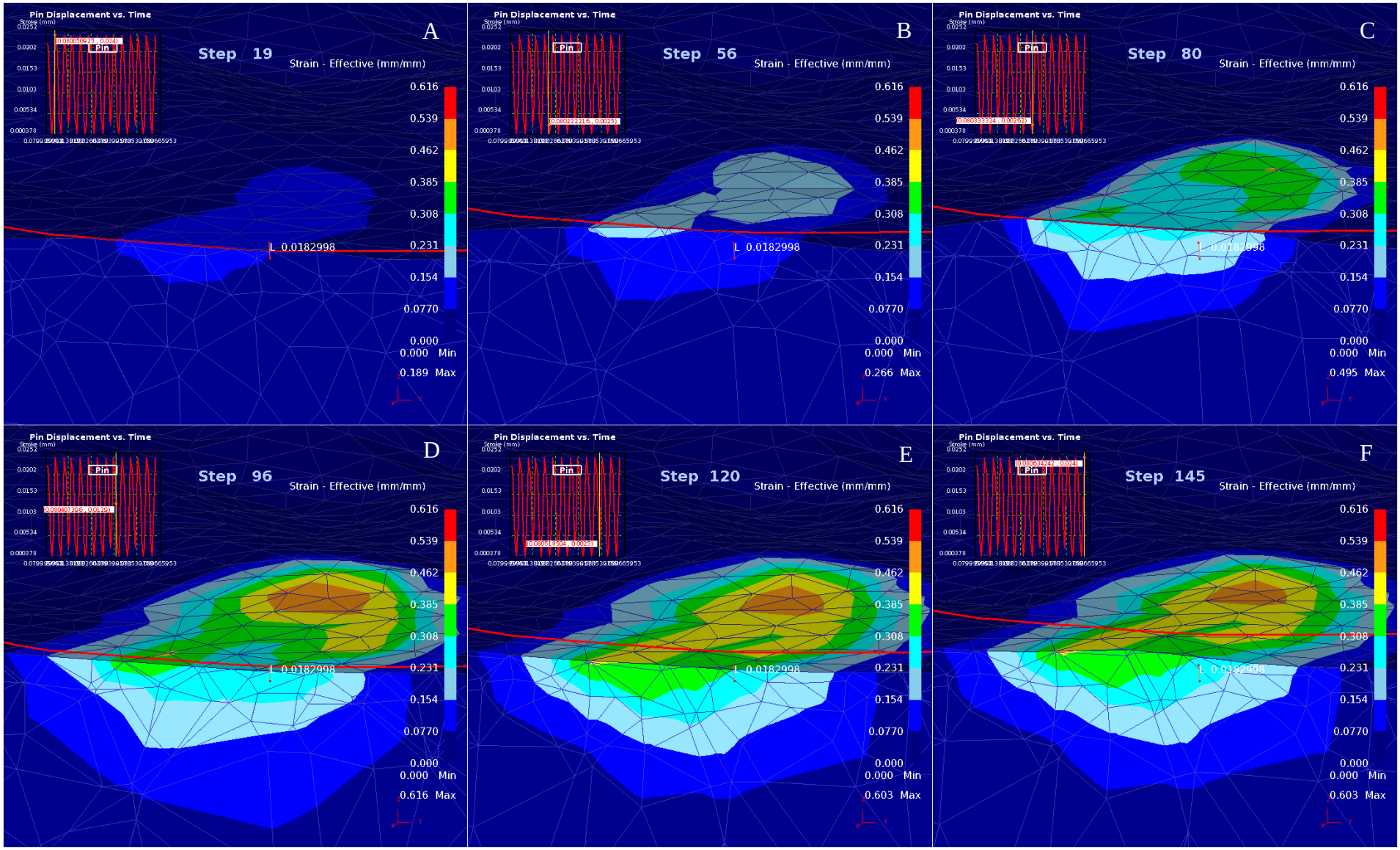

Figure 113. DEFORM 3D modeling simulation snapshots of the UIT process showing the effects of the effective strain after various pin tool cycles: A (2.4), B (7), C (10), D (12) E (15), F (18)

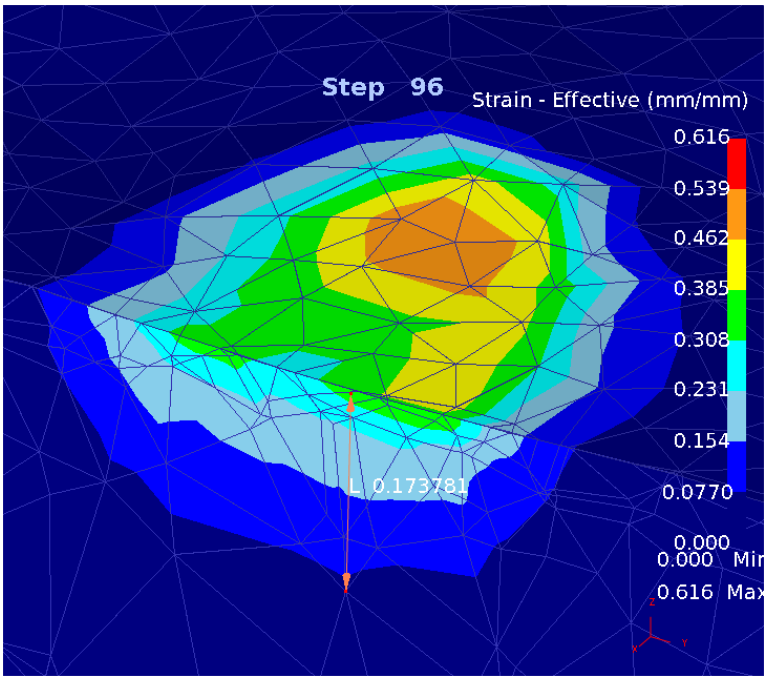

Figure 114. Maximum depth distribution of the effective strain; maximum depth is 0.174 mm

The localized heating observed during the UIT process is illustrated by Figure 115 which shows snap shots obtained at various pin tool cycles: A (2.5), B (8), C (9.9), D (11.5), E (11.6), and F (18.1). Localized heating occurs almost immediately after 2.5 pin tool cycles. With increasing pin tool cycles, the localized temperature fluctuates and the affected volume continues to increase due to thermal conductivity. The temperature continues to fluctuate and reaches a maximum temperature of ~ 32°C after a completion of 11 pin tool cycles. The depth distribution of the temperature gradient extends through the thickness of the surface contour plate as shown in Figure 116. It is noted that the simulation is only for 18 pin tool cycles, therefore in actual production the material surface likely heats to higher temperature. As noted in section 4.3, in order for nanocrystalline grains to form, the material surface temperature due to the SPD process must be at least $0.2T_m$ [59,65].

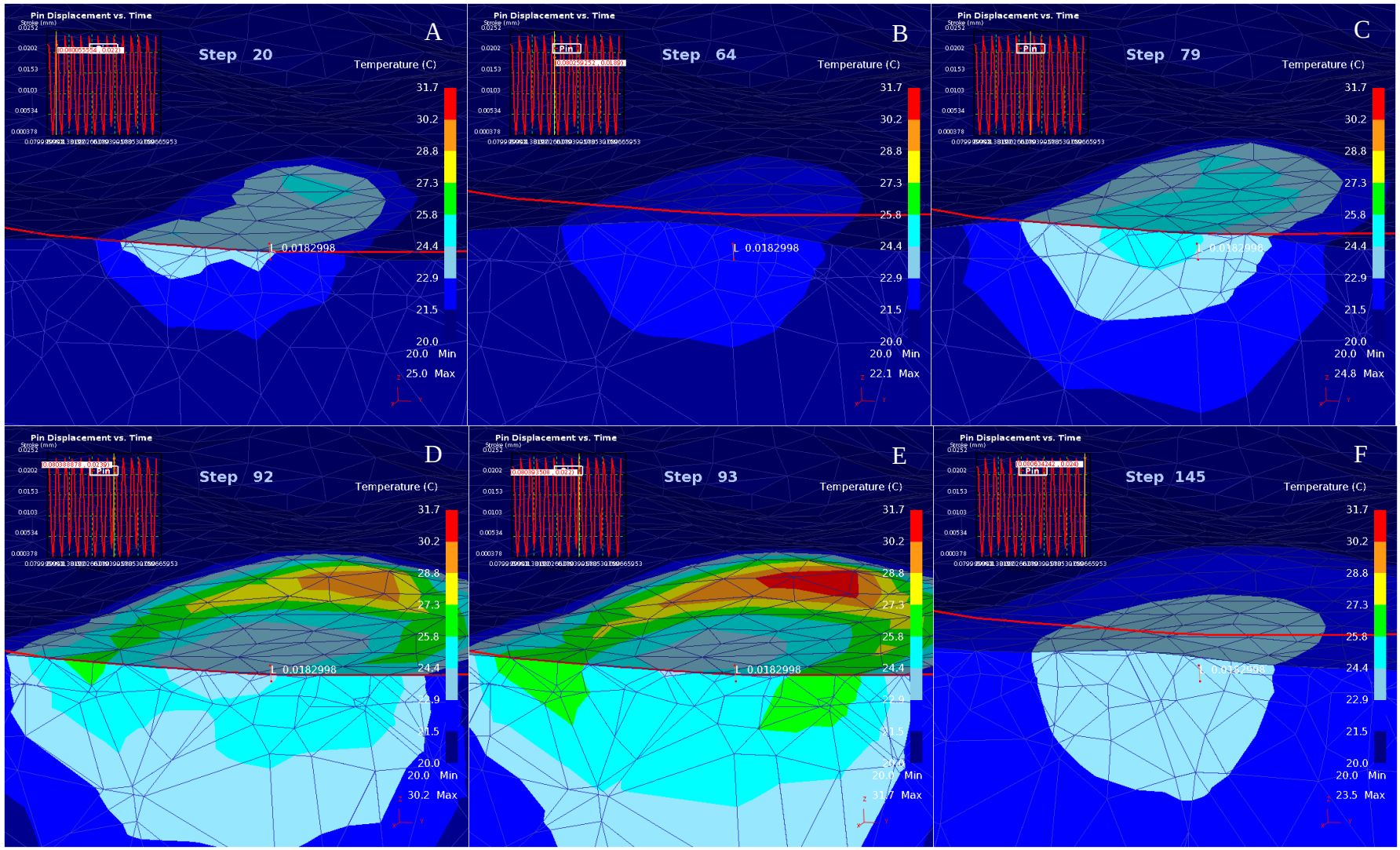

Figure 115. DEFORM 3D modeling simulation snapshots of the UIT process showing localized heating temperature after various pin tool cycles: A (2.5), B (8), C (9.9), D (11.5) E (11.6), F (18.1)

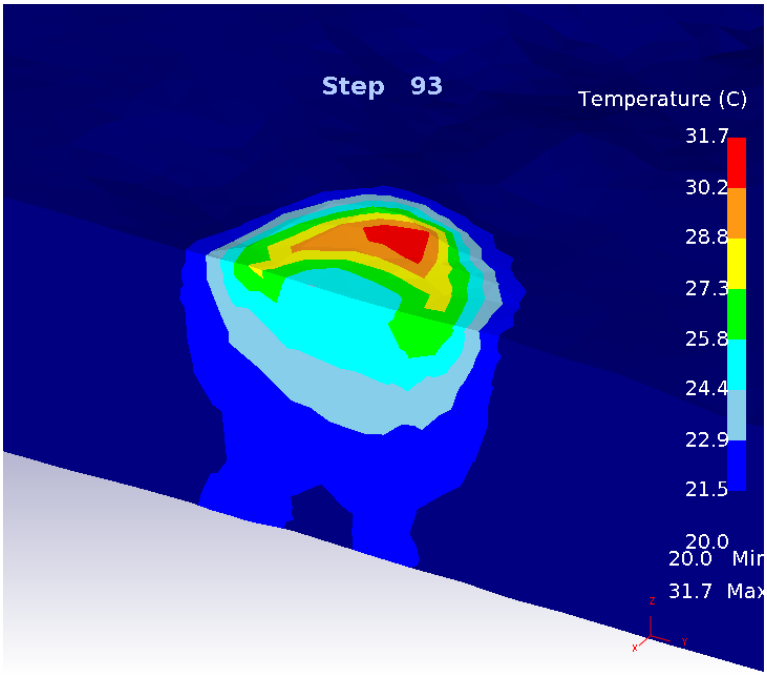

Figure 116. Depth distribution of the localized heating temperature; temperature gradient extends through the thickness of the surface contour plate

6.3 Discussion

Although there was some variability in the surface roughness of the UIT material as measured by the CLSM, the results indicate that the surface roughness is approximately equivalent to the amplitude used during UIT processing. The amplitude is the height that each pin oscillates during the processing. This suggests that penetration depth into the material surface may be altered by changing the pin's amplitude processing parameter.

The rough surface created by UIT may reduce the beneficial effects such as improved strength and nanocrystalline microstructure at the surface. Surface

roughness influences material properties such as fatigue life because it may induce stress concentrations a specific points and thus facilitate crack initiation under fatigue loading conditions [101,102]. Under fatigue loading, cracks always nucleate from the surface at areas of high stress concentration such as notches, dimples, or dents [101,103]. Although the presence of compressive residual stresses produced by SPD processes prevents crack initiation and growth, surface roughness generates localized stress concentration points and accelerates crack initiation [104].

M. Bayoumi and A. Abdellatif showed that the fatigue life decreases with increasing surface roughness in aluminum [103]. The fatigue specimens were prepared with various levels of surface roughness of 1.8, 1.1, 0.95, and 0.45 µm. The fatigue life was found to decrease as the surface roughness increased due to the development of more micro cracks and micro voids as the surface roughness increased. The susceptibility of the specimens to micro crack initiation and crack propagation increased as the roughness parameters including surface roughness, R_a, root mean square deviation profile, R_q, maximum peak height, R_p, and maximum valley depth, R_v increased.

H. Itoga et al. showed that the fatigue life decreases with increasing surface roughness in Ni-Cr-Mo steel [101]. The fatigue specimens were prepared with three different levels of surface roughness; 10.24 µm to 19.26 µm (maximum surface height) and 1.386 µm to 3.154 µm (average roughness). Cracks were found to initiate at the bottom on scratch marks indicating that the surface roughness acts as a small notch. The increased surface roughness induces a stress concentration at the bottom of the starch mark, leading to premature crack initiation and decreased fatigue

strength. At low stress concentrations, crack initiation at the specimen surface occurred more readily due to the stress concentrations created by the surface roughness. With increasing surface roughness which resulted in higher stress concentrations, cracks were found to always initiate at scratch marks on the specimen surface.

The M. Bayoumi and H. Itoga et al. models are based on the surface roughness due to machining marks that are linear [101,103], however the results reported by K. Dai et al. and A. Eftekhari et al. are based on SPD treatments [102,104]. Although fatigue testing of UIT material was not been conducted as part of this research, future work should include an investigation of the fatigue properties of UIT material.

The results of CLSM also showed that the untreated material has a rough topography. The average surface roughness of the untreated material ranges from 18.860 µm and 14.521 µm which is only slightly lower than the average surface roughness values for the UIT material. The surface topography of the material prior to UIT processing will have an effect on the spatial distribution of stress and strain as shown by the deformation modeling.

The preliminary deformation modeling results showed that the plate material undulates as the pin tool impacts and retracts from the surface of the material due to compression followed by expansion until the effective strain exceeds the elastic limit of the material. The timescale of the response is of the same order as the frequency of the pin tool and the calculated residual stress under the tool, ~80 MPa, is of the same order of magnitude as that from XRD measurements near the surface. The maximum

effective stress imparted into the material was 325 MPa which exceeded the yield strength values measured through micro specimen tensile testing. The maximum yield strength value at the UIT surface was 290 MPa (section 5.2.2). The maximum effective stress observed by the model also exceeded the residual compressive stresses of -175 MPa (x direction) and -165 MPa (y direction) measured by XRD. The model demonstrated a large effective stress of -200 MPa almost immediately after just one pin tool stroke. With increasing pin tool cycles, the area of deformation expanded. The results also showed that the effective strain increases with increasing number of pin tool cycles. After 12 complete pin tool cycles the effective strain was 0.616 mm/mm and extends to a depth of 0.174 mm below the surface. The UIT process was shown to result in localized heating up to a maximum temperature of ~ 32°C in a relatively short amount of time. Localized heating occurred rapidly after 2.5 pin tool cycles and the maximum observed temperature was reached after 11 complete pin tool cycles.

It is noted that the modeling results are preliminary and the simulation was only for 18 complete pin tool cycles for a total of 666 µs. The observed effective strain, stresses, and temperature from the model will differ from a complete actual UIT process. However, the model demonstrates that the UIT process can result in large effective strains, stresses, and rapid localized heating in a short time.

The compressive residual stresses observed during DEFROM 3D modeling are comparable to the results reported by Zinn and Scholtes [96]. The shot peening of aluminum 5083 resulted in the highest compressive residual stresses ranging from ~ -200 to -250 MPa near the surface to a depth of 0.10 mm below the surface [96]. With

increasing depth to 0.4 mm, the compressive residual stresses decreased to less than -50 MPa. The results of XRD showed that the compressive residual stresses imparted by UIT were -177 MPa (x-direction) and -165 MPa (y-direction) at a depth of 0.25 mm. These values are comparable to the compressive residual stresses reported by M. Liao et al. for the UIT of aluminum 7075-T6511 [5]. M. Liao et al. reported compressive residual stresses ranging from 150 to 200 MPa on or near the surface and were reduced to around 70 MPa at a depth of 1.0 mm below the surface [5]. These values are greater than the compressive residual stresses reported by Zinn and Scholtes for shot peening of aluminum 5083 at the same depth. The measured residual stresses at a depth of 0.25 mm were reported to be -150 MPa [96]. The results of DEFROM 3D and XRD measurements show that the UIT process can induce deep compressive residual stresses in Al-Mg alloys.

6.4 Summary

The results of confocal microscopy, XRD residual stress measurements, and numerical simulation can be summarized as follows:

- The surface roughness is approximately equivalent to the UIT processing amplitude where the amplitude is the height that each pin oscillates during the processing.
- Numerical deformation modeling showed that the material surface undulates as the pin tool impacts and retracts from the surface of the material. The

undulations represent the elastic response of the surface to the compressive stresses built up during a pin tool cycle.

- Numerical deformation modeling showed that the timescale of the response is of the same order as the frequency of the pin tool. The calculated residual stress under the tool, ~80 MPa, is of the same order of magnitude as the XRD measurements near the surface.
- Numerical deformation modeling showed that the UIT process results in a maximum effective strain of 0.616 mm/mm after 12 complete pin tool cycles and with increasing pin tool cycles, the effective strain increases.
- DEFORM 3D modeling showed that UIT results in rapid localized heating at the material surface to a maximum temperature of ~ 32°C after 11 pin tool cycles.

Chapter 7: Conclusions and Future Work

7.1 Conclusions

The objectives of this work were to correlate the microstructural evolution of UIT material to the effects on material properties and to develop a fundamental understanding of the mechanisms that cause the microstructural evolution through microstructural characterization techniques and materials properties testing. The work included investigating the plastic deformation imparted by UIT on sensitized 5456-H116 plate and untreated sensitized to provide a basis for comparison. The following conclusions can be made from the work in this thesis:

- The UIT process results in the formation of nanocrystalline grains in sensitized aluminum 5456, however the nanocrystalline grains are only present at the deformation layer. The effects of UIT extend below the deformation layer and results in grain refinement. The increased strength and hardness near the UIT surface is attributed to the grain refinement. The results demonstrate that UIT can be used to improve the strength properties of severely sensitized material with a mass loss of >50 mg/cm^2 through the formation of a nanocrystalline layer.
- The deformation layer is also characterized by voids and tearing and a distinct separation or lamination layer between the UIT surface and the metal matrix. This appears to have an effect on the strength properties because the hardness values and strength values were variable at the UIT surface. The voids and tearing also influence the corrosion properties resulting in comparable

properties between UIT and untreated material. These results suggest that the nanocrystalline layer imparted by the UIT process does not improve the intergranular corrosion properties.

- The presence of nanocrystalline grains and lack of a continuous β phase within the deformation layer indicates that the straining and localized heating (which should have been on the order of $0.2T_m$) induced by UIT results in dynamic recrystallization. β phase can only be redissolved by reheating Al-Mg to about 425°C. Dynamic recrystallization is rarely observed in aluminum alloys because it exhibits a high rate of dynamic recovery. However this result suggests that dynamic recrystallization can occur in severely plastically deformed Al-Mg and contributes to the understanding of recrystallization behavior of severely plastically deformed aluminum alloys.
- The nanocrystalline grains are thermally stable to ~ 300°C indicating that the recrystallization temperature for UIT 5456 is ~ 300°C. The activation energy required for grain growth is ~ 32 kJ/mol which is low compared to the activation energy for fully recrystallized grains. However, the low activation energy concurs with the concept of a low activation energy for grain diffusion in ultrafine grain materials because of the non-equilibrium grain boundaries which are characteristic of nanocrystalline grains. High resolution TEM confirmed the presence of curved or wavy grain boundaries in the nanograins formed by UIT. These results contribute to the understanding of the recrystallization and grain growth behavior of aluminum nanocrystalline grains.

- The UIT surface exhibits high hardness and strength; however the results varied showing lower hardness and strength values in some areas. The higher hardness and strength value may be attributed to the formation of the nanocrystalline layer; however the presences of voids and micro voids/micro cracking in the deformation layer result in some lower hardness and strength values. The voids and micro voids/micro cracking in the deformation layer contributed to the mixed corrosion properties. Although UIT results in the formation of a nanocrystalline layer at the surface, the defects induced by the process reduce the benefits of the nanocrystalline layer.
- Numerical deformation modeling shows that the UIT process results in high effective strain; effective stresses, and localized heating almost immediately (666 µs). The model also shows that the material undulates which represents the elastic response of the surface to compressive stresses built up as the pin tool impacts and retracts from the surface of the material. The model also showed that the calculated residual stress under the tool, ~80 MPa, is of the same order of magnitude as the XRD measurements near the surface. The work demonstrates the successful modeling of the UIT process and contributes to the understanding of the physics of the UIT process and physical effects on aluminum 5456.

7.3 Future Work

This work contributed to the understanding of the microstructural evolution of UIT of sensitized 5456 Al-Mg alloy and the effects of UIT on material properties.

The work was focused on the study of sensitized 5456 UIT and untreated material. To further the understanding of UIT on 5456, the following work is recommended:

- Additional HRTEM analysis of UIT material to determine the deformation mechanisms in nanocrystalline grains which have been suggested to occur through the formation of twins and stacking faults in Al-Mg alloys.
- Microscopy of UIT welds fabricated from sensitized 5456 to examine the microstructural evolution in weld metal.
- Additional material properties testing particularly fatigue testing and SCC testing of UIT sensitized 5456 and UIT welds fabricated from sensitized 5456.
- Obtain temperature measurements during UIT in order to determine the localized heating induced by UIT to determine the temperature required for nanocrystalline grains to form and further the understanding of nanocrystalline grain formation.
- Evaluate the microstructural evolution and material properties of UIT processed material treated with different processing parameters (amplitude, frequency) in order to further the understanding of the processing parameters on the microstructure and material properties.
- Additional numerical deformation modeling to simulate the effective strains, effective stresses, and the localized heating observed during UIT for more cycles that are representative of the actual UIT process in production and also to examine different UIT processing parameters. Due to constraints on computational resources, the analysis was limited to only a few dozen cycles for a preliminary study.

References

1. Gubicza, J. et al., "Microstructure and Strength of Severely Deformed FCC Metals", *Materials Science and Engineering A* 462 (2007) 86-90

2. Dai, K. et al., "An Analytical Model of the Surface Roughness of an Aluminum Alloy Treated with a Surface Nanocrystallization and Hardening Process", *Scripta Materialia* 52 (2005) 259-263

3. An, X. et al., " Study of the Surface Nanocrystallization Induced by the Esonix Ultrasonic Impact Treatment on the Near-Surface of 2024-T351 Aluminum Alloy", *Journal of Materials Engineering and Performance* Vol 15(3) June 2006

4. Statnikov, E.S. et al., "Physics and Mechanisms of Ultrasonic Impact", *Ultrasonics* 44(2006) e533-e538

5. Liao, M. et al., "Effects of Ultrasonic Impact Treatment on Fatigue Behavior of Naturally Exfoliated Aluminum Alloys", *International Journal of Fatigue* 30 (2008) 717-726

6. You-Li, M. et al., "Study on Mechanical Properties of Nanocrystal Surface Layer of an Aluminum Alloy", *International Journal of Nonlinear Sciences and Numerical Simulation 3*, 491-494, 2002

7. Hatch, J.E., "Aluminum: Properties and Physical Metallurgy' American Society for Metals, 1983

8. Lancker, M. V., "Metallurgy of Aluminum Alloys", John Wiley & Sons, Inc., New York, New York, 1967

9. Mondolfo, L.F., "Aluminum Alloys: Structure and Properties", Butterworth & Co. Ltd, London, England, 1976

10. American Society for Testing and Materials, "Standard Specification for High Magnesium Aluminum – Alloy Sheet and Plate for Marine Service and Similar Environments", ASTM B928, West Conshohocken, PA, November 2009

11. Van Horn, K.R., "Aluminum *Prepared* by *Engineers, Scientists,* and *Metallurgists* of *Aluminum Company* of *America" American Society for Metals, 1967*

12. Davis, J.R. editor, "Corrosion of Aluminum and Aluminum Alloys," ASM International Metals Park, OH, December 1999

13. Starink, M.J. and Zahra, A.M., "β' and β Precipitation in an Al-Mg Alloy Studied by DSC TEM, *Acta Metallurgica*, Vol 46, No. 10, pp 3381-3397, 1998

14. Unocic, K. et al., “Grain Boundary Precipitate Modification for Improved Intergranular Corrosion Resistance”, *Material Science Forum*, Vols. 519 – 521 (2006) pp 327-332

15. Oguocha, I.N.A. et al, “Effect of Sensitization Heat Treatment on Properties of Al-
Mg Alloy AA5083-H116”, *Journal Material Science* (2008) 43: 4208-4214

16. Searles, J.L. et al, “Stress Corrosion Cracking of Sensitized AA 5083 (Al-4.5Mg-1.0Mn), *Material Science Forum* Vols 396-402 (2002) pp. 1437-1442

17. Davenport, A.J. et al., “Intergranualr Corrosion and Stress Corrosion Cracking of Sensitised AA 5182, *Material Science Forum* Vols 519-521 (2006) pp 641-646

18. Jones, R.H. et al., “ Role of Mg in the Stress Corrosion Cracking of an Al-Mg Alloy”, *Metallurgical and Material Transactions A*, Vol 32A, July 2001

19. Goswami, R. et al., “Precipitation Behavior of the β Phase in Al 5083”, Naval Research Laboratory, Washington DC, to be submitted to *Material Science and Engineering A*

20. Randle, V. and Engler, O., “Introduction to Texture Analysis Macrotexture, Microtexture & Orientation Mapping”, CRC Press, 2000

21. Wong, C. and Whitefield, A., “*Effect of Service Environment on Properties of Marine Grade Structural Aluminum Alloys*, Poster presented at ShipTech Conference 2009

22. Alcoa Report on Aluminum Alloys

23. Totten, G. and MacKenzie, S., “Handbook of Aluminum: Physical Metallurgy and Process”, CRC Press, 2003

24. Dieter, G. “ Mechanical Metallurgy”, 3rd Ed. McGraw Hill, 1986

25. Wu, X. et al., “Microstructure and Evolution of Mechanically-Induced Ultrafine Grain in Surface layer of Al-alloy Subject to USSP”, *Acta Materialia* 50 (2002) 2075-2084

26. Kaneko, K. et al., “Fabrication and Characterization of Supersaturated Al-Mg Alloys by Severe Plastic Deformation and Their Mechanical Properties”, *Materials Transactions*, Vol 50, No. 1 (2009), pp 76-81

27. Mazilkin, A. et al., “Structural Changes in Aluminum Alloys Upon Severe Plastic Deformation”, *Physics of the Solid State*, 2007, Vol 49, No. 5, pp 868-873

28. Sato, M., “Fabrication of Surface Nanocrystalline Aluminum Alloys”, *Material Science Forum*, Vols 426-432 (2003) pp 2753 – 2758

29. Statnikov, E.S. et al., “Physics and Mechanisms of Ultrasonic Impact”, *Ultrasonics* 44(2006) e533-e538

30. American Society for Testing and Materials, “Standard Test Method for Determining the Susceptibility to Intergranular Corrosion of 5xxx Series Aluminum Alloys by Mass Loss After Exposure to Nitric Acid (NAMLT Test),” ASTM G67-04, May 2004

31. “Naval Surface Warfare Center Residual Stress Summary TEC WON No. 60572, Tec Report No. R-2009-096, April 30, 2009

32. Skrotzki, W. et al., “Texture Formation During ECAP of Aluminum AA5019”, *Material Science Forum* Vols (2006) pp 99-106

33. Driver, J.H. et al., “Electron Backscattered Diffraction Microtexture Studies on Hot Deformed Aluminum Crystals”, *Material Science and Technology*, October 1996, Vol. 12, 851

34. Chang, C.S.T. and Duggan, B.J., “Relationship Between Rolled Grain Shape, Deformation Bands, Microstructures and Recrystallization Textures in Al-5%Mg, *Acta Materialia* 58 (2010) 476-489

35. Engle, O. and Yuguo, A., “Correlation of Texture and Plastic anisotropy in the Al-Mg Alloy AA 5005”, *Solid State Phenomena*, Vol 105 (July 2005) pp 277-284

36. http://aluminium.matter.org.uk

37. Humphreys, F.J., “Review: Grain and Subgrain Characterisation by Electron Backscatter Diffraction”, *Journal of Materials Science* 36 (2001) 3833-3854

38. Cullity, B.D., “Elements of X-ray Diffraction” 2nd Ed. Addison-Wesley Publishing Co, Inc., 1978

39. Gubicza, J. et al., “Microstructure and Strength of Severely Plastically Deformed FCC Metals, *Material Science and Engineering A*, 462 (2207) 86-90

40. Schwartz A.J. et al., “Electron Backscatter Diffraction in Material Science”, *Kluwer Academic/Plenum Publishers*, 2000

41. Gholina, A. et al., “Production of Ultra-Fine Grain Microstructures in Al-Mg Alloys by Conventional Rolling”, *Acta Materialia*, 50 (2002) 4461-4476

42. Wagner, L., “Shot Peening”, Pergamon Press, Oxford, UK, 1982

43. Kapoor, R. et al., “Influence of Fraction of High Angle Boundaries on the Mechanical Behavior of Ultrafine Grained Al-Mg Alloy”, *Material Science and Engineering A*, 527 (2010) 5246-5254

44. Liu, W.C. et al., “Effect of Strain Hardening on Texture Development in Cold Rolled al-Mg Alloy, *Material Science and Engineering A*, 527 (2010) 1249-1254

45. Koizumi, M. and Inagaki, H., “Role of Shear Band in Texture Control of Al-Mg Alloys”, *Metals and Materials*, Vol 5, No. 6 (1999), pp 511-517

46. Mao, W. “Formation of Recrystallization Cube Texture in High Purity Face Centered Cubic Metal Sheets”, *Journal of Materials and Engineering and Performance*, Vol 8(5) October 1999

47. Nakayama, Y. et al., “Precipitation Behaviors β-Phase and Changes in Mechanical Properties of Al-Mg System Alloys”, *Material Science Forum* Vols 217-222 (1996) pp 1269-1274

48. Ryen, O. et al., “Strengthening Mechanisms in Solid Solution Aluminum Alloys”, *Metallurgical and Materials Transactions A*, Vol 37A, June 2006

49. Williams, D.B. and Carter, C.B., “Transmission Electron Microscopy, Diffraction II”, Springer Science, 1996

50. Thomas, G., “Transmission Electron Microscopy of Metals”, John Wiley & Sons, 1962

51. Williams, D.B. and Carter, C.B., “Transmission Electron Microscopy, Imaging III”, Springer Science, 1996

52. Wang, J. et al., “An Investigation of Microstructural Stability in an Al-Mg Alloy with Submicrometer Grain Size”, *Acta Materiala*, Vol 44, No 7, pp 2973-2982, 1996

53. Reed-Hill, R. and Abbaschian, R., “Physical Metallurgy Principles”, 3rd Ed. PWS Publishing Co., 1994

54. Voynarovych, I.M., et al., “Characterization of SbSi Nanocrystals by Electron Microscopy, X-Ray Diffraction and Raman Scattering”, *Journal of Optoelectronics and Advanced Materials*, Vol 5, No. 3 September 2003

55. Sato, M. et al., “Formation of Nanocrystalline Surface Layers in Various Metallic Materials by Near Surface Plastic Deformation”, *Science and Technology of Advanced Materials*, 5 (2004) 145-152

56. Neishi, K. et al., “Grain Refinement of Commercial Al-Mg Alloy Using Severe Torsion Straining Process, *Material Science Forum* Vols 503-504 (January 2006) pp 955-960

57. May, J. et al., “Mechanical Properties, Dislocation Density and Grain Structure of Ultrafine-Grained Aluminum and Aluminum Alloys”, *Metallurgical and Materials Transactions A*, Vol 38A, September 2007

58. Horita, Z. et al., “Equal-Channel Angular Pressing of Commercial Aluminum Alloys: Grain Refinement, Thermal Stability and Tensile Properties”, *Metallurgical and Materials Transactions A,* Vol 31A, March 2000

59. Liu, M. et al., “Grain Refinement in Nanostructured Al-Mg Subjected to High Pressure Torsion”, *Journal of Material Science* (2010) 45:4659-4664

60. Gourdet, S. and Montheillet, “An Experimental Study of the Recrystallization Mechanism During Hot Deformation of Aluminum”, *Materials Science and Engineering* A283 (2000) 274-288

61. Doherty, R.D. et al., “Current Issues in Recrystallization: A Review”, *Materials Science and Engineering* A238 (1997) 219-274

62. Hallberg, H. et al., “Modeling of Continuous Dynamic Recrystallization in Commercial-Purity Aluminum”, *Materials Science and Engineering* A527 (2010) 1126-1134

63. Kassner, M.E., and Barrabes, S.R., “New Developments in Geometric Dynamic Recrystallization”, *Materials Science and Engineering A,* 410–411 (2005) 152–155

64. Drury, M.R. and Humphreys, F.J., “The Development of Microstructure in Al-5%Mg During High Temperature Deformation”, *Acta Metallurgical* Vol 34, No. 11, pp 2259-2271, 1986

65. Prangnell, P.B. et al, “Ultra-Fine Grain Structures in Aluminum Alloys by Severe Deformation Processing”, *Materials Science and Engineering A*, 375-377 (2004) 178-185

66. Liao, X.Z. et al., “Deformation Mechanism in Nanocrystalline Al: Partial Dislocation Slip”, *Applied Physics Letters* Vol 83, No. 4, July 2003

67. Chen, M. et al., “Deformation Twinning in Nanocrystalline Aluminum”, *Science* Vol 300, May 2003

68. Zhu, Y.T. et al., ‘Nucleation and Growth of Deformation Twins in Nanocrystalline Aluminum”, *Applied Physics Letters* Vol 85, No. 21, November 2004

69. Liu, M. et al., “Structural Characterization by High Resolution Electron Microscopy of an Al-Mg Alloy Processed by High-Pressure Torsion”, *Material Science and Engineering A*, 503 (2009) 122-125

70. Horita, Z. et al., “An Investigation of Grain Boundaries in Submicrometer-Grained Al-Mg Solid Solution Alloys Using High-Resolution Electron Microscopy”, *Journal of Materials Research*, Vol 11, No. 8, August 1996

71. Varin, R.A. et al., Investigation of Extrinsic Grain Boundary Dislocations in Copper, *Journal De Physiue,* ColloqueC4, supple'ment au no 10, Tome36, Octobre 1975

72. Eikum, A. and Thomas, G., "Precipitation and Dislocation Nucleation in Quenched-Aged Al-Mg Alloys", *Acta Metallurgica*, Vol 12, May 1964

73. Huskins, E.L. et al., "Strengthening Mechanisms in an Al-mg Alloy", *Materials Science and Engineering A*, 527 (2010), 1292-1298

74. Kaibyshev, R. et al., "Deformation Behavior of a Modified 5083 Aluminum Alloy", *Materials Science and Engineering A*, 392 (2005), 373-379

75. Morris, D.G. and Munoz-Morris, M.A., "Microstructure of severely deformed Al-3Mg and its evolution during annealing", *ACTA Materialia*, 50 (2002) 4047-4060

76. Koizumi, M. et al., "Kinetics of Recrystallization in Al-Mg Alloys", *Zeitschrift fur Metallkunde*, Vol 91 (2000) 460-467

77. Ryum N. and Embury, J.D., "A Comment on the Recrystallization Behavior of Al-Mg Alloys", *Scandinavian Journal of Metallurgy* 11 (1982) 51-54

78. Furukawa, M. et al., "Microhardness Measurements and the Hall-Petch Relationship in an Al-Mg Alloy with Submicrometer Grain Size", *ACTA Materials*, Vol 44, No 11, pp 4619-4629, 1996

79. Kubota, M., "Observation of Beta Phase Particles in an Isothermally Aged Al-10 mass%Mg Alloy with and without 0.5 mass% Ag", *Materials Transactions*, Vol 49, No 2(2008) pp 235-241

80. Fu, M.W. et al., "The Grain Refinement of Al-6061 via ECAE Processing: Deformation Behavior, Microstructure and Property", *Materials Science and Engineering A* 526 (2009) 84-92

81. Lloyd, D.J. and Court, S.A., "Influence of Grain Size on Tensile Properties of Al-Mg Alloys", *Material Science and Technology*, October 2003, Vol 19

82. Scheck, C. et al., "Impact of Ultrasonic Impact Treatment on A 5456 Aluminum Alloy Characterized Through Micro-Specimen Testing and X-Ray Tomography, 2010 TMS Proceedings Paper

83. Jones, R.H. et al., "Crack-particle Interactions During Intergranular Stress Corrosion of AA 5083 as Observed by Cross-Section Transmission Electron Microscopy", *Scripta Materialia* 50 (2004) 1355-1359

84. Fang, D.R. et al, "Tensile Properties and Fracture Mechanism of Al-Mg Alloy Subjected to Equal Channel Angular Pressing", *Materials Science and Engineering A* 459 (2007) 137-144

85. Tran, K.N. et al, “Ultrasonic Impact Treatment of Aluminum 5456 Plate and Welds”, Presentation, American Society Welding Conference, Chicago, 2011

86. American Society for Testing and Materials, “Standard Test Method for Tension Testing of Metallic Materials,” ASTM E8-04, May 2004

87. Furukawa, M. et al., “The Significance of the Hall-Petch Relationship in Ultra-Fine Grained Materials”, Ann. Chim. Fr. 1996, 21, pp 493-502

88. Hayes, J.S. et al., “Effect of Grain Size on Tensile Behavior of a Submicron Grained Al-3wt%Mg Alloy Produced by Severe Deformation”, *Materials Science and Technology*, November-December 2000, Vol 16

89. Mukai, T. et al., “Influence of Magnesium Concentration on the Relationship Between Fracture Mechanism and Strain Rate in High Purity Al-Mg Alloys”, *Materials Science and Engineering A*, Vol 176, Issues 1-2, 1999, pp 181-189

90. Sikora, E. et al, “Corrosion Behavior of Nanocrystalline Bulk Al-Mg Based Alloys”, *Corrosion* Vol 60, No 4, April 2004

91. Kus, E. et al, “A Comparison of the Corrosion Behavior of Nanocrystalline and Conventional Al 5083 Samples”, *Corrosion* Vol 62, No 2, February 2006

92. Sharma, M. and Ziemian, C., “Pitting and Stress Corrosion Cracking Susceptibility of Nanostructured Al-Mg Alloys in Natural and Artificial Environments”, *Journal of Materials Engineering and Performance*, Vol 17(6), December 2008

93. Lange, D.A. et al., “Analysis of Surface Roughness Using Confocal Microscopy”, *Journal of Material Science* 28 (1993) 3879-3884

94. Information provided from the University of Virginia, “3D S Parameters – Height (Amplitude) Parameters”, email from R. Kelly to K. Tran, dated April 5, 2011

95. http://www.deform.com

96. Zinn, W. and Scholtes, B., “Mechanical Surface Treatments of Lightweight Materials – Effects on Fatigue Strength and Near-Surface Microstructures”, *Journal of Materials Engineering and Performance*, Vol 8(2) April 1999

97. Grinspan A. and Gnanamoorthy, R., “Surface Modification by Oil Jet Peening in Al Alloys AA6063-T6 and AA6061-T4”, *Applied Surface Science* 253 (2006) 997-1005

98. Abramov, V.O. et al., “Surface Hardening of metals by Ultrasonically Accelerated Small Metal Balls”, *Ultrasonics* 36 (1998) 1013-1019

99. Joseph, A. et al., “Evaluation of Residual Stresses in Dissimilar Weld Joints”, *International Journal of Pressure Vessels and Piping* 82 (2005) 700-705

100. American Society for Testing and Materials, “Standard Specification for Aluminum and Aluminum-Alloy Sheet and Plate,” ASTM B209-10, November 2010

101. Itoga, H. et al. “Effect of Surface Roughness on Step-wise S-N Characteristics in High Strength Steel”, *International Journal of Fatigue* 25 (2003) 379-385

102. Dai, K. et al., “An analytical Model of the Surface Roughness of an Aluminum Alloy Treated with a Surface Nanocrystallization and Hardening Process”, *Scripta Materialia* 52 (2005) 259-263

103. Bayoumi, M.R., and Abdellatif, A.K, “Effect of Surface Finish on Fatigue Strength”, *Engineering Fracture Mechanics*, Vol 51, No. 5, pp 861-870, 1995

104. Eftekhari, A. et al., “Influence of Surface Condition on the Fatigue of an Aluminum-Lithium Alloy (2090-T3)”, *Materials Science and Engineering A* 199 (1995) L3-L6